Universidade Federal do Rio Grande do Sul
Programa de Pós Graduação Em Física
Tese de Doutorado

Extragalactic stellar clusters in high density environments

Aglomerados estelares extragaláticos em ambientes de alta densidade

Emílio José Bento Zanatta

Tese realizada sob orientação da Prof. Dr. Ana Leonor Chies Santiago Santos e apresentada ao Programa de Pós-Graduação em Física da Universidade Federal do Rio Grande do Sul, como requisito parcial para a obtenção do título de Doutor em Física.

Porto Alegre, Novembro 2021

Trabalho financiando pelo CNPq e CAPES

Acknowledgements

This work was only possible given the support of CNPq and CAPES, and the supervision of Ana and Rúben. I known I am not the easiest student to supervise, so I thank every one of my supervisors and professors along the way for the support, teaching and patience. Beyond my supervisors and funding agencies, this work owes its existence not to me, but to several people surrounding it. I was merely a vessel through whom the words in these thesis were written, codes were run and graphs were plotted.

With Maitê, my partner through the last 10 years of my life, not only I was able to find constant support and relief, but also the privilege of countless home lessons on statistics, science, organisation and life itself. I only hope I can be as important and helpful to her scientific career as she was to mine. Luisa kept my motivations in check. Without any doubt most of what made me want to make this thesis as good as possible was the perspective of providing for her opportunities in life that only successful parents are generally able to provide in our country. This is only fair, given the fact that Luisa endured countless hours of my bad humour, lack of motivation, lack of time to be with her and many other consequences of my choices in academia.

About the family I was born in, I can only say that they simply provided me with love, support and money. With no intent whatsoever to sound ungrateful to their support, it is relevant to note that they provided me with what everyone in this country should have the right too, regardless of ethnicity, gender, social class or whatever. Fátima has taught me to be honest above everything and the worth of a hard day of work. These values learned from my mother helped move ahead in the academia more than people can imagine. Lúcia was the greatest support I could have ever asked to conclude a PhD in this country and age. From the start at undergrad to the final months of PhD – when I was left without grants for months – her often unquestioned financial support was absolutely essential. But also, the fact that she was always a phone call away to listen to everything from a life very different from anything she once knew can not be overstated on its importance in my mental health and guidance through life. Arlete, Marcelo and Nelson also were more important than probably even they imagine. From the knowledge that someone in the world would accept me despite any atrocities I could ever commit – as maternal grandmothers often do, to the always present hunger for knowing of my uncle, a safe haven was always waiting for me among them. I remember when I was younger to spend a few days at their house and how many hours I have passed investigating the books that Nelson had on several encyclopedical subjects. Not only that, but he was probably the first adult person to ever consider me as worth of discussing history, politics and other "adult" subjects. Without any doubt I was not the greatest partner for a conversation on these subjects, but nevertheless a seed of knowledge thirst was being planted. It is not fair that I could not be, until the very end, by the side of someone so important to where I am today. The same can be said about Álvaro, who despite some questionable decisions along the way, undeniably was always my role model in pursuing the objective of learning everything that is possible. I wonder how much he would have enjoyed to know where I was able to arrive.

Finally, I want to thank the friends I made along the way. Among them, the most important without a doubt are Sofia, Odin and Chico. Three friends that helped me always have my feet on the ground but above all the meaningless problems the human race has invented. The only things that really matter are enough food in our bowls and finding the most comfortable and safest possible place to sleep. Everything else is optional. Do not ever forget this.

‘It is almost irresistible for humans to believe that we have some special relation to the universe (...) It is very hard to realise that this is all just a tiny part of an overwhelmingly hostile universe. It is even harder to realise that this present universe has evolved from an unspeakably unfamiliar early condition, and faces a future extinction of endless cold or intolerable heat. The more the universe seems comprehensible, the more it also seems pointless. But if there is no solace in the fruits of our research, there is at least some consolation in the research itself. (...) The effort to understand the universe is one of the very few things that lifts human life a little above the level of farce, and gives it some of the grace of tragedy.’

Steven Weinberg, 1993, in the epilogue of The First Three Minutes

Abstract

Stellar clusters are ubiquitous in all luminous galaxies and have the potential to be used as tracers of galaxy formation and evolution if we understand their formation and assembly into their host systems. They have been studied in the astrophysical literature almost since the start of extragalactic astronomy, and the imminent dawn of the next generation of telescopes will enable unprecedented amounts of extragalactic stellar cluster data. However, there are still glaring open issues in our understanding of these objects. We have yet to be able to properly predict, for instance, the colours of extragalactic globular clusters (GCs) in high-density environments and whether or not there is an influence of the environment in the formation of nuclear star clusters (NSCs).

In this work we tackle these two questions. We start by investigating the fraction of galaxies hosting NSCs in the Coma Cluster. NSCs are central stellar clusters, a few pc larger than GCs, present in galaxies of a wide variety of size and masses. Using deep HST data and a Bayesian hierarchical logistic regression technique, we find that the nucleation fraction for galaxies in the Coma cluster is higher than in the Virgo and Fornax clusters for a fixed galaxy luminosity/mass. We discuss the possible environmental influences in the formation and evolution of NSCs, their host galaxies, and associated GCs.

Afterwards we investigate the known discrepancies between the current generation of stellar population models and the observed colours of extragalactic GCs. To this end, we test four state-of-the-art simple stellar population (SSP) models against the observed colours of GCs around M87 in the Virgo cluster and NGC 3311/NGC 3309 in the Hydra cluster. We test whether the discrepancies between models and data increase as a function of environmental density by looking at the very inner regions of these two GC systems with photometric data ranging from the near-ultraviolet (NUV) to the near-infrared (NIR). Besides using data from the literature, we present new K_s band imaging in the NIR from the HAWK-I instrument on ESO/VLT for the centre of the Hydra and Virgo clusters. We investigate whether or not currently available SSP models with increased [α/Fe] ratios are able to better predict extragalactic GC colours, as it has been suggested in the literature. We find that current SSP models with α-enhancement still struggle to match the observed colours of extragalactic GCs. The difference between models with standard Milky-Way chemical abundances and with a constant [α/Fe]=0.4 is not large enough to produce significant differences in colour-colour diagrams. Nevertheless, we find that the increase in discrepancies between SSP model predictions and observed optical colours is present for both Virgo and Hydra cluster GCs, but are not present in important colour-colour diagrams involving a combination of NUV/optical and NIR filters, such as uiK_s. We discuss how these results can be used to constrain the next steps in improving SSP models ahead of the next generation of NIR photometry.

In summary, this work aims to investigate important questions in this current age and in the context of the study of extragalactic stellar cluster systems: i) How can we make the most of the current photometric data using robust statistical techniques, in the context of the open questions of NSC formation, and ii) the importance to improve currently available SSP models to predict colours of extragalactic GCs and the impact of abundance variations in the this matter.

Resumo

Aglomerados estelares estão virtualmente presentes em todas as galáxias luminosas e têm o potencial de serem usados como traçadores da formação e evolução de galáxias se entendermos sua formação e assimilação aos seus sistemas hospedeiros. Eles tem sido estudados na literatura astrofísica praticamente desde o início da astronomia extragalática, e o iminente amanhecer de uma nova geração de telescópios gerará quantidades sem precedentes de dados para aglomerados estelares extragaláticos. No entanto, ainda existem grandes problemas abertos no nosso entendimento destes objetos. Ainda temos, por exemplo, que conseguir predizer corretamente as cores de aglomerados globulares (GCs) extragaláticos em ambientes de alta densidade e se há ou não uma influência do ambiente na formação de aglomerados estelares nucleares (NSCs).

Neste trabalho tratamos destas duas questões. Começamos investigando a fração de galáxias que possuem NSCs no aglomerado de Coma. NSCs são aglomerados estelares centrais, alguns pc maiores que GCs, presentes em galáxias dos mais variados tamanhos e massas. Usando dados profundos do HST e uma técnica de regressão logística hierárquica Bayesiana, nós encontramos que a fração de nucleação para galáxias no aglomerado de Coma é mais alta que nos aglomerados de Virgo e Fornax para uma massa/luminosidade de galáxias fixa. Nós discutimos as possíveis influências ambientais na formação e evolução de NSCs, suas galáxias hospedeiras e os GCs associados.

Posteriormente investigamos as discrepâncias conhecidas entre a atual geração de modelos de populações estelares e as cores observadas de GCs extragaláticos. Para este fim, nós testamos quatro modelos de populações estelares simples (SSPs) no estado-da-arte contra as cores observadas de GCs em torno de M87 no aglomerado de Virgem e NGC 3311/3309 no aglomerado de Hydra. Nós testamos se as discrepâncias entre modelos e dados cresce em função da densidade ambiental olhando nas regiões mais internas deste dois sistemas de GCs com dados fotométricos indo desde o ultra-violeta próximo (NUV) ao infravermelho próximo (NIR). Além de utilizar dados da literatura, apresentamos dados inéditos na banda K_s no NIR do instrumento HAWK-I do VLT do ESO para o centro dos aglomerados de Hydra e Virgo. Investigamos se modelos atuais com razões de [α/Fe] elevados são capazes de prever melhor as cores de GCs, tal como é previsto pela literatura. Encontramos que os modelos SSP atuais com [α/Fe] elevados ainda têm dificuldades em prever as cores observadas de GCs extragaláticos.

A diferença entre modelos com abundâncias químicas no padrão da Via-Láctea e com uma razão constante [α/Fe]=0.4 não é grande o suficiente para produzir diferenças significativas em diagramas cor-cor para os GCs observados. No entanto, nós encontramos que o acréscimo nas discrepâncias entre modelos SSP e as cores óticas observadas está presente tanto para GCs em Virgo quanto em Hydra, mas não estão presentes em importantes diagramas cor-cor envolvendo combinações de filtros NUV/óticos e NIR, como uiK_s. Nós discutimos como estes resultados podem ser usados para restringir os próximos passos em melhorar os modelos SSP à frente da nova geração de fotometria NIR.

Em suma, este trabalho tem por objetivo investigar importantes questões nesta era e no contexto do estudo de aglomerados estelares extragaláticos: i) Como podemos fazer o máximo uso dos dados fotométricos atuais usando métodos estatísticos e robustos, no contexto dos problemas em aberto na formação de NSCs, e ii) a importância de melhorar os modelos de SSPs atualmente disponíveis em predizer as cores de GCs extragaláticos, bem como o impacto de variações de abundâncias neste tema.

Contents

List of Tables

List of Figures

Chapter 1

Introduction

1.1 Galaxy Formation and Assembly

In the beginning of the 20th century, as Edwin Hubble confirmed the existence of galaxies beyond the Milky Way, we already started to wonder how not only ours, but all of the other galaxies in the Universe formed and evolved. This is an incredibly recent scientific field with a lot more questions than answers. Nevertheless, after about one century of observations and theoretical advances, we have a reasonable idea of how most of the galaxies have come to be. Generally speaking, galaxies are thought to be formed as a result of a hierarchical process (See Fig. 1.1, Gunn and Gott, 1972; Press and Schechter, 1974; White and Rees, 1978; Davis et al., 1985; Abadi et al., 2003; Kormendy et al., 2009). In such, galaxies form from a spinning gas cloud inside dark matter haloes that after reaching enough density sparks the creation of the first stellar clusters (Elmegreen and Efremov, 1997; Tegmark et al., 1997; Beasley et al., 2002; Steinmetz and Navarro, 2002; Gao and White, 2007; Ceverino et al., 2015; Garland et al., 2015; Fisher et al., 2017). By looking at high redshift galaxies we see possible examples of objects in this formation stage, where red clumps of bright stars spin in disk structures (Shapiro et al., 2010; Genzel et al., 2011; Garland et al., 2015). These initial stars evolve in a very unstable system, where dynamical friction and mass segregation play a crucial role inducing the formation of bulges and the chemical enrichment of this initial stellar populations over time (Fisher et al., 2017). We observe in the Milky-Way and nearby galaxies that the stellar population of the bulges are indeed comprised mostly of old and metal-rich stars (Feltzing and Gilmore, 2000; Kuijken and Rich, 2002; Valenti et al., 2013; Morelli et al., 2008; Morelli et al., 2013).

Since galaxies are thought to be formed from immense gas clouds in dark matter overdensities, it is not too surprising that galaxies rarely form isolated. Indeed, in the hierarchical scenario, after the initial starburst, galaxies of higher masses are expected to form from sequential mergers of smaller galaxies (Gunn and Gott, 1972; Press and Schechter, 1974; White and Rees, 1978). Such smaller galaxies would not be massive enough to harbour stars as metal-rich as the stars of the larger neighbouring galaxies. Even so, such galaxies would harbour metal-poor stars as well as stellar clusters. Those stellar clusters would, naturally, be also comprised of metal-poor stellar populations. Eventually those smaller galaxies are then incorporated into larger galaxies, in merger events, and end up building the stellar populations of the halos we see today in most massive galaxies (Huang et al., 2016; Oliva-Altamirano et al., 2015; Pastorello et al., 2015; Iodice et al., 2019; Lacerna et al., 2020).

Merger events are, however, very complex processes that have been studied for decades from observations and simulations. It is thought that most of the diversity of galaxy morphologies we see today is a product of different merger histories (Beckman et al., 2008; Oliva-Altamirano et al., 2014; Inagaki et al., 2015; Lidman et al., 2013; Fitzpatrick and Graves, 2015; La Barbera et al., 2014). One such examples are the enormous elliptical galaxies in the centre of clusters which are thought to be brought into this morphology essentially by accreting a large number of galaxies within the high density environment of a galaxy cluster (La Barbera et al., 2014; Fitzpatrick and Graves, 2015; Inagaki et al., 2015). Disk galaxies (spiral and lenticulars), on the other hand, are thought to be less hungry objects which have accreted only a small fraction of smaller galaxies. Imprints of these events can be found in the stellar populations of halos and globular cluster (GC) systems, but were not prevalent enough to alter in any major form its overall morphological structure (Bekki et al., 2005, 2002; Borlaff et al., 2014; Boselli and Gavazzi, 2006). Nevertheless, such diverse are the possibilities in a merger event, that even a single major merger in specific conditions may be enough to induce a drastic transformation

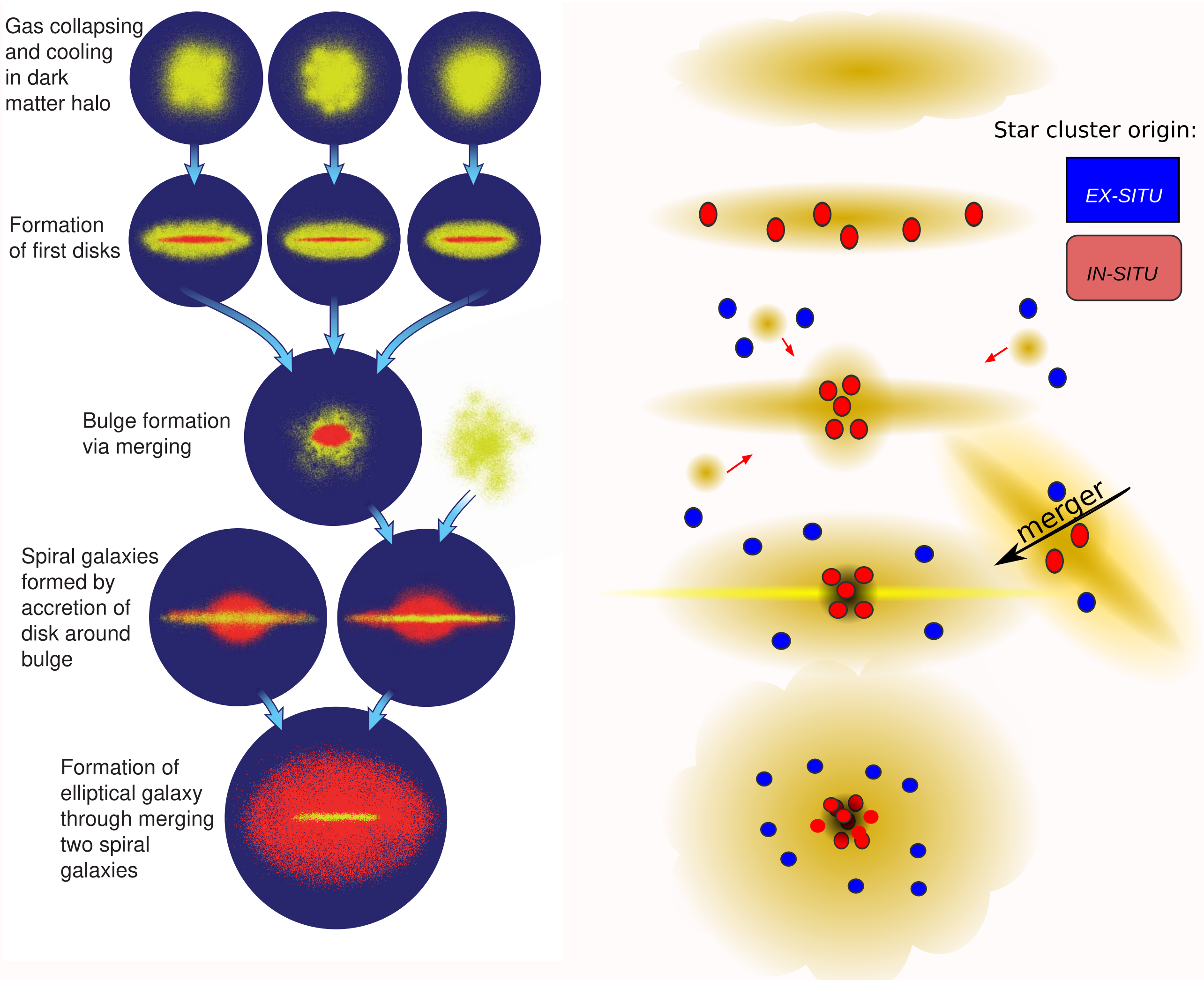

Figure 1.1: Galaxy formation via a hierarchical process (simplified schematics). Adapted from Bertola (2002). *Left, from top to bottom:* Primordial gas cools and collapses into a dark matter halo, due to gravity. The first stars are born and give rise to the formation of the first disks. As galaxies are theorised to rarely form isolated, the primordial disk galaxies tend to interact and eventually merge, originating the first bulges. Disks are reformed after some time around the bulges, forming spiral galaxies, such as the Milky-Way. Minor accretions of smaller satellites and infalling gas from environment interactions with neighbouring galaxies occur at the same time. The subsequent merging of these two, already massive, spiral galaxies gives birth to an elliptical galaxy. While didactic, it is important to note that this simplified scheme does not include several possibilities in current understanding of galaxy evolution that originate the wide diversity in galaxy morphologies we can observe in the universe. *Right, from top to bottom:* The same schematics of galaxy evolution, but highlighting the role of stellar clusters. *In-situ* stellar clusters are formed within the primordial galaxy, while *ex-situ* stellar clusters are accreted other galaxies via interactions. The final elliptical galaxy stellar cluster population is then a combination of all the surviving clusters from the different processes in galaxy evolution, and hence their properties can be used as indicators of their host galaxy evolutionary history.

in a regular spiral galaxy, both morphologically and in stellar populations(Borlaff et al., 2014; Boselli and Gavazzi, 2006).

Among dwarf galaxies, on the other hand, the scenario is more diverse. Among low-massive galaxies there are some that present strong star formation activity (Thronson and Telesco, 1986; Östlin et al., 2004; Pildis et al., 1997) and others which, much like ellipticals, are currently forming very few to no stars (Binggeli and Cameron, 1991; Miller et al., 1998).

On top of those, but with no minor importance, further environmental effects also drastically affect the evolution of galaxies, in processes such as ram-pressure stripping, harassment, starvation and so on (Gunn and Gott, 1972; Boselli and Gavazzi, 2006). Those events mainly affect the cold, molecular gas in galaxies, in ways to enhance or decrease star formation in specific regions or galaxy-wide (Ebeling and Kalita, 2019; Vulcani et al., 2018) and even altering the whole galaxy morphology (Gunn and Gott, 1972; Bekki et al., 2006, 2002).

1.2 Galaxies studied in this work

1.2.1 Central Dominant Elliptical Galaxies

A very well studied class of elliptical galaxies are the ones located in the high-density environments, such as the central regions of galaxy clusters (central dominant galaxies, cD Chiosi and Carraro, 2002; Foster et al., 2011; Dressler et al., 1997). cD galaxies have masses in the range of 10^{10}-$10^{13} M_\odot$ (Chiosi and Carraro, 2002; Foster et al., 2011) and typically host thousands of globular clusters (GCs) (Brodie and Strader, 2006; Wehner et al., 2008a; Durrell et al., 2014). In such massive galaxies, different astrophysical processes shape different substructures in a varying galactocentric radius. For instance, the stellar content at central regions experience effects such as active galactic nuclei (AGN) feedback and have enough stellar density for dynamical friction to play a significant role, while at their halos – which can extend to hundreds of Kpc from the galaxy centre – are home for interactions with the neighbouring cluster environment, such as the accretion of infalling satellites (Lotz et al., 2001; Miller et al., 2020;

Milosavljević, 2004; Seth et al., 2006). Moreover, due to their sizes, central locations within clusters and estimated ages, evidence suggest that the assembly of cD galaxies is intrinsically correlated with its host galaxy cluster evolution (Forbes et al., 1997; Romanowsky et al., 2012; Taylor et al., 2019; Dalal et al., 2008).

M87 and the Virgo Cluster

M87 is a bright (B=9.8 mag, Gavazzi et al., 2005), massive ($\mathcal{M} \sim 10^{12} M_{\odot}$, Wu and Tremaine, 2006) elliptical galaxy and the central galaxy of the Virgo cluster, one the nearest galaxy clusters to the local group. The Virgo cluster is located at a distance of 16.5 ± 0.2 Mpc (Mei et al., 2007) and has over 2000 galaxy members (Binggeli et al., 1987; Gavazzi et al., 2003). It can be divided into 3 main regions, *Virgo A, Virgo B* and *Virgo C* (Boselli et al., 2014). M87 is located at the centre of Virgo A, the densest of these subclusters. Due to its morphological type, size, brightness and closeness to the Milky-Way, the GC system of this galaxy has been focus of photometric studies for many decades already (Boselli et al., 2014; Peng et al., 2006a; Muñoz et al., 2013; Oldham and Auger, 2016b; Chies-Santos et al., 2011b,c; Faifer et al., 2011, and many others). There have also been several spectroscopic studies (Mould et al., 1987; Cohen et al., 1998; Romanowsky et al., 2012; Strader et al., 2011; Ko et al., 2017), but they have limitations both in sample size and spatial coverage. It is complicated to get reasonable signal-to-noise ratios on GC spectra that are located within the halo of M87, specially at very central regions, given the bright background of the galaxy stellar light. Therefore for a larger fraction of the GC system the available data in the literature is from photometry only.

Some noteworthy examples of GC system studies in the Virgo cluster include Grillmair et al. (1986), Cohen (1988) and the Advanced Camera for Surveys Virgo Cluster Survey (ACSVCS) (Peng et al., 2006a). The later introduced a very central sample of deep photometry (in the $F475W$ and $F850LP$ filters of the Hubble Space Telescope) for M87 GCs compared to earlier works. Through the ACSVCS, studies connecting GCs to the formation and dynamics of other types of star clusters were made possible. One example is Hasegan et al. (2005) that tackles the relation between GCs and UCDs. Recently the Next Generation Virgo Survey (NGVS) and its NIR extension (NGVS-IR) (Ferrarese et al., 2012; Muñoz et al., 2013) presented another giant leap in GC data introducing $ugrizKs$ data for thousands of GC candidates around M87 and neighbouring galaxies. Later, Oldham and Auger (2016b) revisited the NGVS data and obtained a catalogue of GC candidates with over 17.000 objects, and ever since became the largest photometric GC sample for M87 GCs.

Some properties of the M87 GC system are worth noting. For instance, we know that there is a very clear colour gradient for most GC systems from the inner regions to the halo, with red GCs dominating the centre and blue GCs comprising the majority of halo GCs (Oldham and Auger, 2016b; Montes et al., 2014). It is very well known that M87 GCs have a clear bimodality in the optical colours (Peng et al., 2006a; Oldham and Auger, 2016b). Tamura et al. (2006) with a wide GC photometric sample out to 0.5 Mpc from the centre of the galaxy has shown also a clear trend for the colour bimodality in $(V-I)$ to be stronger for inner GCs. However, Chies-Santos et al. (2012b) showed that such bimodality may vanish when we look into colours combining optical and NIR filters, such as $(g-K_s)$. One possibility is that a non-linear relation between colour and metallicity drives such optical colour bimodality (Yoon et al., 2011a,b; Chies-Santos et al., 2012b; Cantiello and Blakeslee, 2007; Blakeslee et al., 2012).

NGC 3311 and NGC 3309 in the Hydra Cluster

NGC 3311 is the cD galaxy of the Hydra A1060 cluster (also known as Hydra I), a bright (Postman et al., 2005, $B = 13.2$ mag) galaxy located just around ~ 1.6' away from NGC 3309, very bright (de Vaucouleurs et al., 1991, $B = 12.23$ mag) elliptical galaxy. NGC 3311 is the most well studied galaxy between the two, standing as an attractive target for GC studies due to being relatively nearby (~ 53 Mpc) and hosting a GC population large enough to be comparable to M87 (Wehner et al., 2008b). Ground-based imaging from Secker et al. (1995) and McLaughlin (1995) already indicated the presence of a relatively metal-rich GC system with a hint of bimodality and an ellipicity similar to the cD light envelope. HST imaging from Brodie et al. (2000a) was able to probe that the GC system metallicity distribution was likely bimodal, and intermediate-age GCs ($\sim$ 3-6 Gyrs) were found by Hempel et al. (2005) also with

HST data.

The GC system of NGC 3311 is very likely to be interacting with the one from the nearby giant elliptical NGC 3309. Harris et al. (1983) and McLaughlin (1995) estimated the contamination of NGC 3309 GCs in the NGC 3311 system to be small, considering the large system of NGC 3311, and Wehner et al. (2008b) estimate 16500±2000 as the total number of GCs in the NGC 3311 system, while NGC 3309 would host an unusual low number of 374±210 GCs. This suggests that NGC 3309 might have lost some of its GCs to NGC 3311 (Richtler et al., 2011). Despite their closeness, the lack of distortions in the X-ray isophotes of NGC 3309 detected by Yamasaki et al. (2002) and Hayakawa et al. (2006) strongly support the assumption that NGC 3311 is the *de facto* center of the galaxy cluster potential and actually at some larger distance from NGC 3309 than the projected distance. Furthermore, the lack of distortions in the X-ray isophotes indicate that a merger interaction between the two galaxies is very unlikely to have even ocurred in the past (Yamasaki et al., 2002; Richtler et al., 2011). In fact, using surface brightness fluctuations, Mieske et al. (2005) quotes that NGC 3309 is likely in the foreground relatively to NGC 3311.

Low surface brightness galaxies in the Coma Cluster

Low surface brightness galaxies (LSBGs) are usually defined as the galaxies which effective surface brightness fall below the surface brightness limits of wide-area surveys (such as the Sloan Digital Sky Survey (SDSS), Jester et al., 2005), i.e. around ~ 24 mag arcsec^{-2} in the r-band (Jackson et al., 2021). Therefore, despite overall difficulties in detection, deep surveys such as McGaugh et al. (1995), Bothun et al. (1997) and Dalcanton et al. (1997) were able to first detect these objects. In recent years the interest in them has increased as more and more LSBGs are being detected, usually as satellites of larger galaxies (Amorisco and Loeb, 2016; Carlsten et al., 2021). Moreover, cosmological simulations indicate that LSBGs comprise $\geq$ 85% of objects down to $M \sim 10^7\ M_{\odot}$, constituting the dominant component of galaxy number density (Martin et al., 2009). This fact alone makes LSBGs key figures to understand galaxy formation as a whole.

Nevertheless, understanding the formation of LSBGs has proven to be a challenging task. A myriad of formation processes have been suggested in theoretical works, such as high halo spin (Amorisco and Loeb, 2016), mergers (Wright et al., 2021) and formation from high angular momentum gas (Liao et al., 2019), to name only a few. The presence of LSBGs both in groups (e.g., Merritt et al., 2016) and in the field (e.g., Martínez-Delgado et al., 2016) further complicate constraining their formation processes, since this type of galaxies is not a phenomenon exclusive to cluster environments.

Morphologically speaking, LSBGs form an heterogeneous group. A variety of galaxy classifications further define members of the LSBG class, such as ultra-compact dwarfs (UCDs, van Dokkum and Conroy, 2012). Due to their faint nature, the study of distant LSBGs relies heavily on discrete tracers, such as stellar clusters (e.g. den Brok et al., 2014; Van Dokkum et al., 2017; Sánchez-Janssen et al., 2019, to name a few).

In this work, we explore the population of LSBGs around the central galaxies in the Coma cluster. The Coma cluster is located ~ 100 Mpc from us Carter et al. (2008) and is one of the densest galaxy clusters in the nearby Universe (Blakeslee et al., 2012). Environmental effects on galaxy formation are generally proportional to the environment density (Gunn and Gott, 1972; Brodie and Strader, 2006; Bekki et al., 2006). For instance, galaxy mass assembly in denser environments is expected to occur at a faster rate (Mistani et al., 2016), the fraction of quenched galaxies increases in relation to the field (Dressler, 1980; Coccato et al., 2020) and interactions between galaxies are more common (Yoon et al., 2017). Therefore, the Coma cluster stands as a perfect laboratory to study the effects of environment in several different aspects of galaxy formation, including the LSBG regime (den Brok et al., 2014).

1.3 The role of Star Clusters

Along galaxy formation and assembly, star clusters are formed and destroyed. The ones that survive to be able to be observed and studied today are witnesses and relics of the their host galaxies evolution (Beasley et al., 2002; Brodie and Strader, 2006). They are present in the central regions of galaxies in the form of nuclear star clusters (NSCs), in complex orbiting systems as GCs, in the star forming regions of galaxies in the shape of open clusters or young massive clusters (YMCs), or even in between galaxies, the so-called intracluster GCs. They are one of the most accessible ways to study galaxy evolution, due to their ubiquity among galaxies of almost every size, mass and morphological types (Brodie and Strader, 2006). Furthermore, they are bright enough even in distant galaxies outside our Local Group for several of their physical properties to be measured. For instance, by studying their spectra we can have a general idea on their stellar content. Their ages, metallicites and chemical abundance variations can then be used to infer the existence of important events in their host galaxy evolution. For instance, star-formation inducing events, such as wet mergers, can be detected via the presence of younger subpopulations of stellar clusters (e.g., Fujii et al., 2012). In turn, galaxies that experience a more secular evolution process are thought to present a single population of old, metal-rich GCs (e.g., Beasley et al., 2008). Their kinematics, in conjunction with dynamical models, can help explain galaxies' substructures and reveal hints of their origins (Alabi et al., 2017; Bekki et al., 2005; Bellini et al., 2015; Cortesi et al., 2016). The most easily accessible features of star clusters, however, are their colours, since one can obtain photometric data even at distances where the light is already too faint to obtain reliable spectroscopy. Large scale photometric censuses have become available recently, both for GCs in individual galaxies (Brodie et al., 2014; Forbes et al., 2014; Salinas et al., 2015; Romanowsky et al., 2012; Georgiev et al., 2010, 2009, and so on) and whole galaxy clusters (Muñoz et al., 2013; Jordán et al., 2015; Peng et al., 2006c, and so on.). The number of Nuclear stellar clusters (NSCs) data has also become increasingly available for a large number of galaxies, specially in cluster environments (Georgiev and Böker, 2014; Lim et al., 2018; Sánchez-Janssen et al., 2019; Böker et al., 2002, and so on).

In this thesis, we present studies on two types of star clusters - GCs and NSCs. As aforementioned, the number of available data for these type of star clusters in extragalactic objects has increased significantly in recent years. Our view of the evolution of such systems have been for many decades biased towards GCs in the Milky-Way and the local group galaxies,

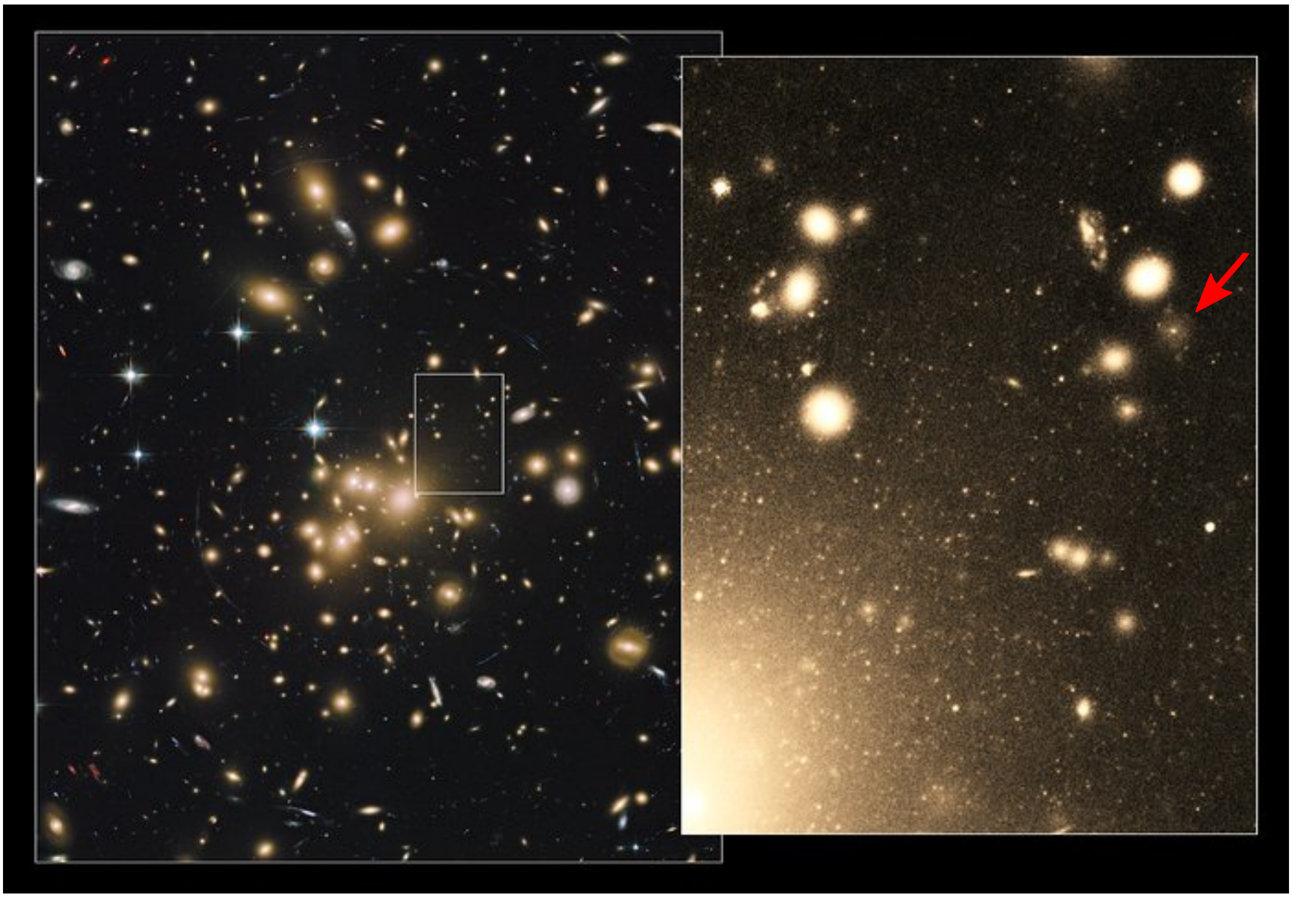

Figure 1.2: Image of the galaxy cluster Abell 1689, showing, on the right-side, a zoomed into the outskirts of the massive central galaxies where we can find thousands of small bright point-sources which are predominantly GCs. The red arrow indicates an example of a dwarf spheroidal galaxy hosting an NSC. Credit: NASA/ESA, J. Blakeslee and K. Alamo-Martinez.

of which some are examples of NSCs. It is not surprising, given the diversity of evolutionary paths already discussed, that extragalactic systems showed up to be very different from these local paradigms. Before discussing these differences, it is important to characterise what we know about these two types of objects that are the central to this thesis.

1.3.1 Globular Clusters

Globular Clusters (GCs) are high density stellar groups formed very early in their host galaxy formation. They have been observed to be in general very old, with ages > 10 Gyr (Blakeslee, 1997; Forbes et al., 2001; Brodie and Larsen, 2002; Chies-Santos et al., 2011c). Their masses span $10^4 - 10^6 M\odot$ with half-light radii of a few pc, in general less than 10 pc (Brodie and Strader, 2006). The GCs we see today in galaxies are expected to have formed after major starburst events (See Fig. 1.1, Oser et al., 2010; Brodie et al., 2014). Such events can be associated to the galaxy formation or processes that happen at a later date, such as wet mergers[1]. A portion of the GCs observed in the systems of large galaxies can also have been formed in smaller galaxies that were accreted into the larger system at some point in time (Gunn and Gott, 1972; Oser et al., 2010; Brodie and Strader, 2006, and references therein). In this context, GC properties such as dynamics, metallicities, ages and chemical abundances can be used to reconstruct important events of a given galaxy's history. GCs are ubiquitously found in almost every galaxy and of all morphological types, but at different amounts. *Early-type* galaxies, for example, usually host an enormous number of GCs (Brodie and Strader, 2006). For instance, M87, the giant elliptical in the centre of the Virgo cluster, is estimated to have over 17 thousand GCs (Oldham and Auger, 2016a). Lenticular galaxies, such as NGC 3115, have over $\sim$ 1000 estimated GCs (Pota et al., 2013; Jennings et al., 2014; Zanatta et al., 2018). *Late-type* galaxies, such as the Milky Way or M31, are estimated to have $\sim$ 200 and $\sim$ 460 GCs, respectively (Massari et al., 2019; Barmby and Huchra, 2001). In Fig. 1.2) an example of a

---

[1] When a merger between galaxies involves the accretion of gas by the larger galaxy it is usually referred to as *wet merger*, in opposition to a *dry merger*. Only the former is associated with an increase of star formation rates (See Oser et al., 2010; Gunn and Gott, 1972; Brodie and Strader, 2006, and references therein).

Hubble Space Telescope (HST) image of the galaxy cluster Abell 1689 is shown. The zoomed-in region illustrates that around galaxies one can see thousands of point-source objects which are mostly GCs.

Star clusters are expected to be present in all galaxy components whereas globular clusters are not likely to survive for long in galactic discs due to rotation effects (Brodie and Strader, 2006)[2] and thus are expected to be found mostly in the central component of galaxies, the bulge, or in their outermost component, the halo. Therefore, metallicities, dynamics and ages of the innermost GC populations of galaxies can offer clues of its in-situ evolution, while GC populations in halos show imprints of environmental processes a galaxy has experienced throughout its history (Bekki et al., 2005; Brodie and Strader, 2006). Radially, GCs are distributed in most cases with the same ellipicity as their host galaxies spheroidal regions, suggesting that at least most of them formed within the galaxy (Brodie and Strader, 2006; Forte et al., 2001; Schuberth et al., 2005), but a fraction of the GC population can result from the accretion of smaller galaxies (Schweizer, 2001).

An important feature of GC populations is the fact that most galaxies display bimodality in their GC population optical colour distribution (see Fig. 1.3)(Ashman and Zepf, 2001; Brodie and Strader, 2006; Chies-Santos et al., 2012b; Peng et al., 2006c). Such bimodality suggests the presence of two distinct GC subpopulations within a galaxy, which would be directly related to its host galaxy evolution. The bluer GC population is generally found in the halo and consist of metal-poor objects, while the redder population, on the other hand, are more metal-rich and present in the inner regions, with similar stellar populations of early-type galaxies such as ellipticals and the thick discs of lenticulars (Cortesi et al., 2013; Pota et al., 2013).

Some physical characteristics, such as mass and size do not differ much between the two populations, while metallicity can show different modes in GC populations that follows the colour bimodality (Yoon et al., 2006; Brodie and Strader, 2006; Cantiello et al., 2014; Lee et al.,

---

[2] Although GCs are not likely to survive in disks, large, old and red star clusters have been found to inhabit the disks of S0 galaxies in the form of faint fuzzies (Chies-Santos et al., 2007; Chies-Santos et al., 2013; Larsen and Brodie, 2000).

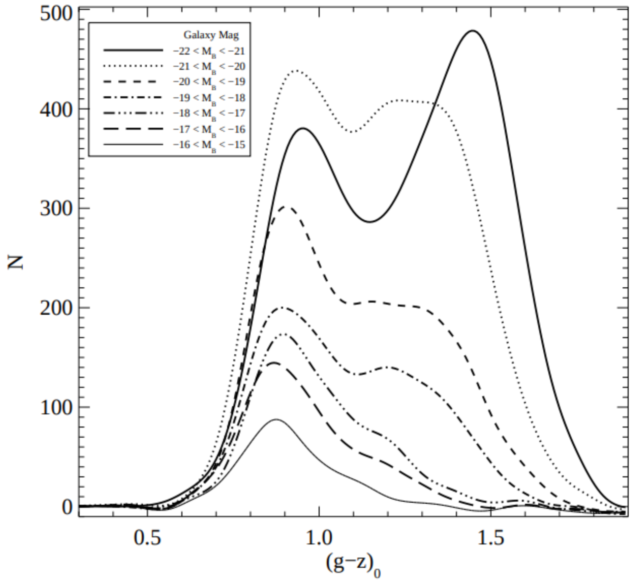

Figure 1.3: Modified figure from Peng et al. (2006c) showing the $(g-z)$ colour distributions for GCs of galaxies in the Virgo cluster, divided in magnitude bins. Here we can see an example of the diversity in colour distributions that scales with mass and brightness. Massive galaxies generally show a bimodal GC distribution, while low-massive galaxies tend to host only the blue peak (Brodie and Strader, 2006; Peng et al., 2006c).

2018). This correlation with metallicity, however, is not universal (Muratov and Gnedin, 2010; Villaume et al., 2019; Fahrion et al., 2020) and alternative views state that it is possible for a flat, almost unimodal metallicity distribution to be present in a GC population that is bimodal in optical colours. Such a fact arises from the choice of SSP models to predict metallicities (Cantiello and Blakeslee, 2007), photometric uncertainties (Cantiello and Blakeslee, 2007; Chies-Santos et al., 2012b; Yoon et al., 2011a), the underlying variance of the metallicity distribution (Lee et al., 2019) as well as the horizontal branch morphology (Yoon et al., 2006). The non-linearity between colour and metallicity becomes clear when we look into colour distributions comprising near-infrared (NIR) filters, for which the colour bimodality for some galaxies is less evident that in purely optical colours. This is the case for NGC 1399 (Blakeslee et al., 2010) and M87 (Chies-Santos et al., 2012), to name a few. Moreover, there are galaxies with GC systems that challenge the paradigm of bimodal GC distributions. A few examples are M31 and NGC 5128, that show flat, almost trimodal GC metallicity distributions (Caldwell et al., 2011; Woodley et al., 2010) and NGC 1277, a lenticular galaxy in the direction of Perseus, that presents a single red GC population suggesting that it experienced almost no merger events, despite its relatively large mass(Beasley et al., 2018).

In elliptical galaxies, GC numbers can reach tens of thousands and extend to several effective radii (Oldham and Auger, 2016a; Muñoz et al., 2013; Jordán et al., 2015; Brodie and Strader, 2006). It is presumed that the innermost GCs of ellipticals are the most likely to be formed within the galaxy in a first major star formation event, in addition to some GCs from accreted galaxies that might have migrated towards the galaxy gravitational potential well. Nevertheless, most of the accreted GCs are thought to be located in the outskirts of galaxies, and indeed in several galaxies we can see a colour gradient that support this hypothesis (Johnston et al., 2018; Oliva-Altamirano et al., 2015; Peng et al., 2006b; Chies-Santos et al., 2012; Oldham and Auger, 2016a). Moreover, some galaxies present GC populations indicative of unique evolutionary histories. NGC 3311 in the Hydra cluster, for instance, displays GCs with a very skewed colour distribution towards the blue, indicating a strong history of merger events (Wehner et al., 2008a,c; Brodie et al., 2000b; Hilker et al., 2018).

Moreover, GCs can also often be disrupted by the influence of dynamical friction and environmental effects alike. This becomes very important both in the bulges of galaxies and inner regions of ellipticals, where today's stellar populations are in some part comprised of stars that once belonged to GCs (Forbes et al., 2001; Kuijken and Rich, 2002). Also, in smaller galaxies, such as dSphs, a fraction of their GCs can also be disrupted in the most central regions and contribute to the formation of NSCs (Neumayer et al., 2020).

1.3.2 Nuclear Star Clusters

At the central regions of galaxies of a wide range of masses, luminosities and morphological types there exists a class of compact stellar systems known as NSCs. Those objects have half-light radii in the range of 1-50 pc, masses from $10^4 M\odot$ to $10^8 M\odot$ and very extreme stellar densities comparable to some GCs and ultra-compact dwarfs (UCDs) (Drinkwater et al., 2000; Hilker et al., 1999). In the zoomed-in panel at Fig. 1.2 one can see an example of an NSC, at the central region of the galaxy indicated by the red arrow. In Fig. 1.4 we show two examples of NSCs and their associated surface brightness profiles when compared to their host galaxies,

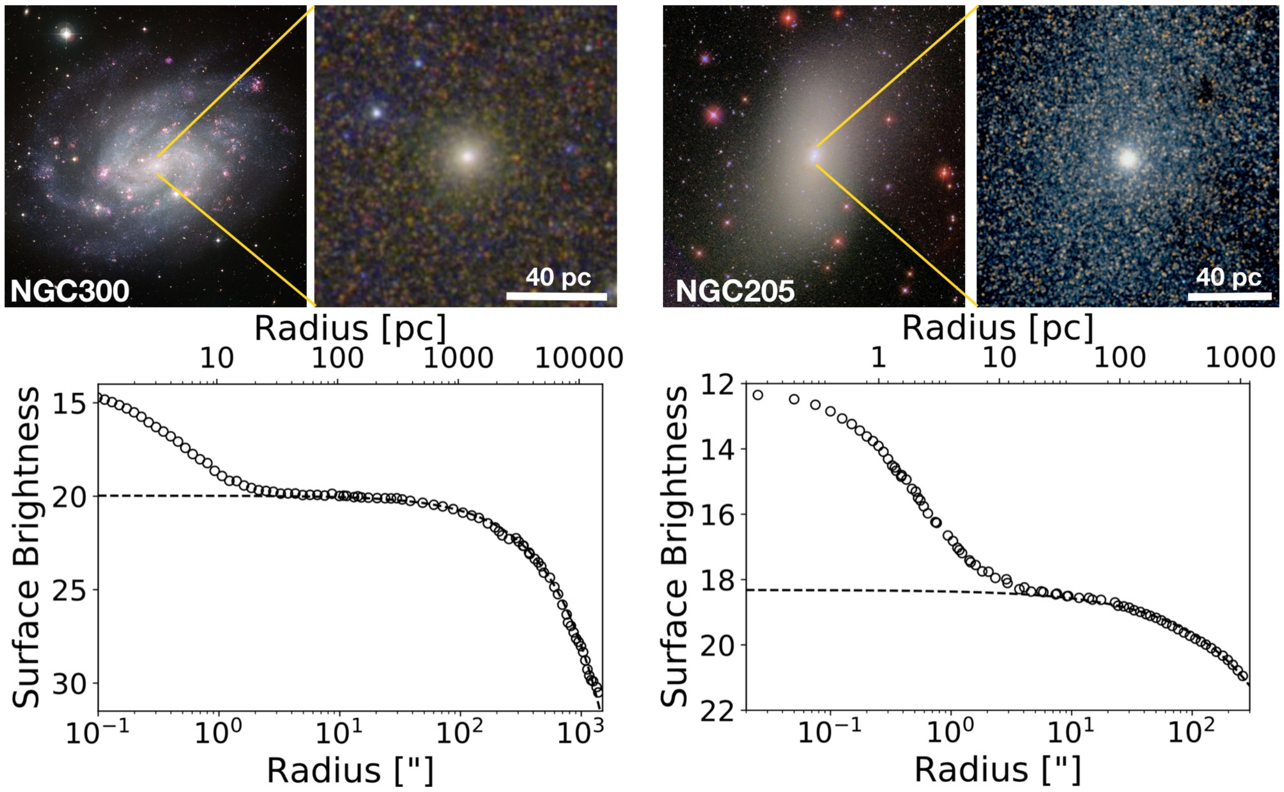

Figure 1.4: Fig. 1 of Neumayer et al. (2020), showcasing the NSCs in the late-type spiral galaxy NGC 300 (left panel) and the early-type galaxy NGC 205 (right panel). The top row shows coloured images of the galaxies with panels zooming in the region around the NSCs, while the bottom row shows the associated surface brightness profiles (in units of I-band mag/arcsec^2). The open circles represent measured data while the dashed line indicates the predicted galaxy profile without the NSC. We refer the reader to Neumayer et al. (2020) for specific details on the data sources.

in this case an early-type and a late-type. Furthermore, in Fig. 1.5 we shown an example of a nucleated dwarf galaxy in the Virgo cluster, adapted from Sánchez-Janssen et al. (2019), and its surface brightness profile (yellow solid line) compared to the one of its host galaxy (red solid line). Notice how the NSC dominates the light profile at inner radii in all cases.

The formation of NSCs has been suggested to derive from two mechanisms, probably non-exclusive, illustrated as a cartoon in Fig. 1.6. At the left side of the figure we show the dissipationless process where already formed stellar clusters decay to the centre of the gravitational potential of the host galaxy and merge forming a large and dense structure (Tremaine et al., 1975; Arca-Sedda and Capuzzo-Dolcetta, 2014; Gnedin et al., 2014). The other mechanism, shown at the right of Fig. 1.6 involves the inflow of gas to the central region of galaxies, where local star formation is triggered at higher rates than usual contributing substantially to

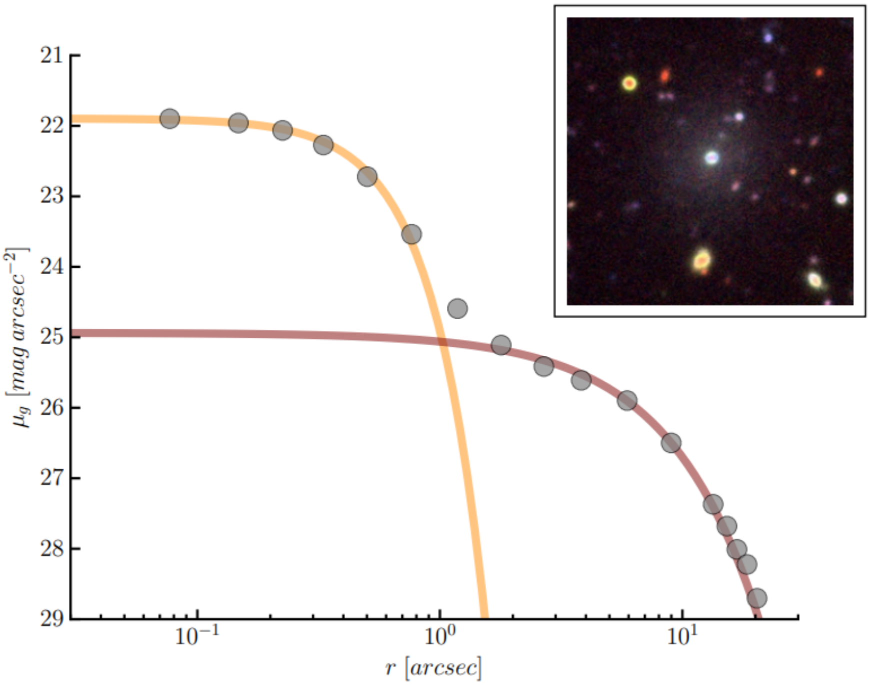

Figure 1.5: Surface brightness profile for the galaxy VCS 1070 in the Virgo cluster (red solid line) and its NSC (yellow solid line). The combination of both is indicated by the grey circles. In the top right panel, in a colour composite image, we find the NSC as the bright object in the centre of the galaxy. Adapted from Sánchez-Janssen et al. (2019).

their mass growth (Bekki et al., 2003; Bekki and Chiba, 2004; Antonini, 2013). Not surprisingly, NSCs display a variety of scaling relations with their parent galaxy, such as stellar mass (Georgiev et al., 2016; Scott and Graham, 2013) and stellar populations (Walcher et al., 2005; Turner et al., 2012; Georgiev and Böker, 2014). Moreover, it has been suggested that there are close relations between the formation of NSCs and GCs in the same galaxy. For instance, in Sánchez-Janssen et al. (2019) it has been shown that at least in the Virgo cluster, the fraction of galaxies hosting either type of star cluster tend to decrease at lower masses in very similar rates. If GCs are suggested to contribute to the formation of NSCs, UCDs on the other hand might be the remains of disrupted nucleated galaxies (Drinkwater et al., 2003; Pfeffer and Baumgardt, 2013; Neumayer et al., 2020).

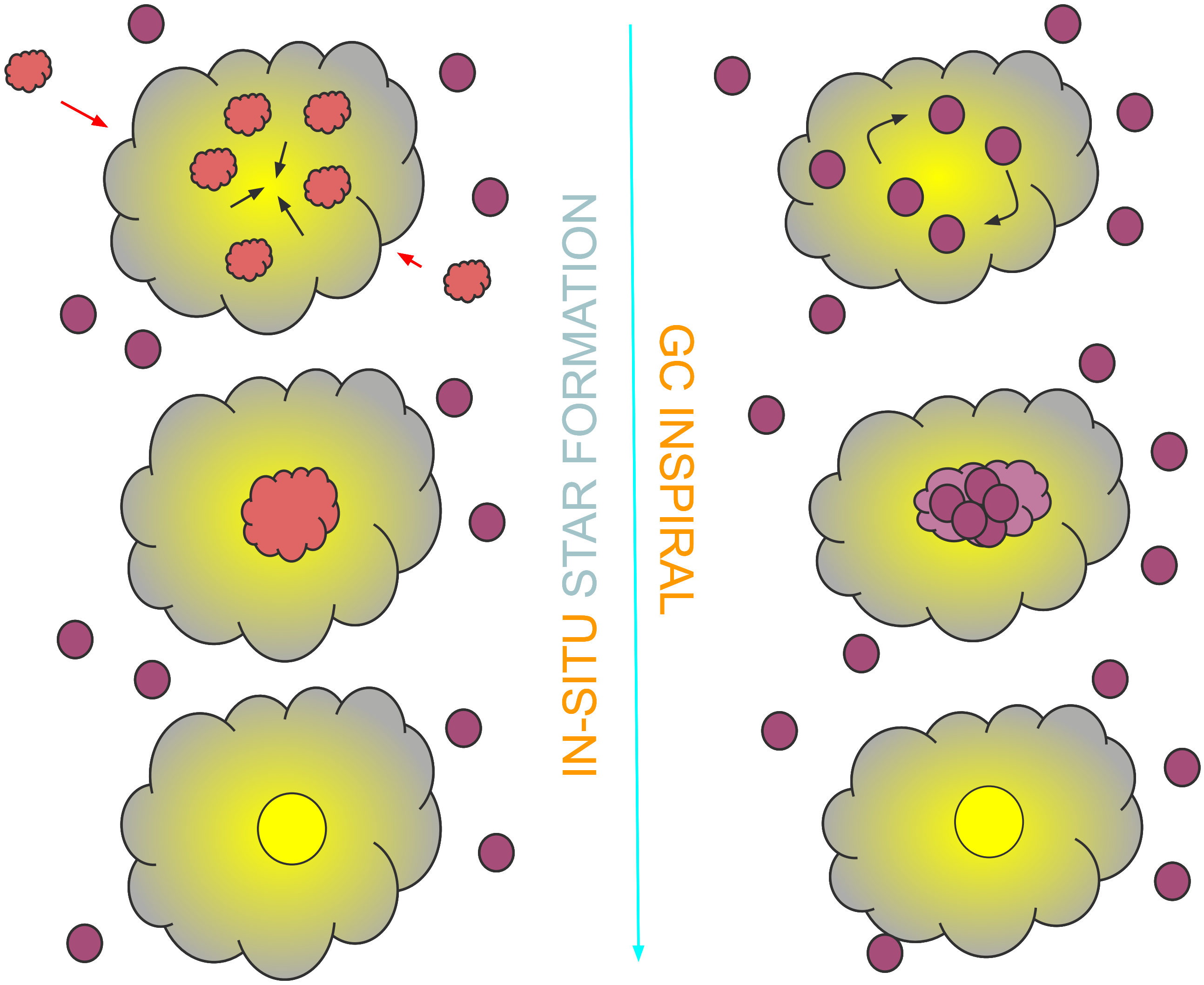

Figure 1.6: NSCs are thought to be formed via two non-exclusive scenarios, showcased in this cartoon. At the left side, we show the inflow of gas (magenta clouds) to the central region of a galaxy (represented as the larger cloud) leading to increased star formation rates and the formation of the NSC (central large yellow circle). At the right, we show the process where some of the already formed GCs within the galaxy (purple circles) are led to its centre via dynamical friction and subsequently merge into a single structure, forming the NSC.

1.4 Motivations

This thesis is divided into two main parts. In chapter 2 the analysis primary focuses on NSCs and in chapter 3 in GCs. Each chapter has unique motivations that are outlined in this section. Nevertheless, we emphasise that the topic that unites the different works within this thesis is the analysis of extragalactic stellar clusters in the context of galaxy evolution, in high density environments.

1.4.1 Is there an environmental dependence on NSC occupation statistics?

Amongst the most fundamental observables informing NSC formation scenarios are their occupation statistics. In other words, what galaxies host NSCs? Stellar nuclei occur almost across the entire spectrum of galaxy types. Historically, much of the early work on NSC demographics focused on galaxies in high density environments such as galaxy clusters, where number statistics are large. As a result, NSC occupation in early-type galaxies tends to be more robustly characterised than in late-types (but for details on star-forming hosts see Carollo et al. 1998, Georgiev et al. 2009, Georgiev and Böker 2014 and Neumayer et al. 2020). Recent studies have established that the nucleation fraction in quiescent galaxies exhibits a strong dependence on galaxy mass or luminosity, with a peak at ∼90% around $\log(\mathcal{M}/\mathcal{M}_{\odot}) \approx 9$ followed by a steady decline toward both higher (Côté et al., 2006; Turner et al., 2012; Baldassare et al., 2014) and lower galaxy masses (den Brok et al., 2014; Ordenes-Briceño et al., 2018; Sánchez-Janssen et al., 2019).

Remarkably, while NSC occupation at the high-mass end seems to be rather universal, dwarf galaxies ($M_{\odot} \lesssim 10^9$) are now known to display a secondary dependence with the environment. By comparing the nucleation fraction from the Next Generation Virgo Cluster Survey (NGVS) (Ferrarese et al., 2012; Muñoz et al., 2013) with literature data for other environments Sánchez-Janssen et al. (2019) show that NSC occurrence is highest in Coma cluster dwarfs, followed by Virgo and Fornax, with the lowest nucleation fraction found in early-type satellites

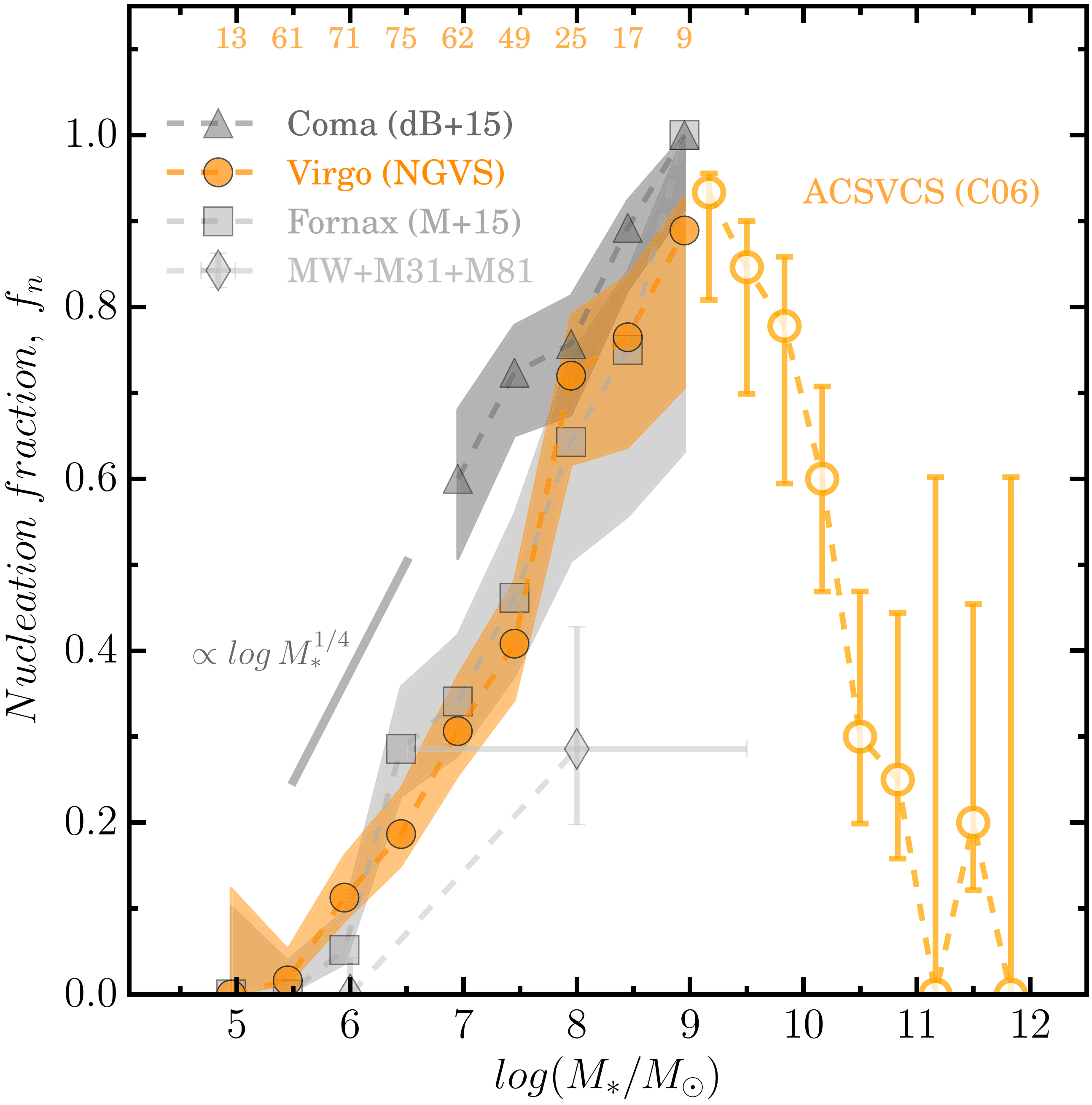

Figure 1.7: Fig. 2 of Sánchez-Janssen et al. (2019) showing the fraction of nucleated galaxies in the Virgo, Fornax and Coma Clusters (circle, squares and triangles, respectively) as a function of stellar mass. Also shown are the nucleation fractions of satellites of three nearby late-type dominated galaxy groups. Shaded regions and error bars show the 68% Bayesian credible interval, with the numbers on top representing the number of galaxies in each bin for the Virgo sample. Notice that the Coma cluster data, in this figure limited to a sample of relatively massive galaxies from the den Brok et al. (2014) catalogue, suggests a larger nucleation fraction at fixed stellar mass than any of the other environments. Would this environmental bias hold up if we included lower massive galaxies in the Coma sample?

in the Local Group (see Fig. 1.7). This is consistent with early results showing that nucleated early-types tend to inhabit the inner, higher density regions of the Virgo cluster (Ferguson and Sandage, 1989; Lisker et al., 2007). But Sánchez-Janssen et al. (2019) expand on these studies to show that the behaviour holds at fixed galaxy mass, i.e, dwarfs of any given luminosity have a higher probability of being nucleated when they inhabit host haloes of larger virial masses. A shortcoming of that analysis is that the limiting magnitude of the Coma cluster sample (den Brok et al., 2014) is significantly brighter than in all the other environments: $M_I \approx -13$ vs $M_I \approx -9$, well over an order of magnitude in luminosity. As a result, the exact behaviour of the nucleation fraction in this most rich environment is not yet fully characterised – does it remain exceptionally high down to the faintest luminosities, or does nucleation become negligible for galaxies of comparable luminosity to those in the Virgo and Fornax cluster?

Chapter 2 aims at finally settling this question through the use of deep *HST/ACS* imaging of the core of the Coma cluster to study the demographics of NSCs. We also develop a novel Bayesian logistic regression framework to model the probability of nucleation, which enables us to self-consistently investigate its dependence on galaxy luminosity and environment for dwarfs in other clusters and groups.

1.4.2 Limitations in the prediction of observed GC colours with current SSP models

In the recent years several new photometric data were released for extragalactic GCs, exponentially improving the amount of available data in field. Some examples include: The aforementioned NGVS, the *SLUGGS* survey (Brodie et al., 2014), the ACS Virgo (Peng et al., 2006c) and Fornax (Jordán et al., 2015) surveys, among several others. Thanks to these, we were able to improve on several topics in the field, such as more precise age and metallicity estimates, the radial extension of GC systems around their host galaxies, specific frequencies, their colour distributions, and many others (Brodie and Strader, 2006). But with each leap in data, old problems are answered and new questions arise.

One of the most well known limitations to characterise globular cluster stellar populations are the issues on the simple stellar population (SSP) models commonly used to estimate their ages and metallicities. As it will be explained in further detail in Chapter 3, SSPs rely on a set of intricate and complex evolutionary tracks and initial conditions to simulate the spectra of stellar populations with fixed metallicities and ages given an initial mass function (IMF). One of the first points where one can see how limitations in SSPs impact GC studies is the simple fact that for a long time GCs were considered prime examples of SSPs, but this paradigm changed radically in recent years. High resolution spectroscopic studies revealed multiple stellar populations in several GCs on the Milky-Way, and today it is thought that this might be a universal feature (Bastian and Lardo, 2018; Cordoni et al., 2019; Bekki, 2019; Bonatto et al., 2019; Barbuy et al., 2021). Not only this, *but SSP models are generally calibrated to match Milky Way GCs observational attributes*. It has been theorised for some time already that GCs in other galaxies could harbour stars with very different chemical content (Cohen et al., 2003; Beasley et al., 2019). For instance, the GCs formed in-situ within big elliptical galaxies such as M87 should harbour stars older[3] than the stars in most of the Milky Way GCs (Cohen et al., 1998; Montes et al., 2014; Oldham and Auger, 2016a). Such clusters would then span a wider range of metallicity than their counterparts in our Galaxy (Kaviraj et al., 2007; Chies-Santos et al., 2012; Romanowsky et al., 2012). GCs that are more metal-poor than Milky-Way GCs are theorised to have, for instance, a higher abundance of α-elements[4]. Galaxies of this size also often present evidence for a rich merger history which produced a new generation of more metal-rich GCs that would show instead higher fractions of Fe-peak elements, more similarly to Milky-Way GCs, but probably not in the same amount (Côté et al., 1998; Lim et al., 2020).

Using photometric NGVS data obtained from the Canada-France-Hawaii Telescope (CFHT) instrument Megacam, P16a showed that the most popular SSP models used by the astronomical community to infer ages and metallicities for stellar populations show a remarkable disagreement with the colour distributions of M87 GCs. As it can be seen in Fig. 1.8, there seems to be an environmental effect that changes the slope of the colour distribution of M87

---

[3] Considering the uncertainties, this difference in ages is theorised to reach up to ~ 8 Gyrs. See Fig. 3 of Montes et al. (2014) for a comparison.

[4] α-elements are defined as those produced in stars as result of converting He atoms into heavier elements. Among the most important of these elements are: Ne, Mg, Si, S, Ar, Ca and Ti.

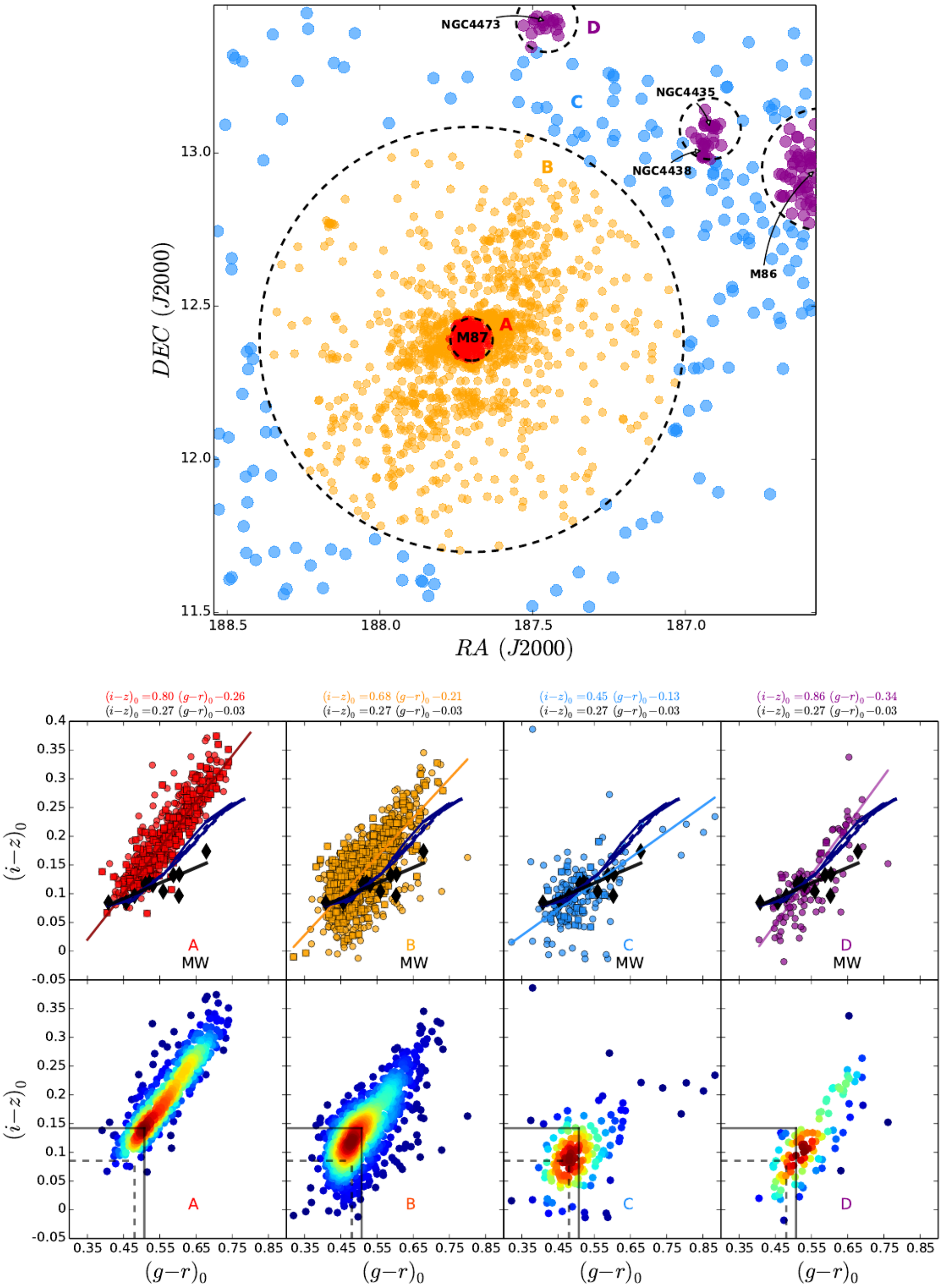

Figure 1.8: Modified from Figures 1 and 2 from P16a, where the NGVS GCs are divided between 4 different regions according to distance to M87 centre (for regions A, B and C) and proximity to neighbouring galaxies (region D), as shown in the top panel. On the bottom, the upper panels show *griz* colour diagrams with Virgo GCs, black diamonds representing a sample of Milky-Way GCs and blue curves which are models from Bruzual and Charlot (2003) with metallicities between $0.0004 \leq Z \leq 0.03$ and ages between $6 \leq t \leq 13$ Gyr. Above each panel it is the linear fit for the best-fit lines showed for GC colour distributions. We see that the models can reproduce the colours of Milky-Way GCs fairly well, while progressively failing when we compare them with GCs in the inner parts of M87. Note also that the mismatch is worst towards the upper part of the diagrams, where we would find the most metal-rich GCs. Interestingly, for the region D, which would be the GCs belonging to neighbouring galaxies, the models do a good job on reproducing their colours (except at the metal-poor end, where those extragalactic GCs seem to be even less metallic than their Milky-Way counterparts). The lower panels on the right side show the density distribution of GCs in each region as well as highlighting with the solid and dashed lines the shift between the highest-density peak from region A (solid) to D (dashed).

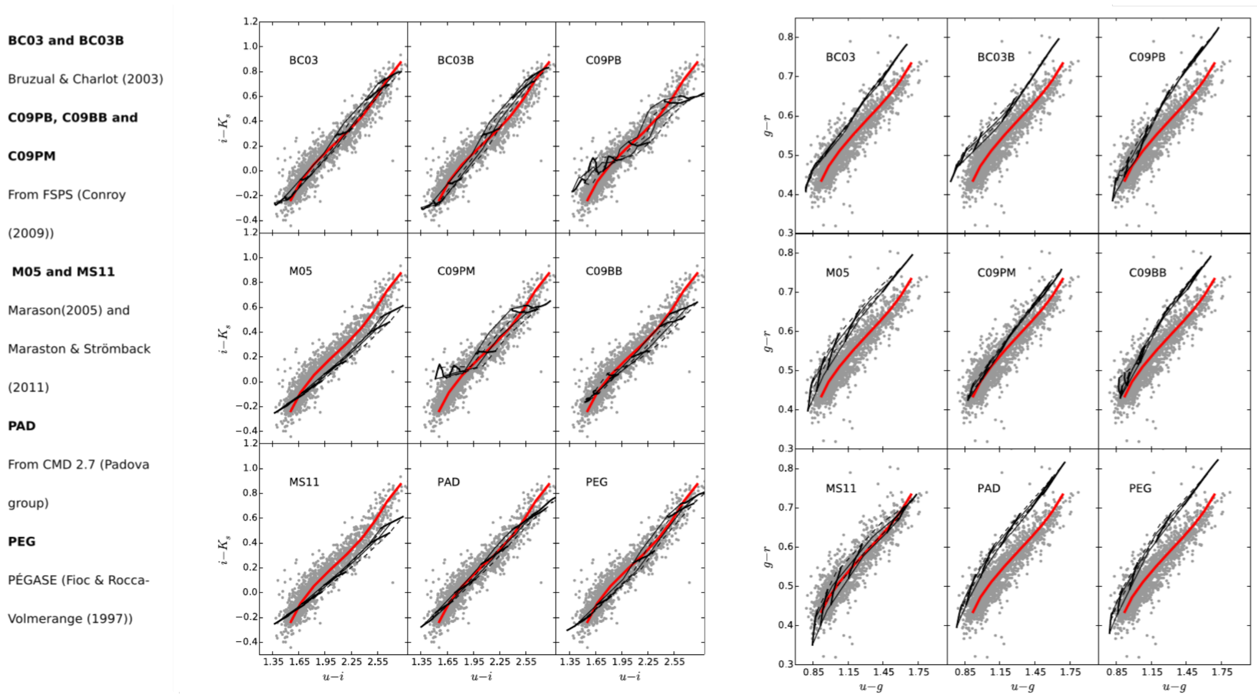

Figure 1.9: Modified from Figures 16 and 17 from P16b, where we see several commonly used SSP models compared to the colours distributions of NGVS GCs (whole sample, not divided by regions), in two different colour diagrams (*uiKs* on the left, and *ugr* on the right). In this work it was shown several other colour diagrams, but here we selected these just as an example of how SSP models can predict correctly colours in one colour-colour diagram, but not in other. Such inconsistency is not in agreement between different models, each one has issues in different colours, i.e., different regions of the spectrum.

GCs in comparison to both the models from Bruzual and Charlot (2003) and Milky-Way GCs. Not only that, but Fig. 1.9 from Powalka et al. (2016a, hereafter P16b) shows examples of how SSP models from different authors inconsistently match the different colour-colour diagrams for NGVS GCs. These results are of utmost importance at the current age where, as already was said, data for extragalactic star clusters has become increasingly available. Without reliable models to correctly reproduce their colour distributions, it would be very limiting (if not biased) to attempt to estimate their ages, metallicities and chemical content.

Possible causes for such problems have been discussed in a few works in recent years. Firstly, P16a itself argues that those results are not due to initial mass functions, differential extinction, calibration uncertainties or simply age and metallicities that go beyond the ones found in Milky-Way GCs. Rather, it is proposed that such environmental effects may be due to intrinsic chemical abundance variations. For instance, the abundance ratios that influence the morphology of the horizontal branch (HB), which were shown to affect the relation between optical and near-infrared colours (Conroy and Gunn, 2010; Maraston and Strömbäck, 2011). Additionally, molecular bands such as the ones related to the CNO-cycle, may influence spectral effects around the r, i and z bands, probably also playing a role into the issue.

The [α/Fe] ratio can also be of significant importance, as suspected by studies such as Mieske et al. (2006) and Choi et al. (2019). Iron-peak elements are produced from supernovae type II and Ia, but only the former produces α elements (Woosley and Weaver, 1995; Nomoto et al., 2006). The different timescales of those two kinds of supernovae offers clues on the star formation timescale in a given system, such that higher values correspond to shorter timescales (Tinsley, 1979; Thomas et al., 1999). Milky-Way stars in different Galactic regions show a distinct chemical signature in its α-enhancement content. Regions with relatively large amounts of star forming gas, such as the thin disk, show stars with negligible α-element abundances at solar metallicities, with a slight α-enhancement at sub-solar regimes (Reddy et al., 2003). However, other Galactic regions such as the thick disk, halo and bulge present stars with increased [α/Fe] abundances at sub-solar metallicites, reaching [α/Fe] $\sim$ 0.3 at [Fe/H] $<$ 0.5 (Di Matteo, 2016; Bensby et al., 2011; Nissen and Schuster, 2010). This is likely to be due to the scarcity of cold gas in these regions at long enough timescales, alongside short-scale star formation events induced by minor mergers (in the case of the halo and thick disk) and the faster collapse of star-forming gas under increased local densities (in the case of the bulge) (Alves-Brito et al., 2010). A similar pattern is seen for stars in the bulge of M31 (Gajda et al., 2021). Spectroscopic studies of GCs in the Milky-Way and nearby galaxies show a similar abundance of α-elements than in Milky-Way stars. This can be seen in Fig. 1.10 from Larsen et al. (2018), where we show the abundance of α-elements such as Mg, Ca and Ti for Milky-Way stars and GCs, as well as for GCs in nearby galaxies. Notice that the increase in the abundance ratios is inversely proportional to [Fe/H] metallicity.

Furthermore, dwarf galaxies in the Galactic neighbourhood also show distinct star-formation timescale signatures. For instance, the Sagittarius and Sculptor dwarf spheroidals show very little α-enhancement (Sbordone et al., 2007; Kirby et al., 2009) while ultra-diffuse galaxies can display increased [α/Fe] ratios, over 0.5 dex, for stars as metal-poor as [Fe/H] $\sim$ -2.5 (Vargas et al., 2013). This is interpreted as evidence of extended star formation for some

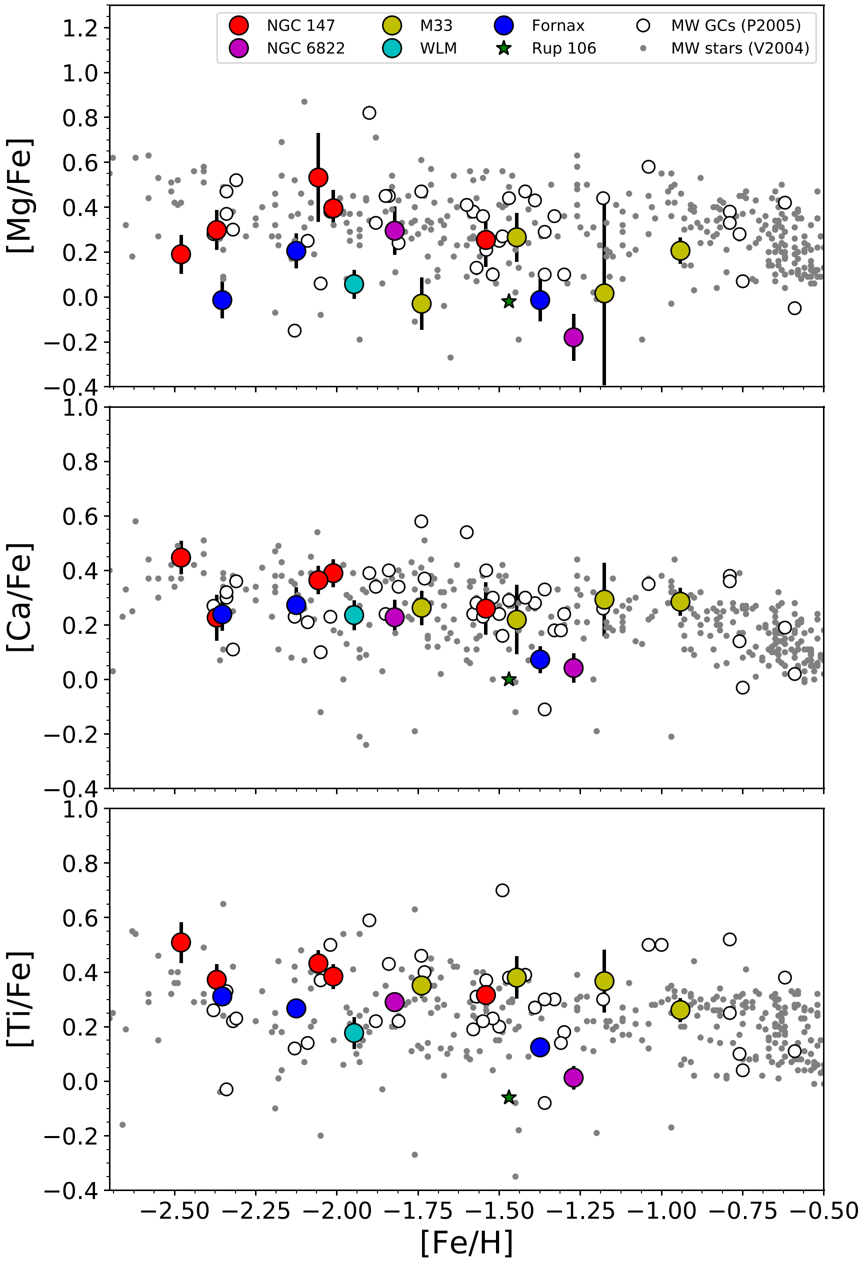

Figure 1.10: Fig. 5 of Larsen et al. (2018), where we can see the ratio of some important α-elements as a function of the abundance ratio of [Fe/H] for the Milky-Way and nearby galaxies. From top to bottom, the ratio [Mg/Fe], [Ca/Fe] and [Ti/Fe]. Empty circles show Milky-Way GCs from Pritzl et al. (2005) and grey dots are Milky-Way stars from Venn et al. (2004). Coloured symbols indicate spectroscopic abundance ratios presented in Larsen et al. (2018) for GCs in the galaxies indicated in the legend.

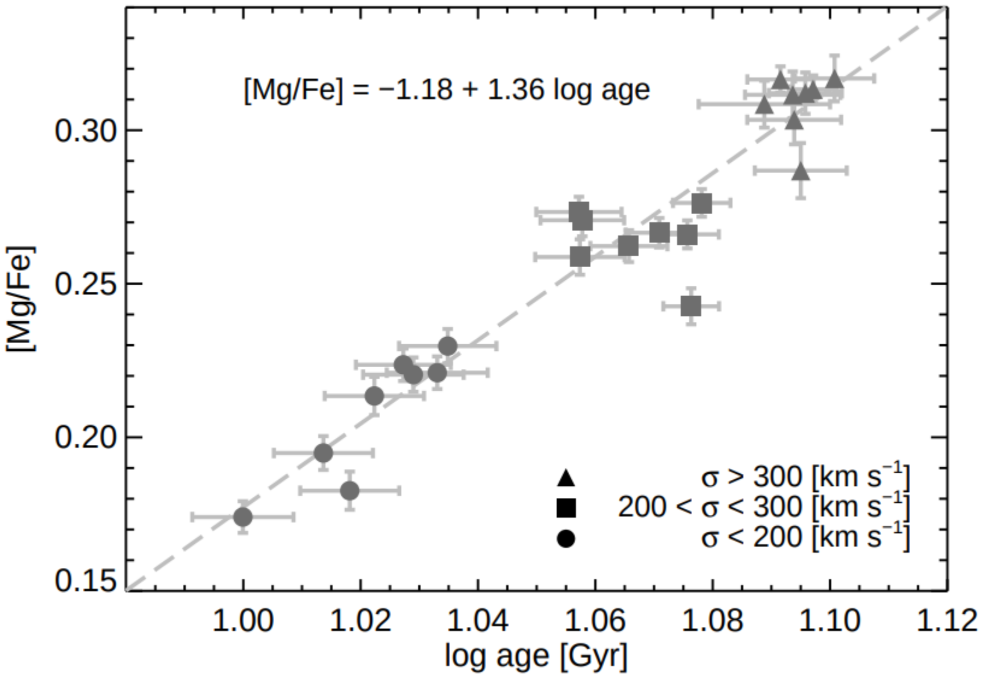

Figure 1.11: [Mg/Fe] ratio as a function of age and velocity dispersion (σ) for 45 elliptical galaxies from the CALIFA survey, from Martín-Navarro et al. (2018). The [Mg/Fe] ratio is a commonly used proxy for the $[\alpha/Fe]$ ratio. Here we can see that the α abundance scales linearly with age and σ, which is also related to galaxy mass. Therefore, for more massive and older GCs in galaxies such as M87, it is reasonable to assume stellar compositions with higher abundances of α elements.

dwarf galaxies at opposition to the theoretical starvation process experienced very early after galaxy formation by ultra-diffuse galaxies (Mistani et al., 2016; Vargas et al., 2013). *Early-type* galaxies have been shown (e.g. Conroy et al., 2014) to have a stellar population with [α/Fe] in the range 0.1 to 0.4 dex. This is thought to be due to *Early-type* being a prime example of galaxies which experienced several minor mergers, inducing short star formation events. At the same time, little to no star forming gas is available for continuous star formation (Behroozi et al., 2014; Khochfar and Silk, 2009; Martín-Navarro et al., 2018). *Late-Type* galaxies, like the Milky-Way, on the other hand, preserve large quantities of gas that are able to form stars over larger periods of time (James and Prescott, 2008; Boselli, 2000). Martín-Navarro et al. (2018) have shown that the enhancement on α elements on elliptical galaxies scales with age (see Fig. 1.11).

It is only recently, however, that SSP models with enhanced α-abundance variations started to become available. This is mainly due to their reliance on high resolution empirical spectra, which are only available for nearby stars, which are generally not metal-poor enough to present enhanced $[\alpha/Fe]$ ratios comparable to the expected for extragalactic GCs (Vazdekis et al., 2015; Conroy et al., 2018). To overcome these limitations, recent efforts were made to include theoretical corrections into empirical libraries (e.g., Conroy and van Dokkum, 2012; Vazdekis et al., 2015; Coelho, 2014; Knowles et al., 2021). Later in chapter 3 this will be explained further in details, as in this work we will employ novel α-enhanced SSP models covering the wavelength range of colours tested by P16a, i.e., $ugriz$, as well as the K_s-band which was barely touched in his work due to the scarcity of available SSP models in the NIR at the time.

Moreover, P16a results were limited to a single extragalactic GC system, that around M87 in the Virgo Cluster. This begs the question if their results on the environmental variations in the colour predictions of SSP models is also present in the GC systems of other galaxies of similar size and at a different environment. In order to test this hypothesis, in this work we will test the aforementioned novel SSP models against the observed colours of GCs around M87 in the Virgo cluster around NGC 3311/NGC 3309 in the Hydra cluster. NGC 3311 is a perfect candidate for a comparison with the Virgo GC system, as the nearest galaxy with a GC system similar in scale to the one of M87, as mentioned in previous sections. We also present in this work new high-quality ESO/VLT photometric data in the NIR for each of these systems, and comprising very central regions of Virgo and Hydra clusters, which are exactly the regions where P16a found most of the discrepancies between SSP models and the observed colours. The importance of high-quality NIR data in this context is the known power of optical/NIR colours to disentangle the degeneracy between ages and metallicities in the comparison between colours and SSP models (Georgiev et al., 2012; Chies-Santos et al., 2011c; Muñoz et al., 2015).

To summarise, in chapter 3 we will investigate whether or not currently available models with varying abundance variations, specially α-enhancements, improve on the issues with colour predictions by the most commonly used models in the literature, while also looking into the environmental variations in this matter presented in P16a for the M87 and Virgo Cluster GC system. The latter will also involve looking if such environmental effects are also present for a GC system of similar size in the Hydra cluster cD galaxy, NGC 3311.

1.5 Specific goals for this work

The ultimate goal of this work is to constrain the formation and evolution of star clusters systems and their relation with galaxy evolution. To such extent, we explore the nucleation fraction of galaxies in the Coma cluster when compared to other galaxy clusters and galaxies in the local volume ($\leq$ 12 Mpc). Furthermore, we also investigate the predictability of colours in the GC systems of the central elliptical galaxies in the Virgo and Hydra clusters, based on state-of-the-art stellar population models and high precision NIR photometry. In this context, we also explore how an increased α-enhancement influence our capability of predicting ages and metallicities for extragalactic GCs in high-density environments and finally we discuss the differences that were detected between the GC systems in Virgo and Hydra and how such discrepancies might help explain the observed mismatch between the observed colours and stellar population models.

To summarise, we hope that the ideas and conclusions introduced in this work pave the way to a more constrained exploration of extragalactic stellar clusters with data from the next generation of telescopes, such as Euclid, Nancy Grace Roman, Chinese Space Station Telescope (CSST) and ground-based Vera Rubin and the Javalambre Physics of the Accelerating Universe Astrophysical Survey (J-PAS). Such next age of astronomy will provide unprecedented amounts of GC and NSC data not only more spatially precise, but also extended to NIR wavelengths with unmatched precision when compared to current available technologies. Therefore, at this stage, it is crucial to: i) develop new statistical techniques to explore to the maximum the available photometric data and ii) investigate the limitations of current SSP models regarding both chemical abundances and NIR wavelengths. These objectives are studied in this thesis in chapter 2 and 3, respectively.

Chapter 2

A high occurrence of nuclear star clusters in faint Coma galaxies, and the roles of mass and environment

In this chapter we present the work which was published in Zanatta et al. (2021) and accepted for publication in the Monthly Notices of the Royal Astronomical Society (MNRAS). We used deep high resolution Hubble Space Telescope/Advanced Camera for Surveys (*HST*/*ACS*) imaging of two fields in the core of the Coma cluster to investigate the occurrence of nuclear star clusters (NSCs) in quiescent dwarf galaxies as faint as $M_I = -10$ mag.

We employ a hierarchical Bayesian logistic regression framework to model the faint end of the nucleation fraction (f_n) as a function of both galaxy luminosity and environment. We find that f_n is remarkably high in Coma: at $M_I \approx -13$ mag half of the cluster dwarfs still host prominent NSCs. Comparison with dwarf systems in nearby clusters and groups shows that, within the uncertainties, the rate at which the probability of nucleation varies with galaxy luminosity is nearly universal. On the other hand, the fraction of nucleated galaxies at fixed luminosity does exhibit an environmental dependence. More massive environments feature higher nucleation fractions and fainter values of the half-nucleation luminosity, which roughly scales with host halo virial mass as $L_{I,f_{n50}} \propto \mathcal{M}_{200}^{-0.2}$. Our results reinforce the role of galaxy luminosity/mass as a major driver of the efficiency of NSC formation and also indicate a clear secondary dependence on the environment, hence paving the way to more refined theoretical models.

In the following sections we further detail the data, methods and results published in the accepted article.

2.1 Data

The Coma cluster data used in this work were obtained as part of Program GO-11711 (PI: J. Blakeslee) using the Advanced Camera for Surveys Wide Field Channel (ACS/WFC) onboard the HST in March 2012, and consists of two fields centered on the bright cD galaxies NGC 4874 and NGC 4889. The observations run for four orbits with the F814W filter ($\approx I$) and one orbit with the F475W filter ($\approx g$). As a result, the former dataset is considerably deeper than the latter, and only the I data are used throughout. The exposure times in I are 10,425 s and 9,960 s for NGC 4874 and NGC 4889, respectively.

The data for NGC 4874 were used previously in Cho et al. (2016) and we refer the reader to that work for additional details on the reduction steps, which are the same for the NGC 4889 field. Briefly, the images were dithered - i.e., small telescope offsets were employed - to fill the 2.5 arcseconds gap between the two ACS/WFC detectors, followed by the standard pipeline processing from the STScI/Mikulski Archive for Space Telescopes (MAST). The charge-transfer efficiency (CTE) correction algorithm of Anderson and Bedin (2010) was applied and finally the CTE-corrected exposures were then processed with APSIS (Blakeslee et al., 2003) to produce the final corrected images shown in Fig. 2.1.

The reference dataset for NSCs in the Coma cluster was introduced in den Brok et al. (2014), with imaging from the HST/ACS Coma Cluster Survey (Carter et al., 2008). The present study and that work are highly complementary. den Brok et al. (2014) data cover a large footprint and have robust number statistics at the bright end of the dwarf galaxy population ($M_I < -13$). On the other hand, such work is limited to two ACS fields, while our deeper

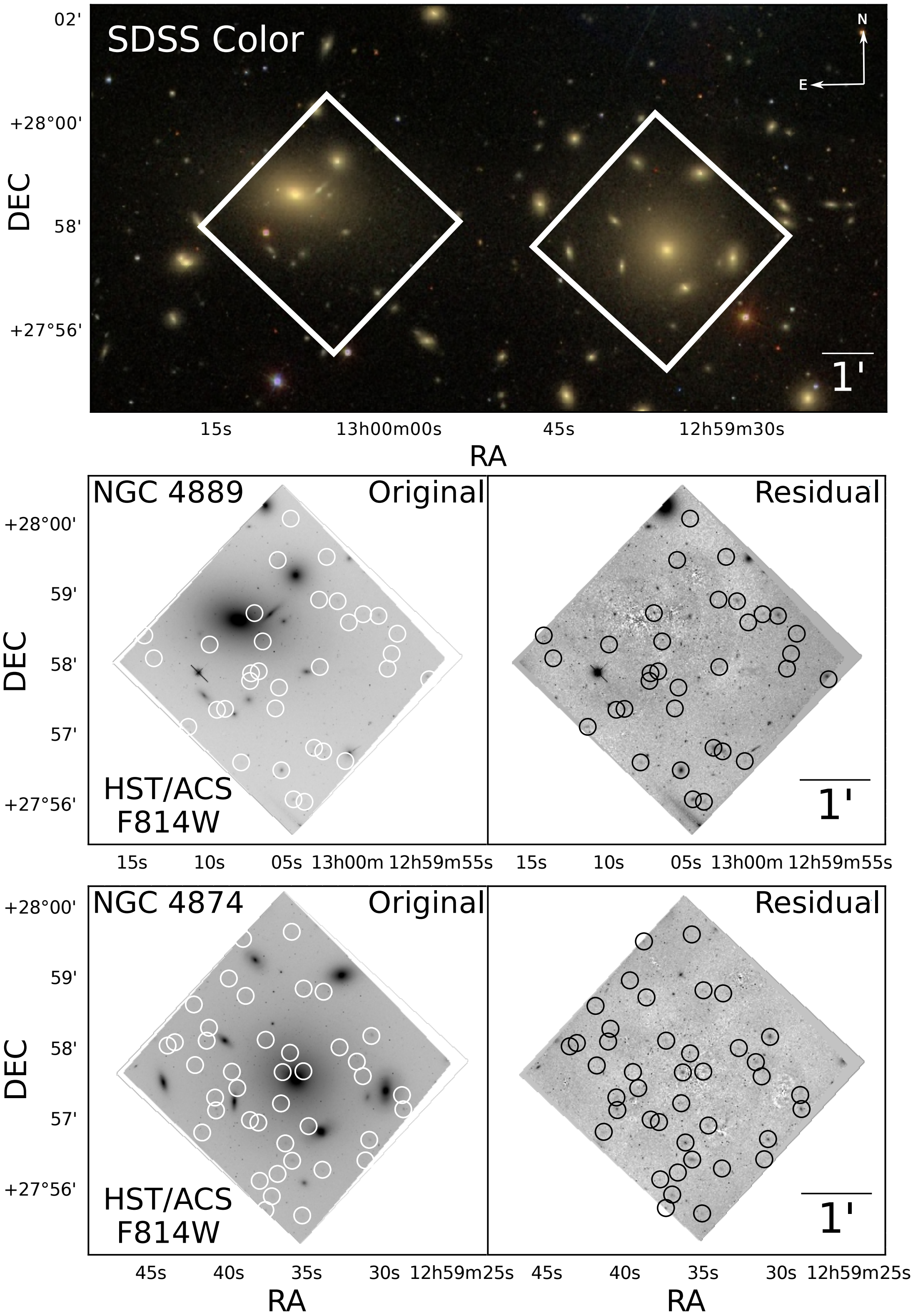

Figure 2.1: Top: SDSS colour-composite image of the central region of the Coma cluster, with white boxes representing the two HST/ACS pointings used in this work. Middle and bottom: The actual HST/ACS images used in this work, after DRIZZLE treatment (left) and after the subtraction of bright galaxies to improve the detection of fainter objects (right). Circles indicate the positions of the detected galaxies in our sample (see Table 2.2).

imaging - reaching $M_I \approx -10$ in comparison to the limiting magnitude of $M_I \approx -13$ of den Brok et al. (2014) - allows us to probe much fainter galaxies and NSCs than ever before in Coma. In Fig.2.2 we present a comparison between the I-band images used in this work and those from den Brok et al. (2014). The top row corresponds to a nucleated galaxy, whereas the bottom one shows a non-nucleated dwarf. The higher signal-to-noise ratio in our frames significantly improves on the detection and characterisation of NSCs and, especially, their low surface brightness hosts.

2.1.1 NSCs in other environments from the literature

In addition to the Coma cluster, in this work we also analyse data for dwarf quiescent galaxies in the Virgo cluster (from Sánchez-Janssen et al., 2019), the Fornax cluster (from Muñoz et al., 2015) and a collection of data for faint quiescent satellites in the local volume ($D < 12$ Mpc). The latter dataset is mainly drawn from Carlsten et al. (2020a), and further complemented with data from Chies-Santos et al. (in prep.) for dwarf companions of NGC 3115. In Table 2.1 we list the other systems included in the analysis. In the table we indicate the number of quiescent satellites in each environment, as well as the literature sources for the photometry and the nucleation classification.

Where applicable, we have converted the published magnitudes to the I-band. We adopt the following filter conversions, based on the ones presented in Blanton and Roweis (2007):

$$(B - i) \approx 1.10, \tag{2.1}$$

$$(i - I) \approx 0.06. \tag{2.2}$$

The detection of nucleated galaxies in the MW, M31 and M81 systems is detailed in Sánchez-Janssen et al. (2019), but can be summarised as follows. From the Karachentsev

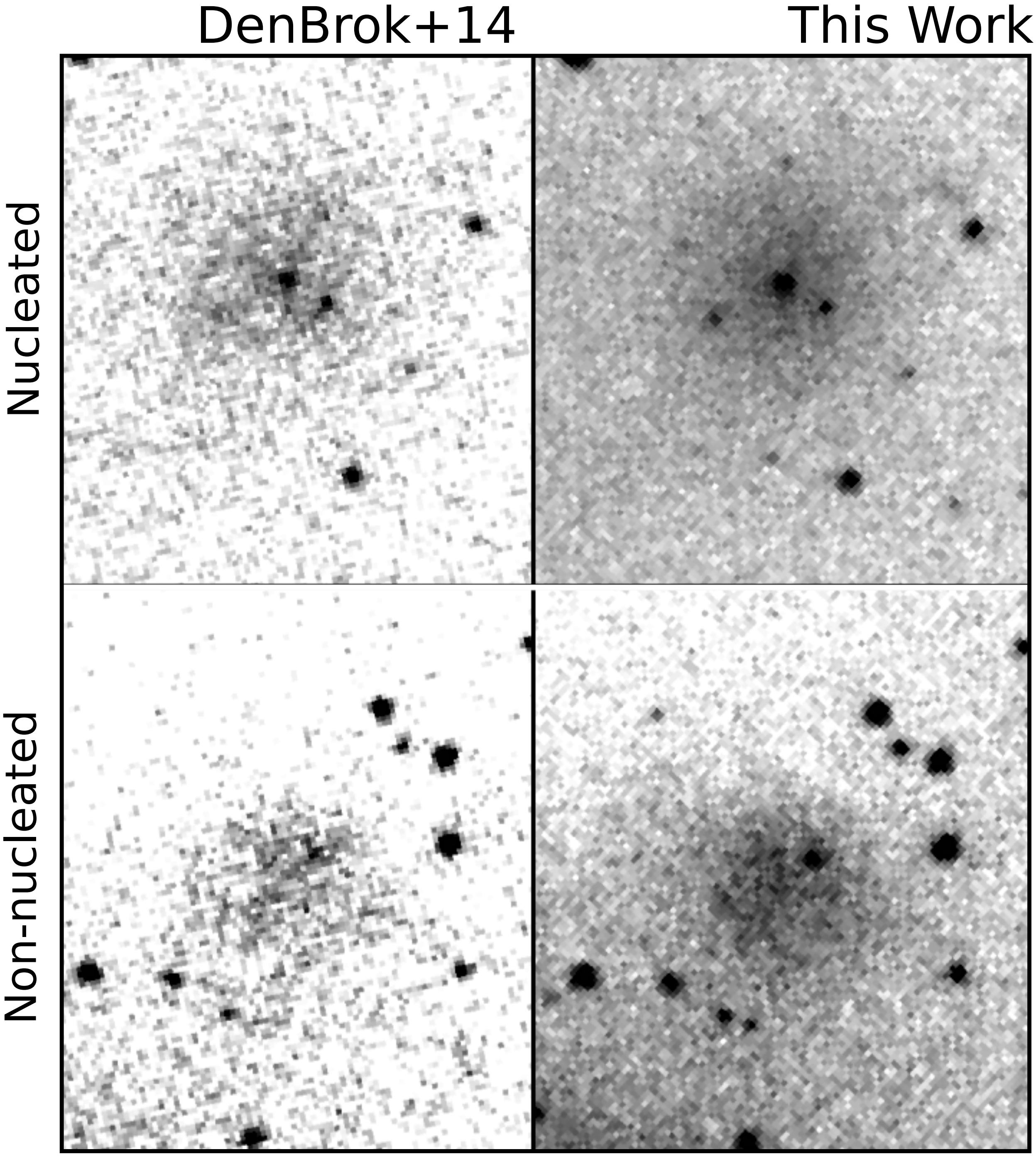

Figure 2.2: Comparison between the depth of images from den Brok et al. (2014) and this work. On the top panels, two images of the same nucleated galaxy present in both the catalogue from den Brok et al. (2014) and this work. On the bottom panel, a non-nucleated galaxy. All images are adjusted to the same scale and in the same HST/F814W filter.

et al. (2013) Updated Nearby Galaxy Catalogue, B-band magnitudes were transformed to the **V**-band assuming (B-V)= 0.7 (Blanton and Roweis, 2007) and stellar masses were computed using $M_*/L_V = 1.6$ (Woo et al., 2008). Then, only galaxies within $10^5 < M_*/M_\odot < 10^9$ with early-type morphologies and whose main perturber was classified in the catalogue as being any of these three spirals were selected. Furthermore, for satellites in the M81 group HST images were visually inspected to find the galaxy candidates from Chiboucas et al. (2013). The remaining galaxies in the low-density systems are drawn from Carlsten et al. (2020a). Among these, we only select galaxies classified as dEs and discard dIrr and transition dwarfs. Carlsten et al. (2020b) present surface brightness fluctuation distances for the galaxies in the original sample, which we make use to consider only galaxies that are flagged as "possible" or "confirmed" satellites in their table 4. The nucleation classification and photometry for the final sample of group satellites is then taken from Carlsten et al. (2020a) and Carlsten et al. (2020b), respectively.

An important aspect of all these datasets is that they all feature roughly the same effective spatial resolution. This is a result of the superbly narrow point-spread function (PSF) delivered by HST which more than compensates for the much larger distance of the Coma cluster–and we therefore expect the NSC detection efficiency to be similar across the different environments. Moreover, the effective HST/ACS PSF FWHM in Coma is ≈ 37.92 pc. NSCs in early-type dwarfs have typical sizes of $\lesssim 20$ pc (Côté et al., 2006; Turner et al., 2012), therefore at the distance of Coma they are all essentially unresolved in our images.

As noted before, only early-type dwarfs are considered in the analysis. This is to avoid complications related to both the morphology-density relation as well as the notoriously difficult task of identifying NSCs in star-forming galaxies due to the presence of star formation and obscuration by dust. More details on the literature data used in this work are presented in Table 2.1.

With this choice of environments we are able to probe NSC occupation in host haloes with masses ranging from 5×10^{15} in Coma to $10^{12}\mathcal{M}_\odot$ in the local volume. When necessary, adopted mass estimates come from Łokas and Mamon (2003), McLaughlin (1999) and Drinkwa-

Table 2.1: Source of the photometry and nucleation classification for the data used in this work. From left to right: First column is the central galaxy for a given group in the local volume or the galaxy cluster. For Local Volume groups the second column indicates the morphology of the central galaxy (ET for early-types and LT for late-types). The next column is the number of quiescent satellite galaxies in each system, with the two subsequent columns presenting the sources for the photometry and the nucleation classification, respectively.

Local Volume Groups

ID	Morph.	N	Photometry Source	Nucleation Source
NGC 1023	ET	15	Carlsten et al. (2020b)	Carlsten et al. (2020a)
M104	ET	23	Carlsten et al. (2020b)	Carlsten et al. (2020a)
Cen A	ET	31	Carlsten et al. (2020b),Müller et al. (2019)[a]	Carlsten et al. (2020a), Müller et al. (2019), Fahrion et al. (2020)[b]
NGC 3115	ET	24	Chies-Santos et al. (in prep.)	Chies-Santos et al. (in prep.)
NGC 4631	LT	7	Carlsten et al. (2020b)	Carlsten et al. (2020a)
NGC 4565	LT	16	Carlsten et al. (2020b)	Carlsten et al. (2020a)
NGC 4258	LT	9	Carlsten et al. (2020b)	Carlsten et al. (2020a)
M51	LT	4	Carlsten et al. (2020b)	Carlsten et al. (2020a)
MW	LT	11	Karachentsev et al. (2013)	Sánchez-Janssen et al. (2019)
M81	LT	13	Karachentsev et al. (2013)	Sánchez-Janssen et al. (2019)
M31	LT	30	Karachentsev et al. (2013)	Sánchez-Janssen et al. (2019)

Galaxy Clusters

ID	N	Photometry Source	Nucleation Source
Coma	255	This work, den Brok et al. (2014)	This work, den Brok et al. (2014)
Virgo	382	Sánchez-Janssen et al. (2019)	Sánchez-Janssen et al. (2019)
Fornax	263	Muñoz et al. (2015)	Muñoz et al. (2015)

---

[a] Müller et al. (2019) is the source photometry for the galaxies KK54 and KK58, and source nucleation for KK54.

[b] Fahrion et al. (2020) is the source nucleation for the galaxy KK58.

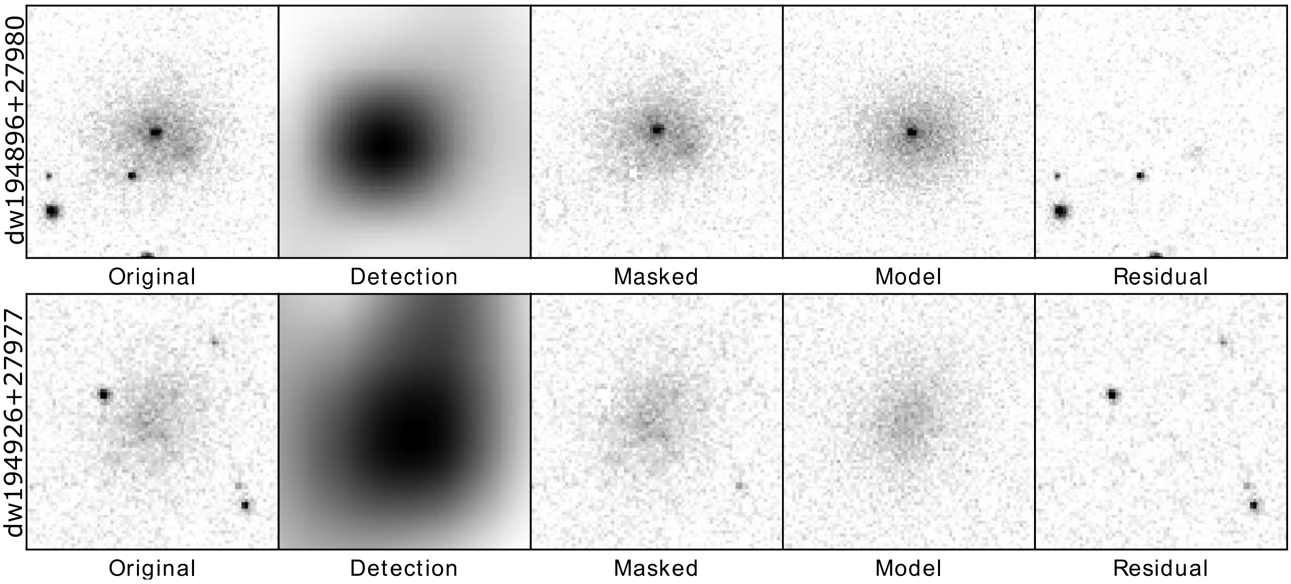

Figure 2.3: Summary of the procedure to detect and extract photometry for faint galaxies and their NSCs. From left to right: Section of the original image showcasing an example galaxy (nucleated on top, non-nucleated at the bottom). In the second panel we show the SOURCEEXTRACTOR background image used for galaxy detection. Notice the significant increase in SNR, which improves the detection limits. The third panel contains the same image as the first panel, but now the point sources detected by the first SOURCEEXTRACTOR are masked–except for the central 6x6 pixels, which are unmasked to reveal the NSC. The fourth panel corresponds to the GALFIT model, to which we have added the typical noise of the *ACS* images for representation purposes. Finally, in the last panel we show the residual image from GALFIT modelling. Both galaxies are presented with the same scaling.

ter et al. (2001) for Coma, Virgo and Fornax, respectively. For the local volume galaxies we derive a mean halo mass using the $log(V_{circ}) - log(\mathcal{M}_{200})$ relation from the Illustris TNG100 simulations (Pillepich et al., 2018) and the V_{circ} values in Table 1 of Carlsten et al. (2020a). Exceptions are: NGC 3115, for which the halo mass estimate comes from Alabi et al. (2017); M81, from Karachentsev et al. (2002); Cen A, from van den Bergh (2000); M31, which comes from Tamm et al. (2012) and the Milky Way, from Taylor et al. (2016).

2.2 Photometry

In this work we build on the methods developed in recent surveys of the Virgo (Ferrarese et al., 2016) and Fornax (Eigenthaler et al., 2018) clusters to study the faint galaxy population and their star cluster systems. Briefly, galaxy detection is carried out automatically using an algorithm optimised for the recovery of low surface brightness objects. Visual inspection of the candidates by one or more individuals follows, and cluster membership is assigned based on expected morphological features for early-type, quiescent dwarfs–namely, ellipsoidal shapes, smooth surface brightness profiles and absence of star formation features. Finally, photometric and structural parameters for the host galaxy and the NSC are derived through two-dimensional modelling of the galaxy images. The detailed steps are as follows.

2.2.1 Bright galaxy subtraction

The two fields in this study are centred on NGC 4874 and NGC 4889, the two dominant ellipticals in the core of the Coma cluster. NGC 4889 is the brightest galaxy in the cluster, but NGC 4874 boasts an extended cD halo and resides somewhat closer to the centroid of the X-ray emission in the cluster. The high density of bright satellite galaxies in these fields renders the detection of faint objects difficult. Therefore, the first step in our analysis consisted in the modelling and subtraction of the largest objects.

We subtract the bright galaxies using the program ELLIPROOF (Tonry et al., 1997; Jordan et al., 2004), which fits a series of elliptical isophotes of varying centres, ellipticities, orientations, and low-order Fourier terms. The algorithm then interpolates smoothly between the isophotes and extrapolates outward beyond the last one. In both of our fields we model and subtract the brightest galaxy along with large neighbouring galaxies that affect the modelling of the central galaxy, as well as fainter galaxies that adversely affect the modelling of the bright satellite galaxies. We adopt an iterative approach: subtracting the brighter galaxies, then subtracting the fainter neighbours, then remodelling the brighter galaxies with the neighbours subtracted, etc. We iterate until we achieved a clean subtraction of all galaxies (about ten in each field) that were large enough to have a significant effect on the detection of the fainter objects we aim to study.

2.2.2 SourceExtractor detection

Galaxy detection is carried out with SourceExtractor (Bertin and Arnouts, 1996) following a two-step approach. The first pass is optimised to extract point sources, whereas the second runs on the background image generated from the first one. The process effectively acts as a low-pass spatial filter, resulting in a smoothed, high signal-to-noise ratio (SNR) image over scales larger than the PSF size.

In the first SourceExtractor run we set the minimum detection area, DETECT_MINAREA, to 10 pixels above the detection threshold (DETECT_THRES) of 1.5σ of the sky background. As described before, these parameters are set so as to detect compact objects such as GCs, foreground stars and background galaxies. We also set a background mesh size (BACK_SIZE) of 32 pixels with a 3x3 grid for the median filter (BACK_FILTERSIZE). Using these parameters, SourceExtractor estimates the local background in each mesh of rectangular grids across the entire image. In the second column of Fig. 2.3 we show an example of such map, where the increase in SNR is evident.

We then proceed to the second run of SourceExtractor, this time on the smoothed image. We set DETECT_MINAREA to 200 pixels above the DETECT_THRES of 1.2σ of the sky background. We then match the positions of the detections with those in the original image, proceeding to visual inspection of the candidates to assign cluster membership and nucleation classification.

2.2.3 Visual classification

Visual classification was independently carried out by Emilio Zanatta and R. Sanchez-Janssen. Because faint early-type dwarfs have low surface brightness, the main contaminants are background late-type galaxies. We classify as members objects with smooth and spheroidal morphologies (Sánchez-Janssen et al., 2016), and discard irregular galaxies or those displaying features consistent with ongoing star formation (clumps, arms, bars). We identify NSCs as compact spherical sources that in projection lie close to the geometric centre of the candidate galaxy (see Fig. 2.2). This requirement is later refined during the process of galaxy modelling (Sect. 2.2.4).

We find that the two independent classifications fully agree down to a limiting magnitude of $m_I = 25$ mag. Because the focus of this work is on the faint-end of the Coma galaxy population, we also set a bright limit of $m_I = 20$ mag. The number of more luminous galaxies in the two fields under study is too low to be statistically meaningful. Our final catalogue is presented in Table 2.2. We found 66 galaxies within $-15 < M_I < -10$ mag, 23 of which are first reported in this work. Among these, 33 have nuclear star clusters candidates.

2.2.4 GALFIT modelling

To determine the structural and photometric properties of the candidate galaxies and their NSCs we model their surface brightness profiles using GALFIT (Peng et al., 2002). We use the segmentation maps from the first SOURCEEXTRACTOR run to mask all objects around our detected galaxies, except for the central point sources in the visually-identified nucleated dwarfs. Furthermore, we use PSF models obtained with PSFEX (Bertin, 2011). We use as initial conditions the MAG_AUTO magnitudes and FLUX_RADIUS results from the SOURCEEXTRACTOR catalogue, as well as an initial Sérsic index of n=0.75, position angle of 45 degrees and axis ratio of 0.8. The non-nucleated galaxies are modelled with a single Sérsic profile, while for the nucleated ones we use a Sérsic profile alongside a PSF component.

Initial magnitudes for the PSF component are the MAG_AUTO measured by the first SOURCEEXTRACTOR run. The two components have initial central positions defined by the positions detected by SOURCEEXTRACTOR for the galaxy or the NSC, in the case of nucleated objects.

To aid in the modelling of the fainter galaxies we employ constraints to the parameters to be fitted by GALFIT. Based on the structural parameters for faint galaxies in the Virgo cluster (Ferrarese et al., 2020) we limit the Sérsic index to vary in the range $0.5 \leq n \leq 1.5$. Constraining the Sérsic index aids GALFIT in converging to realistic values for other

Table 2.2: Photometric and structural parameters for the galaxies detected in Coma obtained using GALFIT using SourceExtractor magnitude and positions as input parameters, as described in the text. From left to right: Identification for each galaxy, right ascension in degrees, declination in degrees, galaxy magnitude in the I filter, NSC magnitude in the I filter, Sérsic index, effective radius in arcseconds, position angle in degrees, axis ratio and flags for previous detections of those galaxies. Such flags are as follows: 1: Godwin et al. (1983); 2: Iglesias-Páramo et al. (2003); 3: Adami et al. (2006a); 4: Yagi et al. (2016); 5: Adami et al. (2006b); 6: Hoyos et al. (2011); 7: den Brok et al. (2014).

ID	RA (deg)	DEC (deg)	$m_{I,gal}$ (mag)	$m_{I,NSC}$ (mag)	n	R_e (arcsec)	b/a	PA (deg)	Prev. Detec.
dw195019+27934	195.0191	27.9344	20.18	24.05	0.91	1.543	0.72	61.26	3,6
dw195007+27981	195.0073	27.9815	20.20	23.34	1.49	2.465	0.88	11.15	2
dw194870+27952	194.8701	27.9521	20.27	27.55	0.98	1.127	0.65	-22.84	2,6
dw195029+27978	195.0296	27.9787	20.28	23.16	1.27	0.806	0.64	3.31	
dw194902+27960	194.9024	27.9609	20.40	25.11	0.74	1.210	0.80	63.29	
dw194920+27952	194.9202	27.9521	20.53	23.69	1.49	0.458	0.94	-38.14	2,6
dw194905+27931	194.9052	27.9315	20.61	25.92	0.79	2.320	0.93	1.08	2,3,4
dw194911+27949	194.9111	27.9496	20.66	23.68	1.49	2.976	0.78	43.22	3
dw194879+27944	194.8791	27.9449	20.71	25.03	0.89	1.280	0.77	15.57	3
dw195011+27945	195.0112	27.9459	20.78	25.15	0.61	2.028	0.68	4.02	3,6,7
dw194907+27928	194.9070	27.9283	20.82	25.98	0.91	0.788	0.84	-57.99	2,3
dw194882+27963	194.8823	27.9634	20.86	26.38	1.34	1.974	0.93	58.48	3,6,7
dw194933+27967	194.9332	27.9672	20.93	26.24	0.96	1.728	0.63	29.73	3,6,7
dw194923+27946	194.9239	27.9466	21.03	25.52	0.88	3.690	0.59	39.13	2,6
dw194896+27961	194.8968	27.9612	21.05	26.09	1.01	1.887	0.81	85.96	
dw194895+27948	194.8954	27.9481	21.19	25.13	0.69	1.843	0.76	78.93	6
dw194913+27992	194.9130	27.9925	21.19		0.82	1.728	0.55	-36.31	6,7
dw194902+27953	194.9026	27.9535	21.33	24.78	1.32	2.289	0.75	24.00	6
dw194870+27955	194.8704	27.9556	21.44	26.22	0.58	4.014	0.29	-55.01	
dw194920+27954	194.9204	27.9549	21.47	26.92	0.50	2.372	0.40	-86.76	2,6
dw195037+27955	195.0375	27.9559	21.53	26.71	0.86	1.262	0.75	37.37	
dw194908+27949	194.9088	27.9490	21.65		0.83	0.949	0.89	-77.68	3,6,7
dw195016+27933	195.0161	27.9338	21.69		0.52	1.655	0.67	-83.23	3,4,5,6,7
dw194891+27937	194.8917	27.9378	21.75	26.70	0.63	1.563	0.77	16.76	2,3,5
dw194900+27965	194.9004	27.9655	21.77	24.87	0.91	2.329	0.90	65.86	6
dw194912+27979	194.9123	27.9790	21.77	25.79	0.65	1.226	0.68	3.71	6
dw195000+27978	195.0003	27.9784	21.82	25.93	0.72	1.340	0.87	64.54	3,6,7
dw195027+27971	195.0272	27.9719	21.82		0.69	2.759	0.75	66.77	
dw195047+27951	195.0475	27.9516	21.85		0.58	1.532	0.56	52.30	3,5
dw194906+27968	194.9069	27.9686	21.86		0.85	1.569	0.59	-31.93	6
dw195033+27943	195.0332	27.9432	21.89	26.56	0.79	1.456	0.76	40.55	3,5,6,7
dw195030+27964	195.0306	27.9644	21.90		0.88	1.493	0.75	86.83	3
dw194897+27927	194.8971	27.9270	21.97	26.50	0.83	1.277	0.90	-64.46	3,5
dw195058+27973	195.0589	27.9731	22.03	26.10	0.70	1.364	0.81	24.79	3
dw195010+27992	195.0100	27.9920	22.05		0.77	2.559	0.57	11.08	
dw194896+27980	194.8969	27.9806	22.10	26.38	0.71	0.996	0.83	80.16	3,6
dw194887+27966	194.8871	27.9667	22.20	26.15	0.93	1.124	0.81	27.66	3,6,7
dw194992+27969	194.9925	27.9692	22.35		0.92	1.496	0.99	-65.99	3,6

Table 2.2: Photometric and structural parameters for the galaxies detected in Coma. (continued)

ID	RA (deg)	DEC (deg)	m_{gal} (mag)	m_{NSC} (mag)	n	R_e (arcsec)	PA (deg)	b/a	Prev. Detec.
dw194914+27957	194.9144	27.9573	22.49		0.51	0.813	0.79	30.38	6
dw195005+27943	195.0052	27.9435	22.51		0.76	1.060	0.62	-65.89	
dw195011+27965	195.0117	27.9658	22.58	25.23	0.99	1.354	0.75	42.23	
dw195022+27961	195.0229	27.9611	22.66		0.99	1.743	0.57	85.86	
dw194993+27965	194.9939	27.9655	22.68	23.68	1.49	0.811	0.71	35.60	
dw195023+27991	195.0231	27.9913	22.72	25.42	0.53	2.215	0.63	37.20	
dw194908+27935	194.9086	27.9351	22.84		0.56	0.720	0.84	-57.49	3
dw195028+27964	195.0285	27.9649	22.84		0.50	0.996	0.94	-52.86	
dw195030+27962	195.0308	27.9626	22.90		0.94	1.518	0.65	-24.14	3
dw194926+27977	194.9261	27.9770	23.29		0.66	0.802	0.77	32.00	3,6
dw194931+27968	194.9312	27.9680	23.29		0.50	1.354	0.71	50.28	
dw195024+27956	195.0240	27.9560	23.33		0.75	1.187	0.59	-8.06	3
dw195056+27968	195.0567	27.9680	23.33		0.93	1.059	0.73	-32.45	3
dw194916+27961	194.9161	27.9610	23.41		0.67	0.965	0.74	-46.73	6
dw194903+27936	194.9037	27.9368	23.48		0.52	0.737	0.90	54.27	3
dw194891+27979	194.8915	27.9799	23.57		0.84	0.674	0.71	26.25	6
dw195019+28001	195.0199	28.0011	23.59		0.62	0.604	0.80	1.25	3
dw195039+27955	195.0397	27.9557	23.67		0.67	0.838	0.66	-9.15	
dw194880+27940	194.8802	27.9400	23.68		0.68	0.747	0.69	7.66	3
dw194880+27960	194.8808	27.9601	23.79		1.12	0.798	0.76	-27.25	
dw194916+27983	194.9167	27.9831	24.08		0.61	0.724	0.71	28.21	
dw194990+27973	194.9909	27.9739	24.25		0.99	0.854	0.85	47.79	
dw194922+27971	194.9221	27.9714	24.40		0.50	0.670	0.76	75.78	
dw195012+27982	195.0121	27.9820	24.44		0.59	0.784	0.65	40.80	
dw194922+27968	194.9225	27.9684	24.45		0.85	0.405	0.63	-63.66	
dw194925+27962	194.9257	27.9626	24.56		0.65	0.511	0.72	-48.45	3,6
dw195041+27971	195.0417	27.9712	24.81	27.74	0.56	0.675	0.75	33.48	
dw195004+27976	195.0041	27.9766	24.90		0.50	0.502	0.66	-55.04	

structural parameters even for faint, low surface brightness galaxies. We also constrain the relative position of the Sérsic and PSF components to be within three pixels of each other. This is inspired by *HST* studies of NSCs showing that stellar nuclei are rarely offset from the geometric centre of the host galaxy (Côté et al., 2003; Turner et al., 2012). It also guarantees that the likelihood of contamination from chance projection of stars or GCs over the galactic body remains insignificant, with the mean number of such contaminants estimated to be $\approx$ 0.002 per galaxy. This is calculated by counting the total number of point sources (CLASS_STAR ≥ 0.6) that have a magnitude difference of less than 0.5 mag with respect to each NSC. The surface density of such candidates is then multiplied by the area enclosed in a circle with a radius of three pixels, which is our criterion for a bona-fide NSC detection. Results are not sensitive to the magnitude difference between putative contaminants and the candidate NSCs.

A summary of the method is shown in Fig. 2.3. The galaxy properties obtained from this procedure are presented in Table 2.2, where magnitudes are dereddened from Galactic extinction using the maps from Schlafly and Finkbeiner (2011). We find that our catalogue has eight common entries with the catalogue from den Brok et al. (2014) and the root mean square deviation of the magnitudes in these common galaxies is only 0.12 mag.

2.2.5 Photometric Uncertainties Estimation

To estimate the uncertainties in the recovered parameters shown in Table 2.2 we run our photometry procedure to mock galaxies randomly placed in the HST images used in this work. Mock galaxies are created using GALFIT using a Sérsic + PSF component, with parameters sampled from the values in Table 2.2. Galaxy magnitudes are chosen randomly from an uniform distribution $U_{m_{gal}}(-14.0, -10.0)$. NSC magnitudes, effective radii and Sérsic indices show significant correlations with galaxy magnitude, with Pearson correlation coefficients of 0.42, -0.54 and -0.44 respectively. Due to this, we group these quantities in 10 bins of galaxy magnitude and calculate the mean, μ_{bin}, and standard deviation σ_{bin}. Then, in each bin, we randomly generate new values for such quantities following a normal distribution $N(\mu_{bin}, \sigma_{bin})$. We do not detect a significant correlation between axis ratios and galaxy magnitude (Pearson corre-

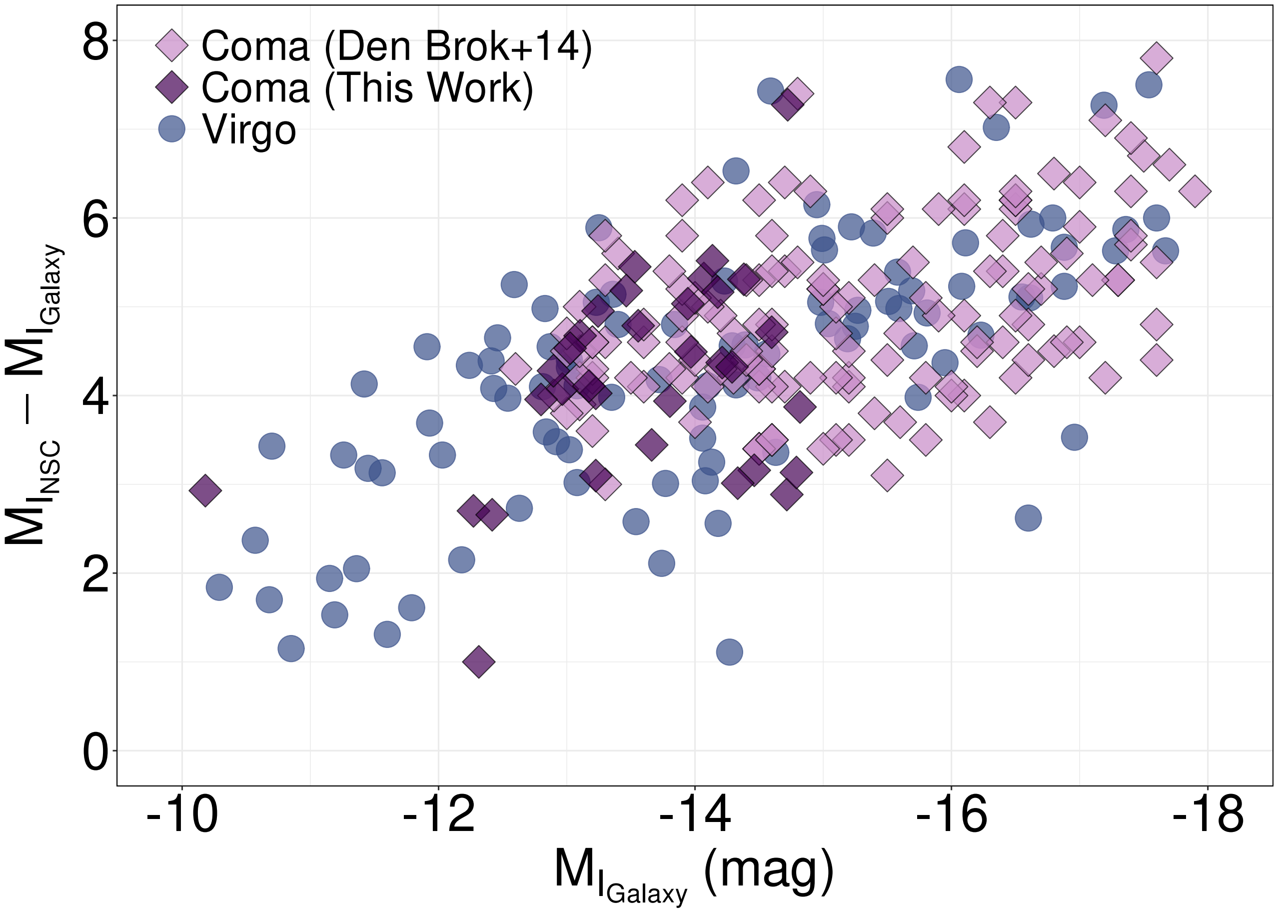

Figure 2.4: Difference between the magnitude of the nuclei, $M_{I,NSC}$ and the one of its host galaxy, $M_{I,Galaxy}$, for all nucleated galaxies in the Coma cluster sample from this work (shown in table 2.2, purple diamonds) and den Brok et al. (2014) (magenta diamonds), as well as nucleated galaxies in the Virgo cluster (from Sánchez-Janssen et al. (2019), blue circles), as a function of the host galaxy absolute magnitude. For both environments, brighter galaxies tend to show larger differences in magnitude from their nuclei, although a scatter is also evident, showcasing its stochastic nature.

lation coefficient of -0.09). For this reason, mock values for the axis ratio are obtained from an uniform distribution $U_q(0.35, 1.0)$. Position angles are set to a fixed value of 75 degrees for every mock galaxy, as this parameter has little impact on the uncertainties we aim to estimate. This sampling technique ensures that we simulated only realistic representations of galaxies as detected in our catalogue. We created a total of 10,000 nucleated galaxies, 5,000 for each HST field. Mock galaxies are added in random positions in the HST images with all galaxies masked. Then we proceed with photometry exactly as done for our real detections except for the step of visual classification.

The results of these simulations are presented in Fig. 2.5. The median uncertainty in galaxy magnitude is ~ 0.2 mag. The 95% and 68% confidence intervals show that GALFIT estimates magnitudes brighter than the true values for galaxies fainter than $M_I \sim 11$ mag. This behaviour was also observed in the simulations of Ferrarese et al. (2020) for the NGVS. Therefore, we do not consider this to be evidence for any systematic bias from our method or observations. Regarding NSC magnitudes the uncertainties are considerably lower, never surpassing 0.1 mag even considering the 95% confidence intervals. Finally, results for effective radii and Sérsic index show a median uncertainty of $\sim 20\%$.

In Fig. 2.4 we show the difference between the magnitude of the NSC and its host galaxy for all the nucleated galaxies in our sample, as well as those from den Brok et al. (2014) and the nucleated galaxies in the Virgo cluster from Sánchez-Janssen et al. (2019). Similarly to what was found in the two latter works, the relative contribution of the NSC to the overall brightness of the host galaxy decreases with galaxy luminosity–albeit with a large scatter in the relation. From the perspective of comparing different environments, we see that the trend in Fig. 2.4 is very similar for both Virgo and Coma galaxies. Overall, it seems clear that the luminosity of the NSC is related to that of the host galaxy regardless of the environment, but the large scatter in the relation indicates that NSC growth varies substantially from one galaxy to another.

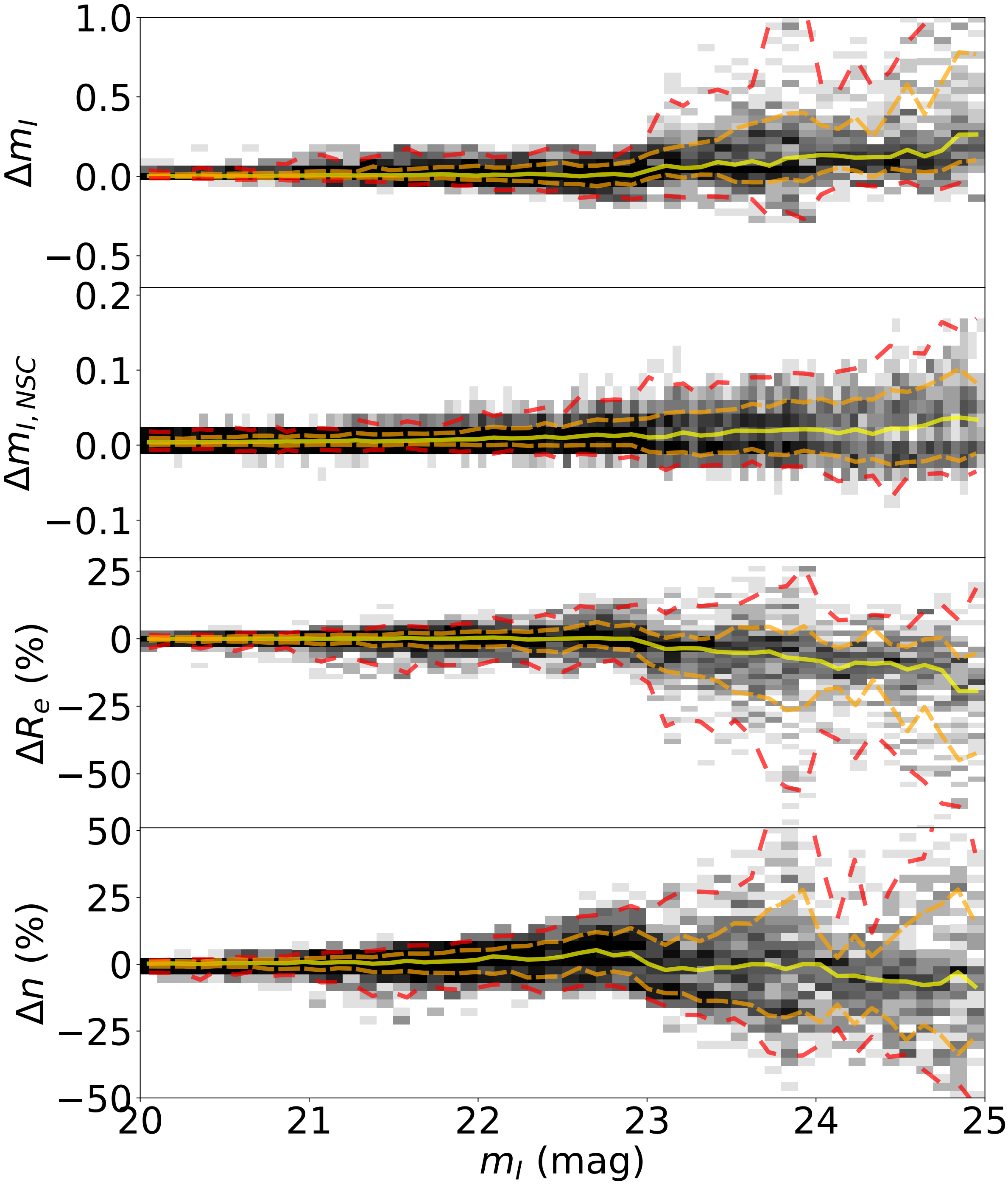

Figure 2.5: Results of our photometry procedure applied to 10,000 mock galaxies randomly positioned in both HST/ACS fields studied in this work; 5,000 in the NGC 4874 field and 5,000 in the NGC 4889 field. We show the difference between the "true" and "fitted" quantities in the form ΔX, where X can be galaxy magnitudes ($m_{I,gal}$), NSC magnitudes ($m_{I,NSC}$), effective radii (R_e) and Sérsic index (n). For R_e and n we show this difference in percentages. In the x-axis we show "true" values of $m_{I,gal}$. The grey scale shows the density of galaxies in bins of galaxy magnitude. Solid yellow lines show the median distribution of points, while orange and red dashed lines show the 95% and 68% confidence intervals, respectively.

2.3 Statistical Modelling of the nucleation fraction

To analyse the nucleation fraction in the Coma cluster and how it compares to other environments we employ Bayesian logistic regression (see e.g. Hilbe et al., 2017, for a detailed description). Logistic regression belongs to the family of generalised linear models, and is particularly suitable for handling Bernoulli-distributed (binary) data. Such distribution characterises processes with two possible outcomes $\{0, 1\}$, be it success or failure, yes or no, or alike – in our case it is nucleation or non-nucleation. Previous applications of logistic models in Astronomy include the studies of star-formation activity in primordial dark matter halos (de Souza et al., 2015), the escape of ionising radiation at high-redshift (Hattab et al., 2019), the effect of environment in the prevalence of Seyfert galaxies (de Souza et al., 2016), and the redshift evolution of UV upturn galaxies (Dantas et al., 2020). While the full behaviour of the nucleation fraction departs significantly from the logistic relation (Sánchez-Janssen et al., 2019), we make use of the fact that for all studied environments f_n appears to peak at masses $\log(\mathcal{M}/\mathcal{M}_\odot) \approx 9$ (Neumayer et al., 2020), and then declines gradually toward lower masses until it becomes negligible.

The regression model is the following:

$$
\begin{aligned}
&\mathrm{y_i} \sim \mathrm{Bern}\left(\mathrm{p_i}\right),\\
&\eta_i \equiv \log\left(\frac{p_i}{1-p_i}\right),\\
&\eta_\mathrm{i} = \beta_{1[\mathrm{k}]} + \beta_{2[\mathrm{k}]}\,\mathrm{M_{I,i}},\\
&\begin{bmatrix}\beta_{1[k]}\\ \beta_{2[k]}\end{bmatrix} \sim \mathrm{Norm}\left(\begin{bmatrix}\mu_\beta\\ \mu_\beta\end{bmatrix}, \Sigma\right); \quad \Sigma \equiv \begin{bmatrix}\sigma_\beta^2 & 0\\ 0 & \sigma_\beta^2\end{bmatrix},\\
&\mu_\beta \sim \mathrm{Norm}(0, 10^2); \quad \sigma_\beta^2 \sim \mathrm{Gamma}(0.1, 0.1).
\end{aligned}
\tag{2.3}
$$

The above model reads as follows. Each of the i-th galaxies in the dataset has its probability to manifest nucleation modelled as a Bernoulli process, whose probability of success relates to $M_{I,i}$ through a logit link function, η_i (to ensure the probabilities will fall between 0 and 1), where the index k encodes the cluster/group environment. A subtle, but important characteristic of our model is the treatment of the intercept $\beta_{1[k]}$ and slope $\beta_{2[k]}$ coefficients via hierarchical partial pooling. For the case studied here, it falls under the umbrella of generalised linear mixed models (see e.g. Hilbe et al., 2017, for details). A simple intuition behind this choice is given below. When modelling the same relationship across multiple groups, there are three common choices: pooled, unpooled, and partially-pooled models. In our case the pooled model implies a fit to the entire data, completely ignoring potential differences across cluster/groups. In other words, this would implicitly assume a universal shape for the nucleation fraction. In the other extreme lies the ubiquitous unpooled model, which implies fitting each individual case, ignoring any potential correlation across cluster/groups. While it seems a harmless choice, this model is very sensitive to differences in sample size and magnitude range between different cluster/group environments. The most conservative option is partial pooling, which infers different parameters for each group, but allows them to share information. This is done via the use of hyper-priors for its coefficients. This is included in our model by assuming a multi-Normal prior for $\beta_{1[k]}$ and $\beta_{2[k]}$ with a common mean μ_β and variance σ^2_β, to which we assigned weakly informative Normal and Gamma hyper-priors respectively.

We evaluate the model using the Just Another Gibbs Sampler (JAGS[1]) package within the R language (R Development Core Team, 2019). We initiate three Markov Chains by starting the Gibbs sampler at different initial values sampled from a Normal distribution with zero mean and standard deviation of 100. Initial burn-in phases were set to 5,000 steps followed by 20,000 integration steps, which are sufficient to guarantee the convergence of each chain, following Gelman-Rubin statistics (Gelman and Rubin, 1992).

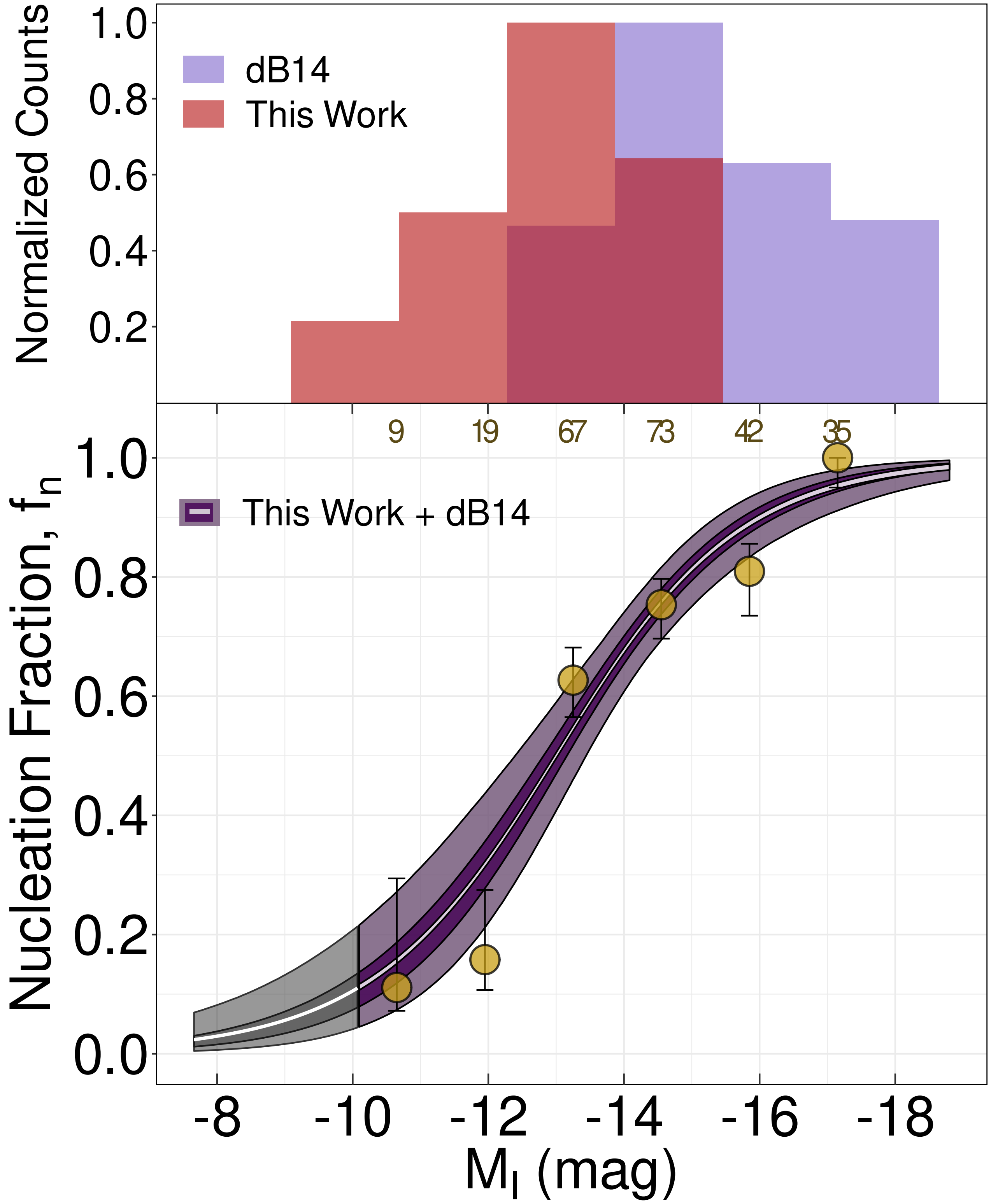

Figure 2.6: *Top:* Distributions, in normalised counts, for the data obtained in this work and presented in Table 2.2 (red histogram) and the catalogue of Coma galaxies from den Brok et al. (2014) (blue histogram). *Bottom:*Nucleation fraction versus absolute magnitude for galaxies in Coma, combining the data from this work and the one from den Brok et al. (2014). In the cases where galaxies were detected in the two datasets, we keep the magnitudes from our own analysis. The white curve is the mean posterior from the Bayesian logistic regression. The purple shaded regions show the 50% and 95% confidence intervals, whereas the grey shades indicate the magnitudes where the model extrapolates the data. The yellow solid circles represent the median nucleation fraction in a binned representation of the data, with uncertainties given by the corresponding 68% Bayesian credible intervals. The number of objects in each bin is shown at the top.

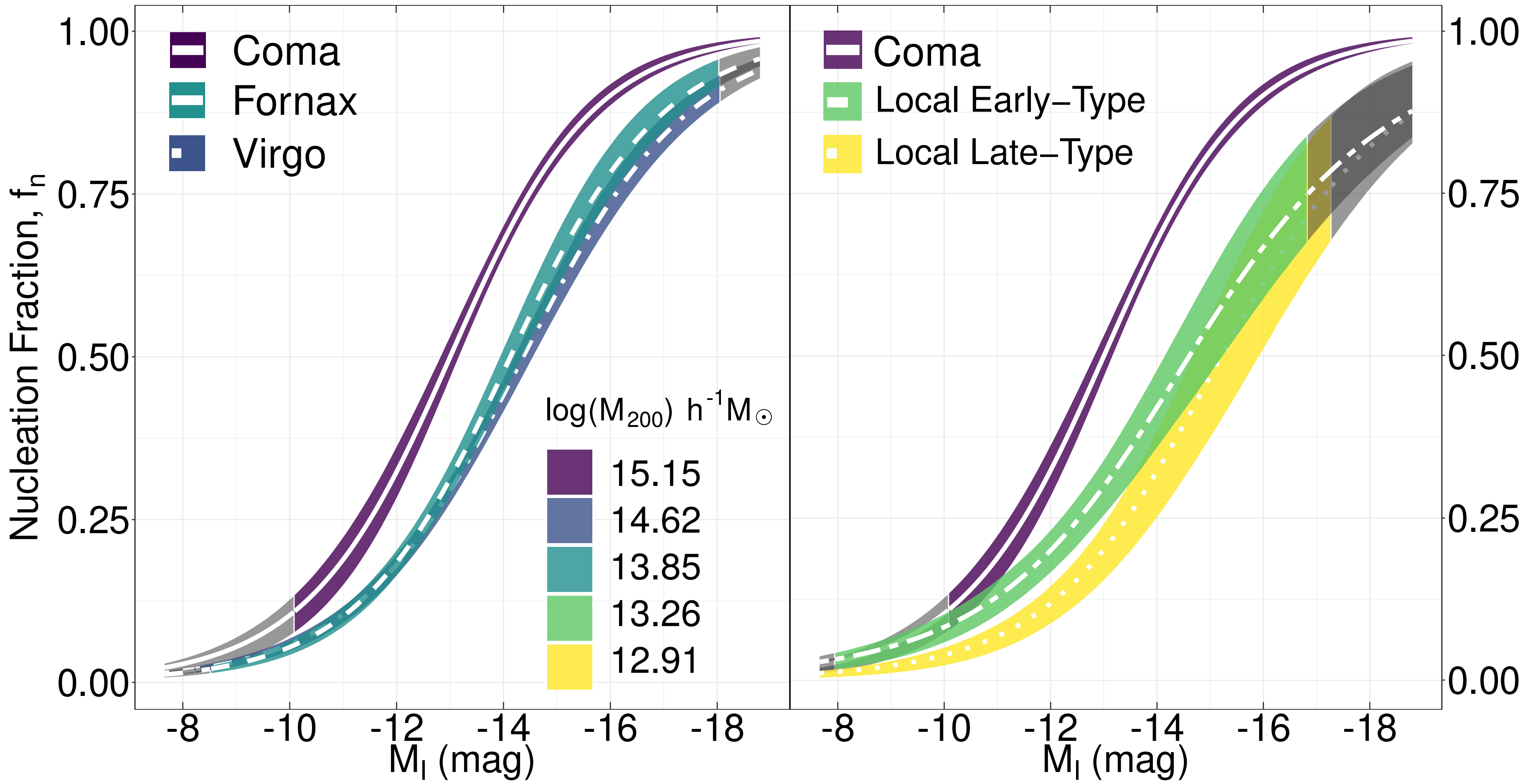

Figure 2.7: Mean posteriors from the Bayesian logistic regression models and 50% confidence intervals, in the left panel, for the Coma cluster data from this work and den Brok et al. (2014), Virgo cluster from Sánchez-Janssen et al. (2019) and Fornax cluster from Muñoz et al. (2015). In the right panel, the Coma cluster again as well as a combined sample of galaxies in the local volume in groups with a central Early or Late-Type galaxy. The samples are colourised by the approximated cluster/group virial halo mass, from the references mentioned in the text. For the case of the local volume environments, the halo mass presented is a mean of the halo masses of the sample galaxies within it. The grey regions of the curves represent the regions where the model extrapolates the actual data. Coma galaxies show a higher probability of nucleation than all other environments at all magnitudes considered.

Table 2.3: Summary of the parameters estimated from the model presented in eq. 2.3. In the first column we show $M_{I,f_{n50}}$, the magnitude at which the estimated probability of nucleation reaches 50%. In the second column ΔOdds represents the expected change in the odds of nucleation by a variation of one unit of magnitude. In the last two columns, β_1 and β_2 are the mean posteriors for the intercept and slope, respectively, of the link function η_i. One can see that ΔOdds is within a 10% difference among all environments, while the variation of $M_{I,f_{n50}}$ present a significant difference in luminosity.

	$M_{I,f_{n50}}$	ΔOdds	$\beta_1(intercept)$	$\beta_2(slope)$
Coma	$-12.98^{+0.26}_{-0.25}$	-52.2%	-9.66 ± 1.56	-0.74 ± 0.11
Virgo	$-14.39^{+0.25}_{-0.25}$	-50.0%	-9.89 ± 1.28	-0.70 ± 0.10
Fornax	$-14.16^{+0.31}_{-0.31}$	-47.3%	-9.25 ± 0.98	-0.64 ± 0.07
Local Early-Type	$-14.64^{+0.98}_{-0.89}$	-41.4%	-7.94 ± 1.76	-0.54 ± 0.14
Local Late-Type	$-15.38^{+0.96}_{-0.89}$	-47.5%	-9.98 ± 2.21	-0.66 ± 0.17

2.4 Results

When modelling the nucleation fraction the Coma sample presented here is merged with the catalogue from den Brok et al. (2014) for completeness purposes at the bright end. The data from this work comprises Coma galaxies with magnitudes in the $-10.0 < M_I < -15.0$ range, while den Brok et al. (2014) data ranges from $-12.8 < M_I < -19.0$. In the few cases where a galaxy is detected in the two studies we keep the magnitudes from our own analysis.

2.4.1 Nucleation fraction in the Coma cluster

Fig. 2.6 shows the Coma nucleation fraction, f_n, as a function of galaxy absolute magnitude, M_I. The shaded areas indicate the 50% and 95% probability intervals around the mean of the posterior for the logistic model (white curve). The means and 68% confidence level values of the corresponding coefficients are shown in Table 2.3. The grey region represents the extrapolated solution beyond which there is no data coverage. For visualisation purposes we also show with yellow circles the nucleation fraction calculated in eight equal-sized bins. The corresponding error bars show the 68% Bayesian confidence level. The tick marks at the top and bottom of the panel indicate the magnitudes for each of the nucleated and non-nucleated galaxies,

---

[1] http://cran.r-project.org/package=rjags

respectively, and the yellow histogram is a binned representation with the purpose to highlight the prevalence of NSCs in brighter galaxies.

We confirm the strong dependence of the nucleation fraction on galaxy luminosity in Coma: it peaks at nearly $f_n \approx 100\%$ at $M_I = -18$ (the characteristic luminosities of classical dE galaxies) and then declines to become almost negligible at $M_I = -10$. Overall, the nucleation fraction is remarkably high, with more than half of the $M_I = -13$ dwarf galaxies still hosting NSCs. This is clearly shown by both the binned nucleation fraction and the logistic model, but only the latter is able to produce a smooth solution while also allowing us to study the rate at which NSCs occur in galaxies of different brightness. More importantly, we are now in a position to quantitatively compare the exact shape of the nucleation fraction in Coma and in other environments.

2.4.2 Nucleation in Other Environments

In Fig.2.7 we show the mean posterior for the nucleation fraction in the Coma cluster compared to that in the Virgo and Fornax clusters (left panel), as well as in nearby groups (right panels). In order to improve the number statistics in these less rich environments we subdivide and stack the samples of group dwarfs into satellites of early- and late-type centrals.

The total number of quiescent satellites in the sub-samples of early- and late-type groups is 93 and 90, respectively. As with Coma, the means and 68% confidence level values of the coefficients for the logistic model are shown in Table 2.3.

In Fig. 2.8 we show the individual posterior distributions from the Bayesian logistic regression alongside binned data points for every environment from the literature considered in Fig. 2.7, with the same captions as in the bottom panel of Fig. 2.6. It is clear that the logistic regression follows closely the binned data despite not relying on arbitrary defined bins. We stress the advantages of not relying on a binned fit, specially when dealing with data from different sources and with different sample sizes. Notice that the local environments have noticeable larger confidence intervals than Virgo, Fornax and Coma (show in Fig. 2.6). Our method of choice is able to efficiently compare the nucleation fraction in different environments in a homogeneous way while not underestimating the uncertainties arisen from small sample sizes.

Two results are readily apparent.

1) *Nucleation has a nearly universal dependence on dwarf galaxy luminosity.* This is shown in Table 2.3 by the very similar β_2 slope parameters for all the different environments, which are consistent with each other at the 1 σ level. In the table we also show the corresponding ΔOdds, which represents the change in nucleation odds given a variation of one unit in magnitude for each environment, i.e., the nucleation rate by magnitude. We find very similar values for all environments, perhaps with the exception of systems dominated by early-type centrals where the nucleation fraction displays a slightly shallower decline.

2) *Nucleation is more common in more massive haloes regardless of dwarf galaxy luminosity.* This is evident from the posterior curves in Fig.2.7, which are colour-coded by the estimated virial halo masses for the systems under study. For example, a $M_I = -15$ dwarf has an $\approx 80\%$ probability of being nucleated in Coma, compared to $\approx 50\%$ for quiescent satellites in groups with both early- and late-type centrals. In order to better quantify this dependence we introduce the $M_{I,f_{n50}}$ index, the magnitude at which the nucleation probability reaches 50% as inferred from the logistic model. In Fig. 2.9 we show how this half-nucleation magnitude varies as a function of the virial halo mass for each environment. We model this relation as a linear regression of the form $M_{I,fn50} = \alpha + \beta \log(\mathcal{M}_{200})$. The mean posteriors and associated standard deviations obtained for the parameters are: $\alpha = -21.6 \pm 2.8$ and $\beta = 0.54 \pm 0.19$. This implies that the half-nucleation luminosity correlates with the host halo mass roughly as $L_{I,f_{n50}} \propto \mathcal{M}_{200}^{-0.2}$. The most extreme environments, Coma and the late-type groups, have $L_{I,f_{n50}}$ values that differ by almost a factor of ten in luminosity. A corollary to this result is that the nucleation fraction in Coma is the highest in all the studied environments over more than three decades in dwarf galaxy luminosity.

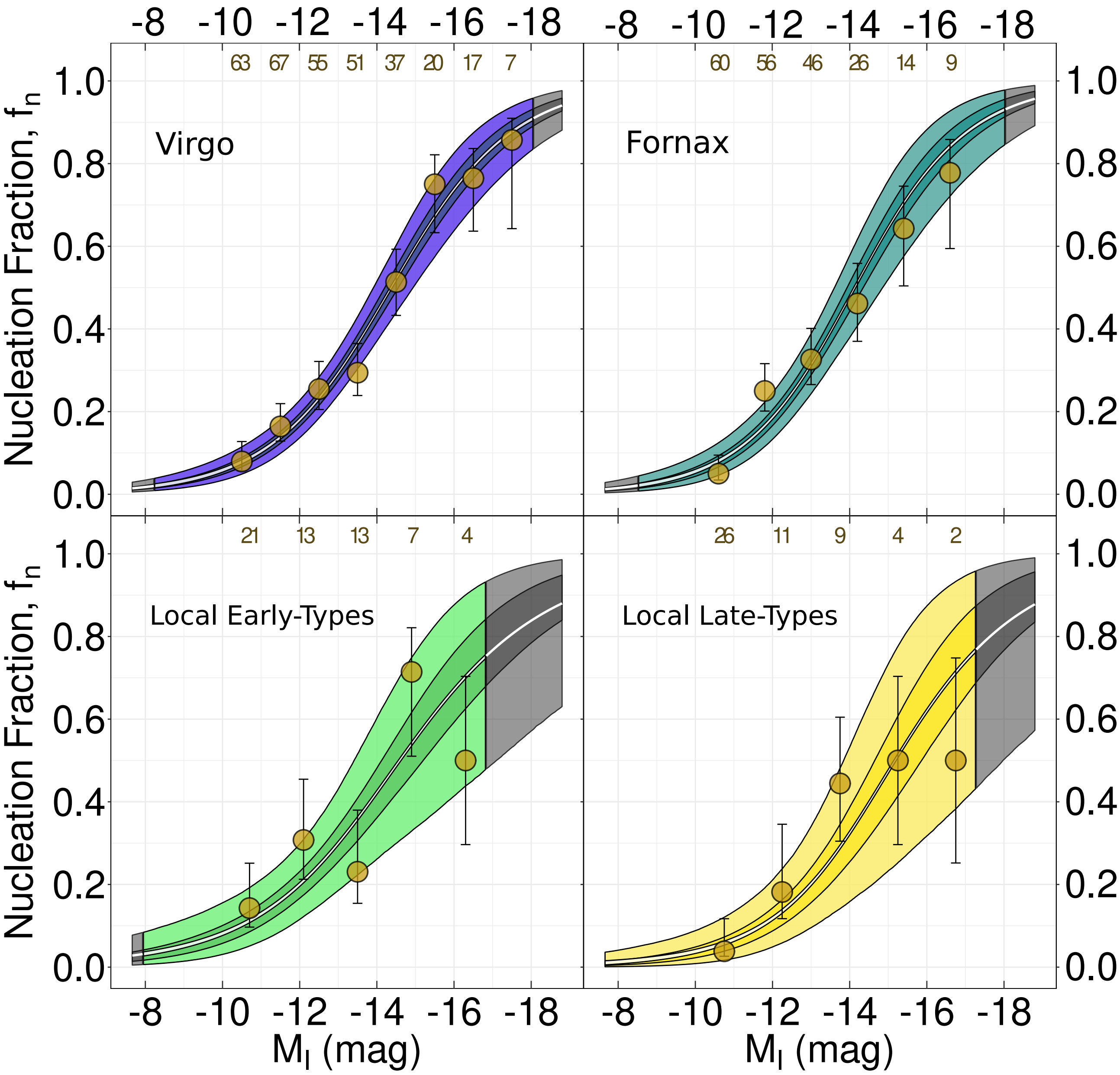

Figure 2.8: Same as the bottom panel of Fig. 2.6, but for every other environment considered in this work, gathered from the literature references described in section 2.1.1. Notice the excellent agreement between the binned data and the logistic regression.

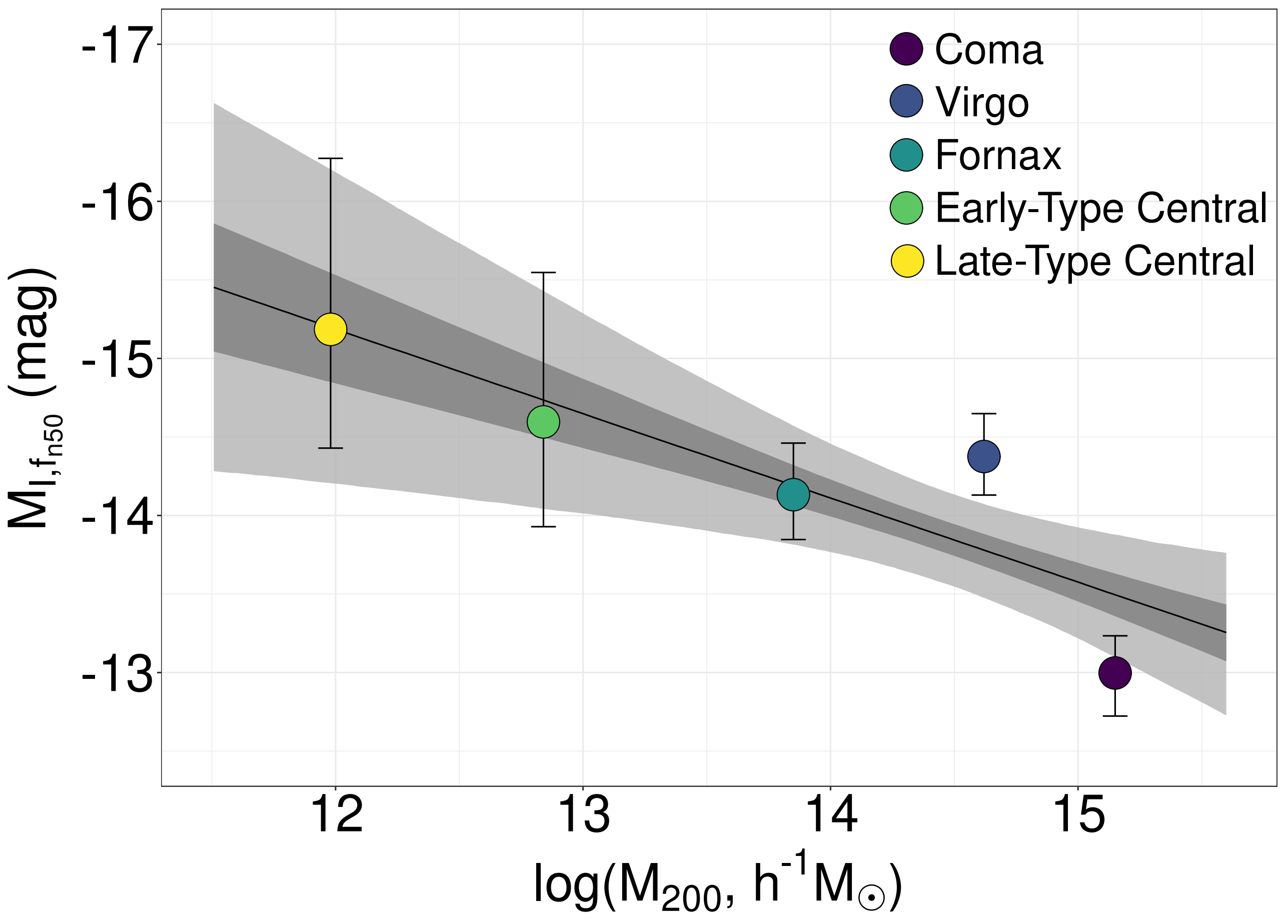

Figure 2.9: Mean posterior for the magnitude at which the probability of nucleation is 50%, $M_{I,fn50}$, as a function of host virial halo mass (references mentioned in the text). The mean, 50% and 95% confidence intervals for a linear model are indicated by the solid line and grey shaded areas, respectively. More massive environments exhibit fainter values of the half-nucleation magnitude.

The main finding of this study is that *the rate at which the probability of nucleation varies with magnitude does not depend substantially on the environment, but the fraction of nucleated dwarfs at a fixed luminosity does.* As a result, any model of NSC formation in low-luminosity/mass galaxies needs to account for the joint dependence of the nucleation fraction on galaxy luminosity/mass and the environment in which they reside. We discuss possible scenarios in the next Section.

2.5 Discussion

We now attempt to frame the two main results of this work in the context of NSC formation scenarios in low-luminosity/mass galaxies. The finding that the nucleation fraction displays a nearly-universal dependence with galaxy luminosity simply implies a higher ability of more massive dwarfs to pile up material in their central regions. Studies of NSC occupation alone cannot constrain whether this process occurs through star cluster inspiral or in situ star formation following gas inflows. There is, however, mounting evidence that the former process is probably dominant for low-mass quiescent galaxies (Neumayer et al., 2020). Observations in support of this picture include the fact that NSCs in faint, early type dwarfs are typically more metal-poor than their host galaxies (Fahrion et al., 2020; Johnston et al., 2020); that the occupation fraction of GCs and NSCs track each other remarkably well (Sánchez-Janssen et al., 2019); and that in this luminosity regime the scaling of NSC mass with galaxy mass is in excellent agreement with the prediction from GC inspiral models (Antonini, 2013; Gnedin et al., 2014; Sánchez-Janssen et al., 2019). Such models require GCs (or their progenitors) to have masses high enough so that their orbits decay in less than a Hubble time as a consequence of dynamical friction, while simultaneously surviving tidal dissolution. Factors that influence NSC growth and may depend on galaxy mass are the GC mass function (GCMF), the GC formation distance, the host galaxy structural properties, and the presence of a massive black hole–but the BH occupation fraction for low-mass galaxies is poorly constrained, and it certainly does not increase for fainter galaxies (Greene et al., 2020). Given that the nucleation fraction peaks at $M_I \approx -18$ ($\mathcal{M} \approx 10^9 \mathcal{M}_\odot$) and then declines, fainter dwarfs must have a comparatively bottom-heavier GCMF, or have GCs that on average form at larger distances from the galactic centre, or be preferentially concentrated and more compact. There are no observational constraints on the first two properties, and the latter is in direct contradiction with the observed mass-size relation of faint dwarfs in the nearby Universe (McConnachie, 2012; Eigenthaler et al., 2018; Ferrarese et al., 2020). Alternatively, it is possible that, even if the GCMF is universal, the formation of GCs in galaxies with such low masses remains a stochastic process. If dwarfs were to form clusters so that the total mass of the GCs is a constant fraction of their stellar mass, this would explain why in the dwarf regime the NSC and GC occupation fractions track each other so closely: the nucleation fraction drops simply because the host galaxies never form enough massive GCs to begin with. A corollary from this proposition is that the GCMF should vary with galaxy luminosity, with very faint dwarfs exhibiting a deficit in massive GCs.

In the context of GC inspiral scenarios, the same arguments apply to the unambiguous environmental dependence we show in Figs. 2.7 and 2.9–but now the differences must arise due to effects related to the host halo at fixed present-day galaxy luminosity. Unfortunately, to our best knowledge the environmental dependence does not arise naturally in any NSC formation model, and there are no observational constraints on the early properties of GCs in different environments. Additionally, the mass-size relation seems to be rather universal in this luminosity regime, with dwarfs in environments ranging from Coma to the Local Group following similar scaling relations. Sánchez-Janssen et al. (2019) speculate that a biased formation scenario for star clusters similar to that proposed by Peng et al. (2008) does a reasonable job at explaining the environmental dependence of the faint nucleation fraction, at least qualitatively. In such a model galaxies that now reside in higher density environments form stars earlier and sustain higher star formation rates (SFR) and SFR surface densities. These are conditions conducive to the formation of bound massive clusters, and if cluster formation efficiency is close to universal and galaxies formed clusters proportionally to their mass at early epochs (Kruijssen, 2015) then one naturally expects a larger mass fraction in star clusters in the more biased environments. In this context it is also important to remember that, for a given present-day stellar mass, the subhaloes in denser environments were at all times prior to infall more massive than those in less dense regions. This, together with earlier infall (and peak mass) times creates conditions that favour efficient formation of star clusters (Mistani et al., 2016). Those that are massive enough and form close to the galaxy centre will experience dynamical friction and decay to the bottom of the potential well. We finally note that some of the masses of NSCs in very faint galaxies are comparable to those of typical GCs (see Fig. 2.4), and therefore very little GC merging is actually required (Fahrion et al., 2020; Neumayer et al., 2020).

The proposition that nucleated dwarfs form a biased subpopulation is well established by numerous observational results. Compared to their non-nucleated counterparts they exhibit more concentrated spatial distributions and a propensity for circularised orbits (Ferguson and Sandage, 1989; Lisker et al., 2007, 2009); they are intrinsically more spherical (Ryden and Terndrup, 1994; Sánchez-Janssen et al., 2019) and possess more concentrated light profiles (den Brok et al., 2014); they host older stellar populations (Lisker et al., 2008); and there is tentative evidence that they feature higher GC mass fractions (Miller et al., 1998; Sánchez-Janssen and Aguerri, 2012). Whether or not this is sufficient to explain the higher occurrence of NSCs in more massive haloes remains to be quantified by detailed models of their formation and evolution.

2.6 Summary and Conclusions

In this work we detect and characterise 66 low-mass, quiescent galaxies in the central regions of the Coma cluster using deep HST/ACS imaging in the F814W band. NSCs are identified by a combination of visual inspection and full image modelling. We perform Bayesian logistic regression to model the joint dependence of the nucleation fraction on galaxy absolute magnitude and environment for dwarf galaxies in nearby clusters and groups. Our main conclusions are:

1) Similar to previous findings (den Brok et al., 2014; Sánchez-Janssen et al., 2019), fainter galaxies in Coma tend to show a smaller difference in magnitude from their nuclei–but

the significant scatter at fixed galaxy luminosity suggests the growth of stellar nuclei is a substantially stochastic process.

2) The nucleation fraction depends on both galaxy mass/luminosity and environment, with the former being the primary parameter. Fainter galaxies have a lower probably of hosting NSCs, as do quiescent satellites of all luminosities in lower mass haloes. The rate at which the probability of nucleation varies with luminosity is remarkably universal.

3) The nucleation fraction in Coma over three decades in dwarf galaxy luminosity is higher than in any other known environment. This is a direct result of the strong environmental dependence of the nucleation fraction. We find that the luminosity at which half of the dwarf galaxies contain an NSC is inversely proportional to the virial mass of the host halo, $L_{I,f_{n50}} \propto \mathcal{M}_{200}^{-0.2}$.

We have shown that nucleation in dwarf galaxies is a complex phenomenon that depends both on luminosity and the environment in which the galaxy resides. We identify several observational constraints that would advance our knowledge of the conditions and environments that are conducive to the formation and growth of stellar nuclei. First, it is critical to rise the statistical significance of the environmental dependence by studying the nucleation fraction in other groups and clusters–and in particular for both more and less massive host haloes than studied here. The rarity of massive clusters like Coma and the sparseness of low-density environments make this a challenging task that might be best tackled with upcoming wide-field space missions like Euclid, the Roman Space Telescope and the Chinese Space Station Telescope. Second, the availability of large NSC samples would allow us to investigate if other physical parameters such as galaxy size also play an important role on the presence of nuclei, as predicted by models (Mistani et al., 2016; Antonini et al., 2015). Finally, occupation studies have little constraining power on the exact physical processes that drive NSC formation and growth. Detailed chemo-dynamical studies of nuclei across a wide range of masses and environments will be instrumental in settling this question (Kacharov et al., 2018; Fahrion et al., 2019; Johnston et al., 2020; Carlsten et al., 2021).

Chapter 3

The effects of environment and abundance variations in the stellar populations of globular clusters in the Virgo and Hydra brightest cluster galaxies

In this chapter we will look into the GCs of elliptical galaxies. Broadly, our main goal is to investigate the impact of models with abundance variations in the prediction of colours of GCs. To this end, we will employ GC photometric catalogues with extensive spectral coverage, spanning from the near ultra-violent (NUV) to the near infrared (NIR). Particularly, we will compare such data with SSP models with the abundance pattern of stars in the Galaxy and with α-enhancement. Then, we will also compare the properties of the GC systems around M87, in the Virgo Cluster, and around NGC3311 and NGC3309 in the Hydra cluster. This comparison will be discussed in the context of how well the SSP models perform in predicting GC colours and which aspects of such models can be improved in the future.

Firstly, in the next section, we will present the novel dataset later used in this work, the K_s-band photometry from the VLT/HAWK-I telescope of Virgo and Hydra fields. Later on we match with GC samples from the literature to build the GC catalogues used in our analysis.

Furthermore, we also discuss our GC selection criteria and possible caveats from missing objects in this selection.

3.1 Observations, Data Reduction and Decontamination

3.1.1 VLT/HAWK-I K_s-band imaging

We present two new catalogues of K_s-band photometry obtained with the HAWK-I instrument (Casali et al., 2006), a near-infrared (NIR) cryogenic imager installed on the UT4 at the Very Large Telescope (VLT) facility at Paranal Observatory, Chile. The observations targeted the inner 40 Kpc^2 of NGC 4486/M87[1], and two fields in the Hydra cluster, each with approximately 88.5 Kpc^2, that when combined are centered in the galaxies NGC 3311 and NGC3309[2] (see Fig. 3.1). The HAWK-I instrument has a pixel scale of 0.106" pix^{-1} and a field-of-view (FOV) of approximately 7.5' x 7.5' with a cross-shaped gap of 15", dividing the FOV into 4 independent CCDs. Due to this, a dithering pattern was applied in the observations of the M87 field and the Hydra F2 field, such that all major galaxies were observed in their entirety. Additionally, in both observations, separate sky exposures at fixed offsets were performed to ensure that the rapid variation of the sky in the NIR was taken into account during reduction procedures. The M87 observations were carried out during the months of April, May and June of 2013, while the observations of the Hydra cluster were performed between the months of December of 2013 and February of 2014. The exposure times summed 7.2 hours for M87 and 10.4 hours for the Hydra cluster. The top-right and bottom-left quadrants of both Hydra fields overlap and contain NGC3311, enabling an effectively deeper imaging in the FOV of this galaxy than in the rest of the Hydra FOV.

We carried out the reduction using the HAWK-I pipeline[3] The raw data are divided between the four CCDs of the instrument, each covering one of the quadrants of the entire

---

[1] Proposal 091.B-0615(A), PI: Ana Chies Santos

[2] Proposal 092.B-0759(A), PI: Iskren Georgiev

[3] HAWK-I pipeline version 2.4.3 (released in August 2018) with GASGANO version 2.4.8 (Eso, 2012) and ESOREX(ESO CPL Development Team, 2015).

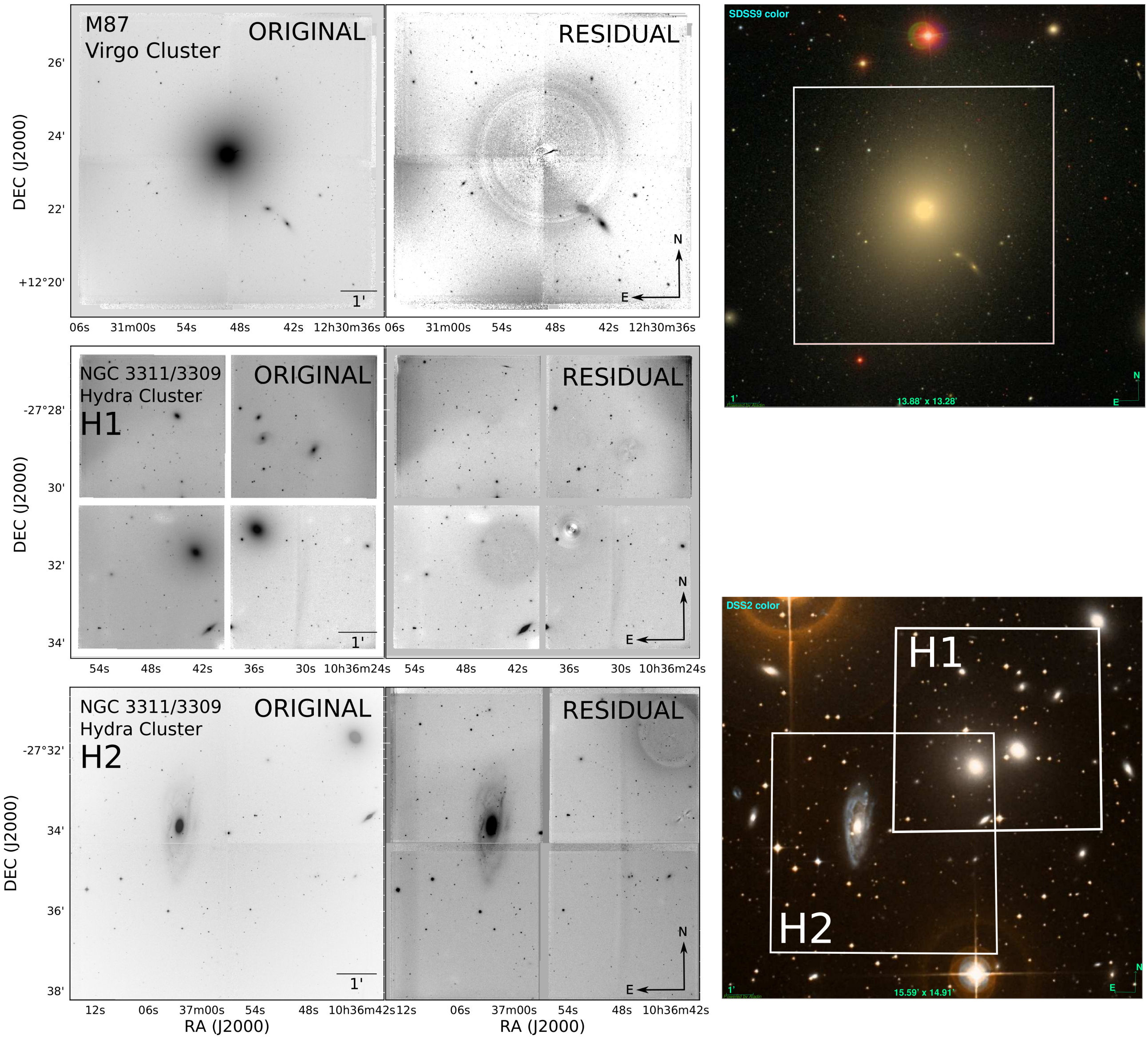

Figure 3.1: *Left panels:* Images used in this work. In the top two right panels, the final reduced Virgo Cluster VLT/HAWK-I K_s image centered on M87 and on the left of it the residual image after subtracting M87 using the model created with IRAF/ELLIPSE. In the middle left panels, same as above but for the H1 field of the Hydra Cluster observations used in this work. And in the lower right panels same as above but for the secondary H2 field of the Hydra cluster observations. *Right panels:* At the top, SDSS coloured Virgo cluster image, centered on M87, with the white rectangle showcasing the approximated FOV of the VLT/HAWK-I observations. At the bottom right, same as above but for the Hydra cluster field and using a DSS colour image. Notice that the H2 and H1 Hydra fields overlap at the location of NGC 3311, the southernmost of the two central elliptical galaxies in the cluster.

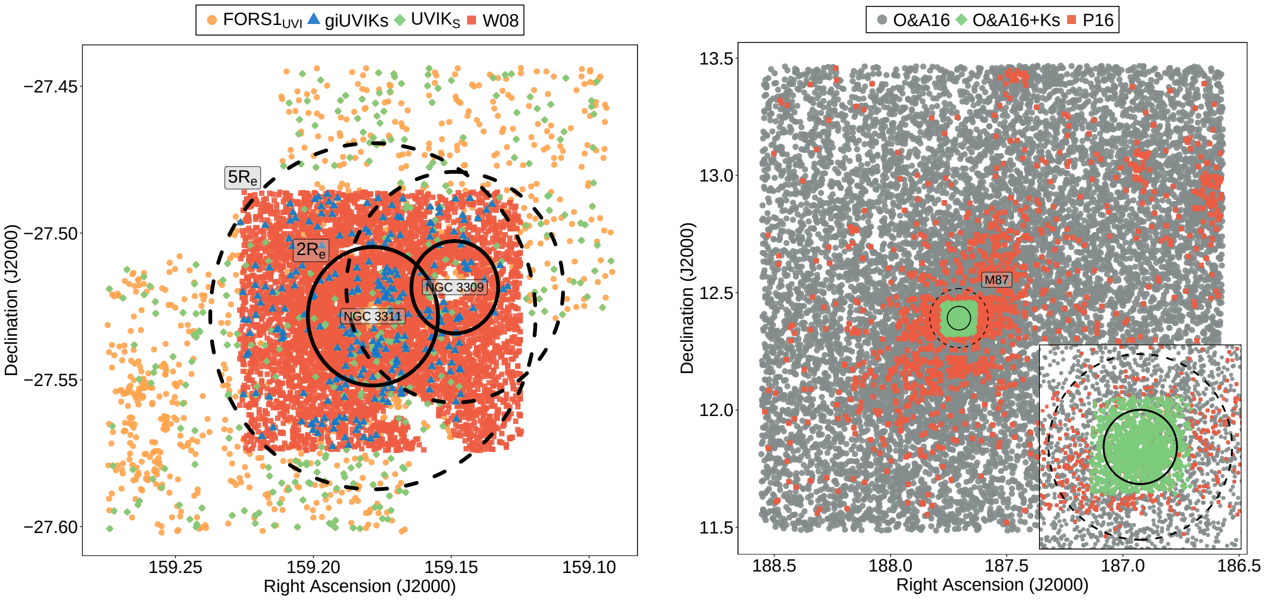

Figure 3.2: Spatial distribution of the GC samples used in this work. Also plotted are solid circles indicating roughly the regions contained within 2 effective radii (R_e) from the brightest galaxies in each field, which are labelled in each panel. *left panel:* FOV of the Hydra observations, comprising GCs around the galaxies NGC 3311 and NGC 3309. *right panel*:FOV of the NGVS observations with an inlet showing the area within $5R_e$ of M87. The region covered by the green circles, representing the GCs detected in the HAWK-I observations, is approximately equal to the area within the FOV of such observations.

FOV. The reduction process follows the standard process of dark correction, flat-fielding and gain correction, followed by sky subtraction using the separate sky exposures at fixed offsets. Astrometric calibrations are performed using 2MASS (Skrutskie et al., 2006) standard stars and for each observing block the individual exposures are stacked, resulting in 4 final reduced science images for each of the 4 CCD images in a single observation. In Fig. 3.1, top panels, we present the merged CCD images in a single figure using SWarp (Bertin et al., 2002).

3.1.2 Photometry

With the HAWK-I data already reduced, we proceed to detect and measure the magnitudes of sources in the K_s-band images.

Bright Galaxy Modelling and Subtraction

For the purpose of detecting the highest number of GCs, we model and subtract the light of the most luminous galaxies in the final reduced images. The modelling and subtraction of the galaxy light is performed using the ellipse and bmodel (Jedrzejewski, 1987) tasks from the iraf (Tody, 1986) software system. In Fig. 3.1, bottom panels, we show the reduced images after subtraction of the galaxies that could interfere with the GC photometry. In the case of M87, the only caveat is its famous extended X-ray jet emitted from its central black hole which creates residual artefacts in the very central region of the subtracted images. For the case of the Hydra fields, we have the drawback of a bright foreground star right in front of NGC3309, also resulting in some residual artefacts. Moreover, in the Hydra fields we opted not to model and subtract the neighbouring spiral galaxy NGC3312 as we will focus mainly on the GCs around NGC3311 and NGC3309.

Source Detection and Photometric Measurements

Source detection and photometry is performed using SourceExtractor(Bertin and Arnouts, 1996) and PSFEx(Bertin, 2011). In table 3.1 we list the main parameters used in this procedure

Table 3.1: SourceExtractor parameters applied for source detection and photometry.

Parameter	Value	
	M87	Hydra
DETECT_MINAREA	10	10
DETECT_THRESHOLD	4.0	1.5
ANALYSIS_THRESHOLD	4.0	1.5
DEBLEND_NTHRESH	64	32
DEBLEND_MINCONT	0.01	0.05
BACK_TYPE	AUTO	AUTO
BACK_SIZE	64	64
BACK_FILTERSIZE	3	3

for both the Virgo and Hydra fields. The extraction followed a very similar configuration for both. The only differences is due to the distances involved, which affected the amount of pixels set for the detection and analysis thresholds, as well as deblending parameters and the depth of the limiting magnitude within reasonable errors. With such depth we expect our dataset to be deeper in the M87 images, given the greater exposure time. Raw K_s magnitudes are derived from the MAG_PSF output of SourceExtractor with an oversampled PSF computed with PSFEx.

Extinction Correction

The K_s-band catalogues are then derredened with the reddening maps of Schlafly and Finkbeiner (2011), but we stress that the reddening in the direction of Virgo and Hydra, specially in the NIR, is almost negligible. Typical reddening corrections amount to 0.06 mag in $(u\text{-}i)$ and 0.04 mag in $(g\text{-}i)$ or $(i\text{-}K_s)$.

Magnitude Zero-Points

For the case of the Hydra fields, standard stars were observed to be compared with 2MASS stars, which enabled the calibration of magnitude zero-points using the HAWK-I pipeline. For Hydra F1 the zero point was calculated to be $ZP_{K_s,HydraF1} = 28.35{\pm}0.10$ mag and for Hydra F2 to be $ZP_{K_s,HydraF2} = 28.45{\pm}0.12$ mag. For M87, standard stars were not observed, due to the availability of literature data in the K_s filter. Specifically, we used the GC catalogue of

P16a to calibrate our instrumental magnitudes. We first select detected sources in the M87 field with K_s magnitude errors (as calculated by SourceExtractor), δK_s, smaller than $<$ 0.1 mag and convert the magnitudes from the HAWK-I original Vega photometric system to the AB system used in the P16a catalogue. This was done using the following relation from (Blanton and Roweis, 2007): $K_{s,AB}$=$K_{s,vega}$ ~1.827. Then we match our source catalogue with the GC catalogue from P16a. Establishing a linear relation results in a zero-point value of $ZP_{K_s,M87}$ =28.12±0.12 mag. In Fig. 3.3 we show the residuals of the HAWK-I magnitudes in the M87 field calibrated with the calculated zero-point and the magnitudes from P16a for matching objects. We find values smaller than 0.3 mag for 95% of the residual distribution and for magnitudes $K_{s,HAWK-I} < 21.8$. After this limit, the difference increases considerably. We attribute this result to the different depth of this work's VLT/HAWK-I observations and the CFHT/Megacam observations used in the NGVS catalogue. It is important to consider that the CFHT is 3.8 meter telescope, while VLT telescope has a diameter of 8.2 meters. Therefore, considering the exposure time of the M87 observations, this enables a more precise photometry than the CFHT/Megacam P16a data even for magnitudes fainter than 21.8 mag, as it can be seen in Fig. 3.4.

3.1.3 Match with complementary literature data

After calibration, we proceed to match the K_s catalogues from both fields with data from other filters already available in the literature. A summary of the literature data used in this work is shown in table 3.2, but here we offer additional details.

For the case of M87, we matched our data with the catalogue from Oldham and Auger (2016b), which is the largest Virgo GC catalogue available to date. It is based on a redone photometry in *ugriz* filters of the NGVS data. We refer the reader to Oldham and Auger (2016b) for details, but the idea behind the revisit to NGVS data in such work was to achieve deeper photometry and therefore a larger GC dataset in the region. We will make use of this larger and deeper dataset to compare Oldham and Auger (2016b) data with the addition of our new K_s magnitudes, hereafter referred to as the O&A16+K_s sample, with the data from

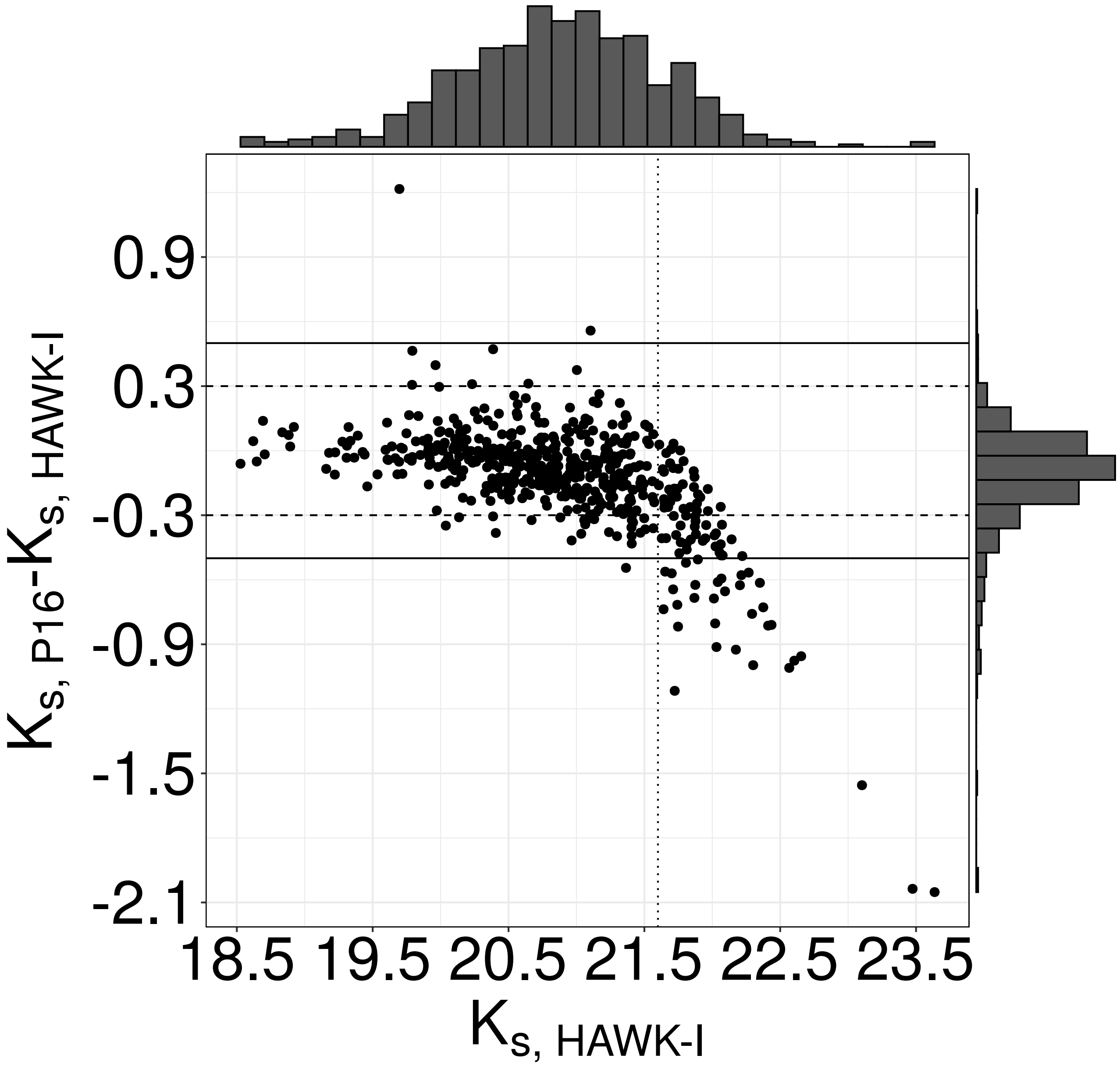

Figure 3.3: Residuals between K_s magnitudes from the M87 HAWK-I observations presented in this work and the ones from the P16a catalogue from CFHT/WIRCAM. The solid lines represent a residual of -0.5 and 0.5, and the dashed lines a residual of -0.3 and 0.3. Also shown are marginal histograms for the distribution of magnitudes and residuals. One can see that the major part of the residual distribution lies within 0.3 mag. A dotted line is also present indicating a detected magnitude limit of ∼ 21.8 mag where the residuals start to become increasingly larger. See text for our interpretation of this result.

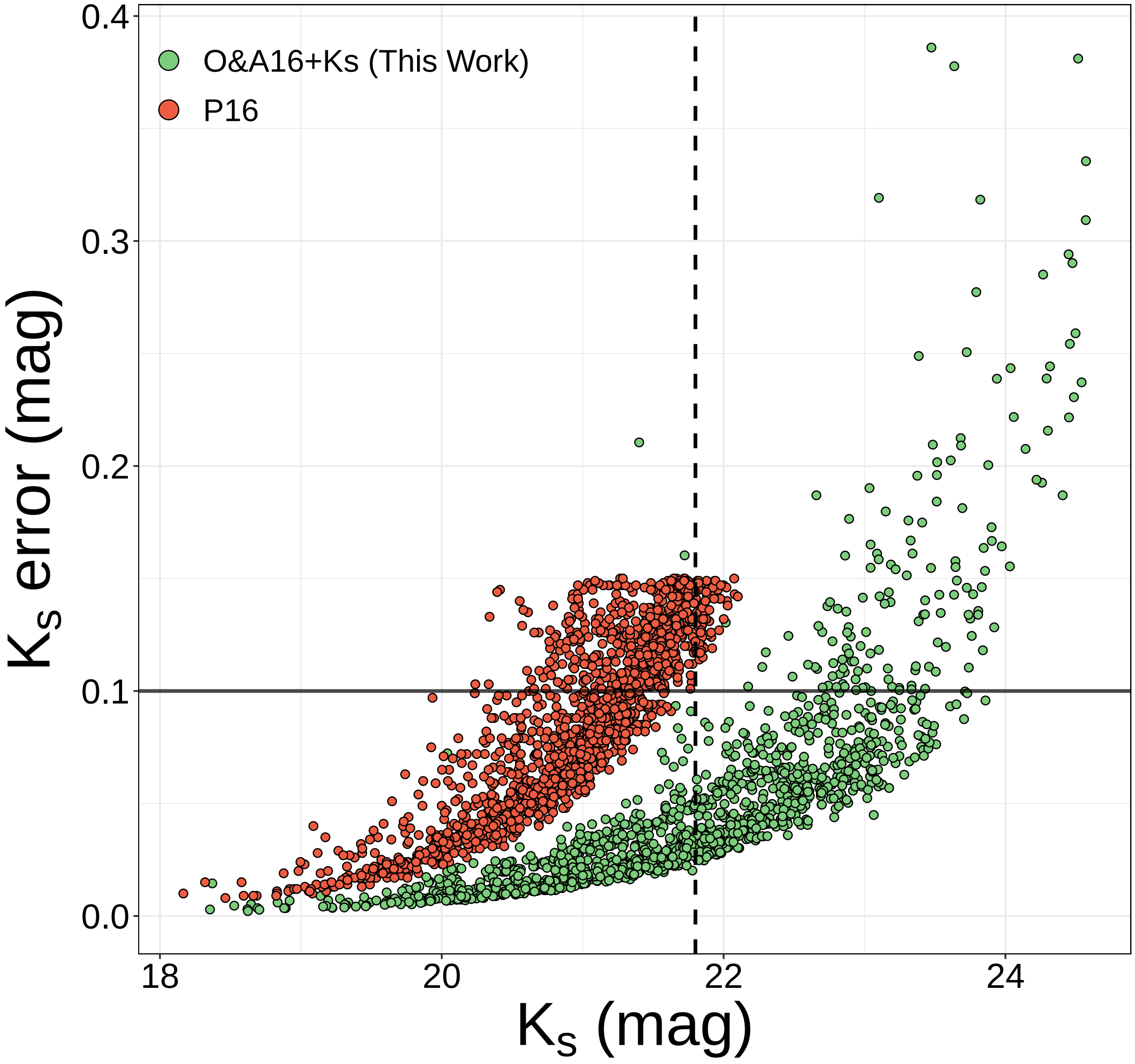

Figure 3.4: Comparison of the errors and calibrated magnitudes in the K_s-band for M87 GC candidates in the O&A16+Ks catalogue and in the P16a catalogue, as a function of magnitude. Green markers represent the decontaminated O&A16+Ks sample used in this work and red markers represent GC candidates from the P16a catalogue.

Table 3.2: General properties of the data used in this work. The samples O&A16+K_s, $UVIK_s$ and giK_s are the main samples used in the results section.

ID	N_{GCs}	Filters	Notes
			M87
P16a	1846	$ugrizK_s$	NGVS-IR
Oldham and Auger (2016b)	17620	$ugriz$	NGVS based GC candidates
VLT/HAWK-I data	3718	K_s	Presented in this work
O&A16+K_s	1457	$ugrizK_s$	Oldham and Auger (2016b) + HAWK-I
			Hydra
Hilker and Richtler (2016)	6382	UVI	VLT/FORS1 data covering NGC3311, NGC3312 and NGC3309
Wehner et al. (2008b)	6881	gi	Gemini/GMOS data covering NGC3311 and NGC 3309
VLT/HAWK-I data	6749	K_s	Presented in this work
$UVIK_s$	559	$UVIK_s$	Hilker and Richtler (2016) + VLT/HAWK-I
$giUVIK_s$	254	$giUVIK_s$	Hilker and Richtler (2016) + Wehner et al. (2008b) + VLT/HAWK-I

P16a. The latter GC data already cover the $ugrizK_s$ filter range due to the inclusion of data from the NIR extension of the NGVS, NGVS-IR (Muñoz et al., 2013). In the right panel of Fig. 3.2 we show the spatial distribution of the M87 samples mentioned throughout this work.

In the Hydra fields we used two different data sets to complement our K_s magnitudes: the gi catalogue from Wehner et al. (2008b) and the UVI GC candidate catalogue from Hilker and Richtler (2016). As each data set comes from observations with drastically different FOVs, we opt to separate the samples used in the Hydra analysis into two: a $UVIK_s$ sample, obtained from a match with the Hilker and Richtler (2016) data, based on which we will perform the GC selection (the reasons for this choice are explained in the following sections) and an additional $giUVIKs$ catalogue with matching objects from the final decontaminated $UVIK_s$ sample and the Wehner et al. (2008b) catalogue. This way we can explore the benefits of the larger spectral range provided by adding gi magnitudes from Wehner et al. (2008b), while at the same time not sacrificing a considerable sample size for the analysis when g-band magnitudes can be neglected.

Conversion to a common photometric system

Since the optical data for Hydra and M87 data used in this work come from different telescopes and observations, it is natural that they originally present themselves in different photometric systems. So before any decontamination or analysis is done, it is important to first choose a common system and convert all available data into it. Otherwise, even the small differences between filters in similar spectral regions can affect significantly the expected colours of GCs – and consequentially our analysis in the following sections of SSP colour predictions (Gonçalves et al., 2020; Conroy et al., 2009).

As most of the data available in the literature datasets is presented in AB magnitudes and in the $ugriz$ SDSS filters, we chose this as our standard photometric system. P16a, Oldham and Auger (2016b) and Wehner et al. (2008b) data is already in this configuration. The K_s magnitudes from HAWK-I originally are in the Vega magnitude system, so we convert to AB magnitudes using $K_{s,AB} = K_{s,Vega} + 1.85$ from Blanton and Roweis (2007). Moreover, the johnson-cousins UVI magnitudes from the Hilker and Richtler (2016) dataset are converted to

AB magnitudes using the relations: $U_{AB} \sim U + 0.79$, $V_{AB} \sim V + 0.02$ and $I_{AB} \sim I + 0.45$, from Blanton and Roweis (2007). Finally, UI magnitudes in the AB system are converted to SDSS ui using $u \sim U + 0.0682$ and $i \sim I + 0.0647$ also from Blanton and Roweis (2007). Hereafter in this work, every time magnitudes and colours are mentioned they are AB magnitudes in SDSS filters, unless otherwise noted.

3.1.4 Decontamination

Apart from actual GCs, there are other astronomical objects that are expected to be present in our samples that need to be distinguished from GC candidates in our final catalogues. Namely, those are background galaxies, foreground stars and image artefacts from the galaxy subtraction and reduction steps. As we match our K_s magnitudes with literature data, a previous decontamination was already present in these data that is carried over. Nevertheless, the addition of NIR photometry, or in the case of M87, its addition with higher precision, enables us to further decontaminate the samples. This is of great importance to avoid biases in the comparison with stellar population models we will be showing later in this work.

Our GC selection is based on a colour selection criteria and comparison with literature samples. The main tool we use to this end is the uiK_s diagram, presented in Muñoz et al. (2013) with data from the NGVS collaboration. The uiK_s diagram is a powerful tool to separate GCs from foreground stars and background galaxies due to the capability of the combination of near-UV (NUV) and NIR colors to probe different stages of stellar evolution within the observed stellar populations. Specifically, the $(i - K_s)$ colour is sensitive to the effective temperature of red giant branch (RGB) stars, while $(u - i)$ colour comprises an spectral region neighbouring the 4000 Å break, which is indicative of the presence of hot stellar evolutionary phases (Muñoz et al., 2013; Cantiello et al., 2018; Powalka et al., 2016a; Georgiev et al., 2012).

Additionally, as we match our HAWK-I data with additional photometric catalogues from the literature, we inherit an initial decontamination. Nevertheless, the addition of NIR information motivates us to proceed and further analyse the GC candidates. Moreover, we expect that the initial GC selection in the additional literature sources to have the effect of

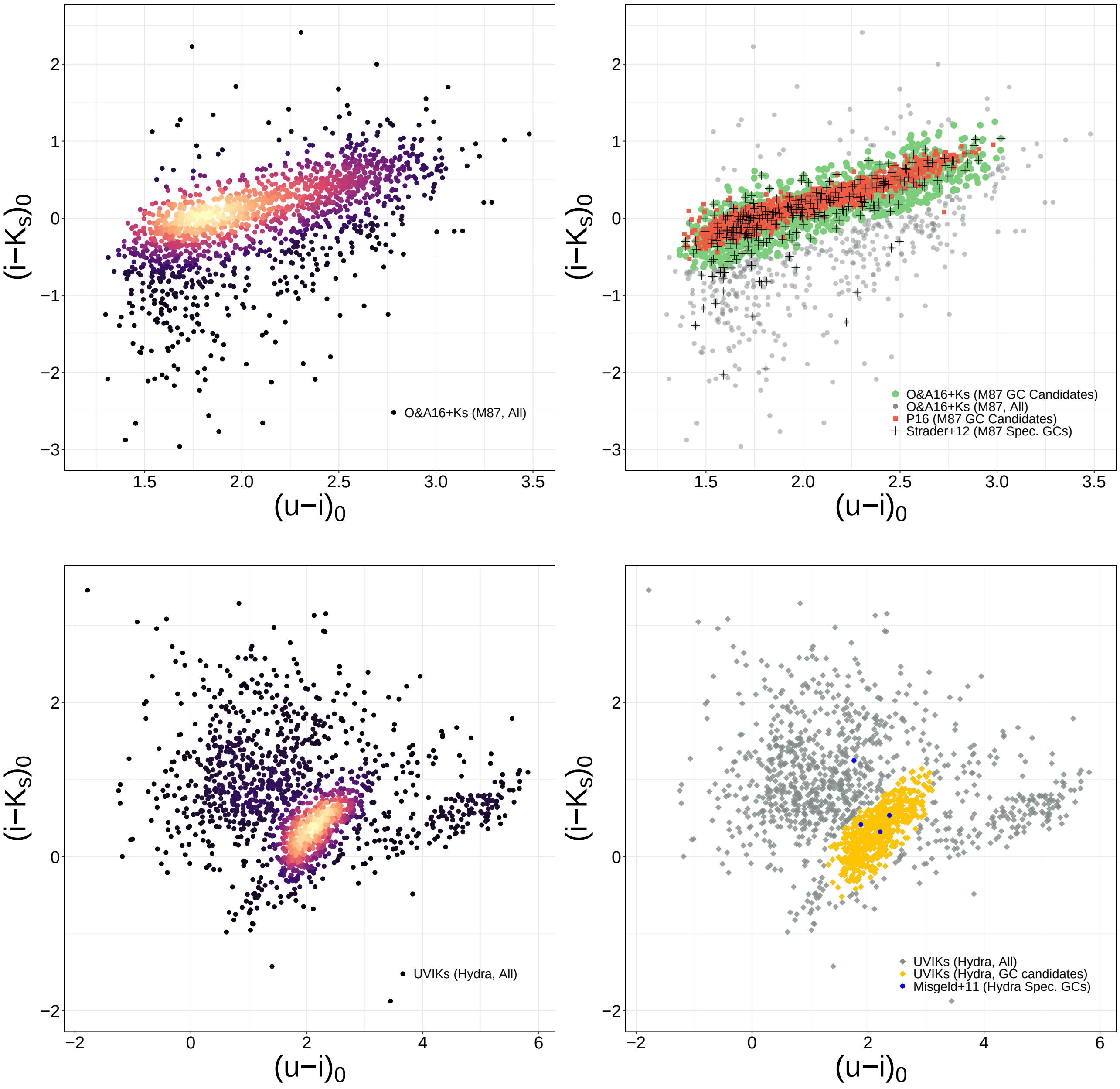

Figure 3.5: GC distribution in the uiK_s colour-colour diagram and loci of GC candidate selection, based on the peak of density distribution (shown in top and bottom left panels). *Top panels:* M87 GC candidates. Gray circles show the initial match between HAWK-I data and the photometric GC catalogues of Oldham and Auger (2016a). Green circles represent the final sample of GC candidates for the M87 field, labelled throughout this work as the O&A16+Ks sample. Red squares show, for comparison purposes, the loci of GC candidates from P16a. As reference, shown as black crosses are spectroscopic GCs that are present in the HAWK-I catalogue and in the M87 sample of Strader et al. (2011). Colours are dereddened, in AB magnitudes. *Bottom panels:* Hydra GC candidates. Grey diamonds represent the entire match between objects detected in the HAWK-I data, in both hydra fields, and the UVI data from Hilker and Richtler (2016). Yellow markers shown the loci of the final selected GC candidates for one of the Hydra samples used in this work, labelled as UVIKs sample. The 4 blue circles represent spectroscopic GCs that match objects in this sample from the catalogue of Misgeld et al. (2011).

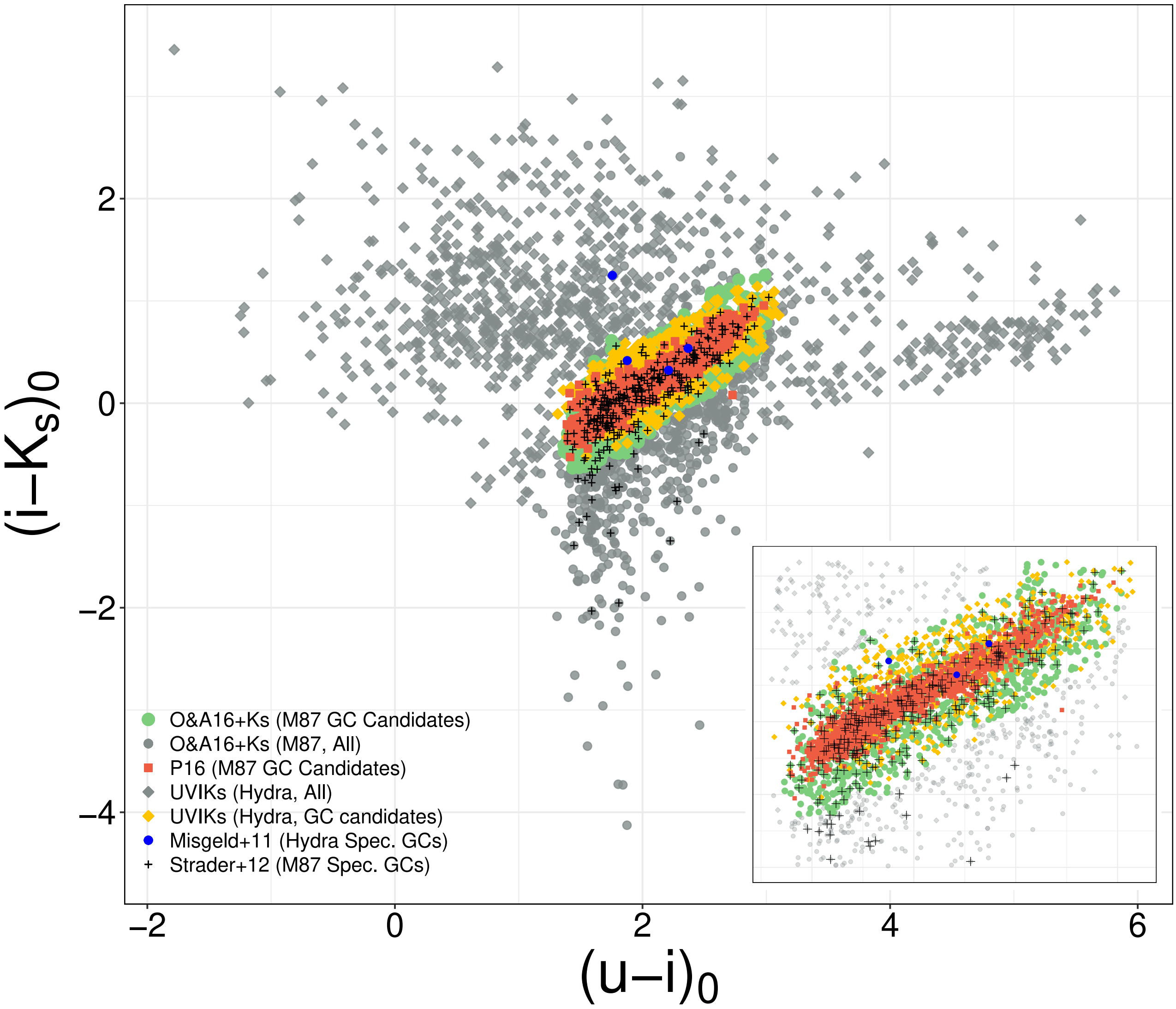

Figure 3.6: uiK_s diagram showcasing the loci of GC candidates of both fields studied in this work. Gray circles and diamonds shown the initial match between HAWK-I data and the photometric GC catalogues of Oldham and Auger (2016a) and Hilker and Richtler (2016), respectively. Green circles and orange diamonds represent the loci of GC candidates for the O&A16+Ks M87 GC sample and for the UVIKs Hydra GC sample, respectively. Red squares show, for comparison purposes, the loci of GC candidates from P16a. Finally, as reference, shown as blue circles and black crosses are spectroscopic GCs that are also present in the data presented in this work, from the Hydra sample of Misgeld et al. (2011) and the M87 sample of Strader et al. (2011). Colours are dereddened, in AB magnitudes. Notice the similar loci for all GC candidate samples. Also of note is the fact that both spectroscopic samples show objects that would not be considered as GCs following our decontamination criteria. See text for a discussion on this fact.

naturally reducing significantly the presence of stars and galaxies in the samples. Therefore a density-based approach for the GC selection in the uiK_s diagram becomes a very natural selection process. Our goal is to have a good compromise between sample size and precision, such that our comparison with stellar population models will not be significantly biased with objects other than GCs.

For the case of M87, the O&A16+K_s sample inherits the decontamination from the catalogue of Oldham and Auger (2016b), which was based on colour cuts of $0.6 \leq (g-i) \leq 1.4$, $0.2 \leq (g-r) \leq 1.0$ and $g \geq 24.0$. We refer the reader to Oldham and Auger (2016b) for complete details. A direct match between such catalogue and our K_s data resulted in 1586 objects with $ugrizK_s$ photometry. For the case of the Hydra data, the UVI catalogue from Hilker and Richtler (2016) is based on a GC selection performed using the *sharpness* parameter of IRAF/DAOPHOT (Tody, 1986) and a colour selection in a $(V-I)$ x $(U-V)$ diagram. A match between this catalogue and our HAWK-I data resulted in an initial $UVIK_s$ catalogue of 1513 objects. In the Hydra fields we also have the addition of the gi magnitudes from Wehner et al. (2008b), which GC selection is based on a colour cut of $1.4 \geq (g-i) \geq 0.6$. The match of such gi catalogue with the HAWK-I K_s magnitudes form an initial giK_s catalogue with 1057 objects.

This GC selection in the uiK_s diagram is shown in Fig. 3.5, where $(i-K_s)_0$ and $(u-i)_0$ are extinction corrected colours in AB magnitudes. The left panels of this figure show the object density distribution. This is computed using a two-dimensional Gaussian kernel estimate with a 1x1 bandwidth as well as 200 and 1000 square grids for the M87 and Hydra data respectively (we refer the reader to (Venables and Ripley, 2002), chapter 5, for additional details on this parameters). To further identify the boundaries of the GC loci, we use additional literature data as reference. For the case of M87, we use the photometric GCs from P16a and the spectroscopic GCs from Strader et al. (2011) that are also present in our initial O&A16+Ks catalogue, which amounts to 297 objects. In the case of Hydra, we include spectroscopic GCs from the Misgeld et al. (2011) catalogue. However, the latter has only 4 matches with our initial UVIKs dataset.

From the compromise between objects located within the densest regions in the expected GC loci in the uiK_s diagram as well as close to the additional literature samples, we selected the final O&A16+Ks dataset (green markers in Fig. 3.5, top left panel), comprising 1457 GC candidates from 1.96 to 36.42 Kpc from the centre of M87 and a final UVIKs dataset (yellow markers in Fig. 3.5, bottom right panel) comprising 559 GC candidates from 4.72 to 119.44 Kpc from the center of NGC 3311. In Fig. 3.6 we show a combined uiK_s diagram with all samples from both fields where one can see how close the loci of GC candidates are located. A match between the $UVIKs$ dataset with the gi magnitudes from Wehner et al. (2008b) results in an additional $giUVIKs$ catalogue (magenta markers in Fig. 3.5, bottom right panel) with 254 GC candidates. This information is summarised in table 3.2.

Caveats from the GC selection from the comparison with Spectroscopic GCs

One potential issue with our GC selection criteria is the fact that for both M87 and Hydra not all spectroscopically confirmed GCs ended up in our final GC samples. Although initially surprising, this incongruence between photometric and spectroscopic samples was also spotted during the GC selection of P16a, as well as in the decontamination of GC catalogues in other galaxy systems, such as around NGC253 in Cantiello et al. (2018), for instance. This fact may arise from several different reasons, such as the natural uncertainties associated with solely photometric analysis of GC systems when compared to spectroscopy or the possibility of false-positives among spectroscopic samples (Powalka et al., 2016b; Cantiello et al., 2018; Göttgens et al., 2019). In the M87 dataset, the spectroscopic GCs missing from our final sample are mostly located in the expected loci of stellar contaminants, and the single missing spectroscopic GC in the Hydra samples is significantly outside the expected boundaries of the GC loci in the uiK_s diagram and appears to have colours of star-forming background galaxy [4]. Nevertheless, our goal is to have a more precise GC sample than to attain a large sample size with significant contamination that could severely bias our analysis.

---

[4] See Fig 4 of Cantiello et al. (2018) for specific details in the regions expected for each astronomical object in the uiK_s diagram.

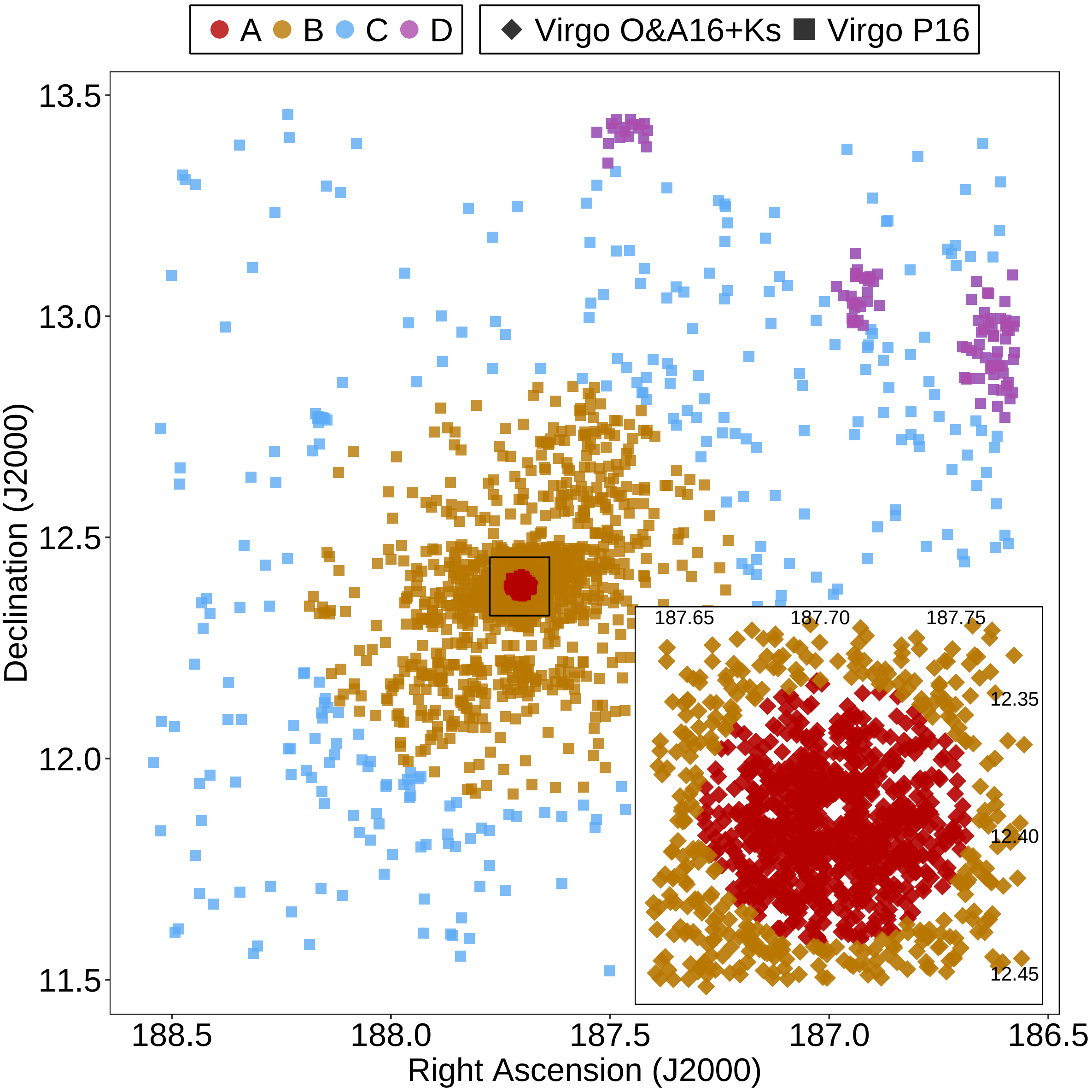

Figure 3.7: P16 and O&A16+Ks samples (diamonds and squares, respectively) distributed in the 4 spatial bins used in P16a to probe the environmental sensitivity of SSP models colour predictions. The A region (red) encompasses objects within 20 Kpc or $2.8R_{e,M87}$ from the centre of M87. The B (orange) region comprises objects between 20 Kpc and 200 Kpc (or $27.8R_{e,M87}$). The C region (cyan) includes objects beyond 200 Kpc. An additional D region contains objects P16a classified as associated to M87's neighbouring galaxies (NGC 4473, NGC 4435, NGC 4438 and M86). In the inset we zoom in the region enclosing all of the O&A16+Ks sample, which is also outlined by the black rectangle in the outer figure. The inset horizontal and vertical axes units and orientation are the same as the outer figure.

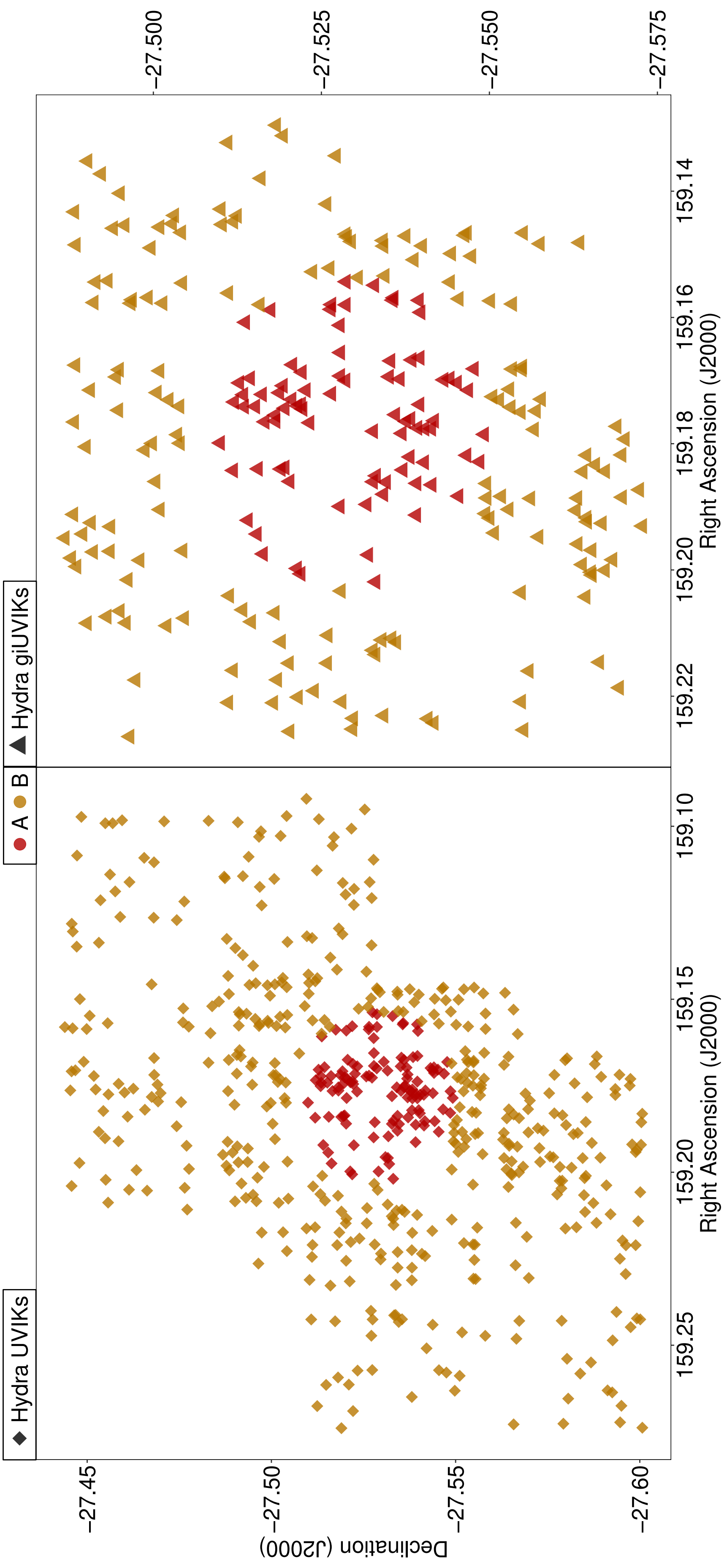

Figure 3.8: Same as Fig. 3.8, but this time for the Hydra samples used in this work. On the left panel, the UVIKs sample and on the right the giUVIKs sample. Similarly to our Virgo O&A16+Ks sample, our Hydra data spans only the A and B regions. Notice the different horizontal and vertical ranges of each panel. The right panel shows a smaller region than the left panel.

3.1.5 Separation into spatial bins

One of the main results of P16a is that the observed mismatch between SSP models and the observed colours of M87 GCs increases as a function of the distance to the centre of M87. As shown in Fig. 1.8, P16a divided its Virgo GC sample in four circular spatial bins, namely: an inner A region within 20 Kpc from M87, an outer B region between 20 and 200 Kpc, a C region comprising objects beyond 200 Kpc and a D region accounting the objects P16a classified as associated to M87's neighbouring galaxies.

Both our Virgo and Hydra data span considerably smaller regions than the NGVS data. However, our data in both environments comprises the entirety of the A region and some part of the B region. Since the A region is shown in P16a to present the largest discrepancies between SSP model predictions and observed colours, it is worth for us to test our model choices in the regions we have available to us in those two environments, as well as in the P16 catalogue. Moreover, the models we will be testing – presented in details in the section 3.2 – were not tested in P16a; P16b or have been updated since. More importantly, we will test the environmental effects on the SSP colour predictions of α-enhanced models.

To proceed with this analysis, we divide our samples in the regions proposed in P16a. The result of this spatial binning for our samples is shown in Figs. 3.7 for Virgo and 3.8 for Hydra. Furthermore, to compensate for the fact that the Hydra cluster is more distant to us than the Virgo cluster, we consider the fact that 20 Kpc is equivalent to 2.8 times M87's effective radius ($R_{e,M87}$), and 200 Kpc is about $28.8 R_{e,M87}$. So we use the effective radius of NGC3311 ($R_{e,NGC3311}$) as reference to define the boundary of the A region for the Hydra samples as $\sim$ 23.52 Kpc from NGC3311, or $2.8 R_{e,NGC3311}$, and the B region outer boundary to be $\sim$ 241.92 Kpc from NGC 3311, or $28.8 R_{e,NGC3311}$. It is important to note that the choice to use NGC 3311 as a reference centre to the Hydra samples is based on the fact that this galaxy is generally considered in the literature to be the main BCG of the Hydra cluster (Misgeld et al., 2011; Wehner et al., 2008b). Nevertheless, as it can be seen in Fig. 3.2, clearly a considerable part of our Hydra sample is at least in projection associated with NGC 3309. We will consider this fact in the analysis of the colour-colour predictions of SSP models in section 3.3.2.

3.2 Models used in this work

In the introduction of this thesis we stated how important it is for the field of galaxy evolution to study the stellar population properties of GCs. We also discussed important open questions still present in the matter, such as the limited spectroscopic data available to build stellar libraries with age, metallicities and chemical abundances not commonly found in the Milky-Way, but theorised to comprise a significant part of the stellar populations of extragalactic systems. We emphasised the results from P16a and P16b which show how some of the most popular SSP models in the literature struggle to reproduce the observed colours of GCs in the Virgo cluster, around M87 and surrounding galaxies. For this reason, in this work, we explore experimental models that expand empirical libraries into the theoretical space by adjusting one important feature: the α-enhancement. In the next section, we present a brief description of these models.

3.2.1 Models with Milky-Way abundances

E-MILES Models with Base MW abundances

In this work we will refer as "base" E-MILES models the SSP models published in Vazdekis et al. (2012), Ricciardelli et al. (2012) and Vazdekis et al. (2016) which cover the spectral range from 1680 to 50000 Å and have [M/H] = [Fe/H]. These models are available as single-age and single-metallicity SSP models. These are constructed by integrating empirical stellar spectra along sets of theoretical isochrones[5]. Two sets of solar-scaled[6] theoretical isochrones were used in computing these models: the ones from Girardi et al. (2000), known as the Padova isochrones, and the ones published in Pietrinferni et al. (2004), known as BaSTI isochrones. In this work we will not go into specific details regarding the isochrone sets and how they are applied in the construction of the SSPs, but we refer the interested reader to Vazdekis et al. (2015) and Vazdekis et al. (2016) where those are presented. There are different age and metallicity coverage between the two datasets, with the important difference that the BaSTI

---

[5] details in the integration approach are presented in Vazdekis et al. (2015)

[6] solar-scaled, i.e., with solar metallicities and chemical abundances

isochrones reach a wider coverage in metallicity. Moreover, the original set of BaSTI isochrones are supplemented by additional computations specific for the MILES collaboration. These additional computations comprise crucially variations in the abundance of α elements, which are important for the computation of E-MILES self-consistent α-enhanced models, as it will be described in the next section. Due to this, in the forthcoming sections we opt for using only E-MILES SSPs constructed with BaSTI isochrones. This way we ensure a completely fair comparison between the model predictions in regards to abundances, which is the main goal of this chapter.

In regards to spectral libraries, to attain a spectral range covering from UV to NIR, the empirical stellar spectra used to compute the Base E-MILES models are a combination of several different stellar libraries we will be briefly describing in the following paragraphs.

In the optical range (3525-7500 Å) these models are based on 985 stellar spectra from the Medium Resolution INT Library of Empirical Spectra (MILES) which has a spectral resolution of 2.5 Å (FWHM) (Sánchez-Blázquez et al., 2006; Falcón-Barroso et al., 2011). To reach the NIR these models are also based on the MIUSCAT spectral library (Vazdekis et al., 2012, 2015) and its extension in the IR presented in Röck et al. (2016), which used the IRTF spectral library (Cushing et al., 2005; Rayner et al., 2009). The MIUSCAT [7] library is a combination of the MILES, CaT and Indo-US libraries and covers the range between 3465 and 9469 Å. The CaT library (Cenarro et al., 2001) includes 706 stellar spectra in the 8350-9020 Å range, at a resolution of 1.5 Å. The Indo-US (Valdes et al., 2004) library comprises $\sim$ 1200 stars with spectra, in average, covering from 3465 to 9469 Å and a resolution of FWHM = 1.36 Å [8]. The MIUSCAT extension in the IR was presented in Röck et al. (2016) who combined single-age, single metallicity model spectra based on the MIUSCAT library with single-age, single-metallicity models based on 180 stars of the IRTF library. This extended the coverage of MILES SSPs to 50000 Å. These models were computed fully consistently using the same evolutionary synthesis codes as previous MILES and E-MILES SSP models and we refer the reader to Röck et al. (2015) and Röck et al. (2016) for complete details on this procedure.

---

[7] MI-US-CAT – MI from MILES, US from Indo-US and CAT from CaT.

[8] Based on the updated estimates of Falcón-Barroso et al. (2011), and not the claim from the original Indo-US paper which stated a resolution of FWHM $\sim$ 1.2 Å

Furthermore, Röck et al. (2016) presented a comparison of predicted colours, for different ages, between the extended MILES and other popular models used in the literature such as the ones from Maraston et al. (2009), Conroy and van Dokkum (2012) and Marigo et al. (2008). One relevant result from this analysis is that the colour with the largest discrepancies in the predictions between models was (J-K), with $\Delta(J-K) \sim 0.06$ at ages older than 7 Gyrs. This is argued by Röck et al. (2016) to be mostly due to different treatment of AGB stars between model prescriptions. We will return later to discuss this result in light of the results from the analysis performed in this work.

The latest extension added to the E-MILES models covers the UV spectral range. It is based on the NGSL stellar library (Gregg et al., 2006), which comprises $\sim$ 400 stars observed by the instrument Space Telescope Imaging Spectrograph (STIS) onboard of the HST and collectively covers a wavelength range from $\sim$ 0.16 to $\sim$ 1.02 μm. The metallicity range of such stars ranges from [Fe/H] $\sim$ -1.5 to [Fe/H] $\sim$ +0.2. Koleva and Vazdekis (2012) calibrated the NGSL spectra for the implementation in the E-MILES models, and we refer the reader to such work and Vazdekis et al. (2016) for further details in this process.

The IMF adopted for the E-MILES models (both base and α-enhanced) used in this work is a bimodal power-law IMF described in Vazdekis et al. (1996). It is described by the following equations:

$$\begin{aligned}
\Phi(m) &= \beta 0.4^{-\mu}, & m &\leq 0.2M_{\odot} \\
\Phi(m) &= \beta p(m), & 0.2 < m &< 0.6M_{\odot} \\
\Phi(m) &= \beta m^{-\mu}, & m &\geq 0.6M_{\odot}
\end{aligned} \tag{3.1}$$

Where $\Phi(m)$ is the mass (m) distribution of stars for a given population, β is a normalisation constant, μ is the IMF slope and p(m) is an exponential spline (see section 2.2, item ii) of Vazdekis et al. (1996) for details in its calculation). In the case of the models tested in this work, we used a fixed slope of 1.3, which is equivalent to the IMF slope of the solar neighbourhood (Salpeter, 1955).

The end product of the base E-MILES models are then single-age, single-metallicity SSP models covering from 1680 to 50000 Å fully based on empirical spectra with metallicities and chemical abundance patterns comparable to the general Galactic population (Vazdekis et al., 2015; Milone et al., 2011). The most important consequence of this feature in the context of this work is that at near-solar metalliticies variations in the abundance of α-elements for Galactic stars is negligible, but at sub-solar metallicites α-enhancement is very significative, specially for stars at the bulge, the thick disk, halo and GCs (Bensby et al., 2003; Alves-Brito et al., 2010, 2011; Nissen and Schuster, 2010; Reddy et al., 2003; Bensby et al., 2011). In fact, [Mg/Fe] measurements for stars in the MILES library from Milone et al. (2011) show a scatter around $\sim$ 0.4 dex for [Fe/H] $<$ -1.0, similar to what can be seen for galactic stars (Alves-Brito et al., 2010; Gonzalez et al., 2011; Bensby et al., 2010; Howes et al., 2016; Di Matteo, 2016; ben, 2015). Therefore, in the context of this work, the base E-MILES models can be considered as representatives of the expected properties of stars with Galactic abundances.

FSPS models with base MW abundances

The set of SSP models hereafter referred as FSPS models, are the models produced using the The Flexible Stellar Population Synthesis (FSPS; Conroy et al. 2009; Conroy and Gunn 2010) stellar population synthesis (SPS) code. In this work we used the version 3.2 [9] of code, which is completely open-source. Beyond the tasks of combining stellar evolution calculations and spectral libraries to produce SSPs, the FSPS code offers a myriad of options to customise the produced models. These options comprise the choice of spectral libraries, isochrones, IMF slope and many advanced tweaks to specific stages of stellar evolution, such as the bolometric luminosity and effective temperature of TP-AGB[10] stars or the option to include extended blue horizontal-branch stars. However, while such advanced modifications of stellar evolution tracks are very interesting from a theoretical standpoint, their contribution to integrated SEDs is still highly uncertain due to issues such as the lack of enough calibrating observations (Conroy and Gunn, 2010).

---

[9] Available at https://github.com/cconroy20/fsps

[10] Turning-Point, asymptotic giant branch (TP-AGB) stars

As such, in this work we do not change any FSPS values from their defaults except for the choice of stellar library, isochrones and IMF slope. Moreover, our choice of parameters was based to as closely as possible mimic the ingredients of the E-MILES base models. The idea is to have an independent comparison of SSPs computed with Milky-Way abundances and not rely only on the models created by a single group to compare the colour predictions of base and α-enhanced models.

Specifically, the FSPS models used in this work are based on the MILES spectral library, the BaSTI isochrones and a Kroupa IMF with a 1.3 slope. The MILES spectral library was chosen since it more closely resembles the spectral library used in the E-MILES models, however obviously it is much more limited since actually the libraries used in E-MILES models comprise a combination of several libraries. In 3.10 we can see that the effect of this limitation is a lack of features in the FSPS models, specially in the NIR range, when compared to the other models used in this work. This is to be taken in consideration in the analysis of the results to be shown later. The isochrones, on the other hand, are exactly the same used in the E-MILES base models.

The IMF type used in this work to generate the FSPS models is a Kroupa IMF, which has the form $\phi(m) = m^{-\alpha}$, where $\alpha = 1.3$. We have chosen this IMF type among the ones availables in FSPS as when compared to the bimodal IMF used in the E-MILES models (equation 3.1), one can notice that for masses $m \geq 0.6 M\odot$ the two IMFs are virtually the same, except for the normalisation constant in the bimodal IMF. This means that the expected differences between the two base models adopted in this work due to the IMF are to be found in the spectral properties related to low-massive stars. Such stars contribute specially in NIR spectral features, due to their relatively cold effective temperatures. Vazdekis et al. (1996) argues that the influence of these stars is larger for steeper IMF slopes than the one considered in this work. It is shown that colours combining optical and NIR filters (in this case represented by $(V - K)$) are virtually identical between SSPs constructed using Kroupa and Bimodal IMFs for slopes of α=1.35, with the exception of greater ages. The colour difference can reach up to ~ 0.2 mag for 16 Gyr SSPs[11] and solar metallicites. This is to be taken in consideration when

---

[11] see Table 5 of Vazdekis et al. (1996).

analysing the results presented in the following section.

3.2.2 Models with α-enhancement

E-MILES SSPs with α-enhancement

SSP models with Galactic abundances have been ubiquitously used to model GC colours in the literature Bruzual and Charlot (2003); Brodie and Strader (2006). However, recently works such as the one from Powalka et al. (2016b); Vazdekis et al. (2015); Conroy et al. (2018) showcase their limitations. Abundance variations not encountered in stars at the solar neighbourhood, and therefore not available in the stellar libraries used to compute current empirical SSP models, have been proposed as needed to correctly reproduce colours of extragalactic GCs. Some suggested abundance enhancements, are in C and N, which have been proven to be effective in improving SSP colour predictions for Early-Type galaxies (Choi et al., 2019). Quiescent galaxies are also strongly enhanced in Na (Conroy et al., 2014). However, α elements are likely one of the most direct improvements to be implemented to current SSP models (Powalka et al., 2017). These elements are intrinsically related to star formation timescales, as already discussed in section 1.4. And such property varies considerably between the Milky-Way and other galaxies. Specially when we look into galaxies of very different morphologies and evolution such as the elliptical galaxies at the centre of galaxy clusters.

Vazdekis et al. (2015) presented scaled-solar and α-enhanced models for SSPs based on the MILES library (Vazdekis et al., 2010) with theoretical corrections from the BaSTI and Padova isochrones. The BaSTI isochrones used in such work were specifically extended to include α-enhanced theoretical isochrones. To construct α-enhanced MILES SSPs, a differential correction is calculated dividing scaled-solar and α-enhanced theoretical SSPs based on the spectral library of Coelho et al. (2005) and built upon α-enhanced isochrones. Such correction is then applied to a reference SSP with solar abundances and built with the same α-enhanced isochrone (See Fig. 3.9 for an illustration of the process). This procedure enables one to obtain a self-consistent SSP spectrum based on the MILES empirical library but at the same time incorporating the effects of the α-enhancement.

The MILES wavelength range is not enough to cover the entire range of the ($ugrizK_s$) colours used in this work. To overcome this limitation we present in this work extended α-enhanced models based on the same principles of Vazdekis et al. (2015), but created instead based on the E-MILES spectral library described in the previous section, which covers from 1680-50000 Å. These models will be presented in Vazdekis et al (*in prep*) and have constant α/Fe = 0.4. Including a combination of NUV/optical and NIR filters in our analysis is very important as colours composed by these filters improve considerably the age/metallicity degeneracy (Puzia et al., 2002; Pessev et al., 2008; Georgiev et al., 2012; Muñoz et al., 2013). This will be later explained in more detail in section 3.3.1. E-MILES α-enhanced models, at the current date, still present a few important limitations. Their main caveat to our analysis is their limited metallicity coverage. It ranges from -0.35 $\leq$ [M/H] $\leq$ +0.26 for the models based on the BaSTI isochrones, which are used in this work[12]. This is significantly more limited than the metallicity range of the E-MILES base models. In addition, in the context of this work, one of the most important observational aspects of GC systems of giant elliptical galaxies is the presence of a significant population of GCs with metallicities as metal-poor as [M/H] $\sim$ -1.7[13] (Villaume et al., 2019). While this is a very important limitation in our analysis, we still are able to employ these models to probe α-enhancement effects in GCs with super-solar metallicities. It is worth noting that even the metal-rich GC subpopulations of some nearby galaxies have been found to have [α/Fe] up to +0.3, such as in NGC 3115 (Kuntschner et al., 2002), M31 (Beasley et al., 2005) and Chies-Santos et al. (2012a).

---

[12] The E-MILES α-enhanced models are also available using PADOVA isochrones, however we choose to use BaSTI isochrones, since only those are also α-enhanced.

[13] Three assumptions were used in this conversion: first, we assume that the [Mg/Fe] abundance ratio is a reliable proxy for [α/Fe] (Vazdekis et al., 2015, and references therein); We also adopt [M/H] = [Fe/H] + A * [Mg/Fe], with A = 0.75. The A constant is dependent on the solar chemical mixture adopted, and our chosen value is based on the one adopted in Vazdekis et al. (2015), which is in turn based on Grevesse and Sauval (1998). Finally, we assume that significantly metal-poor GCs ([Fe/H] $\leq$ -0.7) have [α/Fe] $\sim$ 0.4 (Schiavon, 2007; Martín-Navarro et al., 2018).

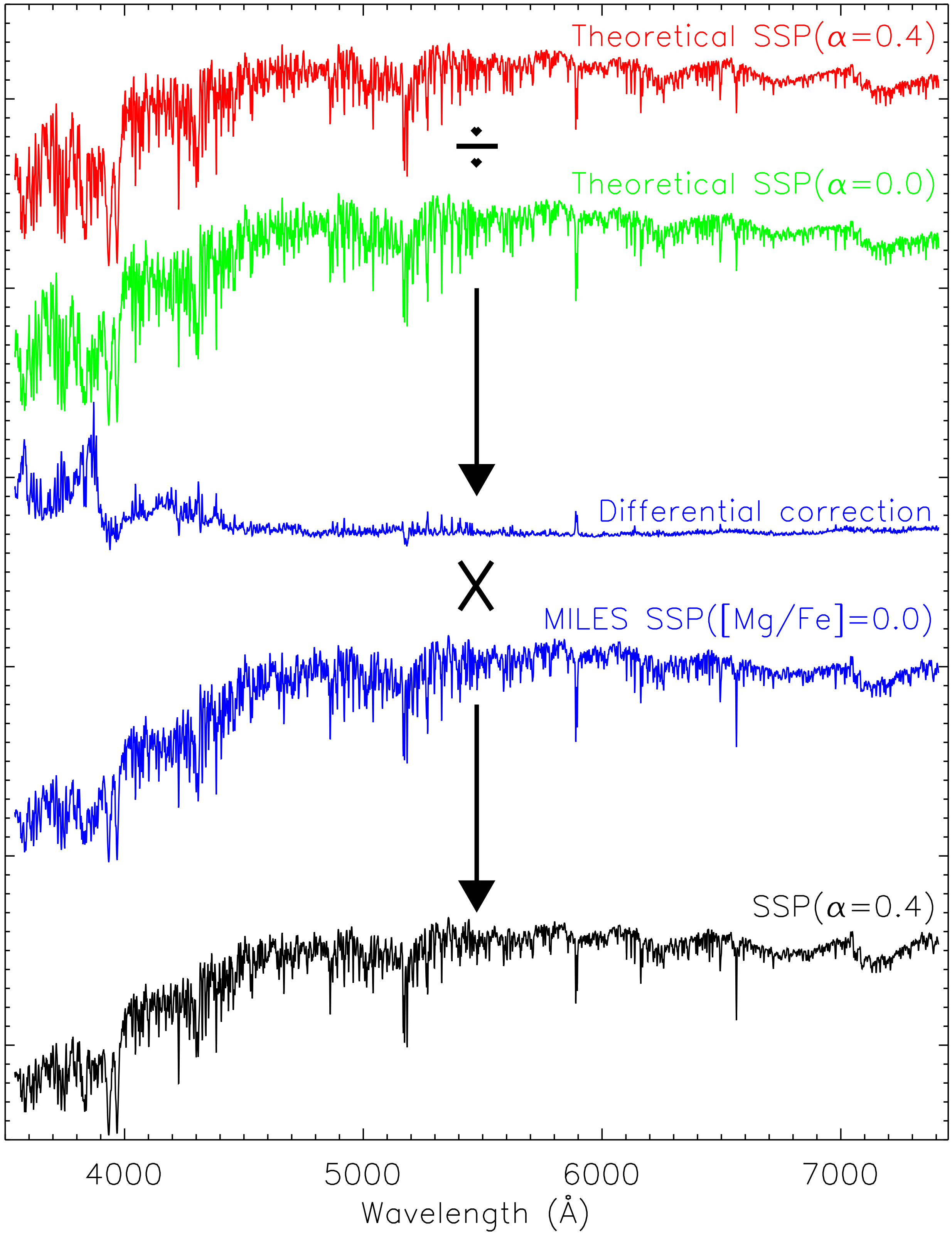

Figure 3.9: Fig. 4 of Vazdekis et al. (2015) illustrating the method for building an α-enhanced SSP, in this case, with [M/H]=+0.06. In red and green two theoretical spectra with different α-enhancements (from Coelho et al. (2007)) are divided in order to obtain a differential correction, shown in blue. Both theoretical spectra are computed using α-enhanced isochrones. Then the differential correction is applied to a reference spectrum with solar abundances, to obtain a final self-consistent α-enhanced SSP model.

ALF-generated SSPs with α-enhancement

The ALF code (Conroy and van Dokkum, 2012; Conroy et al., 2014, 2018) is a full-spectrum fitting tool that models spectra from optical to NIR. It makes use of SSPs based on spectral libraries chosen by the user, and implements age and metallicity dependent response functions to model systems with abundances that differ from those stars that comprise the spectral library. In its "full" mode, it can model simultaneously 19 element abundances, in additional to other parameters such as metallicity, velocity dispersion, age, IMF slopes and etc.

ALF also includes the WRITE_A_MODEL fortran90 code that is able to generate custom SSP models based on a choice of spectral library, individual element abundances among the 19 available as well as 20 other parameters, of which the most important are age, metallicity, IMF type and slope. This is performed with the use of age and metallicity dependent response functions to create SSPs with abundances that differ from those of the stars comprising the spectral library (Tripicco and Bell, 1995; Korn et al., 2005; Lee et al., 2009; Sansom et al., 2013; Conroy et al., 2014). This process is described in details in (Conroy and van Dokkum, 2012), but basically it involves quantifying the fractional change in the spectrum due to a change in a single element abundance. Both the spectral library and response functions used in this work were kindly provided to us from C. Conroy after private request. Furthermore, the response functions employed here are an important updated version, from June 2021, instead of latest published ones presented in (Conroy et al., 2018). This updated version corrected a bug in the generated stellar spectra related to NIR indices (private conversation with C. Conroy). Apart from this bug fix, however, the response functions we use are identical to the ones presented in Conroy et al. (2018).

In this work the ALF-generated SSP models have the following characteristics and ingredients: we use the MILES+IRTF empirical spectral library presented in Villaume et al. (2017) and the MIST isochrones (Choi et al., 2016; Dotter, 2016). For the IMF we use a Kroupa IMF with a slope value of 1.3. Finally and most importantly, we set $[\alpha/\mathrm{Fe}]$=0.4 and vary ages and metallicities in ranges similar to the previous presented models, to ensure a consistent comparison between them. We employ a metallicity range of $-2.27 < [\mathrm{M/H}] < 0.4$ and ages between 3.5 and 14 Gyrs.

ALF-generated SSP models, in summary, enable us to test α-enhanced SSPs in age and metallicities not available to the current E-MILES α-enhanced models. However, it is important to point out the limitations of ALF-generated SSP models. Firstly, currently the MIST isochrones are only available with solar-scaled abundances. Therefore, the models described in this section are not self-consistent, in contrast to the E-MILES α-enhanced models. This will be taken in consideration when analysing the results of model comparisons in the next sections, however we emphasise that, specially at old ages, abundance variations should influence stellar spectra more strongly than differences in the underlying isochrones (Coelho et al., 2007; Vazdekis et al., 2015).

3.2.3 General comparison between models

In Fig. 3.10 we show a direct comparison between some examples of SSP models used in this work for varying ages and metallicities. The first thing of notice is the different features present in SSPs with the same abundance variations. The FSPS base models lack several spectral features present in the E-MILES base models, and this difference is very obvious after around ∼ 7700 Å. For instance, the Ca triplet (CaT) absorption lines at 8498, 8542, and 8662 Å are signature metallicity indicators in old stellar populations (Usher et al., 2019) and almost completely absent in the FSPS models. Also absent are several NIR spectral features after 10000 Å. This is mainly due to the presence of the IRTF library among the spectral libraries used for all models except FSPS. Moreover, E-MILES also include in their spectral libraries the

Table 3.3: Basic ingredients of the SSP models used in this work. From left to right: model label as used throughout this work; one or more stellar libraries used to build the SSPs; isochrones; initial mass function type and adopted slope.

SSP Model	Stellar Libraries	Isochrones	IMF (type, slope)
E-MILES Base	NGSL+MILES+CaT+IndoUS+IRTF	BaSTI	Bimodal, 1.3
FSPS	MILES	BaSTI	Kroupa, 1.3
E-MILES-α	NGSL+MILES+CaT+IndoUS+IRTF	BaSTI ([α/Fe]=0.4)	Bimodal, 1.3
ALF-α	MILES+IRTF	MIST	Kroupa, 1.3

CaT and IndoUS spectral libraries which enhance its NIR features even when compared to the ALF models, which combine only MILES and IRTF spectral libraries. These specific differences in the NIR treatment between models make the E-MILES SSPs, at least in theory, the best models to test the SSP predictions of colours combining optical and NIR filters, among the ones tested in this work. Nevertheless, the ALF models also present rich features in the NIR, despite some detail limitations, therefore we still consider it a reliable way to test effects of α-enhancement at metallicites where E-MILES models are not yet available.

Furthermore, in Fig. 3.11 we show flux ratios obtained by dividing the α-enhanced models by base models of E-MILES and ALF/FSPS. Underlayed are the $ugrizK_s$ filters wavelength range, shown as coloured regions. Each filter label is positioned at its reference wavelength[14]. The first thing of notice is that differences of α-enhancement SSPs become more pronounced at higher metallicities and older ages. This is to be expected given the fact that the MILES stellar library, present in all models used in this work, is increasingly α-enhanced for lower metallicities, as already mentioned. Another aspect clearly visible in this figure is how the difference between ALF and FSPS models is more pronounced than between E-MILES models. This is a consequence of the common ingredients between E-MILES models. The large difference in the ALF/FSPS ratio for wavelengths $\lambda < 4500$ Å is due to the fact that ALF models are limited by a blue cutoff in their underlying MILES library at 3590 Å. Despite this flux difference in the u-band region, Choi et al. (2019) tested stitching abundance corrected FSPS models to ALF spectra at 3600-3700 Å to correct for this missing flux and found only a ≤ 0.02 mag difference in the resulting u-band magnitudes. This is well under the mean photometric

---

[14] Reference wavelengths obtained from Spanish Virtual Observatory (SVO) filter service (http://svo.cab.inta-csic.es)

Table 3.4: Additional information on the SSP models used in this work. From left to right: model label; minimum and maximum ages available for each model; same for metallicities (in [M/H]; see text for details) and abundance variation ("base" abundance is based on the abundance of MILES stellar library, which is α-enhanced for sub-solar metallicities).

SSP Model	Min. - Max. Ages (Gyr)	Min. - Max. [M/H] (dex)	Abundances
E-MILES Base	0.03 - 14.0	-2.27 - +0.40	base
FSPS	0.03 - 14.0	-1.52 - +0.30	base
E-MILES-α	01.0 - 14.0	-0.40 - +0.22	$[\alpha/Fe]$=+0.4
ALF	03.5 - 14.0	-2.27 - +0.40	$[\alpha/Fe]$=+0.4

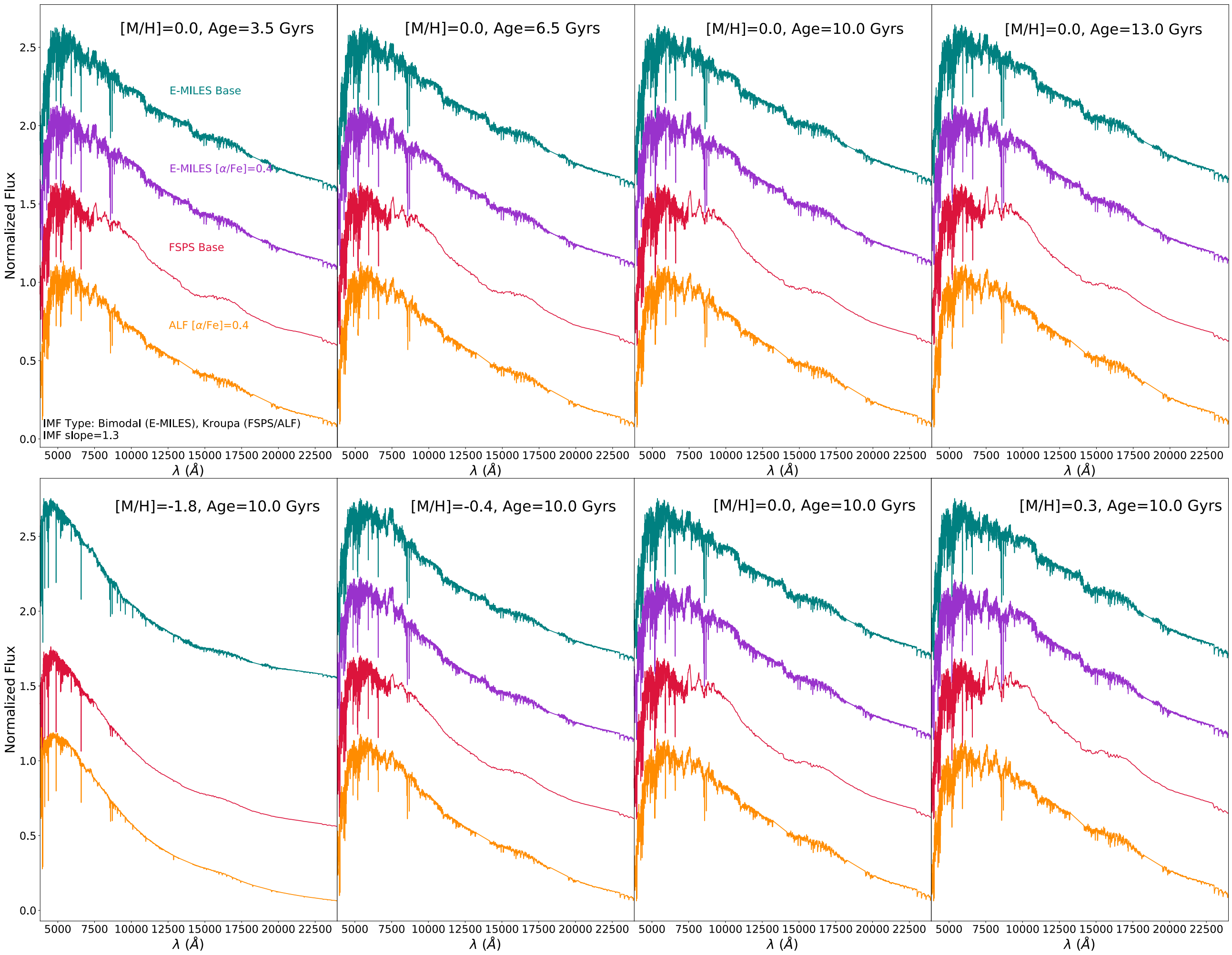

Figure 3.10: Example of each kind of SSP model used in this work. In the y-axis fluxes are normalised by the flux at 6550 Å and a constant added for all spectra to be able to be inspected simultaneously. The colours represent the same model families in every panel, see labels in the top left panel. *Top panels:* Fixed solar metallicity and varying ages. *Bottom panels:* Fixed age in 10.0 Gyrs with varying metallicities. Due to the limited metallicity range available in the E-MILES α-enhanced models used in this work, there is no SSP of this kind for [M/H] $\leq$ -0.35. Therefore, we don't show such type of models in the first panel at the bottom (from left to right) and we show a [M/H] = -0.35 E-MILES α-enhanced SSP at the second panel at the bottom. All the other panels show SSPs of all families with the same metallicities as indicated at the top of each panel.

uncertainties in our data for this filter, therefore this missing flux would not be detectable in our analysis of the models colour predictions.

Section 4 of Vazdekis et al. (2015) similarly discuss the effects of α-enhancement using flux ratios, but with a ratio constructed from dividing an α-enhanced model with solar-scaled SSPs. This means that they compare enhanced models with models with no abundance enhancements at any level, i.e., with solar chemical abundance. As aforementioned, all models labelled as "base" in this work have chemical abundances comparable to the mean trends of Milky-Way stars, and therefore are increasingly α-enhanced for sub-solar metallicities. Despite this consideration, some remarks of Vazdekis et al. (2015) in his comparison are worth of noting in our case. For instance, there is a clear increase in flux in the E-MILES models when α-enhanced for wavelengths smaller than 4500Å. Vazdekis et al. (2015) argues that such feature can be attributed to the decreased Fe abundance in α-enhanced models. This would incur in lower opacity with respect to a solar-scaled model. In our case, with the comparison with a base model, the flux excess in this region is still present in the E-MILES models, albeit smaller in intensity that what is seen in Vazdekis et al. (2015). We cannot compare this flux excess in the E-MILES ratios and FSPS/ALF due to the aforementioned ALF missing flux at wavelengths smaller then 3590 Å.

The potential of Fig. 3.11 to show which filters are more sensitive to the effects of α-enhancement can be used for the choice of colour-colour diagrams to be analysed in section 3.3.1. We aim to find colours composed by the difference of a more sensitive filter and a reference filter where the α-enhancement influence is minimal. This way we can more properly investigate the effects of α-enhancement in SSP colour predictions by minimising potential confounding

Table 3.5: Additional information on the SSP models used in this work. From left to right: model label; minimum and maximum ages available for each model; same for metallicities (in [M/H]; see text for details) and abundance variation ("base" abundance is based on the abundance of MILES stellar library, which is α-enhanced for sub-solar metallicities).

SSP Model	Min. - Max. Ages (Gyr)	Min. - Max. [M/H] (dex)	Abundances
E-MILES Base	0.03 - 14.0	-2.27 - +0.40	base
FSPS	0.03 - 14.0	-1.52 - +0.30	base
E-MILES-α	01.0 - 14.0	-0.40 - +0.22	$[\alpha/Fe]$=+0.4
ALF	03.5 - 14.0	-2.27 - +0.40	$[\alpha/Fe]$=+0.4

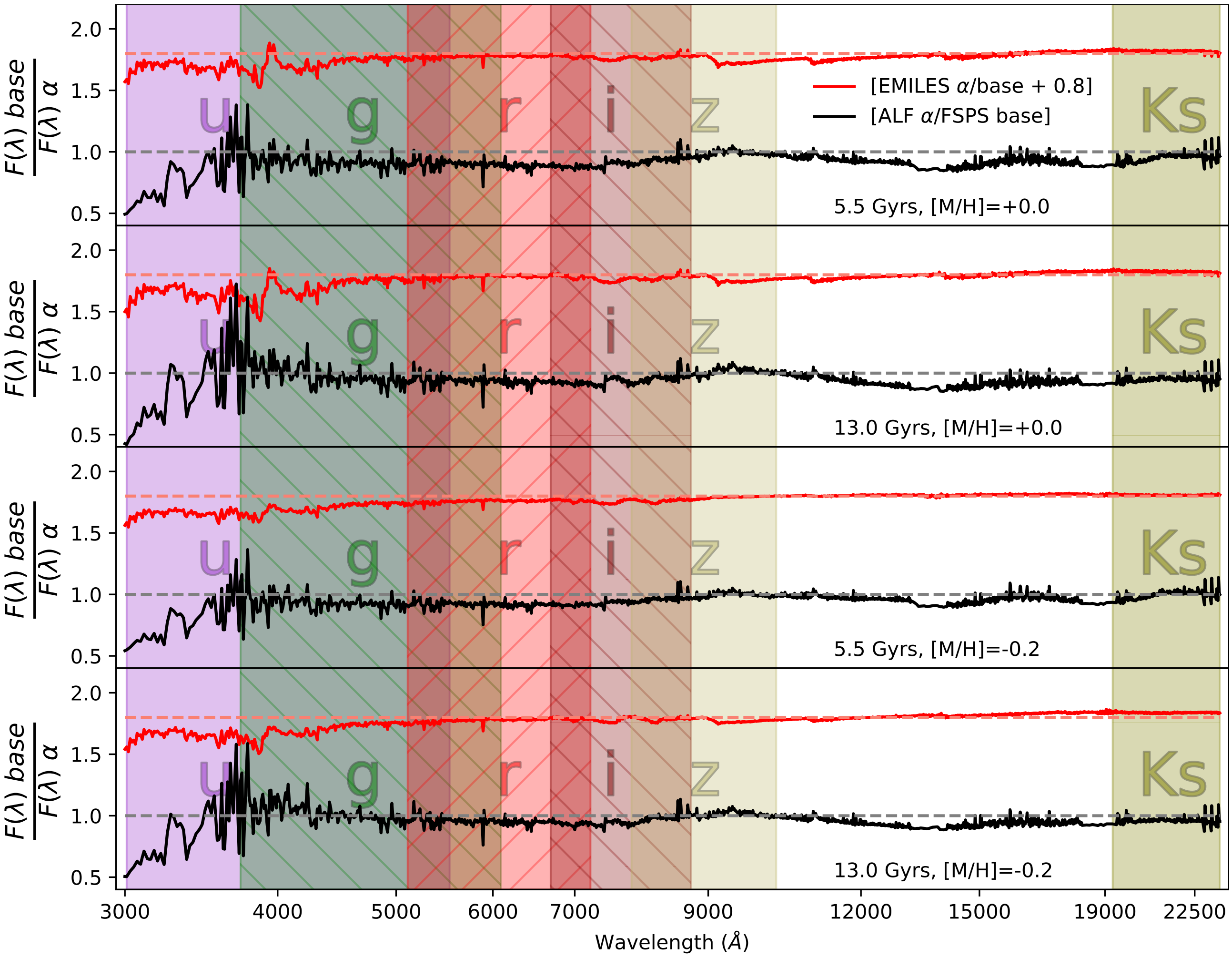

Figure 3.11: Flux ratios obtained from the division of α-enhanced and base models. The red solid line show the ratio for E-MILES models, while the black solid line show the ratio for ALF and FSPS models. The E-MILES ratio has a constant of 0.8 added, for better visualisation. To guide the eye, dashed lines show the line where each ratio would be if no difference was found between models, for each of the comparisons. Underlayed are the wavelength range of each of the $ugrizK_s$ filters.

elements. The i and K_s filters seem to be the filters least affected by α-enhancement. Apart from what we assume to be due to the limitations in the FSPS spectral library, these filters show enhanced features with increased [α/Fe] only at the very end of their wavelength coverage, probably due to the Ca Triplet at $\sim$ 8498 Å and Mg at $\sim$ 8807 Å, for i and z respectively. In fact, any filter redder than the g-band is not strongly affected by variations in α-enhancement – this was already noticed in the Vazdekis et al. (2015) analysis and we confirm to be the case also for the FSPS and ALF models.

On the contrast, in the u and g filters the impact of α-enhancement is considerably stronger than in the other filters, specially at solar metallicities but for all ages. This can be attributed to several features such as O II, at $\sim$ 3727 Å, CN at $\sim$ 3900 Å, Ca II HK at $\sim$ 3950 Å, Ca I at $\sim$ 4227 Å and CN at $\sim$ 4150 Å, to name a few. These indices are known to be sensitive to variations in Mg (Coelho et al., 2007; Vazdekis et al., 2015; Sansom et al., 2013). The region between r and z filters show few, but relevant features. The most enhanced is a deeper Na doublet at $\sim$ 5895 Å, but one can also find deeper Fe lines at $\sim$ 5270 Å and $\sim$ 5335 Å. The Mg and Ca features present at the end of the i filter are almost central in the z filter. These features make the r and z filter particularly interesting for our analysis, however, due to the fact that these filters are not present in the Hydra data, its analysis will be limited to Virgo.

3.3 Estimation of GC Stellar Population Properties based on SSP model predictions

In this section we will show the results about the differences in colour predictions from base and α-enhanced models, as well as the inconsistencies and similarities between different model prescriptions and different colour-colour diagrams, both for the Virgo and Hydra GC samples. We will also discuss the influence of the environment in this matter. Finally we will quantitatively investigate the differences between the predictions of models tested in this work using the distance to a 10 Gyr isocrhone in each colour-colour diagram as a reference point.

3.3.1 Colour predictions of SSP models with and without α-enhancement

Synthetic Photometry

To compute the colour-colour diagrams, first we need to compute the synthetic photometry for the models we use in this work, so as to obtain magnitudes in the $ugrizK_s$ filters available in our data. This is done via the following equations[15]:

$$\begin{aligned} f_\nu &= \frac{1}{c}\frac{\int S T_x \lambda \, d\lambda}{\int T_x/\lambda \, d\lambda}, \\ m_{\rm AB} &= -2.5 \log f_\nu - 48.6 \end{aligned} \tag{3.2}$$

Where f_ν is the average flux density, $S \equiv S(\lambda | age, [M/H])$ is an SSP spectra in units of erg/s/cm^2/Å[16], T_x is the transmission curve for filter x, c is the speed of light in Å/s and λ the wavelength in Å. The final AB magnitudes were calculated by taking the trivial logarithm of the average flux density using the zero-point $zp_{\rm AB}$=-48.6 (Bessell and Murphy, 2012). Spectra are K-corrected to the redshifts of M87 and NGC 3311[17]. Significant care is needed to ensure that the synthetic photometry process does not bias the final analysis of model colour predictions. To this end, we adopted transmission curves of the specific filters of the telescopes used in the observations of our samples, and at the time window of these observations. These were obtained from the Spanish Virtual Observatory (SVO) filter service (http://svo.cab.inta-csic.es).

From Fig. 3.12 to 3.17 we present colour-colour diagrams for both Virgo and Hydra GC samples described in Table 3.2 and the models from Table 3.3. In Fig. 3.12, we show only Virgo GCs, due to the absence of r and z filters in the Hydra data used in this work. Moreover, where possible we use the Hydra UVIKs sample as it has a larger sample size than the giUVIKs sample, although no significant difference was found when comparing the two samples in the

---

[15] As a side note, we consider important to add that there is considerable conflict in the definitions of relevant quantities, standard equations and zero-points for different photometric systems in the context of synthetic photometry in the literature. A beacon of light in this confusion is Bessell and Murphy (2012) and we refer the reader to it for a detailed explanation and clarification of such definitions.

[16] None of the models used in this work are originally in these units. For simplicity sake, they were converted using the appropriate transformations, to the same units of f_λ in order to calculate the synthetic photometry.

[17] obtained from NED

same colour-colour diagrams. SSP isochrones and iso-metallicity curves for the SSP models are plotted side-by-side for easy comparison. Similarly, $\alpha - enhanced$ models and base models are also side-by-side for comparison purposes.

To guide the eye, we also show a smoothed curve constructed using the R language (R Development Core Team, 2019) implementation of the locally weighted running line smoother (LOESS) algorithm (Cleveland et al., 1992; Jacoby, 2000) in white dashes, with 95% confidence intervals as shaded regions (which are very small for most of the diagrams and therefore almost not visible). For brevity sake, we will not go into details on the specifics of the LOESS algorithm, and we refer the reader to Jacoby (2000) for a complete description. But in summary, for a given data point in the colour-colour plane, LOESS works by fitting a linear model (in our case, polynomials of degree 1) based on a limited sample of neighbouring points. The size of this sample is determined by an α_{LOESS} parameter which gives the proportion of observations used in each local regression. In our case, we used for all colour-colour plots a value of α_{LOESS} of 0.15, which means that for each data point the local linear regression incorporates 15% of neighbouring data points. There are several advantages in using a LOESS algorithm over a global linear regression in our case. For one, most colour-colour diagrams present a significant number of outliers that introduce leverage into a global linear fit. LOESS weights unfavourably points with few neighbours, thus exempting us from the need of imposing arbitrary cuts into the data. In addition, some colour-colour diagrams have been found to present non-linear features, such as being better represented by more than one linear model with different slopes (e.g., Chies-Santos et al. 2012b; Blakeslee et al. 2010). Local regression is an improvement in this regard by providing a good compromise between smoothness of the fit and fidelity to non-linear features present in the observed data structure.

Colour-Colour Diagrams

The choice of colours for these diagrams is based on the analysis of Fig. 3.11 in the previous section. However, in order to compare colour predictions for models considered in this work with the results shown for several other models in P16a and P16b, we first look into Fig. 3.12 where we present a *griz* diagram. In this figure we show only Virgo GC samples due to the absence of the r and z bands in our Hydra data. Similarly to what have been found in P16a; P16b, different models show inconsistencies in reproducing the same optical colours for Virgo GCs. The E-MILES base SSPs loci lies blueward in relation to the centre of the data distribution and to FSPS base models, which in turn are more age degenerated but following more closely the centre of the colour-colour distribution. In this diagram FSPS base models are in general ~ 0.2 mag redder than E-MILES base SSPs. The comparison between α-enhanced models also show two distinct scenarios. The E-MILES α-enhanced SSPs, in the range of metallicities available, are very similar when compared to the E-MILES base models, only having the youngest SSPs slightly bluer. ALF α-enhanced models present generally redder older ages and a much more degenerate age/metallicity situation. In respect to metallicities, in this diagram all models indicate a wide distribution of metallicities for Virgo GCs, from [M/H] = -2.27 to +0.4 ,from red to blue, respectively, and for both base and α-enhanced models.

Next, in Fig. 3.13, we show a *ugi* diagram. In this figure we also include Hydra GCs. This colour-colour diagram is specially interesting due to the high sensitivity of the u and g filters to α-enhancement, as we showed previously. Nevertheless, we do not find significant differences in these colour predictions by the models with different abundances. In fact, even the differences between E-MILES and FSPS models are not as prominent as in the $(g-r)$ versus $(i-z)$ diagram. This might arise from the overlapping nature of the u and g filters cancelling each other features. This figure is an example of what we referred in the previous section regarding the importance of constructing colours where one filter is sensitive to α-enhancement and the other is not.

From Fig. 3.14 to 3.16 we show colour-colour diagrams using the VLT/HAWKI K_s-band magnitudes presented in this work. This enables us to look into colours combining NUV/optical and the NIR filters, which are known to have strong age/metallicity prediction advantages over purely optical colours (Muñoz et al., 2013; Georgiev et al., 2012; Chies-Santos et al., 2012b). In such diagrams we see once more inconsistencies between models with the same abundance variations. ALF models are generally more degenerate in age/metallicity, similarly to FSPS base models, when compared to E-MILES SSPs. In general, Hydra GCs suggest an younger population than in Virgo, due to the closeness of intermediate age SSPs (~ 3.5 Gyrs) to the centre of the diagrams, along the smoothed linear fit.

Comparing all diagrams, the ones that at least qualitatively seem to better agree with the spectroscopic ages found for most GCs in Virgo and Hydra (≥ 10 Gyrs) (Misgeld et al., 2011; Strader et al., 2011; Romanowsky et al., 2012; Peng et al., 2008) are the uiK_s and the $uigK_s$ diagrams. $(i - K_s)$ and $(g - K_s)$ colours are known to be sensitive to the temperature of stars at the red giant branch (RGB) and the main-sequence, respectively, while the $(u - i)$ colour is sensitive to hot stellar phases due to the fact that it compares fluxes around the 4000 Å break (Muñoz et al., 2013). Therefore, such diagrams are expected to be relatively good at detecting ages. The fact that they seem also to not be significantly affected by α-enhancement effects, despite the presence of the u and g filters, suggests that age variations are also not significantly affected by the variations in α-enhancement in the models tested in this work.

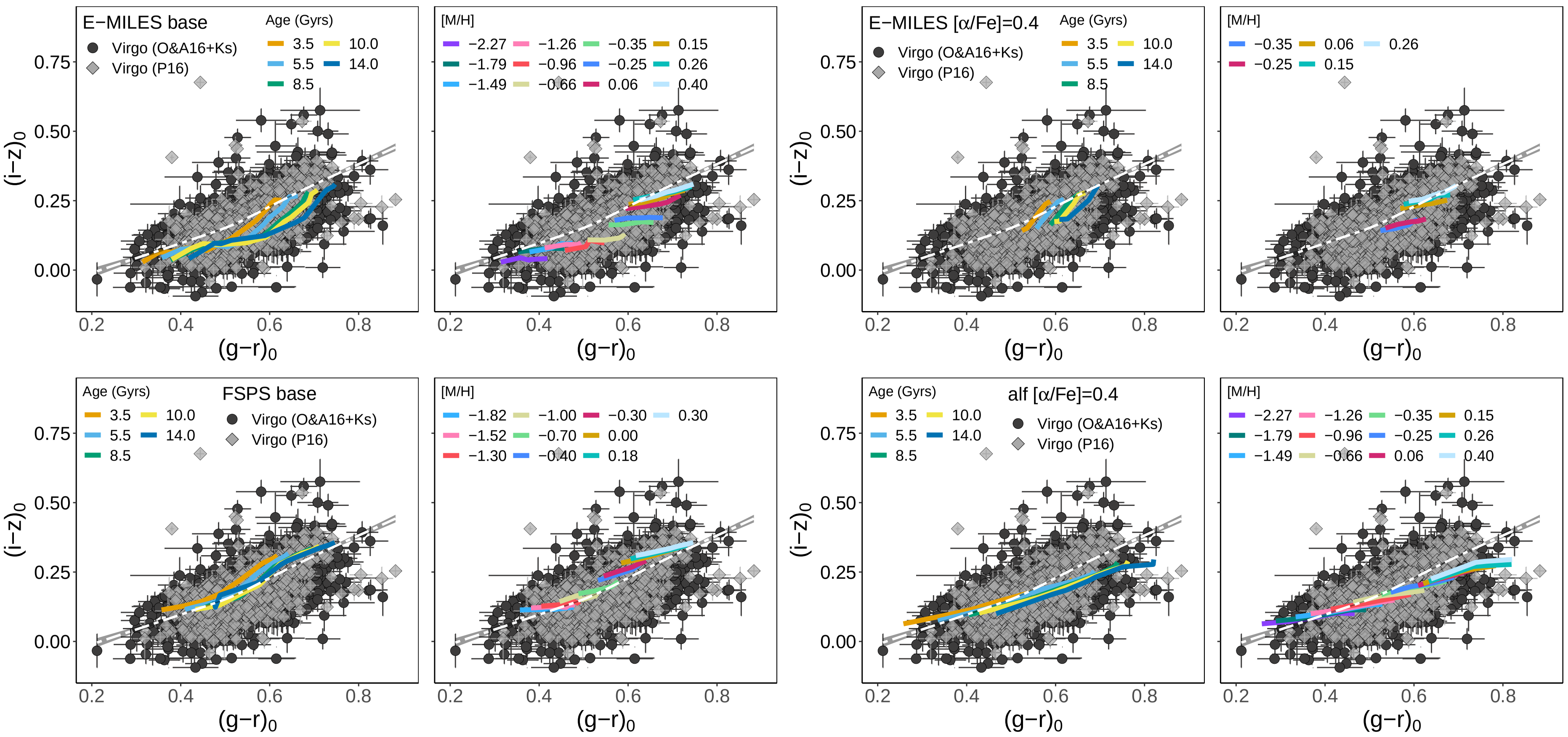

Figure 3.12: SSP model colour predictions for Virgo GCs in a $(g-r)_0$ versus $(i-z)_0$ diagram. In black squares we show the O&A16+Ks Virgo GC sample from this work and in grey diamonds the Virgo GCs from the P16a NGVS sample. The white dashed line shows a LOESS smoothing curve of the data, with associated . For all models tested in this work we show on one panel selected SSPs coloured by age and in the immediately next panel to its right the same SSPs coloured by [M/H]. The four leftmost panels show E-MILES base models on top and FSPS base models below, while the four rightmost panels show E-MILES α-enhanced models on top and ALF α-enhanced models on the bottom. The α-enhancement is always fixed at $[\alpha/\text{Fe}]=0.4$. Notice the discrepancies between different models even when comparing only models with the same abundances. Only Virgo GCs are shown in this figure due to the lack of the r and z filters in the Hydra samples of this work.

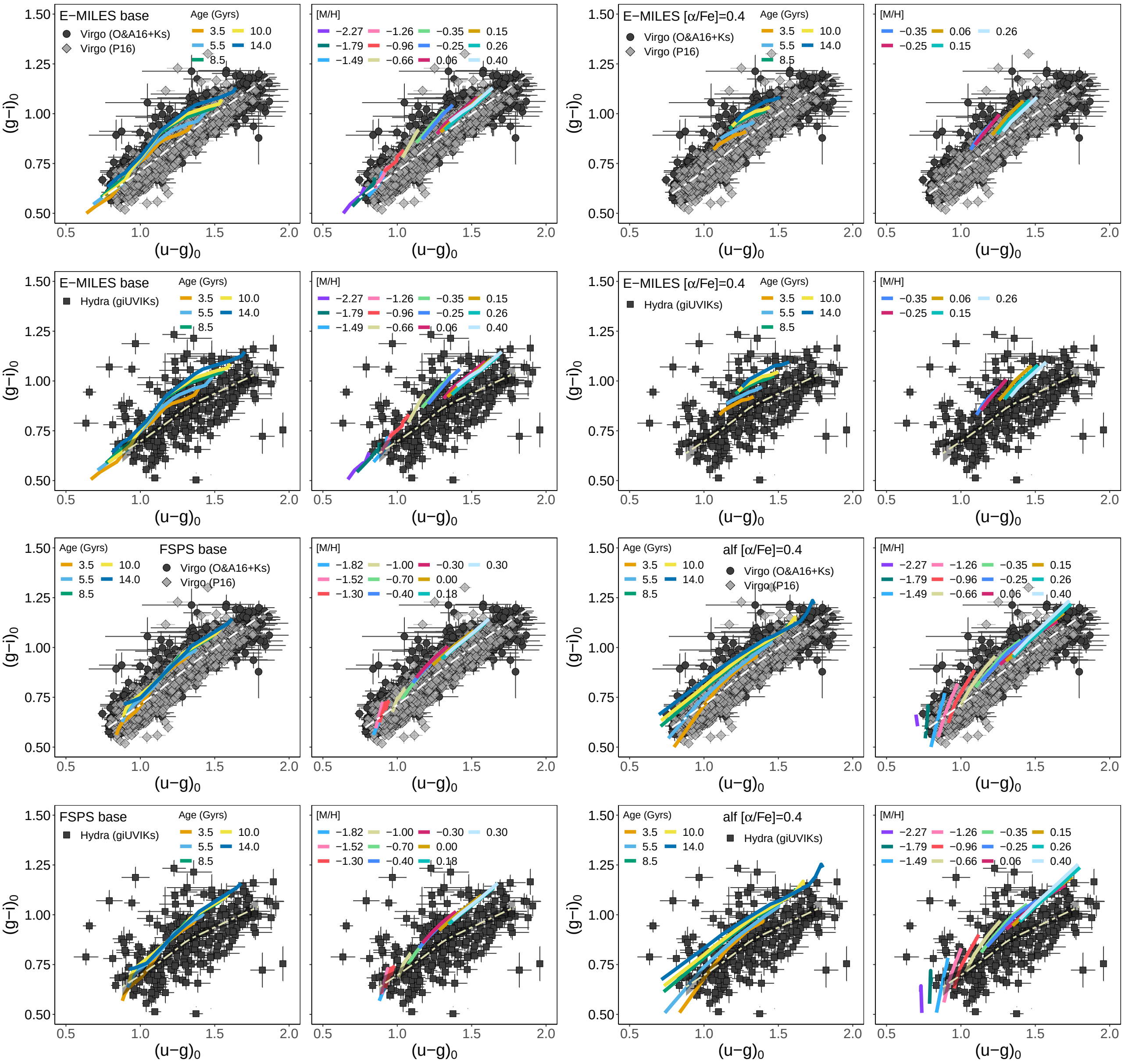

Figure 3.13: Same as Fig. 3.12, but for *ugi*and with the addition of Hydra GCs at the bottom panels of each quadrant.

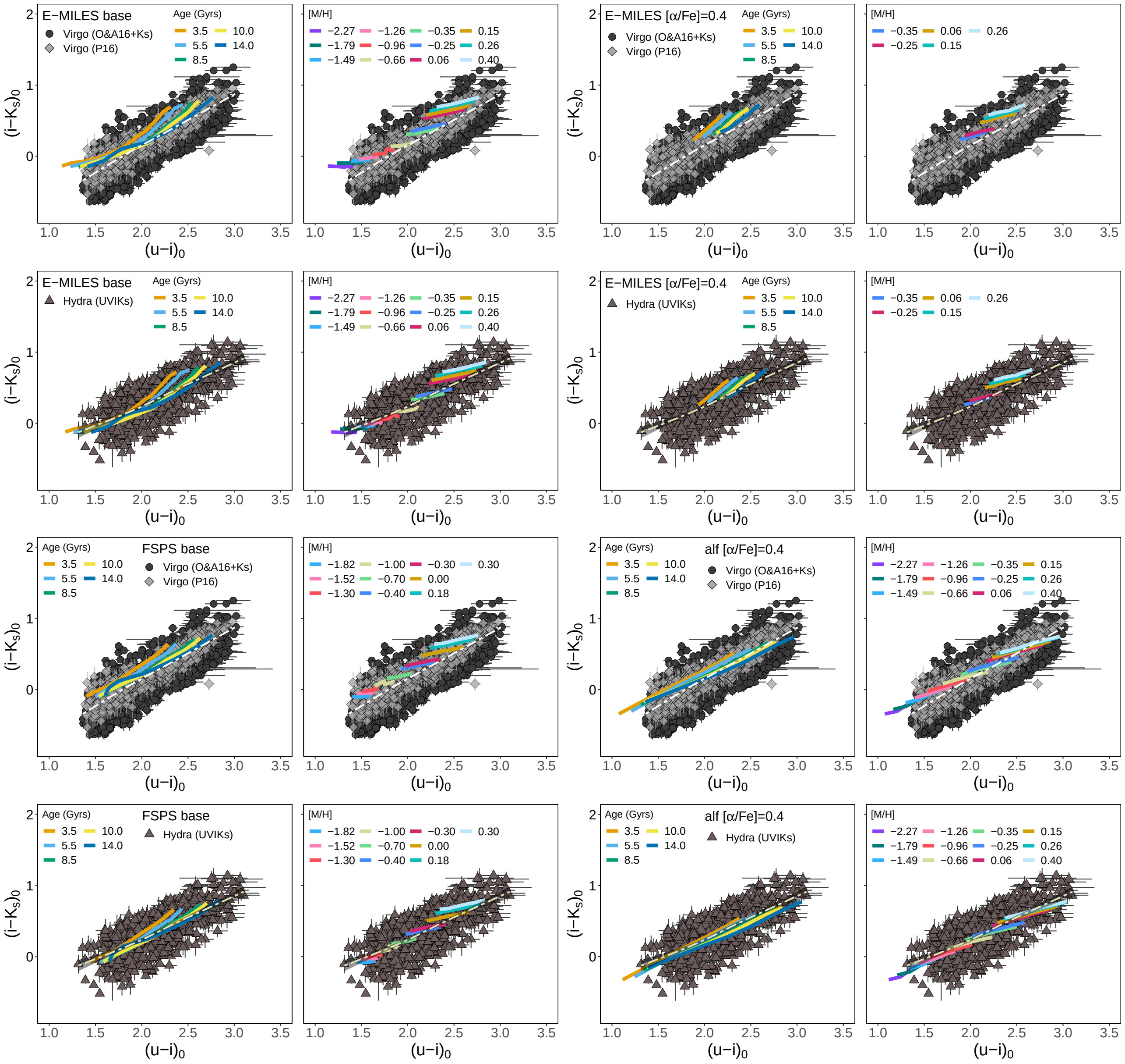

Figure 3.14: Same as Fig. 3.13, but for uiK_s.

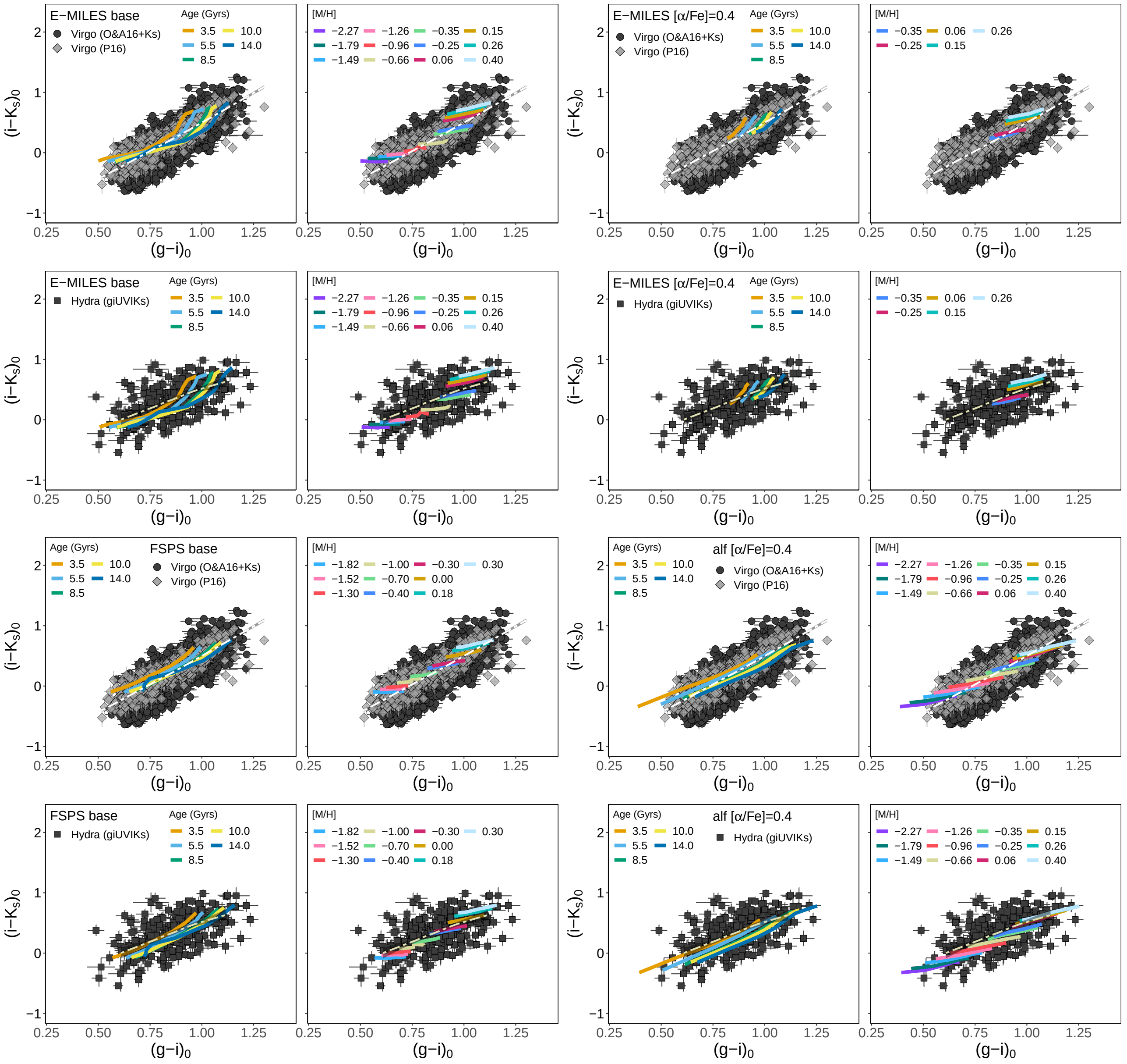

Figure 3.15: Same as Fig. 3.14, but for giK_s.

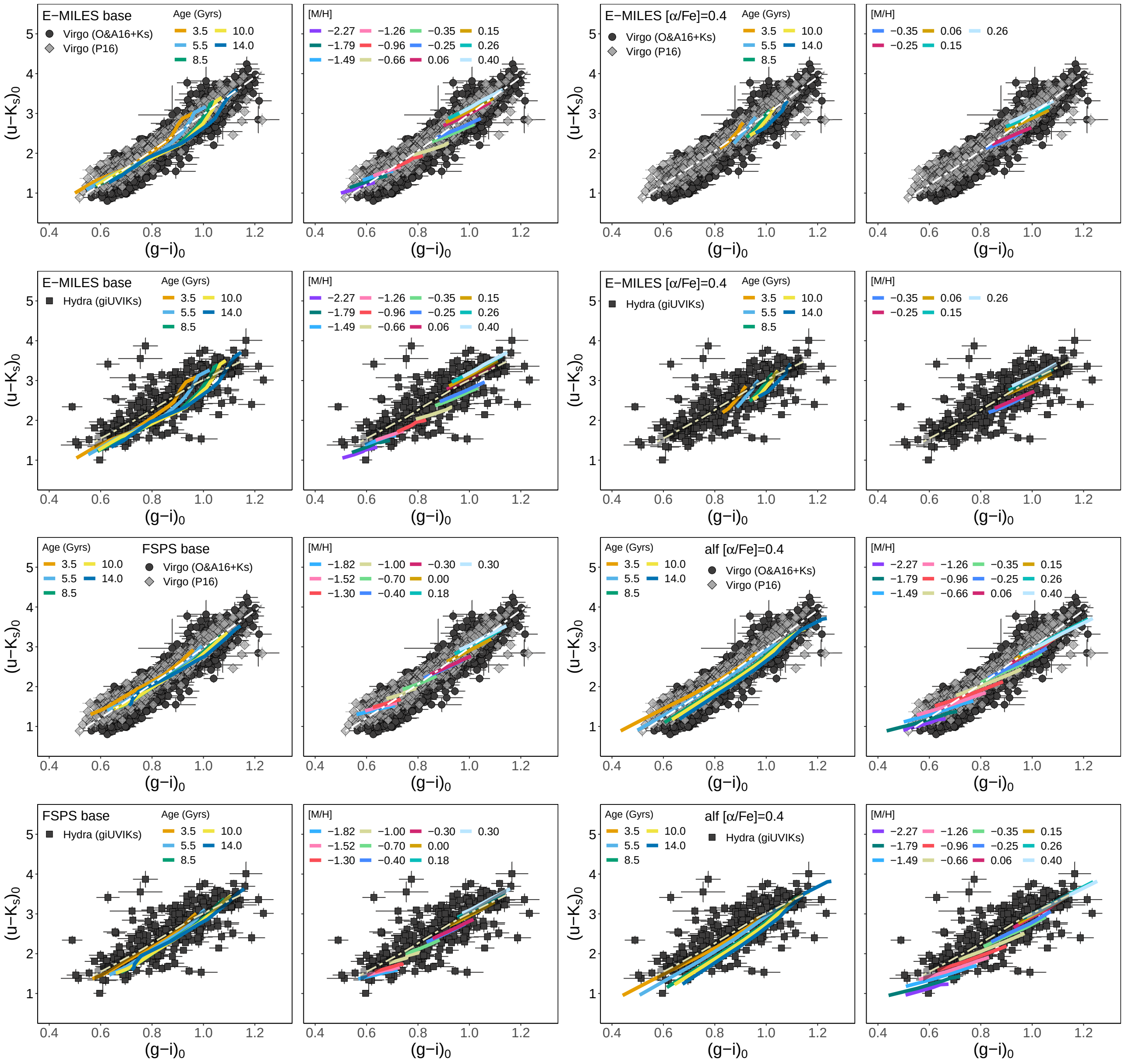

Figure 3.16: Same as Fig. 3.13, but for $giuK_s$.

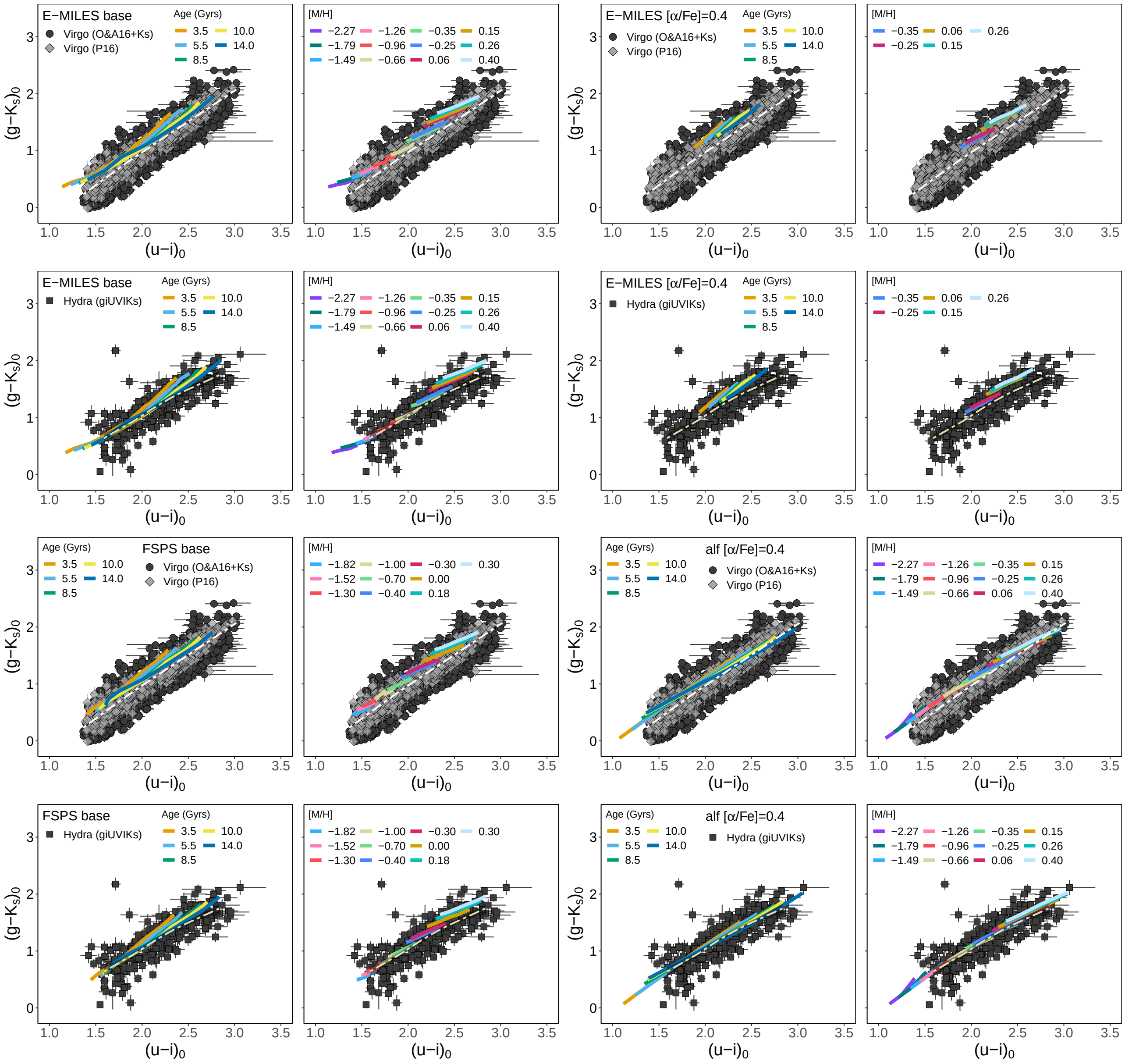

Figure 3.17: Same as Fig. 3.13, but for $uigK_s$.

3.3.2 Environmental Effects

Now we present the same colour-colour diagrams of the last section, but this time with our GC samples divided in spatial bins. Such spatial bins follow a pattern used in P16a and detailed in section 3.1.5. In summary, we divide the samples considering an inner region, labelled as region A, within $\sim 2.8R_e$ of M87, in the case of the Virgo data, or NGC 3311 in the case of the Hydra samples. Then we define region B as the region confined between $\sim$2.8R_e and $\sim$28.8R_e and a region C for objects more distant than $\sim$28.8R_e to the associated central galaxy (see Figs. 3.7 and 3.8). This is a revisit of the analysis presented by P16a, with the addition of new Ks band imaging from HAWK-I (see Section 3.1) for Virgo GCs and the new Hydra GC catalogue. The results from P16a suggested that discrepancies between model colour predictions and observed Virgo GC colours increase as a function of the distance to the centre of M87.

We show the region separated colour-colour diagrams for Virgo samples in the Figs. 3.18 to 3.23 and for the Hydra samples from 3.24 to 3.28. As shown in Fig. 3.2, the P16 and O&A16+Ks Virgo samples, as well as the Hydra samples used in this work have very different spatial distributions. Our samples comprise a considerably smaller and more central region than the P16 sample, therefore in the Virgo figures we show only the A, B and C regions and for Hydra we show only the A and B regions.

Virgo GCs

In the same fashion as in the last section, the first diagram analysed is a *griz* diagram for the Virgo samples, shown in Fig. 3.18. This diagram is the same one presented in Fig. 1 of P16a (and in the bottom panel of Fig. 1.8 in this work). The two models tested in this work with most complete metallicity/age coverage and stellar libraries, E-MILES base and ALF α-enhanced, show similar results in this diagram, despite the ALF SSPs to be much more degenerated in age/metallicity. The comparison between these two models colour predictions and the observed Virgo colours of both the O&A16+Ks and the P16 are in accordance to what have been shown in P16a using the Bruzual and Charlot (2003) SSP models. This is, these SSP models optical colour predictions are better in accordance to the observed data in the outermost bin, region C. In this same region, however, E-MILES *alpha*-enhanced SSPs are bluer than most part of the observed data. This effect for this specific model is probably exagerated due to the lack of more metal-poor SSPs at the current time (Vazdekis et al., 2015). Nevertheless, the α-enhancement seems to improve the agreement of the E-MILES models to the data in the inner regions, albeit very subtly, and mostly in the B region. This evidentiates that, although an α-enhancement of $[\alpha/\mathrm{Fe}]=0.4$ is not enough to completely match E-MILES SSPs with the colours of Virgo GCs in this diagram, it is likely an important step in the right direction. Finally, the FSPS base models show a very different behaviour than the E-MILES base models. This once more shows the inconsistencies between SSPs of different models despite the same abundance variations.

In Fig. 3.19, the *ugi* diagram, we see that the SSP models are remarkably more consistent, despite the strong age/metallicity degeneracy already discussed in the last section for this specific diagram. There are still environment variations, but they are much more subtle than what can be seen in the *griz* diagram. This suggests that the relation between environment, GC colours and SSP predictions is also not consistent between different colour-colour diagrams. This fact becomes even more clear when we look at the colour-colour diagrams including colours combining NUV/optical and the K_s filter, uiK_s and $uigK_s$, in Figs. 3.20 to 3.23. There is a remarkable agreement with the smoothed linear fit curve and the expected old ages ($\geq$ 10 Gyrs) of Virgo GCs (Strader et al., 2011; Romanowsky et al., 2012; Villaume et al., 2019; Chies-Santos et al., 2012b; Peng et al., 2008), even at the innermost regions. This is in agreement with the results shown for the full GC samples in the last section for this colour-colour diagram (Fig. 3.6). Given the aforementioned reassuring capabilities of the uiK_s diagram to probe ages, these results suggests that, within radial variations, the main age distribution for Virgo GCs is not only very similar, but also independent of α-enhancement effects. Similar results are found in the $giuK_s$ diagram in Fig. 3.22, despite the expected sensitivity of these colours to variations in $[\alpha/\mathrm{Fe}]$.

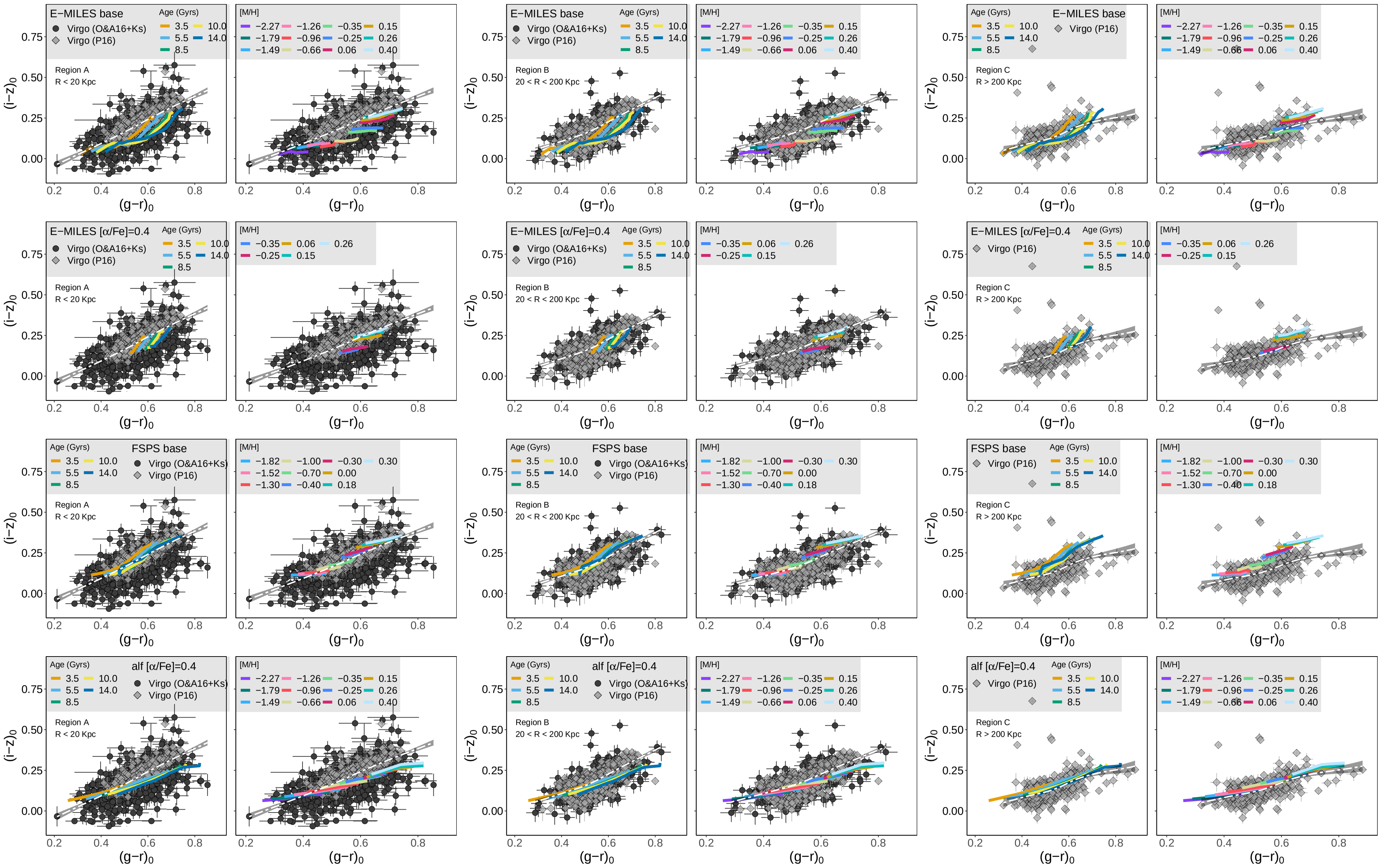

Figure 3.18: Same as Fig. 3.12, but now for three different spatial bins of Virgo GCs. On the two leftmost columns, only GCs within 20 Kpc from M87. In the two middle columns, only GCs between 20 and 200 Kpc from M87 and in the two last columns GCs beyond 200 Kpc – which are only available in the P16a sample.

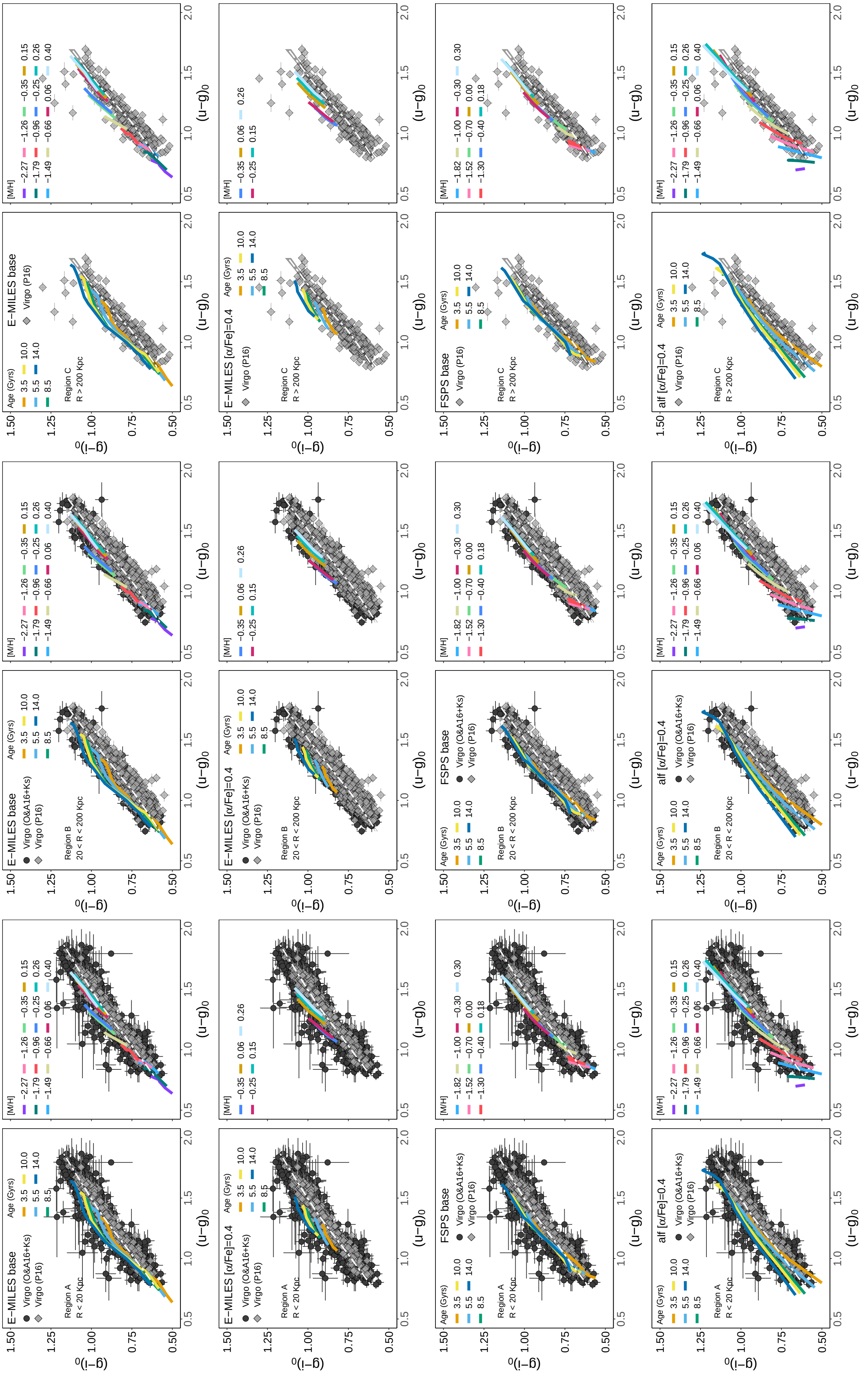

Figure 3.19: Same as Fig. 3.18, but now for *ugi*.

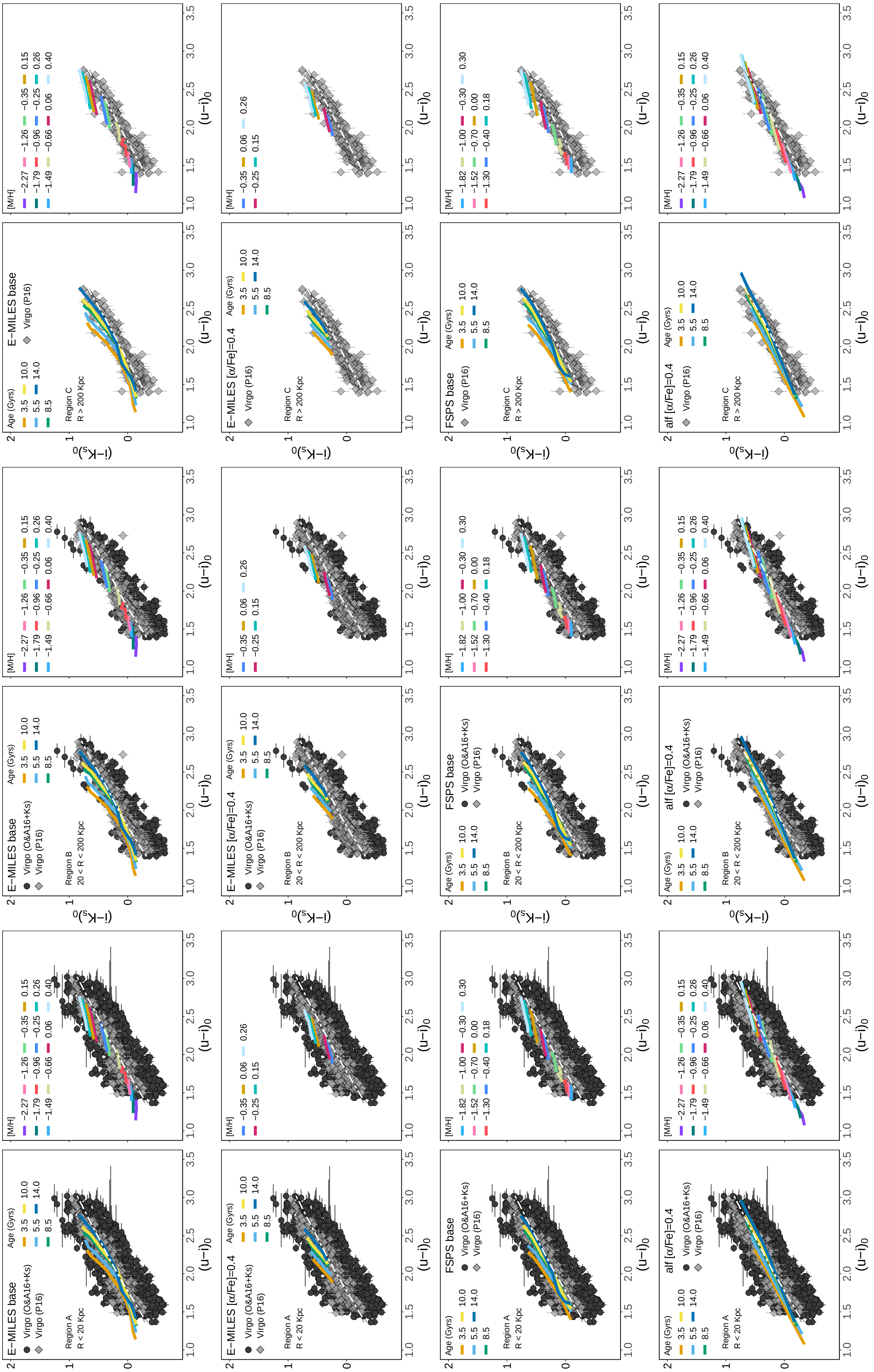

Figure 3.20: Same as Fig. 3.18, but now for uiK_s.

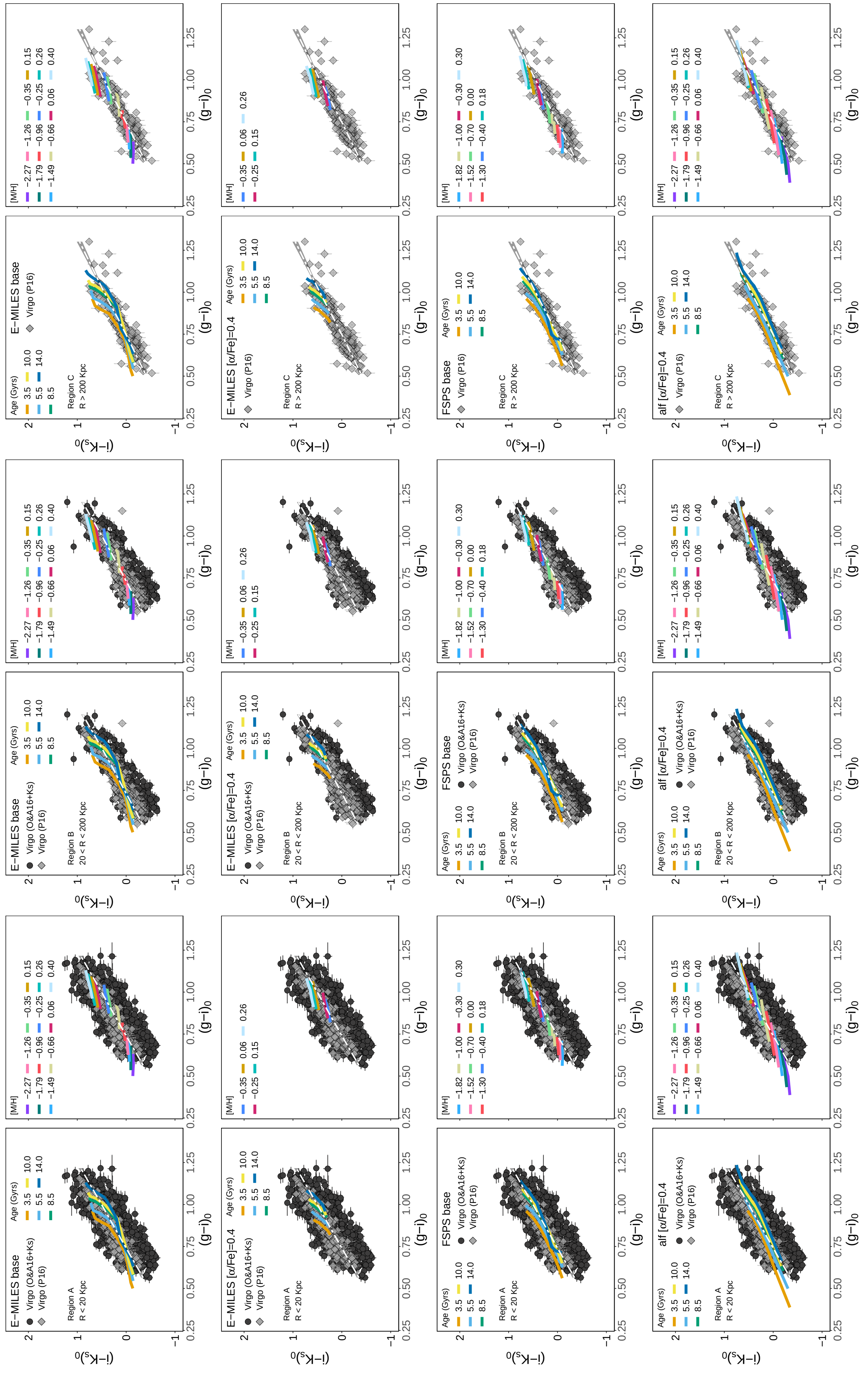

Figure 3.21: Same as Fig. 3.18, but now for giK_s.

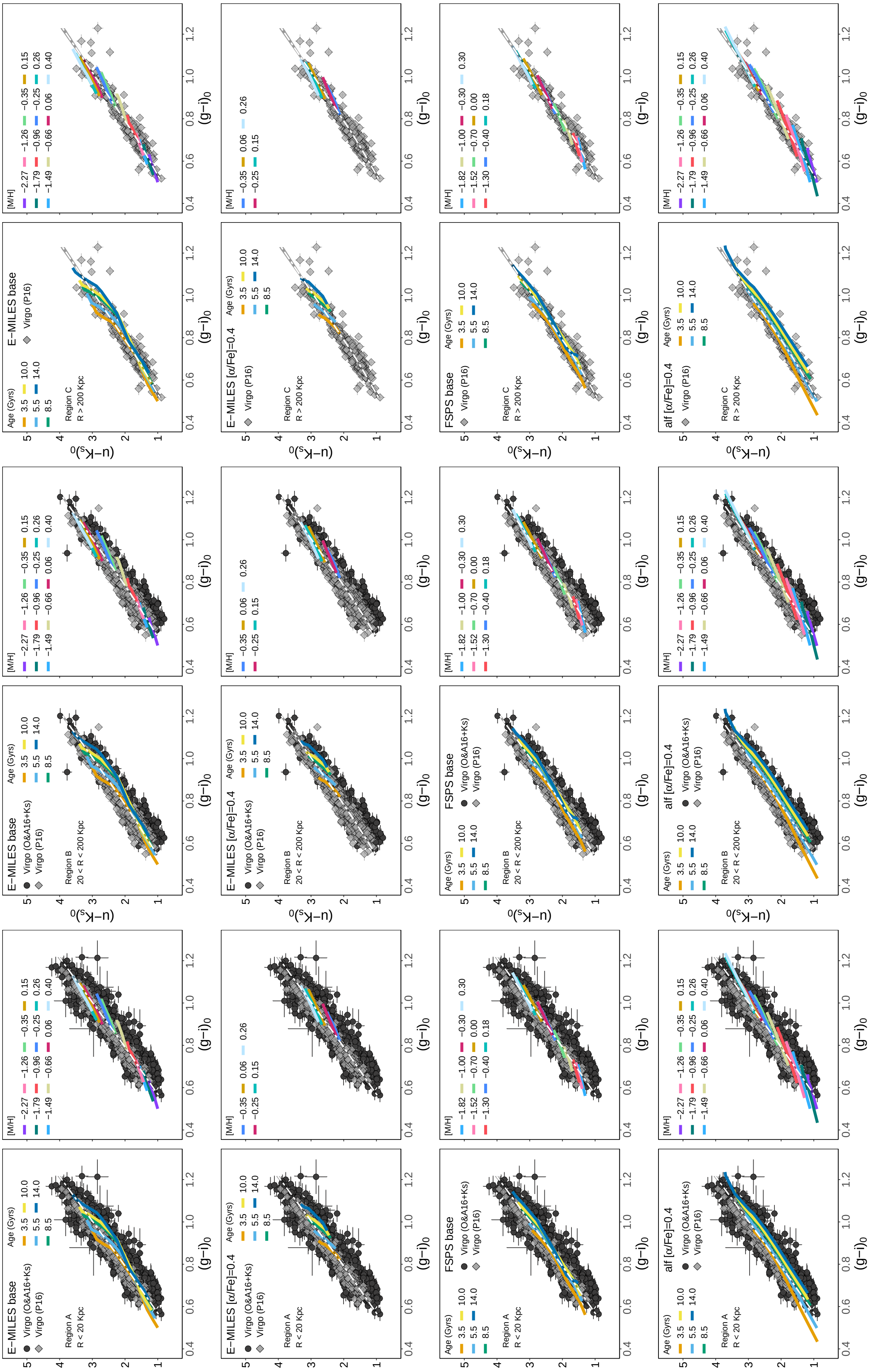

Figure 3.22: Same as Fig. 3.18, but now for $giuK_s$.

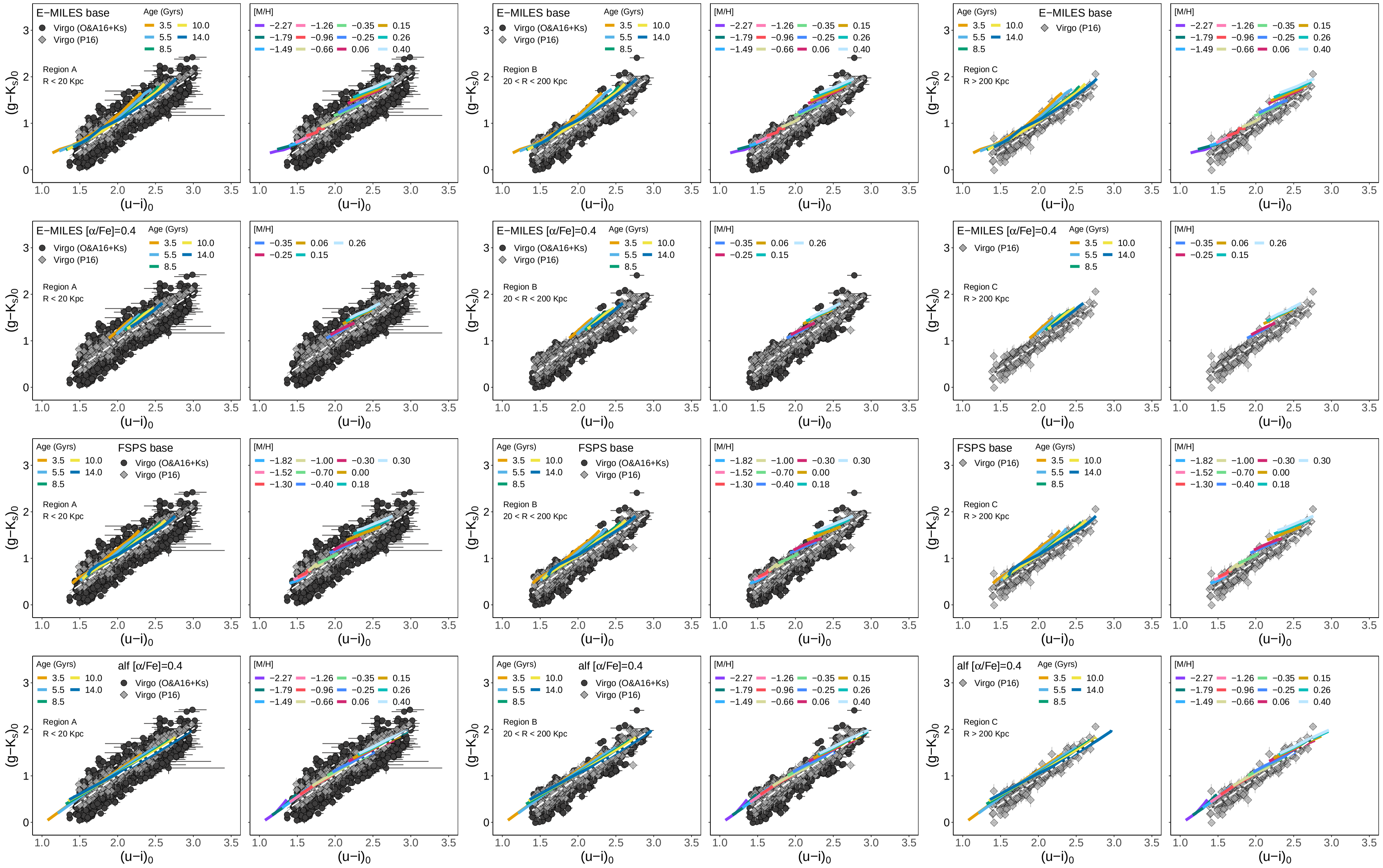

Figure 3.23: Same as Fig. 3.18, but now for $uigK_s$.

Hydra GCs

The region where most of our Hydra data is located is region B, due to fact that for both the UVIKs and the giUVIKs sample, region A is considerably lacking in sample size compared to the region B and the Virgo samples. Nevertheless, it is interesting to analyse the colour predictions of SSP models with and without α-enhancement in the Region B of Hydra GC samples due to the fact that this region is expected to contain at least some mixture of objects associated with NGC 3311 and NGC 3309.

In Fig. 3.24 we present the region separated ugi diagram for Hydra GCs. All SSP models seem to be bluer than the observed loci of Hydra GCs, specially when compared to the same diagram for Virgo GCs in region B, in Fig. 3.19. Region A data is too sparse and scattered for a statistically relevant analysis in this diagram. The age sensitive uiK_s diagram of Fig. 3.25 suggests that Hydra GCs in region B are consistent with old ages ($\geq$ 10 Gyrs), similarly to Virgo GCs, while region A GCs are seem more in accordance with intermediate age isocrhones. This in agreement with photometric and spectroscopic age estimates for NGC 3311 GCs (Misgeld et al., 2011; Richtler et al., 2020; Wehner et al., 2008b), and also supports the idea that GCs in the outer haloes of NGC 3311 and M87 are not significantly different in age, despite the aforementioned potential mixture of GCs between NGC 3311 and NGC 3309 in our sample. In Figs. from 3.26 to 3.28 the comparison of observed colours of Hydra GCs and the predicted colours of SSP models are very similar to Virgo GCs, with negligible variation due to α-enhancement between regions and different colours. Later in this work we will return to the question of the suggested age differences between the Hydra and Virgo GC samples noticed in this section.

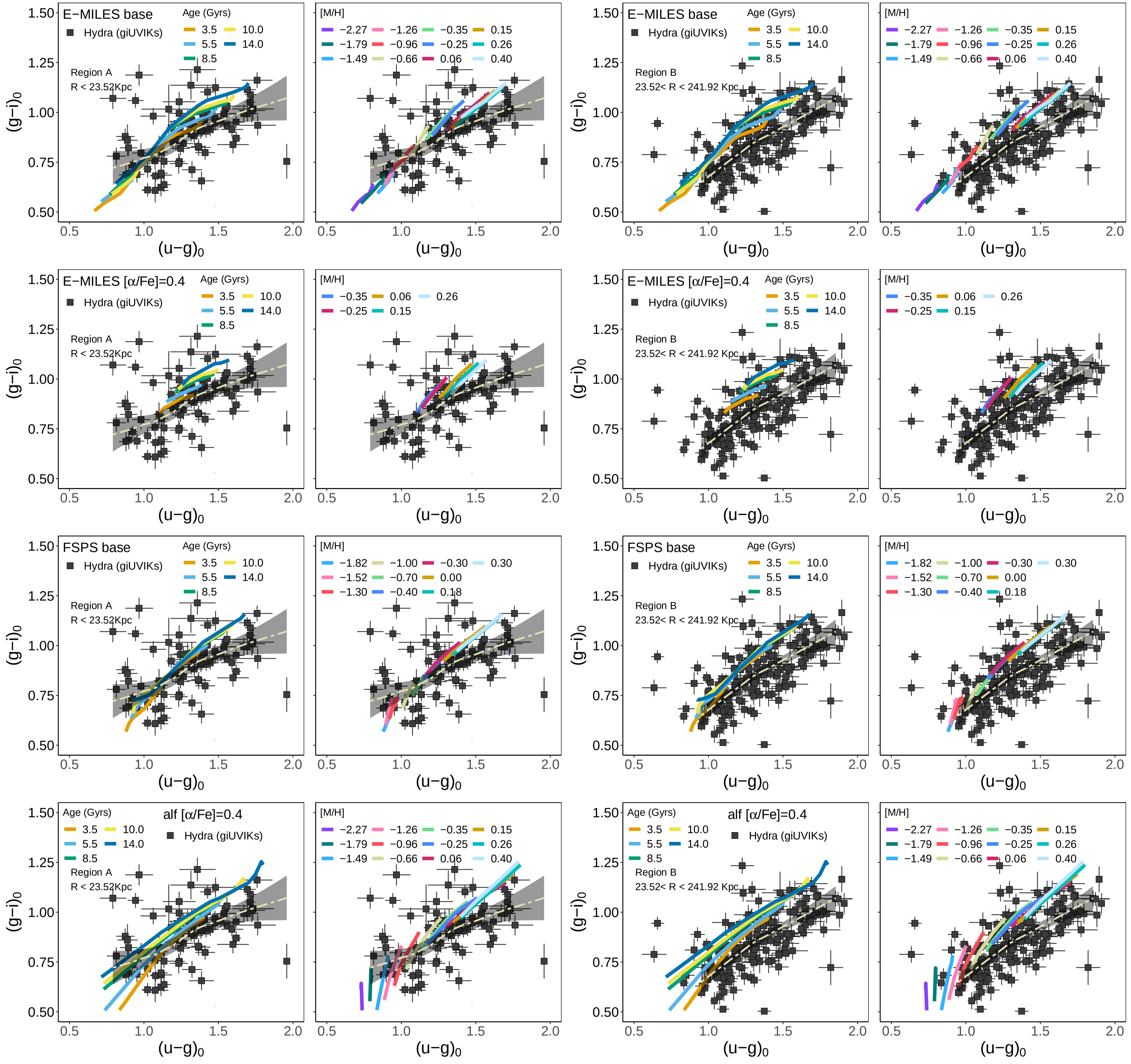

Figure 3.24: Same as Fig. 3.19, but now for two different spatial bins of Hydra GCs. On the two leftmost columns, only GCs within 23.52 Kpc from NGC 3311. In the two rightmost columns, only GCs between 23.52 and 241.92 Kpc from NGC 3311.

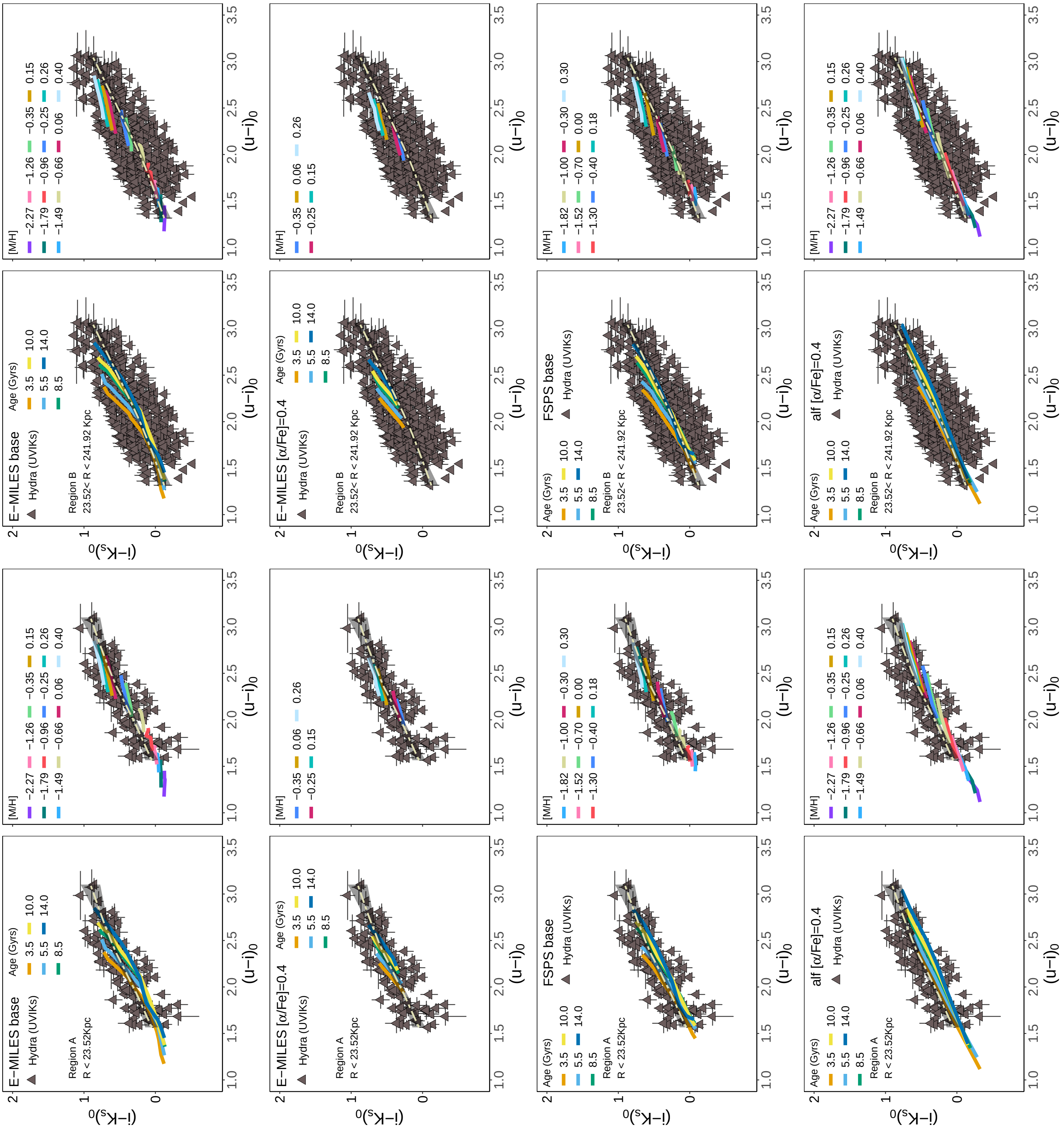

Figure 3.25: Same as Fig. 3.19, but now for uiK_s.

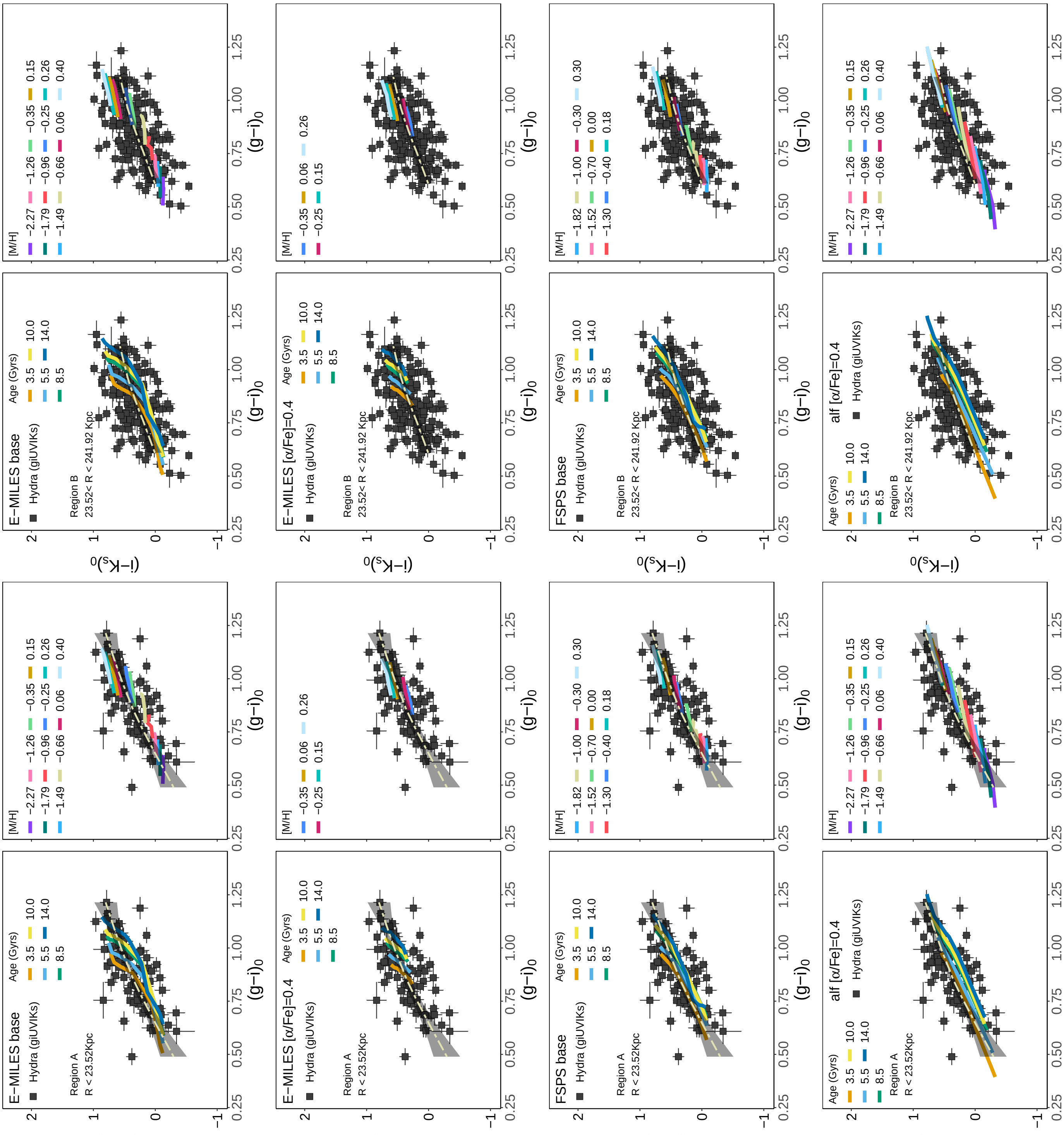

Figure 3.26: Same as Fig. 3.19, but now for giK_s.

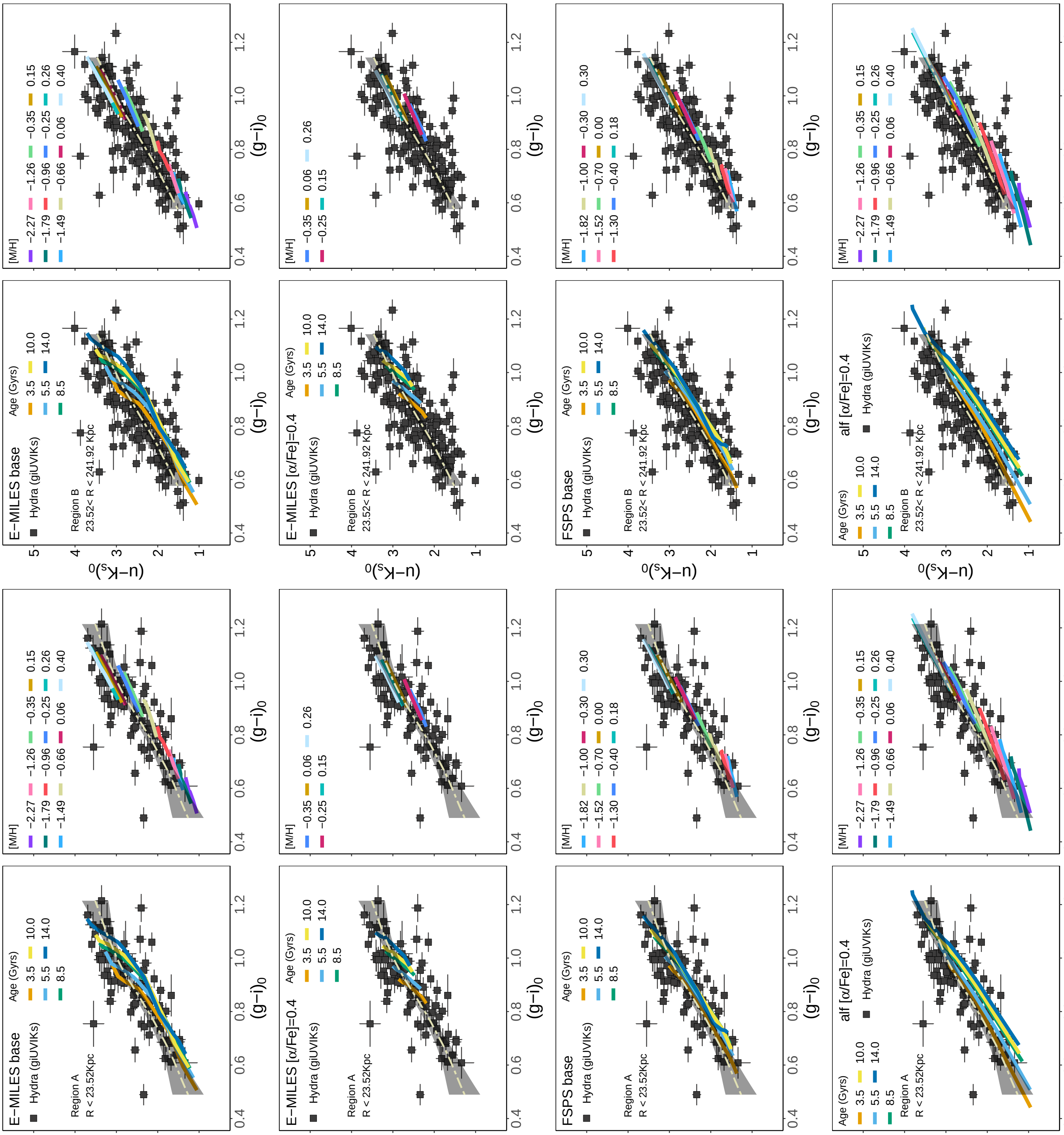

Figure 3.27: Same as Fig. 3.19, but now for $giuK_s$.

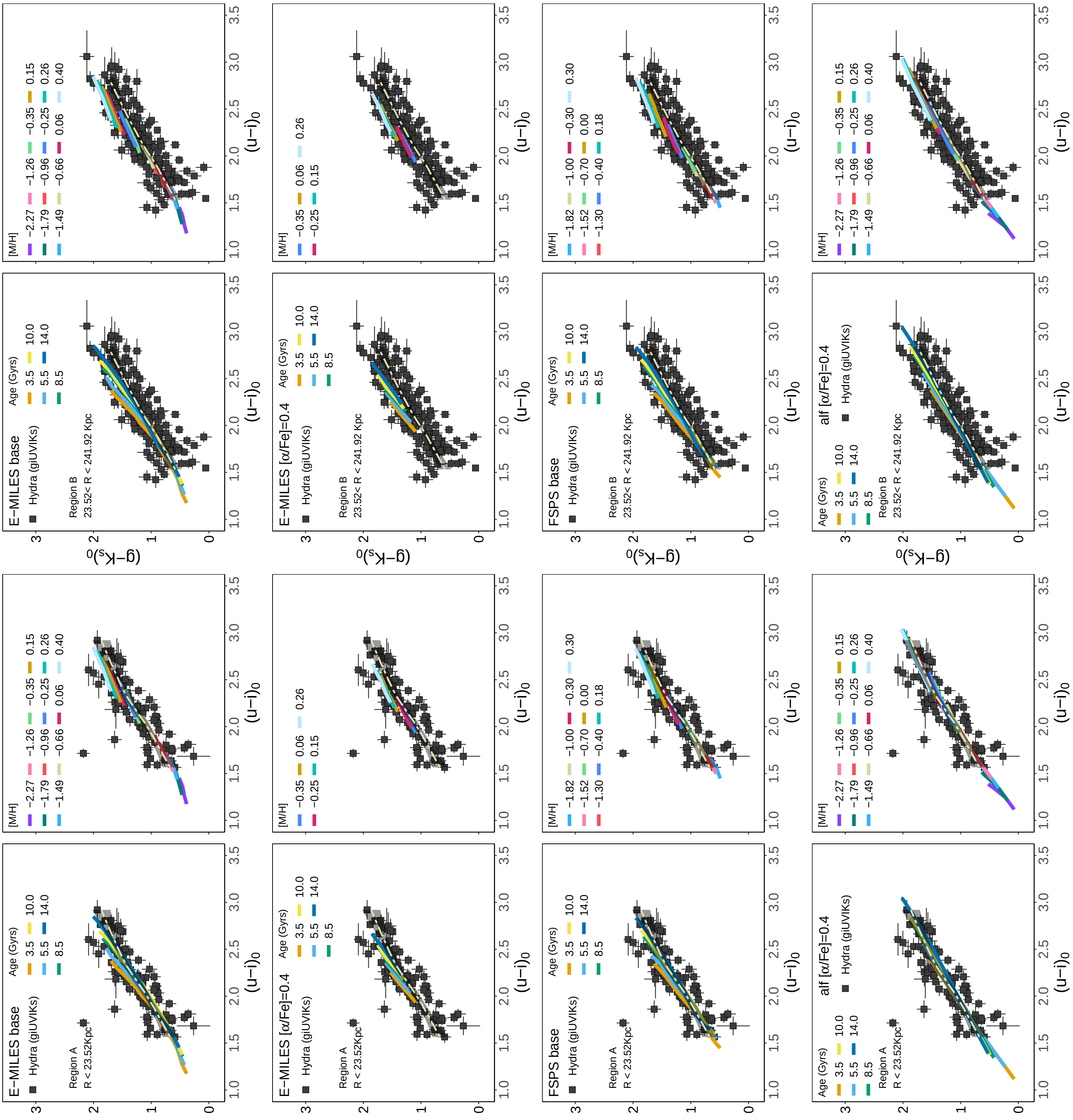

Figure 3.28: Same as Fig. 3.19, but now for $uigK_s$.

3.3.3 Statistical differences between base and α-enhanced models from colour-colour diagrams of Hydra and Virgo GCs

In order to quantitatively visualise how different SSP models compare in each colour-colour diagram, we calculated for each data point, of each sample, the euclidean distance to each model 10 Gyr isochrone, d_{10Gyr}, shown in Eq. 3.3.

$$\begin{aligned} & d_{10Gyr}(\mathrm{GC}_i|x,y;m) = \sqrt{d_x(\mathrm{GC}_i|m)^2 + d_y(\mathrm{GC}_i|m)^2}, \\ & d_x(\mathrm{GC}_i|m) = p_x(\mathrm{GC}_i) + p_x(10Gyr|m), \\ & d_y(\mathrm{GC}_i|m) = p_y(\mathrm{GC}_i) + p_y(10Gyr|m). \end{aligned} \tag{3.3}$$

Where x and y are two colours for a given colour-colour diagram, m an specific SSP model, and GC_i a given data point in the diagram. This quantity is constructed in such a way that when d_{10Gyr} is *positive* for a given object, it means that its observed colours are *redder* than a model 10 Gyr isochrone. When the d_{10Gyr} is negative, it means that its observed colours are *bluer* than the 10 Gyr isocrhone. Usually this means that positive values of d_{10Gyr} indicate younger ages and vice-versa. However, notice that in specific cases, such as in the *ugi* diagram, the opposite is true, given the disposition of model isocrhones. We calculate this quantity for all samples and models, except for the E-MILES α-enhanced model, due to the fact its limited metallicity range makes the comparison with other SSPs meaningless in terms of this distance. From Fig. 3.29 to 3.38 we show the $d_{10Gyr}(\mathrm{GC}_i|x,y;m)$ distribution for all models and environments, divided by samples and colour-colour diagrams. The top panel of each figure shows the kernel density estimate for the probability density distribution for all models for the full samples (odd numbered figures) and for each spatial bin (even numbered figures). Such density was calculated using a Gaussian kernel and scaled to a maximum of unity. The bottom panel of each figure shows the associate empirical cumulative distribution function (ECDF) for each SSP model. Finally, in the bottom right of the bottom panels, we show p-values for Kolmogorov-Smirnov (K-S) tests run for each pair of models in these figures. The null hypothesis states that a pair of models are likely drawn from the same distribution.

We assume a significance level of 0.05, i.e., we reject the null hypothesis when the p-values < 0.05. Under this circumstance, the K-S test indicates that the a model pair is statistically likely to indicate two different age estimates for the same colour-colour diagram and sample.

Differences between models with distinct abundance variations

When not dividing the GC samples in region bins, from Figs. 3.29 to 3.37 (odd numbered figures), the K-S tests indicate that the E-MILES base and ALF α-enhanced models d_{10Gyr} distributions are different in 66% out of the different combinations of samples and colour-colour diagrams. FSPS base and ALF α are different 86% of these combinations and the E-MILES base and FSPS base are different 53% of these combinations. In the situation that base and α-enhanced models are different based on the K-S tests, the α-enhanced models predict younger ages for the observed GC data independently of colour-colour diagram.

Moreover, we see that the shape of the d_{10Gyr} ECDFs do not vary between the three models. This indicates that the age spread in the GC samples as inferred by the models is the same, regardless of abundance variations. The same analysis shows that the P16 sample has a consistently shorter age spread when compared to the other GC samples. This is very clear, for instance, in the uiK_s colour space, shown in Fig. 3.29.

The effects of environment: Regions

In the even numbered figures from Fig 3.30 to 3.38, we find that the effects of ALF α-enhancement in the model age predictions are sensitive to separating our samples in different region bins. Out of all combinations of colour-colour diagrams and GC samples, the K-S tests indicate that E-MILES base and ALF models are different 66% of the time in region A, while 46% for region B and 20% in region C. Between FSPS base and ALF models, the K-S tests indicate differences 66% of time for region A, 86% for region B and never for region C. Finally, the K-S tests between E-MILES and FSPS base models show differences 60% of the time in region A, 40% of the time in region B and 20% of time in region C.

In the cases where the K-S tests indicate difference between α-enhanced and base models, in most of the colour-colour diagrams, the ALF α-enhanced SSPs indicate younger ages than the base models. The *ugi* diagram shows the opposite trend. When looking at the differences between samples, for the Virgo P16 and O&A16+Ks samples the model predictions are generally similar, although the P16 sample shows a larger difference between models with different abundance variations in region A.

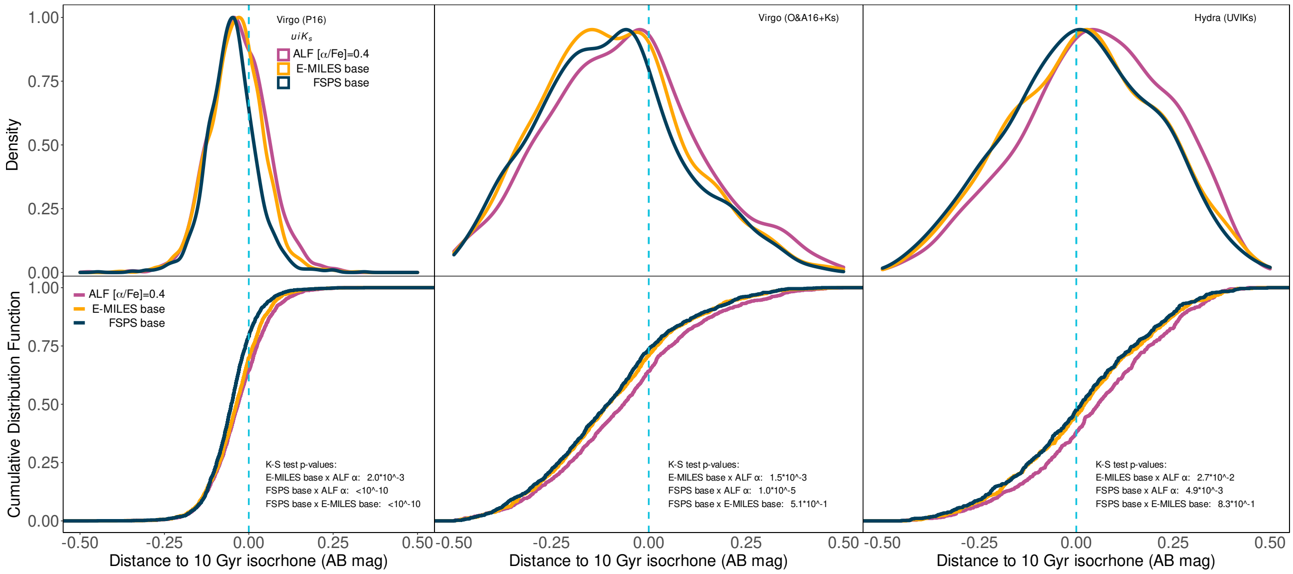

Figure 3.29: Comparison of the distributions of the distance (in magnitude) between to 10 Gyrs isocrhone from each GC candidate in the uiK_s diagram. We show such distribution for each of model tested in this work, except E-MILES α-enhanced for the full samples studied in this work. The leftmost panel shows the Virgo P16 sample, while the middle panel shows the Virgo O&A16+Ks sample and the rightmost panel shows the Hydra UVIKs sample. On the top panels we show kernel density estimates for the distributions. The bottom panels show the associated empirical cumulative distribution functions.

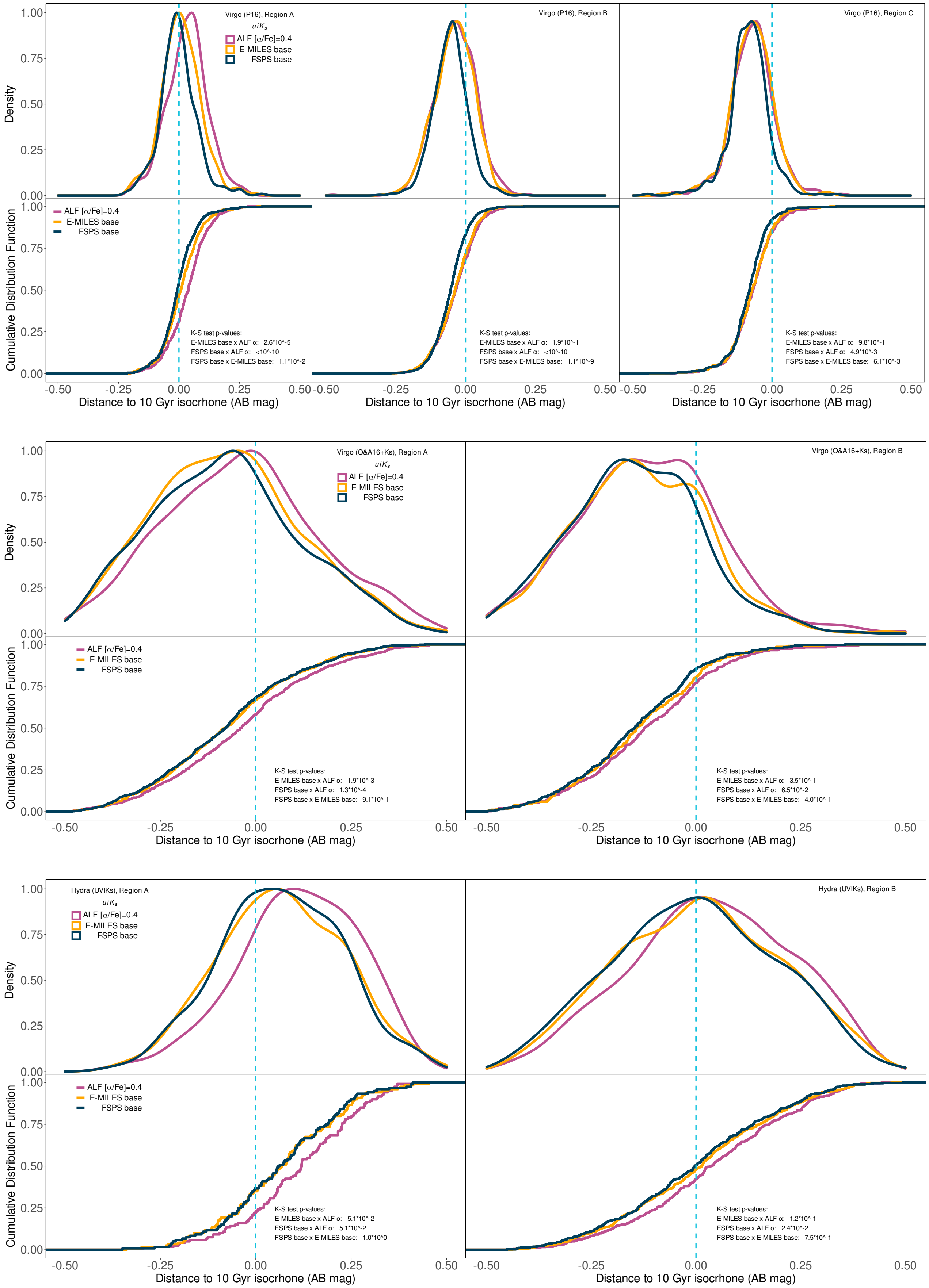

Figure 3.30: Same as Fig. 3.29, but for each sample tested in this work separated by the different spatial bins. From top to bottom, Virgo P16 sample, Virgo O&A16+Ks sample and the Hydra UVIKs sample.

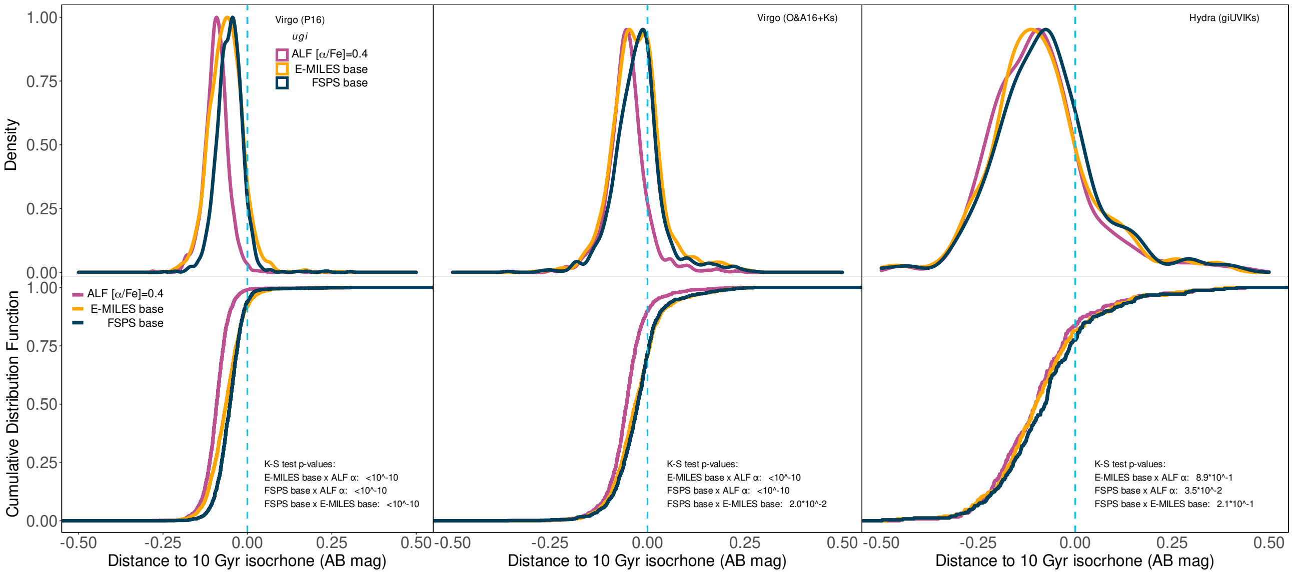

Figure 3.31: Same as Fig. 3.29, but for distances calculated in the *ugi* diagram.

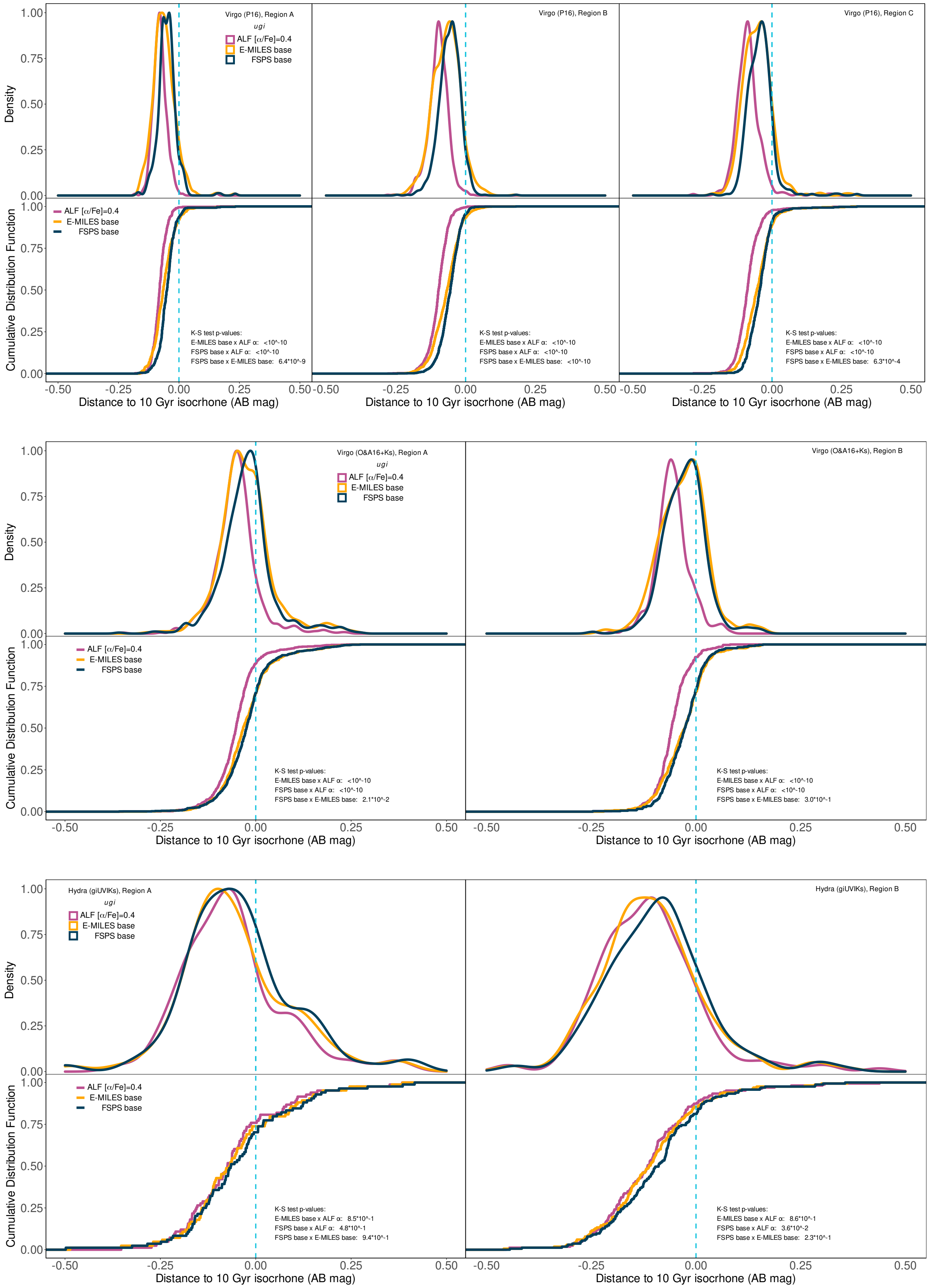

Figure 3.32: Same as Fig. 3.30, but for distances calculated in the *ugi* diagram.

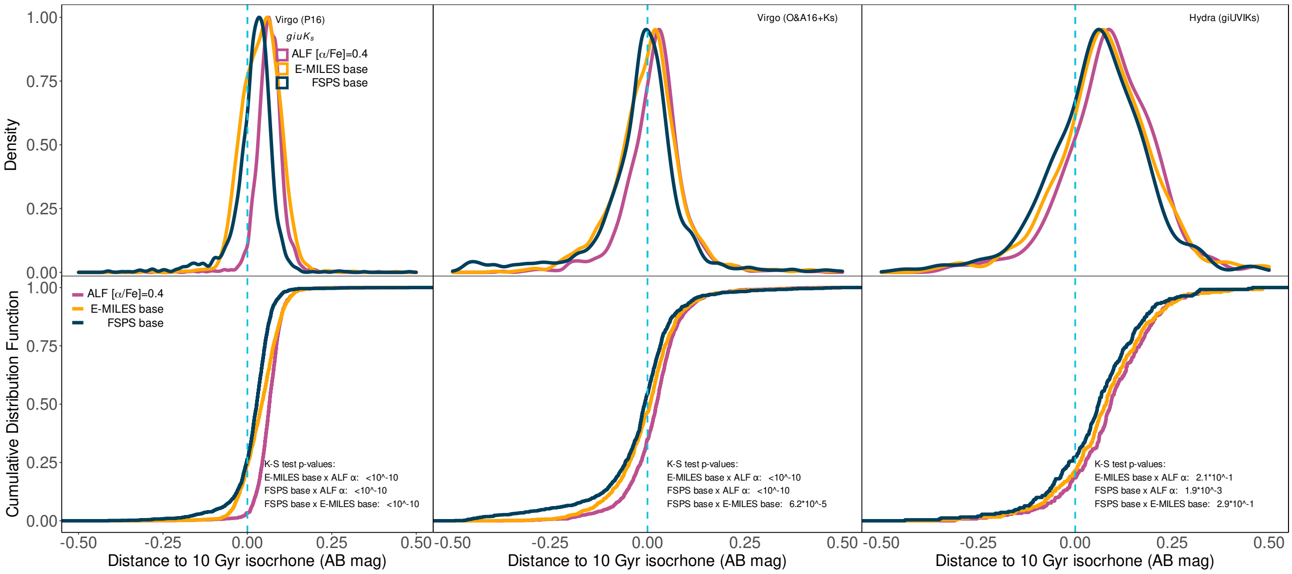

Figure 3.33: Same as Fig. 3.29, but for distances calculated in the $giuK_s$ diagram.

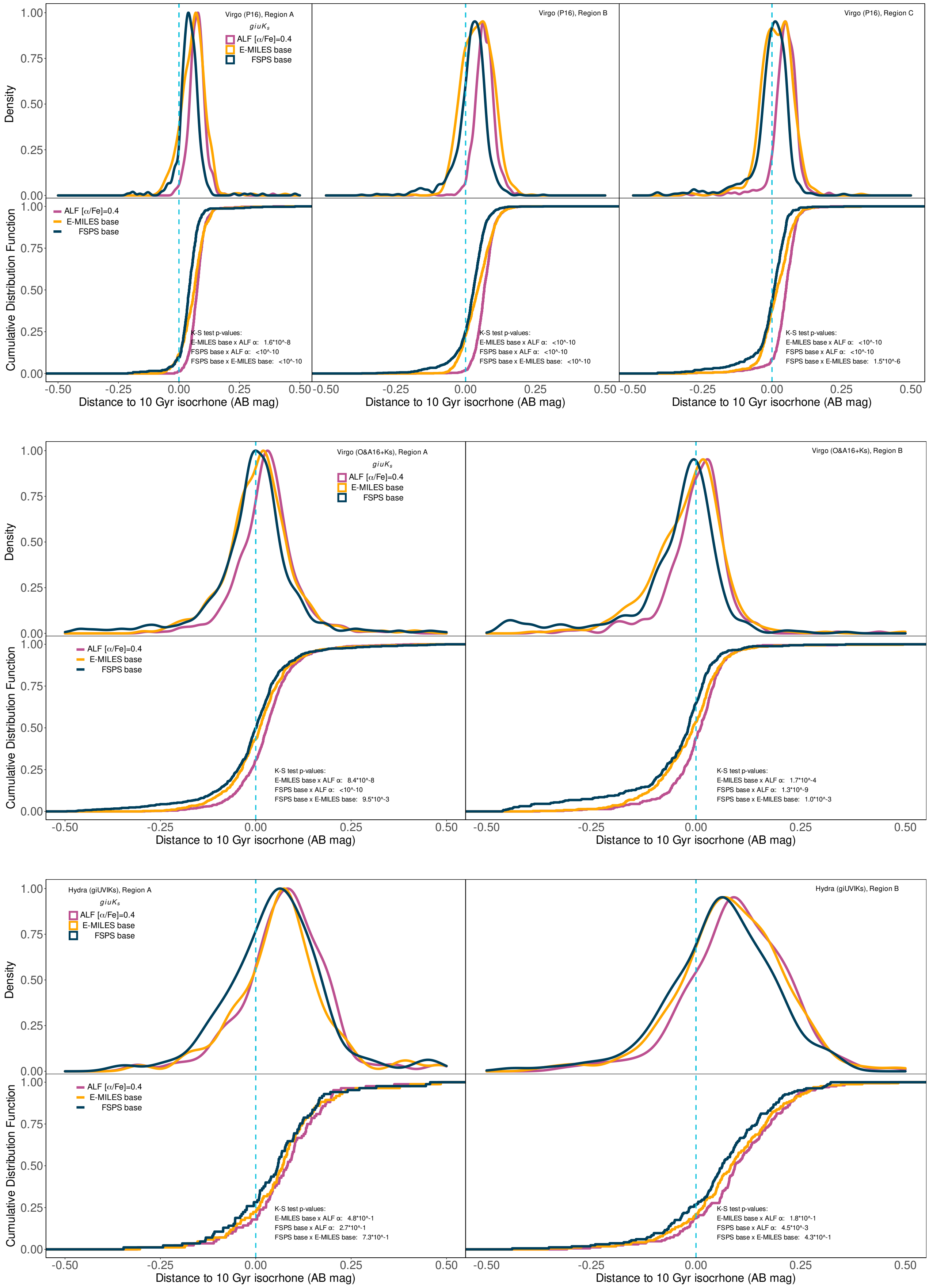

Figure 3.34: Same as Fig. 3.30, but for distances calculated in the $giuK_s$ diagram.

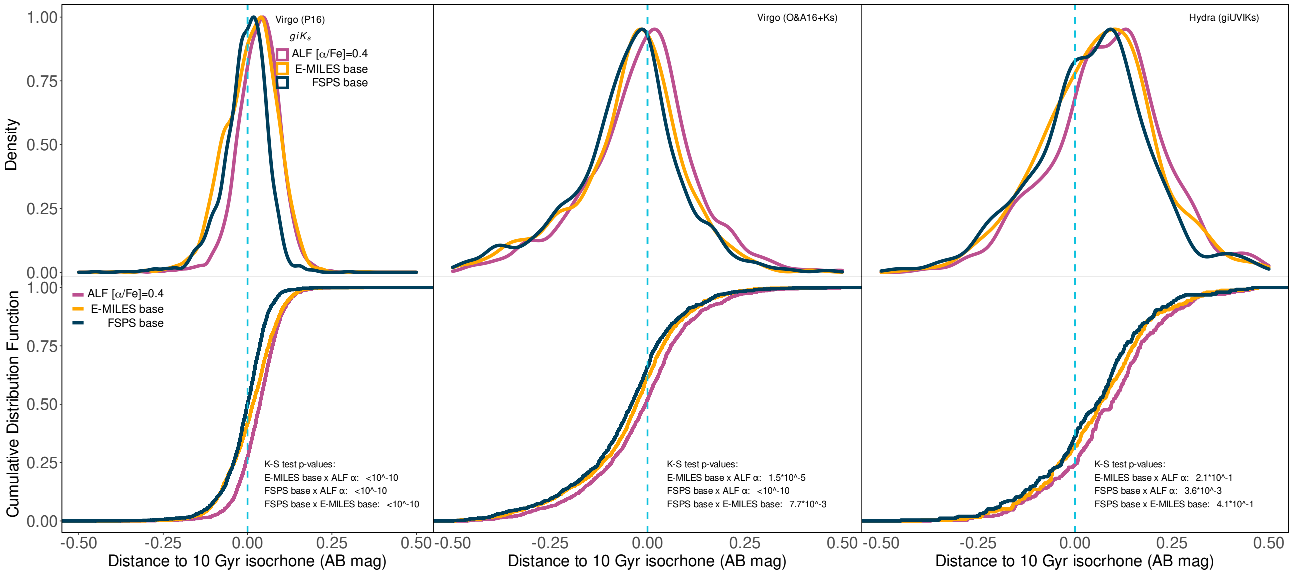

Figure 3.35: Same as Fig. 3.29, but for distances calculated in thegiK_s diagram.

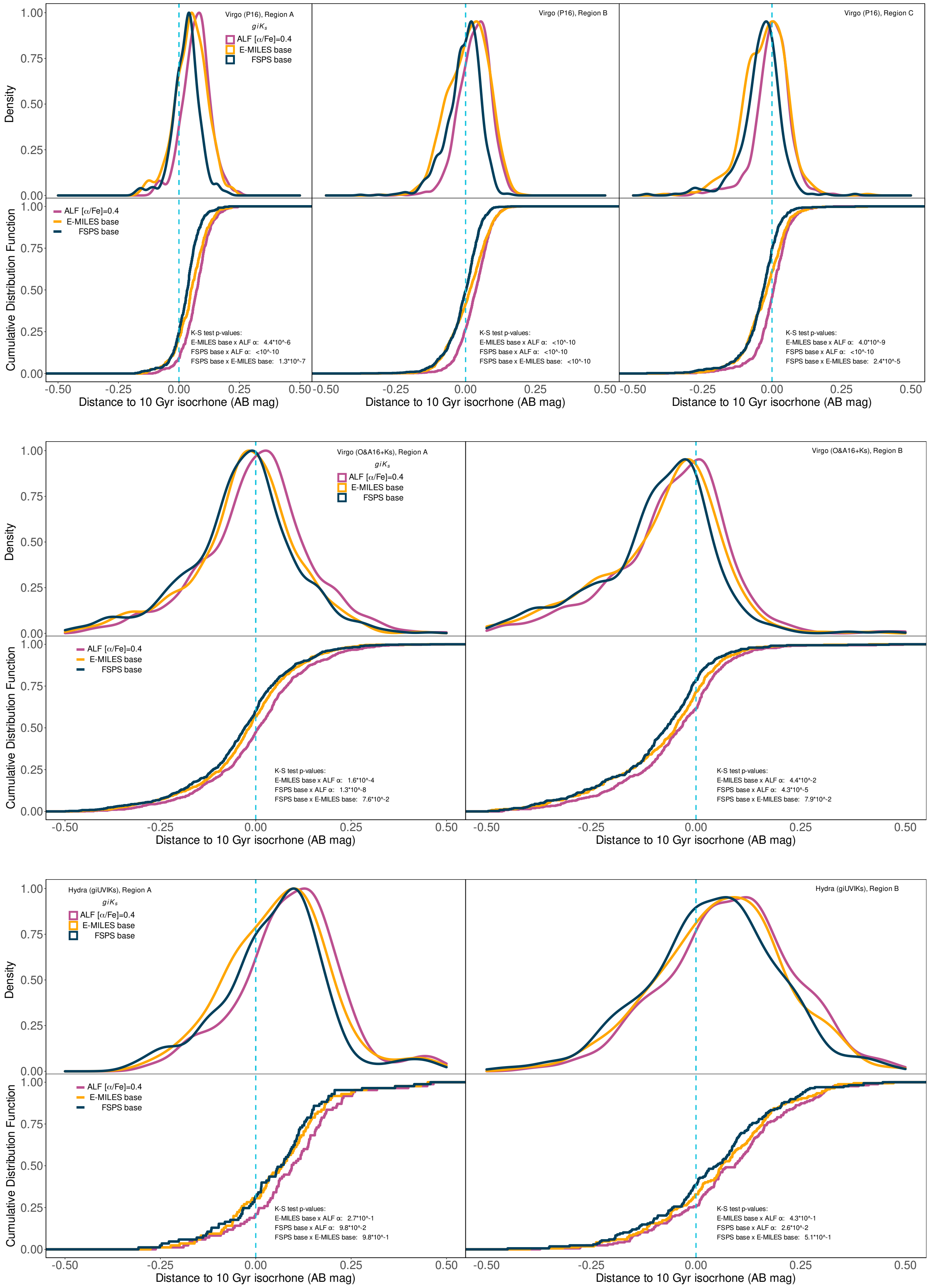

Figure 3.36: Same as Fig. 3.30, but for distances calculated in thegiK_s diagram.

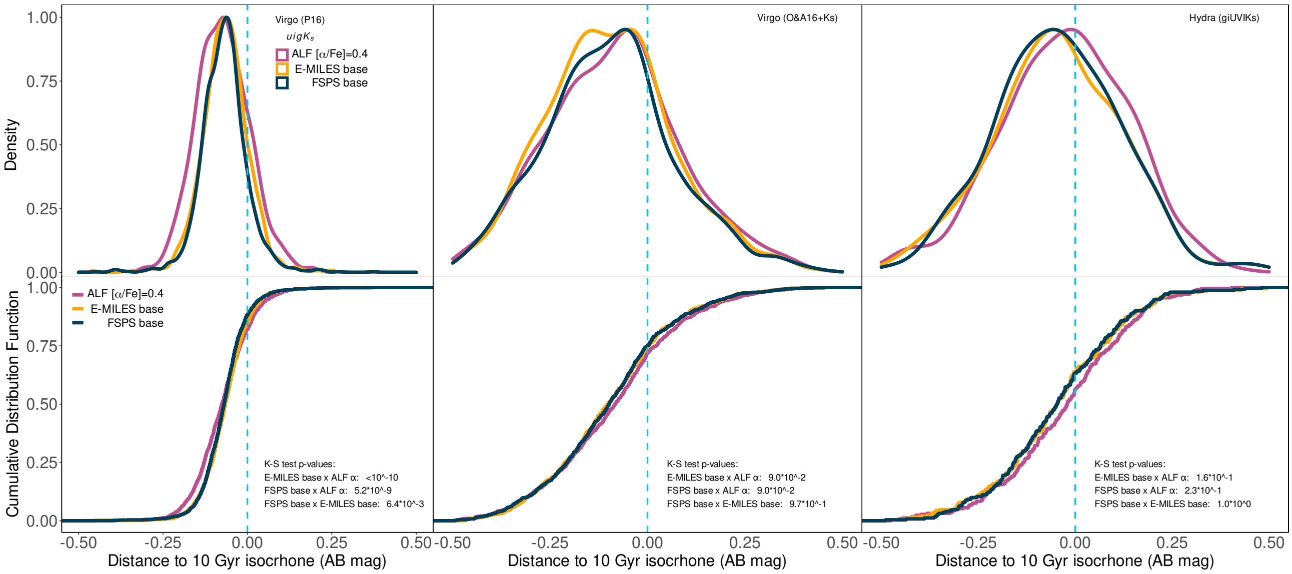

Figure 3.37: Same as Fig. 3.29, but for distances calculated in the $uigK_s$ diagram.

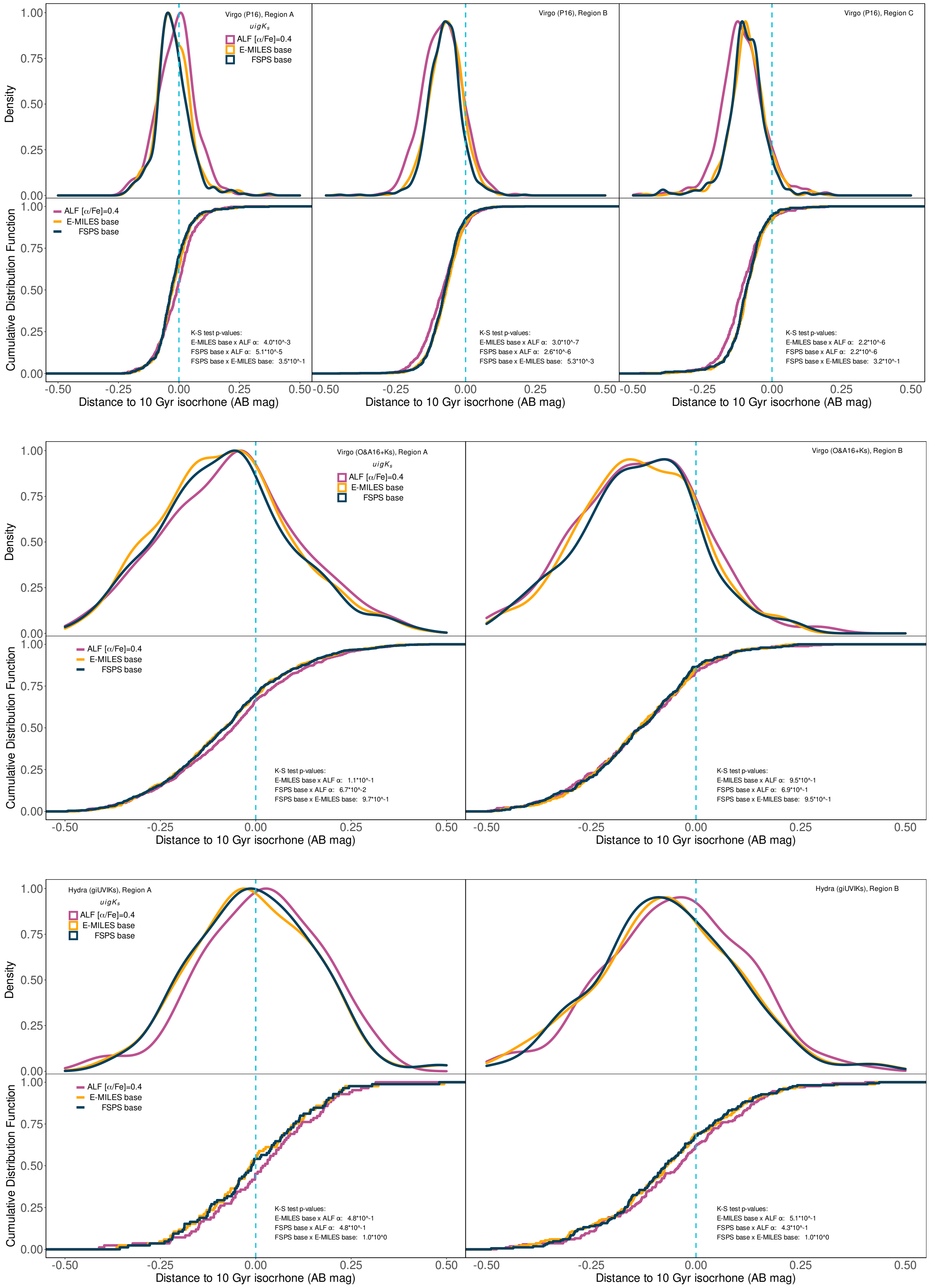

Figure 3.38: Same as Fig. 3.30, but for distances calculated in the $uigK_s$ diagram.

The effects of environment: Differences between Virgo and Hydra GCs

In Fig. 3.39 we show d_{10Gyr} kernel density estimates in several panels divided by Virgo and Hydra samples for each different model (columns) and colour-colour diagrams (rows). The Virgo sample in this figure comprises a sum of P16 and O&A16+Ks sample, except for repeated objects. Within each panel we also divide the samples into the different regions.

In all diagrams and models, we see evidences for Hydra having a younger GC population than Virgo. This feature is more easily noticeable in the uiK_s diagram, and the width of the Hydra GC sample density distributions is generally larger, suggesting a greater age range than the Virgo GC sample. This is interesting considering that there are evidences of an ongoing process of disruption of dwarf galaxies in the NGC 3311 halo (Arnaboldi et al., 2012; Coccato et al., 2011). These accreted dwarfs are likely to host GCs with ages and metallicities different from the original population, thus explaining, at least, the suggested large age range of Hydra GCs. However, improved SSP models, a larger GC sample size and/or follow-up spectroscopic samples are needed to further confirm or deny the age difference between Virgo and Hydra GCs. The Hydra giUVIKs sample is considerably more spatially extended than the Virgo GC samples used in this work, being more concentrated in region B ($2.8R_e < R_{GC} < 28.8R_e$), while the Virgo P16 and O&A16+Ks samples are more numerous in region A ($\leq 2.8R_e$). Nevertheless, we do not find consistent differences in the d_10Gyr distributions for the different regions, in both Hydra and Virgo GC samples, and regardless of the colour combinations employed. It is interesting to notice, however, that for the $uigK_s$ and uiK_s diagrams, two very age sensitive diagrams as mentioned previously in section 3.2, differences in region bins appear more clearly: Region A, for both Virgo and Hydra samples, shows a larger age spread than regions B and C, as well having the peak of the estimated age distributions centered around 10 Gyrs. Other regions show the peak of the density distributions shifted to the the left, negative values of d_{10Gyr}, suggesting GC ages greater than 10 Gyrs.

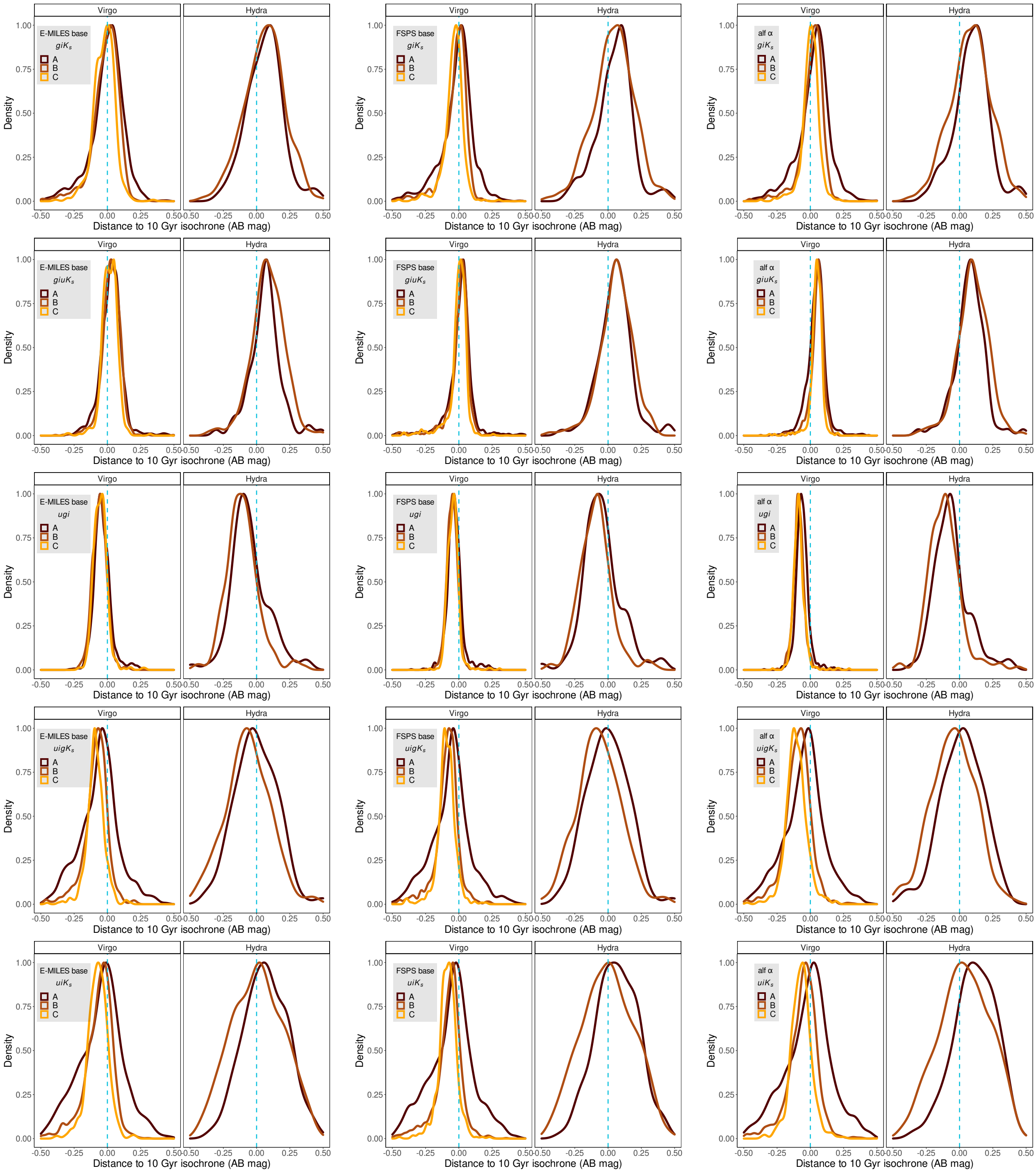

Figure 3.39: Comparison of the kernel density estimates for the distances to a 10 Gyr isocrhone for the Virgo and Hydra GCs, as per different models tested (columns) or colour-colour diagrams (rows). Positive or negative values for the distances indicate *redder* or *bluer* colours for the observed GC candidates than a given model 10 Gyr isochrone in a colour-colour diagram. This usually means that positive distances indicate ages *older* than 10 Gyrs and negative distances ages *younger*, but notice that the opposite is true for the *ugi* diagram, as by how the model isocrhones present themselves in such diagram.

3.4 Discussion

The results of section 3.3.1 show that all SSP models tested, regardless of [α/Fe] ratio, are inconsistent between their colour predictions for different colour-colour diagrams. This is in agreement with the results already presented by P16a; P16b (See also Chies-Santos et al., 2012b; Georgiev et al., 2012). In Powalka et al. (2017), age and metallicity estimations from 10 different SSP models in colour-colour diagrams for the P16 sample were compared using a maximum likelihood method. No models tested in their work accounted for specific abundance variations. Their results indicated a tendency for SSP models to assign younger ages for Virgo core GCs when compared to estimated ages for Milky-Way GCs. This pattern can be seen when we look into the SSP model predictions in a $griz$ diagram, such as in Fig. 3.12, where the youngest isochrones match a large portion of the observed GC colours. However, our results show that this is not consistent between all colour-colour diagrams if we take into consideration diagrams including colours constructed with the K_s-band. In diagrams such as uiK_s and $uigK_s$, our results show that the oldest isocrhones of the E-MILES and FSPS base models match more closely the smoothed regression of the observed GC colours of Virgo and Hydra GCs. This is also true for the E-MILES α-enhanced models, but the ALF α-enhanced SSPs are generally bluer than the smoothed linear distribution of the observed data.

There are several evidences for intermediate ages ($\sim$ 3-5 Gyrs) among extragalactic GCs, such as about 20% of the inner GC population of M87 (Montes et al., 2014), a few GCs in M31 (Puzia, 2005) and the variety of morphologies in the age/metallicity plane found for simulated disk galaxies in Kruijssen et al. (2019). However, the processes to form GCs later in time to explain a large amount of intermediate age ($\sim$ 3-5 Gyrs) objects in extragalactic samples of elliptical galaxies is not very well understood. Late mergers of gas-rich galaxies (Whitmore et al., 1993; Renaud and Gieles, 2015) could provide a source of renewed GC formation, but morphological evidences for major mergers disappear on small timescales of a few Gyr (Borne and Richstone, 1991) and there are no available detailed simulations to provide reliable constraints to the survival of GCs after major mergers occurring in high-density environments such as the core of the Virgo and Hydra clusters. Due to this, Powalka et al. (2017) argues that current SSP models indicate an excess in intermediate ages for Virgo GCs probably due to unsuitable assumptions for the synthetic stellar populations, stressing the fact that SSP models are able to match the expected old ages ($\geq$ 10 Gyrs) for Milky-Way GCs. Moreover, Powalka et al. (2017) tested only one colour with the K_s band, the $(g - K_s)$ colour, and concluded that the K_s band constraints might be diluted in the other colours and not affect the SSP colour estimations.

Our results show that, at least for the both tested E-MILES models and FSPS, SSPs are able to predict older ages in some – but not all – colour-colour diagrams constructed with colours using the K_s band. If we consider the fact that diagrams such as uiK_s are theorised to be good age indicators, this potentially shows both the power of these diagrams as good age indicators and the effectiveness of E-MILES models, both $alpha$-enhanced and base models, to better match the observed colours in these diagrams. The fact that FSPS and E-MILES models both show these improvements despite very different underlying spectral libraries shows how important the choice of colour-colour diagram impacts the age estimation with the current age SSP models.

In fact, when revisiting the environmental impact on the SSP and observed colour discrepancies noted by P16a, we find that it is also very dependent on the choice of colour-colour diagram. In section 3.3.2 we show that in the $griz$ diagram observed GCs for both the Virgo samples used in this work indeed more closely match the SSPs colour predictions in the outermost region bin, the C region ($\geq$ 200 Kpc from M87, or $28.8R_{e,M87}$), as presented in P16a. However, no such environmental differences are found for any other of the colour-colour diagrams tested in the present work. Therefore, we conclude that if such environmental effects exist in the SSP colour predictions, they are restricted to the range of the $griz$ filters. Investigating this question for the Hydra GCs show also not a significant difference between the two region bins we separated our available data for this environment in. However, we note the fact that the sample size for Hydra GCs is considerably smaller than the one available for Virgo GCs in this work, despite the two GC systems being estimated to host similar amounts of GCs. Therefore, some environment effects may be not evident in our analysis for Hydra GCs.

3.4.1 The impact of α-enhancement

As mentioned previously in section 3.2, the "base" abundance variation present for one of the E-MILES and for the FSPS model used in this work are based on the empirical abundance pattern present in the Milky-Way stars in the underlying stellar libraries of these models. This means that when we compare base and α-enhanced models in this work we are effectively comparing models with an anti-correlation between $[\alpha/\mathrm{Fe}]$ and metallicity and models with constant $[\alpha/\mathrm{Fe}]=0.4$ for all metallicities, even supersolar ones. While no work in the literature has pointed α-enhancement as the unique solution to match the current SSP models to observed extragalactic GC colours, it has been cited in many works as one of the most important steps towards improving SSP models to match the abundance patterns of GCs in other galaxies, specially in high-density environments such as the core of elliptical galaxies (Coelho et al., 2007; Lee et al., 2009; Coelho, 2014; Conroy and van Dokkum, 2012; Vazdekis et al., 2015; Conroy et al., 2018; Choi et al., 2019, to name a few).

Our results show that a constant enhancement of $[\alpha/\mathrm{Fe}]=0.4$ for supersolar metallicities does not consistently improve SSP colour predictions for extragalactic GCs, neither in the view of improving age/metallicity degeneracy problems, nor in the view of predicting more realistic age/metallicity estimations for the GCs in Virgo and Hydra systems across different colour-colour diagrams. In fact, as shown in section 3.3.3, when the ALF α-enhanced models age estimations are statistically significantly different from the base models, they are likely to indicate younger ages, with varying degrees between colour choices. Dividing the observed GC samples in different regions, we find also that the ALF α-enhanced models age estimations are more likely to be statistically different in the innermost regions (within $2.8R_e$, 20 Kpc for Virgo and 23.52 Kpc for Hydra). The GCs at the inner regions of elliptical galaxies are thought to be mostly metal-rich (Brodie and Strader, 2006). As base models are not α-enhanced at supersolar metallicities, if we consider the possibility of such inner GCs to be at least as α-enhanced as $[\alpha/\mathrm{Fe}] = 0.4$, then our results indicate they are likely to be younger than the GCs in outer regions. Recent simulations on GC formation at galactic scales from the E-MOSAICS project (Reina-Campos et al., 2019) indicate that metal-poor ($-2.5 < [\mathrm{Fe/H}] < -1.5$, at extended radii) and metal-rich (-1.0 < [Fe/H] < -0.5, at inner regions) GC subpopulations formed $\sim$ 12 and $\sim$ 10 Gyrs ago respectively, therefore indeed pointing to an younger innermost GC population[18]. Increased [α/Fe] ratios in the inner GC population would also mean that star formation in these high-density regions took place in several bursts instead of a continuous process. However, the spread in the observed colours for GCs in all environments and in all colour-colour diagrams suggest a larger age range which would be more likely result of a continuous process of star formation. This scenario is supported by GC formation simulations of Kruijssen (2015) and Reina-Campos et al. (2019), although in both cases the simulations are focused on Milky-Way-sized galaxies. In addition, P16b showed that the width range of observed GC colours, at least for the Virgo P16 sample, can not be explained only by random errors arising from photometric uncertainties. Therefore, although it is likely that the age ranges predicted by the comparison between models and colours is exaggerated to some extent, some degree of a continuous age distribution is real in the observed samples. Another possibility is that younger ages observed are actually effects of stellar evolution processes that are able to make a considerable portion of stars within GC populations to mimic colours associated with young ages (Chies-Santos et al., 2011a; Yoon et al., 2006). Among those are blue horizontal-branch populations due to peculiar helium abundances (Renzini et al., 2015) or strong winds on the red giant branch (González-Lópezlira et al., 2019), to name a few. In this context, we conclude that the differences detected between α-enhanced and base models, where it is statistically significant, are likely exaggerated or effects of abundance variations not accounted in the tested SSP models.

3.4.2 Perspectives on future improvement of SSP models regarding abundance variations

The E-MILES α-enhanced models at the current time have a limited metallicity range, which severely constrains analysis of extragalactic GCs. However, its predictions overall seem to better match the observed colours in the available metallicity range on some aspects, when compared to the base models and even to ALF α-enhanced models. For instance, E-MILES α-

---

[18] It is important to note that Reina-Campos et al. (2019) results also indicate that there is a significant amount of metal-rich GCs at extended radii in the simulated galaxies

enhanced models colour predictions show less effects of age/metallicity degeneracy in almost all colour-colour diagrams tested, as well as predicting redder colours than the other models. The latter feature enables the E-MILES α-enhanced models to better match the observed colours for Virgo and Hydra GCs in the innermost region, where all the other models tested struggle to match the redder colours of Virgo and Hydra GCs compared to the colours of Milky-Way GCs (P16a). Fortunately, Knowles et al. (2021) just recently released a new MILES α-enhanced stellar library which will likely result in the release of a new version of E-MILES α-enhanced models with a more flexible metallicity range.

In general, it is clear that SSP models need to address several problems in initial theoretical assumptions and the range of available underlying stellar libraries to better match extragalactic GC colours. Additional abundance variations over the α-enhancement are needed to be included, such as C and N variations, as proposed in Choi et al. (2019) to better match the colours of quiescent galaxies (and also mentioned in Georgy et al., 2013; Vazdekis et al., 2015; Dotter et al., 2017; Conroy et al., 2018, to name a few). Furthermore, additional work is needed to further understand complicated phases of stellar evolution associated with strong NIR indices (Baldwin et al., 2018; Riffel et al., 2019). Additionally, it is important to consider that when looking at extragalactic GCs in the core of elliptical galaxies we are inevitably observing very massive and bright GCs, simply by the fact that they are the more easily detected. Some of theses objects are even likely remnant galactic nuclei from accreted satellites (Ferrarese et al., 2016; Neumayer et al., 2020). The most massive Milky-Way GCs are known to display multiple stellar populations, hence it is unlikely that this class of object is correctly described by abundances and ages with a single value (Piotto et al., 2015; Renzini et al., 2015).

3.5 Summary and Conclusions

In this chapter we investigated the impact of α-enhancement in the difficulties of current state-of-the-art SSP models to properly predict GC colours, first presented in P16a; P16b for Virgo GCs. We presented new photometry from VLT/HAWKI for Virgo and Hydra GCs in the

K_s band. By matching our K_s GC catalogues with photometric data from the literature, we used NUV to the NIR of GC candidates in the core of both the Virgo and Hydra clusters to access the colour predictions of four different SSP models. Such models were the E-MILES and FSPS models with abundances based on the ones from Milky-Way stars (i.e., with increasing [α/Fe] ratio for subsolar metallicities) and the E-MILES and ALF generated models with a constant value of [α/Fe]=0.4 for all metallicities. Furthermore, we investigated the environment variations in such discrepancies as shown in P16a to be present for Virgo GCs.

- When compared to the GC sample for Virgo studied by P16a, the Virgo GC data presented in this work with the new VLT/HAWK-I K_s-band imaging has a considerably more precise magnitudes, larger sample size and hence a more complete GC sample, specially at the innermost regions.

- We found that, regardless of abundance variations, SSP models present no consistent colour predictions across different colour-colour diagrams. Powalka et al. (2017) found a consistent pattern of SSP models predicting younger ages than expected for GCs at the high-density regions of elliptical galaxies (e.g., Cohen et al., 1998; Chies-Santos et al., 2011c; Strader et al., 2011), but our results show that such age predictions are more inconsistent when we look into colour-colour diagrams using colours constructed with a combination of NUV/optical and NIR filters and for the E-MILES, FSPS and ALF-generated SSP models.

- We revisited the P16a analysis of variations in the SSP models colour predictions discrepancies in different region bins for Virgo GCs, this time with an improved Virgo GC photometry and the addition of a sample of GCs in the Hydra cluster. Our results show that the environmental effect claimed in P16a is largely dependent on the choice of colour-colour diagram, being almost negligible in diagrams which colours includes the K_s band.

- We quantify whether or not there is significant differences by analysing the distribution of the distance to a 10 Gyr isochrone for every object in each colour-colour diagram and for each model tested. We find that when there is significant difference in the distance to a 10 Gyr isochrone distribution for ALF α-enhanced model compared to base models, most of the time the α-enhanced models predict younger ages than the base models. This can be due to several reasons, from problems in the theoretical assumptions and stellar libraries underlying the α-enhanced models, to actual age spreads in the GC samples, to old stellar populations whose colours mimic those of younger populations by means of effects such as an extended blue horizontal-branch CMD morphology. Whether or not this difference in age predictions based on α-enhanced models is real or not depends on the actual abundances present in the stellar populations of Hydra and Virgo GCs.

- Analysing the distribution of distances to a 10 Gyr isocrhone for the models tested. in regards to the difference between the Virgo and Hydra GC samples, we found evidences for a younger GC population in Hydra when compared to Virgo. This might be related to detected ongoing assembly of NGC 3311 halo, by the accretion and disruption of dwarf galaxies (Arnaboldi et al., 2012; Coccato et al., 2011). The eventual accretion of GCs from this process into the NGC 3311 system are likely to increase the observed diversity in ages. However, improved SSP models and follow-up observations are needed to further investigate this evidence.

- Finally, we conclude that while an increased [α/Fe] ratio is discussed in the literature as one of the most prominent aspects where SSP models need to improve to match observed extragalactic GC colours, most likely several other aspects need to be improved in the SSP model assumptions and underlying stellar libraries.

To summarise, we hope that the ideas and results introduced in this work pave the way to a more constrained exploration of extragalactic stellar clusters with data from the next generation of telescopes, such as EUCLID, Nancy Grace Roman, Chinese Space Station Telescope (CSST) and ground-based Vera Rubin and J-PAS. Such next age of astronomy will provide unprecedented and homogeneous amounts of multi-band GC data not only more spatially precise, but also extended to NIR wavelengths with unmatched precision when compared to current available technologies. Therefore, at this stage, it is crucial to investigate the limitations of current SSP models regarding both chemical abundances and NIR wavelengths.

Chapter 4

Summary and Concluding Remarks

The central subject of this thesis was the investigation of extragalactic stellar clusters, specifically GCs and NSCs, in high density environments. This thesis was divided into two main chapters.

First, we investigated the presence of NSCs in galaxies of all environments where nucleation data is available in the literature. The main results of this work, published in Zanatta et al. (2021), are:

- We used HST images for the central regions of the Coma Cluster, a robust photometry technique and hierarchical Bayesian logistic regression to find that the fraction of galaxies in Coma hosting an NSC is higher than in all other environments where similar data is available.
- Such finding implies an environmental dependence on the nucleation fraction that is not clearly explained by the current proposed formation scenarios for NSCs.
- We discuss these findings in regards to the influence of environment and galaxy mass, finding evidences that the nucleation fraction for a given environment is linearly related to the cluster/group dark matter halo mass.

Secondly we investigated the difficulties of the current generation of SSP models to predict the colours of extragalactic GCs and tested the impact of abundance variations, specifically the currently available α-enhanced SSP models in the literature. We also tested the effect of environment by comparing the data of GCs in the central elliptical galaxies of the Virgo and Hydra Clusters. The main results of this work are:

- We revisit the findings of Powalka et al. (2016b,a) regarding the discrepancies in colour predictions between current SSP models and GCs in the Virgo cluster, and how these discrepancies vary with distance to the host galaxy. We extend the analysis to GCs in the Hydra cluster, introducing new deep K_s band data from the VLT/HAWK-I instrument for GC candidates in the innermost regions of Virgo and Hydra.

- We test four different state-of-the-art SSP models with abundance variations matching those of stars in the Milky-Way (that we defined as "base" abundances) as well as SSP models with a constant [α/Fe] ratio of 0.4 for all available metallicities. We use several colour-colour diagrams and the distributions of distances to a 10 Gyr isocrhone in each model and diagram.

- We find that where α-enhanced models predict ages significantly differently than base models, this difference is generally towards younger ages than expected for GCs at the core of elliptical galaxies. Moreover, the SSP models predictions, regardless of abundance variations, are not consistent between different colour-colour diagrams.

- We revisited the P16a analysis of variations in the SSP models colour predictions discrepancies in different region bins for Virgo GCs, this time with an improved Virgo GC photometry and the addition of a GC sample in the Hydra cluster. Our results show that the environmental effect claimed in P16a is largely dependent on the choice of colour-colour diagram, being almost negligible in diagrams which colours include the K_s band.

- We find evidences of a younger GC population in Hydra when compared to Virgo. This might be related to detected ongoing assembly of the NGC 3311 halo, by the accretion and disruption of dwarf galaxies previously observationally detected (Arnaboldi et al., 2012; Coccato et al., 2011). However, improved SSP models and follow-up observations are needed to further investigate this evidence.

4.1 Perspectives

Future work regarding chapter 2, involves the application of the same photometric and statistical techniques to other environments, specially the ones even more dense than the Coma Cluster. This will enable us to access whether or not the increase in nucleation fraction is actually related to environmental density. The immediate follow-up to the work presented in this thesis will comprise already observed and publicly available HST data from the galaxy cluster A3558, which lies at the centre of the Shapley supercluster and is one of the richest galaxy clusters known, as well as its neighbouring clusters A3558 and A1736.

Furthermore, the Euclid mission will be launched in late 2022 and provide data as deep as the HST, but for a significantly larger FOV. This will enable the detection of low surface brightness galaxies in virtually every galaxy group or cluster within 12 Mpc, opening the possibilities for the analysis of the nucleation fraction in low-density environments. This will further complete the panorama of possible environment densities after we have finished working on the nucleation fraction in the high-density Shapley supercluster. All the methods and software employed in the nucleation fraction analysis with HST data will be able to be easily adapted to work on Euclid data.

Regarding the colour predictions of extragalactic GCs by SSP models, future work involves testing difference abundance variations, specially C and N. This is possible to be tested using ALF-generated models, since they allow for this specific abundance variations. Also interesting to be tested are different configurations of the FSPS models, specially different HB morphologies. It is also important to include data from other environments in different galaxies and clusters, such that any environment aspect of the discrepancies between colour and models can help further constraint where the next steps in their improvement needs to be. To this end, we already have available VLT/HAWK-I K_s data for the galaxy NGC 3962, an isolated elliptical galaxy in the direction of the Crater constellation. Moreover, we also plan on using the data for Hydra and Virgo GCs presented in this work to study the relation between metallicity and colour bimodality. The motivation for this is non-linear relation between metallicity and colours observed in extragalactic GC systems (Villaume et al., 2019; Blakeslee et al., 2012; Chies-Santos et al., 2011a). In this context, the $ugrizK_s$ central Virgo data and the $giuK_s$ central Hydra data presented in this work have the potential to help unravel important clues. Optical-NIR colors have been shown to be better proxies of metallicity than optical colours alone. An obvious next step is to analyse the optical/NIR colours of the Virgo and Hydra samples presented in section 3.1.

In summary, this work aims at providing groundwork ideas and results paving the way towards extragalactic stellar cluster studies with data from the next generation of telescopes. Telescopes such as: the Nancy Grace Roman, the Chinese Space Station Telescope (CSST) and ground-based Vera Rubin and J-PAS, to name a few, will provide unprecedented amounts of extragalactic GC photometric data. Therefore, at this stage, it is crucial to investigate the limitations of SSP models regarding their colour predictions. Moreover, in this work robust photometric and statistical techniques were developed to better model NSC occupation statistics in galaxy clusters and groups, which provide important clues to how star clusters in general form and evolve.

Appendices

Appendix A

Papers

The analysis of the impact of currently available α-enhanced SSP models in the predicted colours for GCs in the Virgo and Hydra cluster will be submitted to MNRAS in the first months of 2022, after revision by co-authors. The VLT/HAWK-I K_s band GC candidate catalogues for the Hydra and Virgo observations presented in Section 3.1 will be made public at CDS/Vizier (Wenger et al., 2000).

The article "A high occurrence of nuclear star clusters in faint Coma galaxies, and the roles of mass and environment" has been accepted and published in the MNRAS (Zanatta et al., 2021, https://doi.org/10.1093/mnras/stab2348). The catalogue of faint Coma galaxies and the nucleation information presented in Table 2.2 will be made public in machine readable form at CDS/Vizier.

Monthly Notices
of the
ROYAL ASTRONOMICAL SOCIETY

MNRAS **508,** 986–998 (2021)
Advance Access publication 2021 August 23

https://doi.org/10.1093/mnras/stab2348

A high occurrence of nuclear star clusters in faint Coma galaxies, and the roles of mass and environment

Emílio Zanatta ,[1★] Rubén Sánchez-Janssen,[2] Ana L. Chies-Santos ,[1] Rafael S. de Souza[3]
and John P. Blakeslee[4,5]

[1] *Departamento de Astronomia, Instituto de Física, Universidade Federal do Rio Grande do Sul, Porto Alegre, RS, 91509-900, Brazil*
[2] *STFC UK Astronomy Technology Centre, Royal Observatory, Blackford Hill, Edinburgh EH9 3HJ, UK*
[3] *Key Laboratory for Research in Galaxies and Cosmology, Shanghai Astronomical Observatory, Chinese Academy of Sciences, 80 Nandan Road, Shanghai 200030, China*
[4] *Herzberg Astronomy and Astrophysics Research Centre, National Research Council of Canada, Victoria, BC V9E 2E7, Canada*
[5] *Gemini Observatory, NSF's NOIRLab, Tucson, AZ 85719, USA*

Accepted 2021 August 10. Received 2021 August 2; in original form 2021 February 24

ABSTRACT

We use deep high-resolution *Hubble Space Telescope* (*HST*)/Advanced Camera for Surveys (ACS) imaging of two fields in the core of the Coma Cluster to investigate the occurrence of nuclear star clusters (NSCs) in quiescent dwarf galaxies as faint as $M_I = -10$ mag. We employ a hierarchical Bayesian logistic regression framework to model the faint end of the nucleation fraction ($f_{\rm n}$) as a function of both galaxy luminosity and environment. We find that $f_{\rm n}$ is remarkably high in Coma: at $M_I \approx -13$ mag half of the cluster dwarfs still host prominent NSCs. Comparison with dwarf systems in nearby clusters and groups shows that, within the uncertainties, the rate at which the probability of nucleation varies with galaxy luminosity is nearly universal. On the other hand, the fraction of nucleated galaxies at fixed luminosity does exhibit an environmental dependence. More massive environments feature higher nucleation fractions and fainter values of the half-nucleation luminosity, which roughly scales with host halo virial mass as $L_{I,f_{\rm n50}} \propto \mathcal{M}_{200}^{-0.2}$. Our results reinforce the role of galaxy luminosity/mass as a major driver of the efficiency of NSC formation and also indicate a clear secondary dependence on the environment, hence paving the way to more refined theoretical models.

Key words: galaxies: dwarf – galaxies: evolution – galaxies: nuclei – galaxies: photometry.

1 INTRODUCTION

At the central regions of galaxies of a wide range of masses, luminosities, and morphological types there exists a class of compact stellar systems known as nuclear star clusters (NSCs). These objects have half-light radii in the range of 1–50 pc, masses from 10^4 to $10^8\ \mathcal{M}_\odot$, and very extreme stellar densities comparable to globular clusters (GCs) and ultracompact dwarfs (UCDs) – but differ from these other compact systems in that they can exhibit a wide range of ages and metallicities. For a detailed overview of their properties we refer the reader to the comprehensive review by Neumayer, Seth & Böker (2020).

The formation of NSCs has been suggested to derive from two mechanisms, probably non-exclusive. One is a dissipationless process where already formed stellar clusters decay to the centre of the gravitational potential of the host galaxy and merge forming a large and dense structure (Tremaine, Ostriker & Spitzer 1975; Arca-Sedda & Capuzzo-Dolcetta 2014; Gnedin, Ostriker & Tremaine 2014). The other mechanism involves the inflow of gas to the central region of galaxies, where local star formation is triggered at higher rates than usual contributing substantially to their mass growth (Bekki et al. 2003; Bekki & Chiba 2004; Antonini 2013). Not surprisingly, NSCs display a variety of scaling relations with their host galaxies involving both their stellar mass (Scott & Graham 2013; Georgiev et al. 2016) and stellar populations (Walcher et al. 2005; Turner et al. 2012; Georgiev & Böker 2014). Finally, if GCs are suggested to contribute to the formation of NSCs, UCDs on the other hand might be the remains of disrupted nucleated galaxies (Drinkwater et al. 2003; Pfeffer & Baumgardt 2013; Seth et al. 2014; Afanasiev et al. 2018; Ahn et al. 2018; Neumayer et al. 2020).

Amongst the most fundamental observables informing NSC formation scenarios are their occupation statistics. In other words, what galaxies host NSCs? Stellar nuclei occur almost across the entire spectrum of galaxy types. Historically, much of the early work on NSC demographics focused on galaxies in high-density environments such as galaxy clusters, where number statistics are large. As a result, NSC occupation in early-type galaxies tends to be more robustly characterized than in late types (but for details on star-forming hosts see Carollo, Stiavelli & Mack 1998; Georgiev et al. 2009; Georgiev & Böker 2014; Neumayer et al. 2020). Recent studies have established that the nucleation fraction in quiescent galaxies exhibits a strong dependence on galaxy mass or luminosity, with a peak at ∼90 per cent around $\log(\mathcal{M}/\mathcal{M}_\odot) \approx 9$ followed by a steady decline toward both higher (Cote et al. 2006; Turner et al. 2012;

[★] E-mail: emiliojbzanatta@ufrgs.br

Published by Oxford University Press on behalf of Royal Astronomical Society

Baldassare et al. 2014) and lower galaxy masses (den Brok et al. 2014; Ordenes-Briceño et al. 2018; Sánchez-Janssen et al. 2019b). Remarkably, while NSC occupation at the high-mass end seems to be rather universal, dwarf galaxies ($\mathcal{M}_{\odot} \lesssim 10^9$) are now known to display a secondary dependence with the environment. By comparing the nucleation fraction from the Next Generation Virgo Cluster Survey (NGVS) with the literature data for other environments, Sánchez-Janssen et al. (2019b) show that NSC occurrence is highest in Coma Cluster dwarfs, followed by Virgo and Fornax, with the lowest nucleation fraction found in early-type satellites in the Local Group. This is consistent with early results showing that nucleated early types tend to inhabit the inner, higher density regions of the Virgo Cluster (Ferguson & Sandage 1989; Lisker et al. 2007). But Sánchez-Janssen et al. (2019b) expand on these studies to show that the behaviour holds at fixed galaxy mass, i.e. dwarfs of any given luminosity have a higher probability of being nucleated when they inhabit host haloes of larger virial masses. A shortcoming of that analysis is that the limiting magnitude of the Coma Cluster sample (den Brok et al. 2014, hereafter dB14) is significantly brighter than in all the other environments: $M_I \approx -13$ versus $M_I \approx -9$, well over an order of magnitude in luminosity. As a result, the exact behaviour of the nucleation fraction in this most rich environment is not yet fully characterized – does it remain exceptionally high down to the faintest luminosities, or does nucleation become negligible for galaxies of comparable luminosity to those in the Virgo and Fornax Cluster? This work aims at finally settling this question through the use of deep *Hubble Space Telescope* (*HST*)/Advanced Camera for Surveys (ACS) imaging of the core of the Coma Cluster to study the demographics of NSCs. We also develop a novel Bayesian logistic regression framework to model the probability of nucleation, which enables us to self-consistently investigate its dependence on galaxy luminosity and environment for dwarfs in other clusters and groups.

This paper is structured as follows. In Section 2, we present the data used in this work, followed by a detailed description of the galaxy and NSC detection and measurement techniques in Section 3. In Section 4, we present the statistical methodology developed to infer the nucleation fraction in Coma, which is compared to that of other environments in Section 5. In Section 6, we discuss the main results within the context of observational and theoretical work on the galaxy nucleation fraction. Finally, in Section 7, we summarize our results and their significance for NSC formation scenarios. Throughout this work we adopt a distance to the Coma Cluster of $D = 100$ Mpc (Carter et al. 2008), which corresponds to a physical scale of 485 pc arcsec^{-1} and a distance modulus of $(m - M) = 35$ mag.

2 DATA

The Coma Cluster data used in this work were obtained as part of Program GO-11711 (PI: J. Blakeslee) using the ACS/Wide Field Channel (WFC) onboard the *HST* in 2012 March, and consists of two fields centred on the bright cD galaxies NGC 4874 and NGC 4889. The observations run for four orbits with the F814W filter ($\approx I$) and one orbit with the F475W filter ($\approx g$). As a result, the former data set is considerably deeper than the latter, and only the I data are used throughout. The exposure times in I are 10 425 and 9960 s for NGC 4874 and NGC 4889, respectively.

The data for NGC 4874 were used previously in Cho et al. (2016) and we refer the reader to that work for additional details on the reduction steps, which are the same for the NGC 4889 field. Briefly, the images were dithered to fill the gap between the two ACS/WFC detectors, followed the standard pipeline processing from the Space Telescope Science Institute (STScI)/Mikulski Archive for Space Telescopes (MAST), and had the charge transfer efficiency (CTE) correction algorithm of Anderson & Bedin (2010) applied. Finally, the CTE-corrected exposures were then processed with APSIS (Blakeslee et al. 2003) to produce the final corrected images shown in Fig. 1.

The reference data set for NSCs in the Coma Cluster was introduced in dB14, with imaging from the *HST*/ACS Coma Cluster Survey (Carter et al. 2008). This study and that work are highly complementary. dB14 cover a large footprint and have robust number statistics at the bright end of the dwarf galaxy population ($M_I < -13$). On the other hand, this work is limited to two ACS fields, but our deeper imaging – reaching $M_I \approx -10$ in comparison to the limiting magnitude of $M_I \approx -13$ of dB14 – allows us to probe much fainter galaxies and NSCs than ever before in Coma. In Fig. 2, we present a comparison between the I-band images used in this work and those from dB14. The top row corresponds to a nucleated galaxy, whereas the bottom one shows a non-nucleated dwarf. The higher signal-to-noise ratio (SNR) in our frames significantly improves on the detection and characterization of NSCs and, especially, their low surface brightness hosts.

2.1 NSCs in other environments from the literature

In addition to the Coma Cluster, in this work we also analyse data for dwarf quiescent galaxies in the Virgo Cluster (from Sánchez-Janssen et al. 2019b), the Fornax Cluster (from Muñoz et al. 2015), and a collection of data for faint quiescent satellites in the local volume ($D < 12$ Mpc). The latter data set is mainly drawn from Carlsten et. al. (2020a), and further complemented with data from Chies-Santos et al. (in preparation) for dwarf companions of NGC 3115. An important aspect of all these data sets is that they all feature roughly the same effective spatial resolution. This is a result of the superbly narrow point spread function (PSF) delivered by *HST* that more than compensates for the much larger distance of the Coma Cluster – and we therefore expect the NSC detection efficiency to be similar across the different environments. Moreover, the effective *HST*/ACS PSF full width at half-maximum (FWHM) in Coma is $\approx$37.92 pc. NSCs in early-type dwarfs have typical sizes of $\lesssim$20 pc (Cote et al. 2006; Turner et al. 2012), therefore at the distance of Coma they are all essentially unresolved in our images.

As noted before, only early-type dwarfs are considered in the analysis. This is to avoid complications related to both the morphology–density relation and the notoriously difficult task of identifying NSCs in star-forming galaxies due to the presence of star formation and obscuration by dust. More details on the literature data used in this work are presented in Appendix A.

With this choice of environments we are able to probe NSC occupation in host haloes with masses ranging from 5×10^{15} in Coma to $10^{12}\mathcal{M}_{\odot}$ in the local volume. When necessary, adopted mass estimates come from Łokas & Mamon (2003), McLaughlin (1999), and Drinkwater, Gregg & Colless (2001) for Coma, Virgo, and Fornax, respectively. For the local volume galaxies we derive a mean halo mass using the $\log(V_{\rm circ})$–$\log(\mathcal{M}_{200})$ relation from the Illustris TNG100 simulations (Pillepich et al. 2018) and the $V_{\rm circ}$ values in table 1 of Carlsten et. al. (2020a). Exceptions are NGC 3115, for which the halo mass estimate comes from Alabi et al. (2017); M81, from Karachentsev et al. (2002); Cen A, from van den Bergh (2000); M31, from Tamm et al. (2012); and the Milky Way, from Taylor et al. (2016).

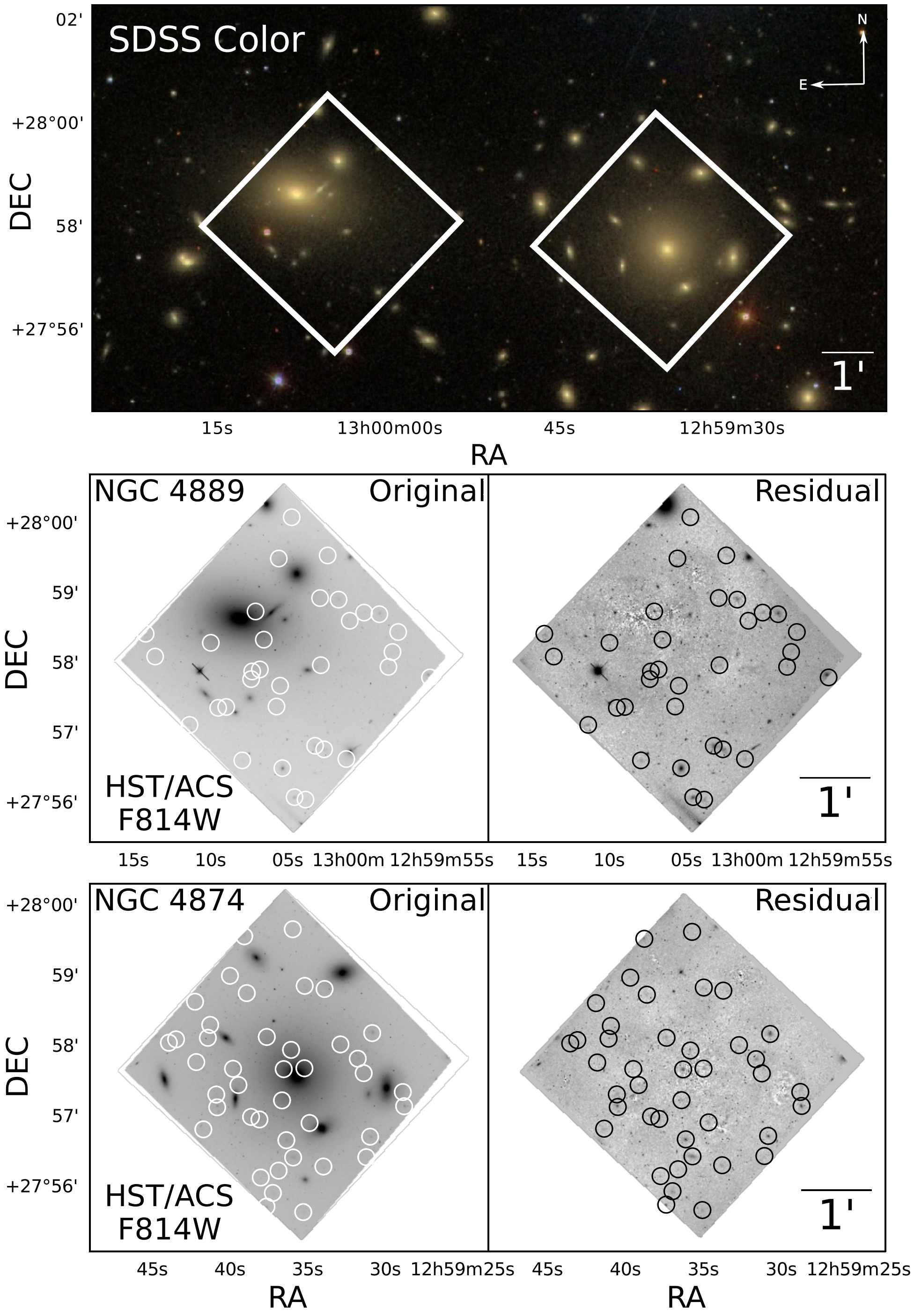

Figure 1. Top: Sloan Digital Sky Survey (SDSS) colour composite image of the central region of the Coma Cluster, with white boxes representing the two *HST*/ACS pointings used in this work. Middle and bottom: the actual *HST*/ACS images used in this work, after DRIZZLE treatment (left) and after the subtraction of bright galaxies to improve the detection of fainter objects (right). Circles indicate the positions of the detected galaxies in our sample (see Table 1).

3 DETECTION, MEMBERSHIP, AND PHOTOMETRY

In this work, we build on the methods developed in recent surveys of the Virgo (Ferrarese et al. 2016) and Fornax (Eigenthaler et al. 2018) clusters to study the faint galaxy population and their star cluster systems. Briefly, galaxy detection is carried out automatically using an algorithm optimized for the recovery of low surface brightness objects. Visual inspection of the candidates by one or more individuals follows, and cluster membership is assigned based on expected morphological features for early-type, quiescent dwarfs – namely, ellipsoidal shapes, smooth surface brightness profiles, and absence of star formation features. Finally, photometric and structural parameters for the host galaxy and the NSC are derived through two-dimensional

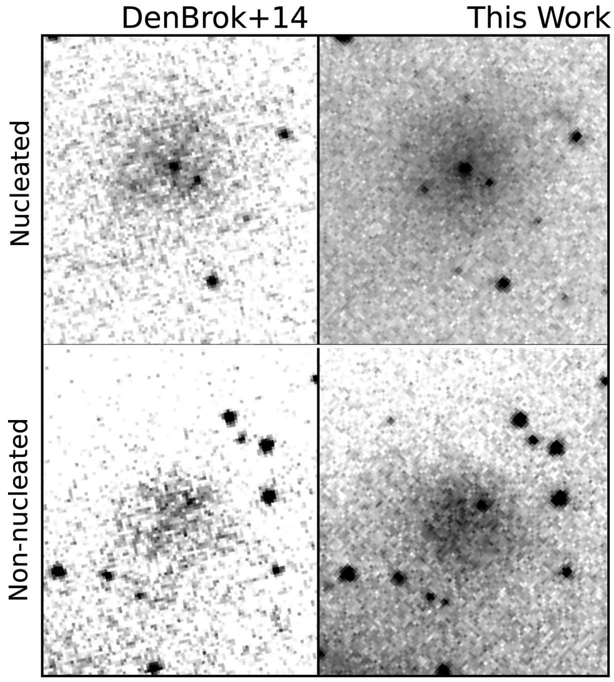

Figure 2. Comparison between the depth of images from dB14 and this work. On the top panels, two images of the same nucleated galaxy present in both the catalogue from dB14 and this work. On the bottom panel, a non-nucleated galaxy. All images are adjusted to the same scale and in the same *HST*/F814W filter.

modelling of the galaxy images. The detailed steps are as follows.

3.1 Bright galaxy subtraction

The two fields in this study are centred on NGC 4874 and NGC 4889, the two dominant ellipticals in the core of the Coma Cluster. NGC 4889 is the brightest galaxy in the cluster, but NGC 4874 boasts an extended cD halo and resides somewhat closer to the centroid of the X-ray emission in the cluster. The high density of bright satellite galaxies in these fields renders the detection of faint objects difficult. Therefore, the first step in our analysis consisted in the modelling and subtraction of the largest objects.

We subtract the bright galaxies using the program ELLIPROOF (Tonry et al. 1997; Jordan et al. 2004), which fits a series of elliptical isophotes of varying centres, ellipticities, orientations, and low-order Fourier terms. The algorithm then interpolates smoothly between the isophotes and extrapolates outward beyond the last one. In both of our fields we model and subtract the brightest galaxy along with large neighbouring galaxies that affect the modelling of the central galaxy, as well as fainter galaxies that adversely affect the modelling of the bright satellite galaxies. We adopt an iterative approach: subtracting the brighter galaxies, then subtracting the fainter neighbours, then remodelling the brighter galaxies with the neighbours subtracted, etc. We iterate until we achieved a clean subtraction of all galaxies (about 10 in each field) that were large enough to have a significant effect on the detection of the fainter objects we aim to study.

3.2 SOURCEEXTRACTOR detection

Galaxy detection is carried out with SOURCEEXTRACTOR (Bertin & Arnouts 1996) following a two-step approach. The first pass is optimized to extract point sources, whereas the second runs on the background image generated from the first one. The process effectively acts as a low-pass spatial filter, resulting in a smoothed, high SNR image over scales larger than the PSF size.

In the first SOURCEEXTRACTOR run we set the minimum detection area, DETECT_MINAREA, to 10 pixels above the detection threshold (DETECT_THRES) of 1.5σ of the sky background. As described before, these parameters are set so as to detect compact objects such as GCs, foreground stars, and background galaxies. We also set a background mesh size (BACK_SIZE) of 32 pixels with a 3 × 3 grid for the median filter (BACK_FILTERSIZE). Using these parameters, SOURCEEXTRACTOR estimates the local background in each mesh of rectangular grids across the entire image. In the second column of Fig. 3, we show an example of such map, where the increase in SNR is evident.

We then proceed to the second run of SOURCEEXTRACTOR, this time on the smoothed image. We set DETECT_MINAREA to 200 pixels above the DETECT_THRES of 1.2σ of the sky background. We then match the positions of the detections with those in the original image, proceeding to visual inspection of the candidates to assign cluster membership and nucleation classification.

3.3 Visual classification

Visual classification was independently carried out by two of the authors (EZ and RS-J). Because faint early-type dwarfs have low surface brightness, the main contaminants are background late-type galaxies. We classify as members objects with smooth and spheroidal morphologies (Sánchez-Janssen et al. 2016), and discard irregular galaxies or those displaying features consistent with ongoing star formation (clumps, arms, bars). We identify NSCs as compact spherical sources that in projection lie close to the geometric centre of the candidate galaxy (see Fig. 2). This requirement is later refined during the process of galaxy modelling (Section 3.4).

We find that the two independent classifications fully agree down to a limiting magnitude of $m_I = 25$ mag. Because the focus of this work is on the faint end of the Coma galaxy population, we also set a bright limit of $m_I = 20$ mag. The number of more luminous galaxies in the two fields under study is too low to be statistically meaningful. Our final catalogue is presented in Table 1. We found 66 galaxies within $-15 < M_I < -10$ mag, 23 of which are first reported in this work. Among these, 33 have NSCs candidates.

3.4 GALFIT modelling

To determine the structural and photometric properties of the candidate galaxies and their NSCs, we model their surface brightness profiles using GALFIT (Peng et al. 2002). We use the segmentation maps from the first SOURCEEXTRACTOR run to mask all objects around our detected galaxies, except for the central point sources in the visually identified nucleated dwarfs. Furthermore, we use PSF models obtained with PSFEX (Bertin 2011). We use as initial conditions the MAG_AUTO magnitudes and FLUX_RADIUS results from the SOURCEEXTRACTOR catalogue, as well as an initial Sérsic index of $n = 0.75$, position angle of 45° and axial ratio of 0.8. The non-nucleated galaxies are modelled with a single Sérsic profile, while for the nucleated ones we use a Sérsic profile alongside a PSF component.

Initial magnitudes for the PSF component are the MAG_AUTO measured by the first SOURCEEXTRACTOR run. The two components have initial central positions defined by the positions detected by

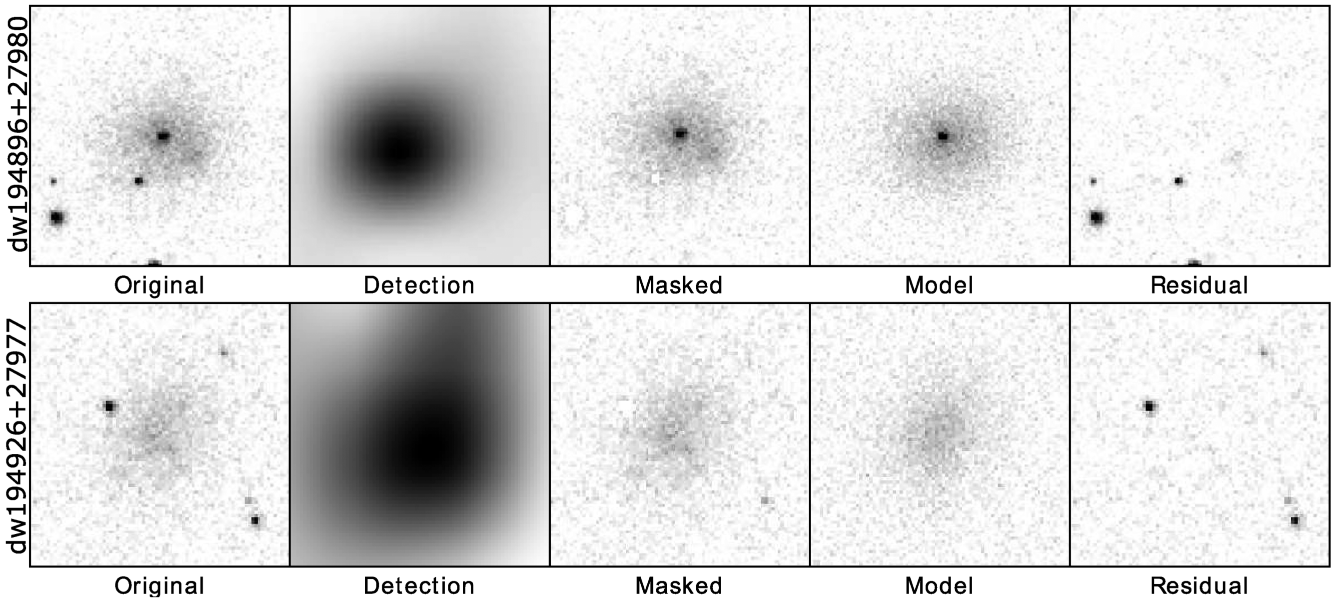

Figure 3. Summary of the procedure to detect and extract photometry for faint galaxies and their NSCs. From left to right: section of the original image showcasing an example galaxy (nucleated on the top, non-nucleated at the bottom). In the second panel we show the SOURCEEXTRACTOR background image used for galaxy detection. Notice the significant increase in SNR, which improves the detection limits. The third panel contains the same image as the first panel, but now the point sources detected by the first SOURCEEXTRACTOR are masked – except for the central 6 × 6 pixels, which are unmasked to reveal the NSC. The fourth panel corresponds to the GALFIT model, to which we have added the typical noise of the ACS images for representation purposes. Finally, in the last panel we show the residual image from GALFIT modelling. Both galaxies are presented with the same scaling.

SOURCEEXTRACTOR for the galaxy or the NSC, in the case of nucleated objects.

To aid in the modelling of the fainter galaxies we employ constraints to the parameters to be fitted by GALFIT. Based on the structural parameters for faint galaxies in the Virgo Cluster (Ferrarese et al. 2020), we limit the Sérsic index to vary in the range $0.5 \leq n \leq 1.5$. Constraining the Sérsic index aids GALFIT in converging to realistic values for other structural parameters even for faint, low surface brightness galaxies. We also constrain the relative position of the Sérsic and PSF components to be within 3 pixels of each other. This is inspired by *HST* studies of NSCs showing that stellar nuclei are rarely offset from the geometric centre of the host galaxy (Cote et al. 2003; Turner et al. 2012). It also guarantees that the likelihood of contamination from chance projection of stars or GCs over the galactic body remains insignificant, with the mean number of such contaminants estimated to be ≈0.002 per galaxy. This is calculated by counting the total number of point sources (CLASS_STAR ≥ 0.6) that have a magnitude difference of less than 0.5 mag with respect to each NSC. The surface density of such candidates is then multiplied by the area enclosed in a circle with a radius of 3 pixels, which is our criterion for a bona fide NSC detection. Results are not sensitive to the magnitude difference between putative contaminants and the candidate NSCs.

A summary of the method is shown in Fig. 3. The galaxy properties obtained from this procedure are presented in Table 1, where magnitudes are dereddened from Galactic extinction using the maps from Schlafly & Finkbeiner (2011). We find that our catalogue has eight common entries with that from dB14. The root mean square deviation of the galaxy magnitudes is only 0.12 mag. See Appendix C for a full description of our photometric uncertainty estimation. This was done by applying our photometry procedure to 10 000 mock galaxies randomly positioned in the two *HST* fields used in this work. Based on the results of these simulations, we estimate mean uncertainties of $\delta m_{I,\mathrm{gal}} \sim 0.2$ mag for the magnitudes obtained in Table 1. Uncertainties to the other parameters are shown in Appendix C.

In Fig. 4, we show the difference between the magnitude of the NSC and its host galaxy for all the nucleated galaxies in our sample, as well as those from dB14 and the nucleated galaxies in the Virgo Cluster from Sánchez-Janssen et al. (2019b). Similarly to what was found in the two latter works, the relative contribution of the NSC to the overall brightness of the host galaxy decreases with galaxy luminosity – albeit with a large scatter in the relation. From the perspective of comparing different environments, we see that the trend in Fig. 4 is very similar for both Virgo and Coma galaxies. Overall, it seems clear that the luminosity of the NSC is related to that of the host galaxy regardless of the environment, but the large scatter in the relation indicates that NSC growth varies substantially from one galaxy to another.

4 STATISTICAL MODELLING OF THE NUCLEATION FRACTION

To analyse the nucleation fraction in the Coma Cluster and how it compares to other environments, we employ Bayesian logistic regression (see e.g. Hilbe, de Souza & Ishida 2017, for a detailed description). Logistic regression belongs to the family of generalized linear models, and is particularly suitable for handling Bernoulli-distributed (binary) data. Such distribution characterizes processes with two possible outcomes $\{0, 1\}$, be it success or failure, yes or no, or alike – in our case it is nucleation or non-nucleation. Previous applications of logistic models in astronomy include the studies of star formation activity in primordial dark matter haloes (de Souza et al. 2015), the escape of ionizing radiation at high redshift (Hattab et al. 2019), the effect of environment in the prevalence of Seyfert galaxies (de Souza et al. 2016), and the redshift evolution

Table 1. Photometric and structural parameters for the galaxies detected in Coma obtained using GALFIT using SOURCEEXTRACTOR magnitude and positions as input parameters, as described in the text. From left to right: identification for each galaxy, right ascension in degrees, declination in degrees, galaxy magnitude in the *I* filter, NSC magnitude in the *I* filter, Sérsic index, effective radius in arcseconds, axial ratio, position angle in degrees, and flags for previous detections of those galaxies. Such flags are as follows: 1: Godwin, Metcalfe & Peach (1983); 2: Iglesias-Páramo et al. (2003); 3: Adami et al. (2006a); 4: Yagi et al. (2016); 5: Adami et al. (2006b); 6: Hoyos et al. (2011); and 7: dB14.

ID	RA (°)	Dec. (°)	$m_{I,\mathrm{gal}}$ (mag)	$m_{I,\mathrm{NSC}}$ (mag)	n	R_e (arcsec)	b/a	PA (°)	Prev. detec.
dw 195019+27934	195.0191	27.9344	20.18	24.05	0.91	1.543	0.72	61.26	3, 6
dw 195007+27981	195.0073	27.9815	20.20	23.34	1.49	2.465	0.88	11.15	2
dw 194870+27952	194.8701	27.9521	20.27	27.55	0.98	1.127	0.65	– 22.84	2, 6
dw 195029+27978	195.0296	27.9787	20.28	23.16	1.27	0.806	0.64	3.31	
dw 194902+27960	194.9024	27.9609	20.40	25.11	0.74	1.210	0.80	63.29	
dw 194920+27952	194.9202	27.9521	20.53	23.69	1.49	0.458	0.94	– 38.14	2, 6
dw 194905+27931	194.9052	27.9315	20.61	25.92	0.79	2.320	0.93	1.08	2, 3, 4
dw 194911+27949	194.9111	27.9496	20.66	23.68	1.49	2.976	0.78	43.22	3
dw 194879+27944	194.8791	27.9449	20.71	25.03	0.89	1.280	0.77	15.57	3
dw 195011+27945	195.0112	27.9459	20.78	25.15	0.61	2.028	0.68	4.02	3, 6, 7
dw 194907+27928	194.9070	27.9283	20.82	25.98	0.91	0.788	0.84	– 57.99	2, 3
dw 194882+27963	194.8823	27.9634	20.86	26.38	1.34	1.974	0.93	58.48	3, 6, 7
dw 194933+27967	194.9332	27.9672	20.93	26.24	0.96	1.728	0.63	29.73	3, 6, 7
dw 194923+27946	194.9239	27.9466	21.03	25.52	0.88	3.690	0.59	39.13	2, 6
dw 194896+27961	194.8968	27.9612	21.05	26.09	1.01	1.887	0.81	85.96	
dw 194895+27948	194.8954	27.9481	21.19	25.13	0.69	1.843	0.76	78.93	6
dw 194913+27992	194.9130	27.9925	21.19		0.82	1.728	0.55	– 36.31	6, 7
dw 194902+27953	194.9026	27.9535	21.33	24.78	1.32	2.289	0.75	24.00	6
dw 194870+27955	194.8704	27.9556	21.44	26.22	0.58	4.014	0.29	– 55.01	
dw 194920+27954	194.9204	27.9549	21.47	26.92	0.50	2.372	0.40	– 86.76	2, 6
dw 195037+27955	195.0375	27.9559	21.53	26.71	0.86	1.262	0.75	37.37	
dw 194908+27949	194.9088	27.9490	21.65		0.83	0.949	0.89	– 77.68	3, 6, 7
dw 195016+27933	195.0161	27.9338	21.69		0.52	1.655	0.67	– 83.23	3, 4, 5, 6, 7
dw 194891+27937	194.8917	27.9378	21.75	26.70	0.63	1.563	0.77	16.76	2, 3, 5
dw 194900+27965	194.9004	27.9655	21.77	24.87	0.91	2.329	0.90	65.86	6
dw 194912+27979	194.9123	27.9790	21.77	25.79	0.65	1.226	0.68	3.71	6
dw 195000+27978	195.0003	27.9784	21.82	25.93	0.72	1.340	0.87	64.54	3, 6, 7
dw 195027+27971	195.0272	27.9719	21.82		0.69	2.759	0.75	66.77	
dw 195047+27951	195.0475	27.9516	21.85		0.58	1.532	0.56	52.30	3, 5
dw 194906+27968	194.9069	27.9686	21.86		0.85	1.569	0.59	– 31.93	6
dw 195033+27943	195.0332	27.9432	21.89	26.56	0.79	1.456	0.76	40.55	3, 5, 6, 7
dw 195030+27964	195.0306	27.9644	21.90		0.88	1.493	0.75	86.83	3
dw 194897+27927	194.8971	27.9270	21.97	26.50	0.83	1.277	0.90	– 64.46	3, 5
dw 195058+27973	195.0589	27.9731	22.03	26.10	0.70	1.364	0.81	24.79	3
dw 195010+27992	195.0100	27.9920	22.05		0.77	2.559	0.57	11.08	
dw 194896+27980	194.8969	27.9806	22.10	26.38	0.71	0.996	0.83	80.16	3, 6
dw 194887+27966	194.8871	27.9667	22.20	26.15	0.93	1.124	0.81	27.66	3, 6, 7
dw 194992+27969	194.9925	27.9692	22.35		0.92	1.496	0.99	– 65.99	3, 6
dw 194914+27957	194.9144	27.9573	22.49		0.51	0.813	0.79	30.38	6
dw 195005+27943	195.0052	27.9435	22.51		0.76	1.060	0.62	– 65.89	
dw 195011+27965	195.0117	27.9658	22.58	25.23	0.99	1.354	0.75	42.23	
dw 195022+27961	195.0229	27.9611	22.66		0.99	1.743	0.57	85.86	
dw 194993+27965	194.9939	27.9655	22.68	23.68	1.49	0.811	0.71	35.60	
dw 195023+27991	195.0231	27.9913	22.72	25.42	0.53	2.215	0.63	37.20	
dw 194908+27935	194.9086	27.9351	22.84		0.56	0.720	0.84	– 57.49	3
dw 195028+27964	195.0285	27.9649	22.84		0.50	0.996	0.94	– 52.86	
dw 195030+27962	195.0308	27.9626	22.90		0.94	1.518	0.65	– 24.14	3
dw 194926+27977	194.9261	27.9770	23.29		0.66	0.802	0.77	32.00	3, 6
dw 194931+27968	194.9312	27.9680	23.29		0.50	1.354	0.71	50.28	
dw 195024+27956	195.0240	27.9560	23.33		0.75	1.187	0.59	– 8.06	3
dw 195056+27968	195.0567	27.9680	23.33		0.93	1.059	0.73	– 32.45	3
dw 194916+27961	194.9161	27.9610	23.41		0.67	0.965	0.74	– 46.73	6
dw 194903+27936	194.9037	27.9368	23.48		0.52	0.737	0.90	54.27	3
dw 194891+27979	194.8915	27.9799	23.57		0.84	0.674	0.71	26.25	6
dw 195019+28001	195.0199	28.0011	23.59		0.62	0.604	0.80	1.25	3
dw 195039+27955	195.0397	27.9557	23.67		0.67	0.838	0.66	– 9.15	
dw 194880+27940	194.8802	27.9400	23.68		0.68	0.747	0.69	7.66	3
dw 194880+27960	194.8808	27.9601	23.79		1.12	0.798	0.76	– 27.25	

Table 1 – *continued*

ID	RA (°)	Dec. (°)	$m_{I,\mathrm{gal}}$ (mag)	$m_{I,\mathrm{NSC}}$ (mag)	n	R_e (arcsec)	b/a	PA (°)	Prev. detec.
dw 194916+27983	194.9167	27.9831	24.08		0.61	0.724	0.71	28.21	
dw 194990+27973	194.9909	27.9739	24.25		0.99	0.854	0.85	47.79	
dw 194922+27971	194.9221	27.9714	24.40		0.50	0.670	0.76	75.78	
dw 195012+27982	195.0121	27.9820	24.44		0.59	0.784	0.65	40.80	
dw 194922+27968	194.9225	27.9684	24.45		0.85	0.405	0.63	– 63.66	
dw 194925+27962	194.9257	27.9626	24.56		0.65	0.511	0.72	– 48.45	3, 6
dw 195041+27971	195.0417	27.9712	24.81	27.74	0.56	0.675	0.75	33.48	
dw 195004+27976	195.0041	27.9766	24.90		0.50	0.502	0.66	– 55.04	

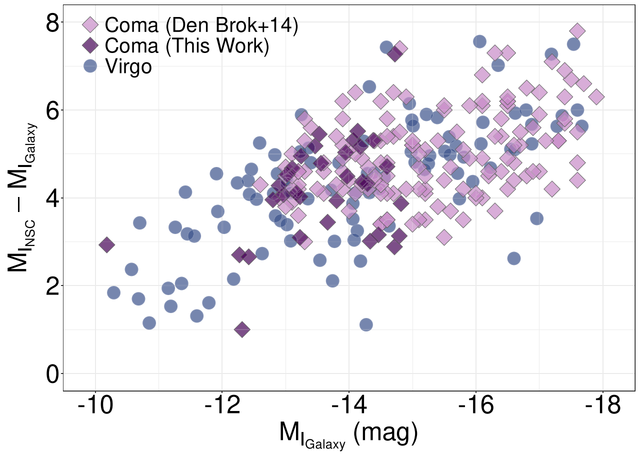

Figure 4. Difference between the magnitude of the nuclei, $M_{I,\mathrm{NSC}}$, and the one of its host galaxy, $M_{I,\mathrm{Galaxy}}$, for all nucleated galaxies in the Coma Cluster sample from this work (shown in Table 1; purple diamonds) and dB14 (magenta diamonds), as well as nucleated galaxies in the Virgo Cluster (from Sánchez-Janssen et al. 2019b; blue circles), as a function of the host galaxy absolute magnitude. For both environments, brighter galaxies tend to show larger differences in magnitude from their nuclei, although a scatter is also evident, showcasing its stochastic nature.

of ultraviolet (UV) upturn galaxies (Dantas et al. 2020). While the full behaviour of the nucleation fraction departs significantly from the logistic relation (Sánchez-Janssen et al. 2019b), we make use of the fact that for all studied environments f_n appears to peak at masses $\log(\mathcal{M}/\mathcal{M}_\odot) \approx 9$ (Neumayer et al. 2020), and then declines gradually toward lower masses until it becomes negligible.

The regression model is the following:

$$
\begin{aligned}
&y_i \sim \mathrm{Bern}\,(p_i)\,,\\
&\eta_i \equiv \log\left(\frac{p_i}{1-p_i}\right),\\
&\eta_i = \beta_{1[k]} + \beta_{2[k]}\, M_{I,i}\,,\\
&\begin{bmatrix}\beta_{1[k]}\\ \beta_{2[k]}\end{bmatrix} \sim \mathrm{Norm}\left(\begin{bmatrix}\mu_\beta\\ \mu_\beta\end{bmatrix}, \Sigma\right); \quad \Sigma \equiv \begin{bmatrix}\sigma^2_\beta & 0\\ 0 & \sigma^2_\beta\end{bmatrix},\\
&\mu_\beta \sim \mathrm{Norm}(0, 10^2); \quad \sigma^2_\beta \sim \mathrm{Gamma}(0.1, 0.1). \qquad (1)
\end{aligned}
$$

The above model reads as follows. Each of the ith galaxies in the data set has its probability to manifest nucleation modelled as a Bernoulli process, whose probability of success relates to $M_{I,i}$ through a logit link function, η_i (to ensure the probabilities will fall between 0 and 1), where the index k encodes the cluster/group environment. A subtle but important characteristic of our model is the treatment of the intercept $\beta_{1[k]}$ and slope $\beta_{2[k]}$ coefficients via hierarchical partial pooling. For the case studied here, it falls under the umbrella of generalized linear mixed models (see e.g. Hilbe et al. 2017, for details). A simple intuition behind this choice is given below. When modelling the same relationship across multiple groups, there are three common choices: pooled, unpooled, and partially pooled models. In our case the pooled model implies a fit to the entire data, completely ignoring potential differences across cluster/groups. In other words, this would implicitly assume a universal shape for the nucleation fraction. In the other extreme lies the ubiquitous unpooled model, which implies fitting each individual case, ignoring any potential correlation across cluster/groups. While it seems a harmless choice, this model is very sensitive to differences in sample size and magnitude range between different cluster/group environments. The most conservative option is partial pooling, which infers different parameters for each group, but allows them to share information. This is done via the use of hyperpriors for its coefficients. This is included in our model by assuming a multi-Normal prior for $\beta_{1[k]}$ and $\beta_{2[k]}$ with a common mean μ_β and variance σ^2_β, to which we assigned weakly informative Normal and Gamma hyperpriors, respectively.

We evaluate the model using the Just Another Gibbs Sampler (JAGS)[1] package within the R language (R Development Core Team 2019). We initiate three Markov chains by starting the Gibbs sampler at different initial values sampled from a Normal distribution with zero mean and standard deviation of 100. Initial burn-in phases were set to 5000 steps followed by 20 000 integration steps, which are sufficient to guarantee the convergence of each chain, following Gelman–Rubin statistics (Gelman & Rubin 1992).

5 RESULTS

When modelling the nucleation fraction the Coma sample presented here is merged with the catalogue from dB14 for completeness purposes at the bright end. The data from this work comprise Coma galaxies with magnitudes in the $-10.0 < M_I < -15.0$ range, while dB14 data in the range $-12.8 < M_I < -19.0$. In the few cases where a galaxy is detected in the two studies we keep the magnitudes from our own analysis.

5.1 Nucleation fraction in the Coma Cluster

Fig. 5 shows the Coma nucleation fraction, f_n, as a function of galaxy absolute magnitude, M_I. The shaded areas indicate the 50 per cent and 95 per cent probability intervals around the mean of the posterior for the logistic model (white curve). The means and 68 per cent confidence level values of the corresponding coefficients are shown in Table 2. The grey region represents the extrapolated solution beyond

---

[1] http://cran.r-project.org/package=rjags

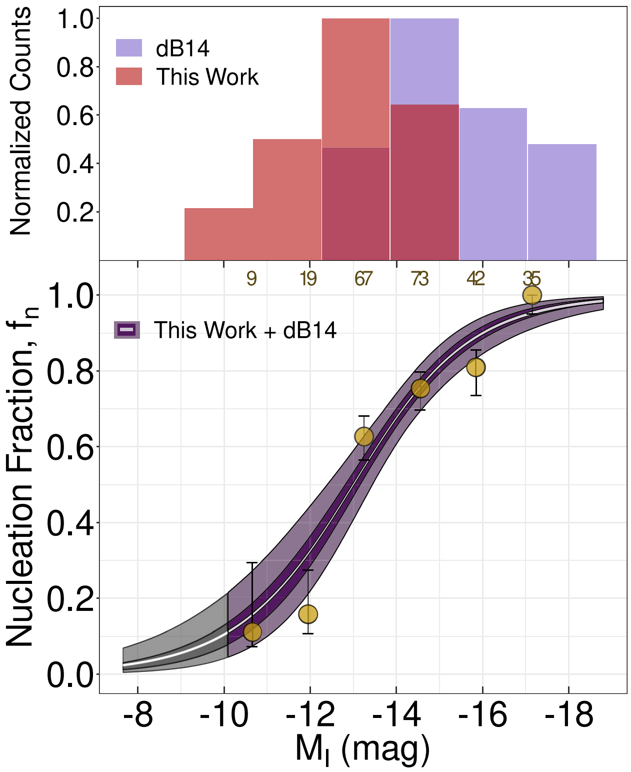

Figure 5. Top: distributions, in normalized counts, for the data obtained in this work and presented in Table 1 (red histogram) and the catalogue of Coma galaxies from dB14 (blue histogram). Bottom: nucleation fraction versus absolute magnitude for galaxies in Coma, combining the data from this work and the one from dB14. In the cases where galaxies were detected in the two data sets, we keep the magnitudes from our own analysis. The white curve is the mean posterior from the Bayesian logistic regression. The purple shaded regions show the 50 per cent and 95 per cent confidence intervals, whereas the grey shades indicate the magnitudes where the model extrapolates the data. The yellow solid circles represent the median nucleation fraction in a binned representation of the data, with uncertainties given by the corresponding 68 per cent Bayesian credible intervals. The number of objects in each bin is shown at the top.

Table 2. Summary of the parameters estimated from the model presented in equation (1). In the first column we show $M_{I,f_{\mathrm{n}50}}$, the magnitude at which the estimated probability of nucleation reaches 50 per cent. In the second column ΔOdds represents the expected change in the odds of nucleation by a variation of one unit of magnitude. In the last two columns, β_1 and β_2 are the mean posteriors for the intercept and slope, respectively, of the link function η_i. One can see that ΔOdds is within a 10 per cent difference among all environments, while the variation of $M_{I,f_{\mathrm{n}50}}$ presents a significant difference in luminosity.

	$M_{I,f_{\mathrm{n}50}}$	ΔOdds (per cent)	β_1(intercept)	β_2(slope)
Coma	$-12.98^{+0.26}_{-0.25}$	−52.2	-9.66 ± 1.56	-0.74 ± 0.11
Virgo	$-14.39^{+0.25}_{-0.25}$	−50.0	-9.89 ± 1.28	-0.70 ± 0.10
Fornax	$-14.16^{+0.31}_{-0.31}$	−47.3	-9.25 ± 0.98	-0.64 ± 0.07
Local early type	$-14.64^{+0.98}_{-0.89}$	−41.4	-7.94 ± 1.76	-0.54 ± 0.14
Local late type	$-15.38^{+0.96}_{-0.89}$	−47.5	-9.98 ± 2.21	-0.66 ± 0.17

which there is no data coverage. For visualization purposes we also show with yellow circles the nucleation fraction calculated in eight equal-sized bins. The corresponding error bars show the 68 per cent Bayesian confidence level. The tick marks at the top and bottom of the panel indicate the magnitudes for each of the nucleated and non-nucleated galaxies, respectively, and the yellow histogram is a binned representation with the purpose to highlight the prevalence of NSCs in brighter galaxies.

We confirm the strong dependence of the nucleation fraction on galaxy luminosity in Coma: it peaks at nearly $f_{\mathrm{n}} \approx 100$ per cent at $M_I = -18$ [the characteristic luminosities of classical dwarf elliptical (dE) galaxies] and then declines to become almost negligible at $M_I = -10$. Overall, the nucleation fraction is remarkably high, with more than half of the $M_I = -13$ dwarf galaxies still hosting NSCs. This is clearly shown by both the binned nucleation fraction and the logistic model, but only the latter is able to produce a smooth solution while also allowing us to study the rate at which NSCs occur in galaxies of different brightness. More importantly, we are now in a position to quantitatively compare the exact shape of the nucleation fraction in Coma and in other environments.

5.2 Nucleation in other environments

In Fig. 6, we show the mean posterior for the nucleation fraction in the Coma Cluster compared to that in the Virgo and Fornax clusters (left-hand panel), as well as in nearby groups (right-hand panels). In order to improve the number statistics in these less rich environments we subdivide and stack the samples of group dwarfs into satellites of early- and late-type centrals (see Appendix A for details). The total number of quiescent satellites in the subsamples of early- and late-type groups is 93 and 90, respectively. As with Coma, the means and 68 per cent confidence level values of the coefficients for the logistic model are shown in Table 2. Two results are readily apparent.

(1) *Nucleation has a nearly universal dependence on dwarf galaxy luminosity*. This is shown in Table 2 by the very similar β_2 slope parameters for all the different environments, which are consistent with each other at the 1σ level. In the table we also show the corresponding ΔOdds, which represents the change in nucleation odds given a variation of one unit in magnitude for each environment, i.e. the nucleation rate by magnitude. We find very similar values for all environments, perhaps with the exception of systems dominated by early-type centrals where the nucleation fraction displays a slightly shallower decline.

(2) *Nucleation is more common in more massive haloes regardless of dwarf galaxy luminosity*. This is evident from the posterior curves in Fig. 6, which are colour coded by the estimated virial halo masses for the systems under study. For example, a $M_I = -15$ dwarf has an ≈80 per cent probability of being nucleated in Coma, compared to ≈50 per cent for quiescent satellites in groups with both early- and late-type centrals. In order to better quantify this dependence we introduce the $M_{I,f_{\mathrm{n}50}}$ index, the magnitude at which the nucleation probability reaches 50 per cent as inferred from the logistic model. In Fig. 7, we show how this half-nucleation magnitude varies as a function of the virial halo mass for each environment. We model this relation as a linear regression of the form $M_{I,f_{\mathrm{n}50}} = \alpha + \beta \log(\mathcal{M}_{200})$. The mean posteriors and associated standard deviations obtained for the parameters are $\alpha = -21.6 \pm 2.8$ and $\beta = 0.54 \pm 0.19$. This implies that the half-nucleation luminosity correlates with the host halo mass roughly as $L_{I,f_{\mathrm{n}50}} \propto \mathcal{M}_{200}^{-0.2}$. The most extreme environments, Coma and the late-type groups, have $L_{I,f_{\mathrm{n}50}}$ values that differ by almost a factor of 10 in luminosity. A

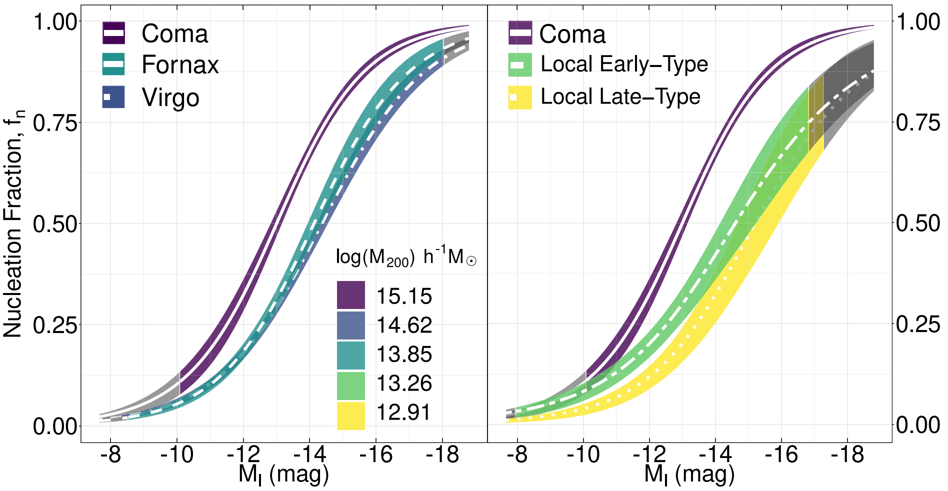

Figure 6. Mean posteriors from the Bayesian logistic regression models and 50 per cent confidence intervals, in the left-hand panel, for the Coma Cluster data from this work and dB14, Virgo Cluster from Sánchez-Janssen et al. (2019b), and Fornax Cluster from Muñoz et al. (2015). In the right-hand panel, the Coma Cluster again and a combined sample of galaxies in the local volume in groups with a central early- or late-type galaxy (see Appendix A for references). The samples are colourized by the approximated cluster/group virial halo mass, from the references mentioned in the text. For the case of the local volume environments, the halo mass presented is a mean of the halo masses of the sample galaxies within it. The grey regions of the curves represent the regions where the model extrapolates the actual data. Coma galaxies show a higher probability of nucleation than all other environments at all magnitudes considered.

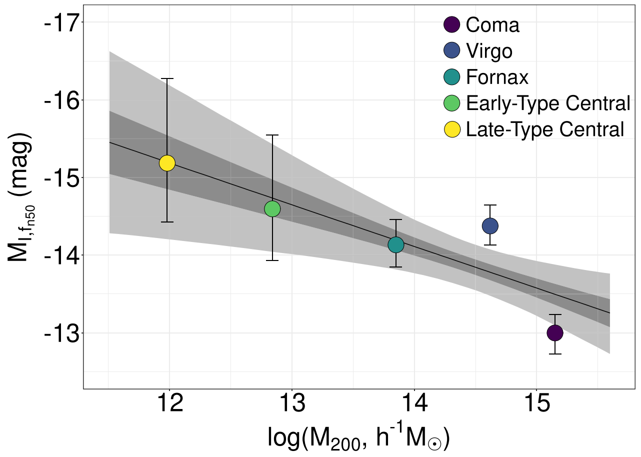

Figure 7. Mean posterior for the magnitude at which the probability of nucleation is 50 per cent, $M_{I,f_{n50}}$, as a function of host virial halo mass (references mentioned in the text). The mean, 50 per cent and 95 per cent confidence intervals for a linear model are indicated by the solid line and grey shaded areas, respectively. More massive environments exhibit fainter values of the half-nucleation magnitude.

corollary to this result is that the nucleation fraction in Coma is the highest in all the studied environments over more than three decades in dwarf galaxy luminosity.

The main finding of this study is that *the rate at which the probability of nucleation varies with magnitude does not depend substantially on the environment, but the fraction of nucleated dwarfs at a fixed luminosity does*. As a result, any model of NSC formation in low-luminosity/mass galaxies needs to account for the joint dependence of the nucleation fraction on galaxy luminosity/mass and the environment in which they reside. We discuss possible scenarios in the next section.

6 DISCUSSION

We now attempt to frame the two main results of this work in the context of NSC formation scenarios in low-luminosity/mass galaxies. The finding that the nucleation fraction displays a nearly universal dependence with galaxy luminosity simply implies a higher ability of more massive dwarfs to pile up material in their central regions. Studies of NSC occupation alone cannot constrain whether this process occurs through star cluster inspiral or *in situ* star formation following gas inflows. There is, however, mounting evidence that the former process is probably dominant for low-mass quiescent galaxies (Neumayer et al. 2020). Observations in support of this picture include the fact that NSCs in faint, early-type dwarfs are typically more metal poor than their host galaxies (Fahrion et al. 2020; Johnston et al. 2020); that the occupation fraction of GCs and NSCs track each other remarkably well (Sánchez-Janssen et al. 2019b); and that in this luminosity regime the scaling of NSC mass with galaxy mass is in excellent agreement with the prediction from GC inspiral models (Antonini 2013; Gnedin et al. 2014; Sánchez-Janssen et al. 2019b). Such models require GCs (or their progenitors) to have masses high enough so that their orbits decay in less than a Hubble time as a consequence of dynamical friction, while simultaneously surviving tidal dissolution. Factors that influence NSC growth and may depend on galaxy mass are the GC mass function (GCMF), the GC formation distance, the host galaxy structural properties, and the presence of a massive black hole (BH) – but the BH occupation fraction for low-mass galaxies is poorly constrained, and it certainly does not increase for fainter galaxies (Greene, Strader & Ho 2020). Given that the nucleation fraction peaks at $M_I \approx -18$ ($\mathcal{M} \approx 10^9\mathcal{M}_\odot$) and then declines, fainter dwarfs must have a comparatively bottom-heavier GCMF, or have GCs that on average form at larger distances from the galactic centre, or be preferentially concentrated and more compact. There are no observational constraints on the first two properties, and the latter is in direct contradiction with the observed mass–size relation of faint dwarfs in the nearby Universe (McConnachie 2012; Eigenthaler et al. 2018; Ferrarese et al. 2020). Alternatively, it is possible that, even if the GCMF is universal, the formation of GCs in galaxies with such low masses remains a stochastic process. If dwarfs were to form clusters so that the total mass of the GCs is a constant fraction of their stellar mass, this would explain why in the dwarf regime the NSC and GC occupation fractions track each other so closely: the nucleation fraction drops simply because the host galaxies never form enough massive GCs to begin with. A corollary from this proposition is that the GCMF should vary with galaxy luminosity, with very faint dwarfs exhibiting a deficit in massive GCs.

In the context of GC inspiral scenarios, the same arguments apply to the unambiguous environmental dependence we show in Figs 6 and 7 – but now the differences must arise due to effects related to the host halo at fixed present-day galaxy luminosity. Unfortunately, to our best knowledge the environmental dependence does not arise naturally in any NSC formation model, and there are no observational constraints on the early properties of GCs in different environments. Additionally, the mass–size relation seems to be rather universal in this luminosity regime, with dwarfs in environments ranging from Coma to the Local Group following similar scaling relations. Sánchez-Janssen et al. (2019b) speculate that a biased formation scenario for star clusters similar to that proposed by Peng et al. (2008) does a reasonable job at explaining the environmental dependence of the faint nucleation fraction, at least qualitatively. In such a model galaxies that now reside in higher density environments form stars earlier and sustain higher star formation rates (SFRs) and SFR surface densities. These are conditions conducive to the formation of bound massive clusters, and if cluster formation efficiency is close to universal and galaxies formed clusters proportionally to their mass at early epochs (Kruijssen 2015), then one naturally expects a larger mass fraction in star clusters in the more biased environments. In this context it is also important to remember that, for a given present-day stellar mass, the subhaloes in denser environments were at all times prior to infall more massive than those in less dense regions. This, together with earlier infall (and peak mass) times, creates conditions that favour efficient formation of star clusters (Mistani et al. 2016). Those that are massive enough and form close to the galaxy centre will experience dynamical friction and decay to the bottom of the potential well. We finally note that some of the masses of NSCs in very faint galaxies are comparable to those of typical GCs (see Fig. 4), and therefore very little GC merging is actually required (Fahrion et al. 2020; Neumayer et al. 2020).

The proposition that nucleated dwarfs form a biased subpopulation is well established by numerous observational results. Compared to their non-nucleated counterparts they exhibit more concentrated spatial distributions and a propensity for circularized orbits (Ferguson & Sandage 1989; Lisker et al. 2007, 2009); they are intrinsically more spherical (Ryden & Terndrup 1994; Sánchez-Janssen et al. 2019a) and possess more concentrated light profiles (dB14); they host older stellar populations (Lisker, Grebel & Binggeli 2008); and there is tentative evidence that they feature higher GC mass fractions (Miller et al. 1998; Sánchez-Janssen & Aguerri 2012). Whether or not this is sufficient to explain the higher occurrence of NSCs in more massive haloes remains to be quantified by detailed models of their formation and evolution.

7 SUMMARY AND CONCLUSIONS

In this work, we detect and characterize 66 low-mass, quiescent galaxies in the central regions of the Coma Cluster using deep *HST*/ACS imaging in the F814W band. NSCs are identified by a combination of visual inspection and full image modelling. We perform Bayesian logistic regression to model the joint dependence of the nucleation fraction on galaxy absolute magnitude and environment for dwarf galaxies in nearby clusters and groups. Our main conclusions are as follows.

(1) Similar to previous findings (dB14; Sánchez-Janssen et al. 2019b), fainter galaxies in Coma tend to show a smaller difference in magnitude from their nuclei – but the significant scatter at fixed galaxy luminosity suggests the growth of stellar nuclei is a substantially stochastic process.

(2) The nucleation fraction depends on both galaxy mass/luminosity and environment, with the former being the primary parameter. Fainter galaxies have a lower probably of hosting NSCs, as do quiescent satellites of all luminosities in lower mass haloes. The rate at which the probability of nucleation varies with luminosity is remarkably universal.

(3) The nucleation fraction in Coma over three decades in dwarf galaxy luminosity is higher than in any other known environment. This is a direct result of the strong environmental dependence of the nucleation fraction. We find that the luminosity at which half of the dwarf galaxies contain an NSC is inversely proportional to the virial mass of the host halo, $L_{I,f_{\mathrm{n}50}} \propto \mathcal{M}_{200}^{-0.2}$.

We have shown that nucleation in dwarf galaxies is a complex phenomenon that depends both on luminosity and the environment in which the galaxy resides. We identify several observational constraints that would advance our knowledge of the conditions and environments that are conducive to the formation and growth of stellar nuclei. First, it is critical to rise the statistical significance of the environmental dependence by studying the nucleation fraction in other groups and clusters – and in particular for both more and less massive host haloes than studied here. The rarity of massive clusters like Coma and the sparseness of low-density environments make this a challenging task that might be best tackled with upcoming wide-field space missions like *Euclid*, the *Roman Space Telescope*, and the *Chinese Space Station Telescope*. Second, the availability of large NSC samples would allow us to investigate if other physical parameters such as galaxy size also play an important role on the presence of nuclei, as predicted by models (Antonini, Barausse & Silk 2015; Mistani et al. 2016). Finally, occupation studies have little constraining power on the exact physical processes that drive NSC formation and growth. Detailed chemodynamical studies of nuclei across a wide range of masses and environments will be instrumental in settling this question (Kacharov et al. 2018; Fahrion et al. 2019; Johnston et al. 2020; Carlsten et al. 2021).

ACKNOWLEDGEMENTS

We thank the anonymous referee for all the insightful suggestions that greatly improved the presentation of this paper. We also thank R. Flores-Freitas for the insightful contributions. This work is based on observations with the NASA/ESA *Hubble Space Telescope*, obtained at the Space Telescope Science Institute, which is operated by AURA, Inc., under NASA contract NAS 5-26555. These observations are associated with GO Programs #11711. EZ acknowledges funding from Conselho Nacional de Desenvolvimento Científico e Tecnológico (CNPq) through grant CNPq-162480/2017-2, Coordenação de Aperfeiçoamento de Pessoal de N’ıvel Superior (CAPES), and the Newton Fund. ALC-S acknowledges funding from CNPq and Fundação de Amparo à Pesquisa do Estado do Rio Grande do Sul (FAPERGS) through grants CNPq-403580/2016-1, CNPq-11153/2018-6, PqG/FAPERGS-17/2551-0001, FAPERGS/CAPES 19/2551-0000696-9 and L’Oréal UNESCO ABC Para Mulheres na

Ciência. JPB was supported in part by the International Gemini Observatory, a programme of NSF's NOIRLab, managed by AURA, Inc., under a cooperative agreement with the National Science Foundation, on behalf of the Gemini partnership.

DATA AVAILABILITY

The data underlying this paper are available in the paper and at the MAST *HST* archive (https://archive.stsci.edu/hst/) under the program ID 11711.

REFERENCES

Adami C. et al., 2006a, A&A, 451, 1159
Adami C. et al., 2006b, A&A, 459, 679
Afanasiev A. V. et al., 2018, MNRAS, 477, 4856
Ahn C. P. et al., 2018, ApJ, 858, 102
Alabi A. B. et al., 2017, MNRAS, 468, 3949
Anderson J., Bedin L. R., 2010, PASP, 122, 1035
Antonini F., 2013, ApJ, 763, 62
Antonini F., Barausse E., Silk J., 2015, ApJ, 812, 72
Arca-Sedda M., Capuzzo-Dolcetta R., 2014, MNRAS, 444, 3738
Baldassare V. F., Gallo E., Miller B. P., Plotkin R. M., Treu T., Valluri M., Woo J. H., 2014, ApJ, 791, 133
Bekki K., Chiba M., 2004, A&A, 417, 437
Bekki K., Forbes D. A., Beasley M. A., Couch W. J., 2003, MNRAS, 344, 1334
Bertin E., 2011, in Evans I. N., Accomazzi A., Mink D. J., Rots A. H., eds, ASP Conf. Ser. Vol. 442, Astronomical Data Analysis Software and Systems XX. Astron. Soc. Pac., San Francisco, p. 435
Bertin E., Arnouts S., 1996, A&AS, 117, 393
Blakeslee J. P., Anderson K. R., Meurer G. R., Benítez N., Magee D., 2003, in Payne H. E., Jedrzejewski R. I., Hook R. N., eds, ASP Conf. Ser. Vol. 295, Astronomical Data Analysis Software and Systems XII. Astron. Soc. Pac., San Francisco, p. 257
Blanton M. R., Roweis S., 2007, AJ, 133, 734
Carlsten S. G., Greco J. P., Beaton R. L., Greene J. E., 2020a, ApJ, 891, 144
Carlsten S. G., Greene J. E., Peter A. H. G., Greco J. P., Beaton R. L., 2020b, ApJ, 902, 124
Carlsten S. G., Greene J. E., Beaton R. L., Greco J. P., 2021, preprint (arXiv:2105.03440)
Carollo C. M., Stiavelli M., Mack J., 1998, AJ, 116, 68
Carter D. et al., 2008, ApJS, 176, 424
Cho H., Blakeslee J. P., Chies-Santos A. L., Jee M. J., Jensen J. B., Peng E. W., Lee Y.-W., 2016, ApJ, 822, 95
Cote P., McLaughlin D. E., Cohen J. G., Blakeslee J. P., 2003, ApJ, 591, 850
Cote P. et al., 2006, ApJS, 165, 57
Dantas M. L., Coelho P. R., de Souza R. S., Gonçalves T. S., 2020, MNRAS, 492, 2996
den Brok M. et al., 2014, MNRAS, 445, 2385 (dB14)
de Souza R. S. et al., 2015, Astron. Comput., 12, 21
de Souza R. S. et al., 2016, MNRAS, 461, 2115
Drinkwater M. J., Gregg M. D., Colless M., 2001, ApJ, 548, L139
Drinkwater M. J., Gregg M. D., Hilker M., Bekki K., Couch W. J., Ferguson H. C., Jones J. B., Phillipps S., 2003, Nature, 423, 519
Eigenthaler P. et al., 2018, ApJ, 855, 142
Fahrion K. et al., 2019, A&A, 628, A92
Fahrion K. et al., 2020, A&A, 634, A53
Ferguson H. C., Sandage A., 1989, ApJ, 346, L53
Ferrarese L. et al., 2016, ApJ, 824, 10
Ferrarese L. et al., 2020, ApJ, 890, 128
Gelman A., Rubin D. B., 1992, Stat. Sci., 7, 457
Georgiev I. Y., Böker T., 2014, MNRAS, 441, 3570
Georgiev I. Y., Hilker M., Puzia T. H., Goudfrooij P., Baumgardt H., 2009, MNRAS, 396, 1075
Georgiev I. Y., Böker T., Leigh N., Lützgendorf N., Neumayer N., 2016, MNRAS, 457, 2122
Gnedin O. Y., Ostriker J. P., Tremaine S., 2014, ApJ, 785, 71
Godwin J. G., Metcalfe N., Peach J. V., 1983, MNRAS, 202, 113
Greene J. E., Strader J., Ho L. C., 2020, ARA&A, 58, 257
Hattab M. W., De Souza R. S., Ciardi B., Paardekooper J. P., Khochfar S., Vecchia C. D., 2019, MNRAS, 483, 3307
Hilbe J. M., de Souza R. S., Ishida E. E. O., 2017, Bayesian Models for Astrophysical Data Using R, JAGS, Python, and Stan. Cambridge Univ. Press, Cambridge
Hoyos C. et al., 2011, MNRAS, 411, 2439
Iglesias-Páramo J., Boselli A., Gavazzi G., Cortese L., Vílchez J. M., 2003, A&A, 397, 421
Johnston E. J. et al., 2020, MNRAS, 495, 2247
Jordan A. et al., 2004, ApJS, 154, 509
Kacharov N., Neumayer N., Seth A. C., Cappellari M., McDermid R., Walcher C. J., Böker T., 2018, MNRAS, 480, 1973
Karachentsev I. D. et al., 2002, A&A, 383, 125
Karachentsev I. D., Makarov D. I., Kaisina E. I., 2013, AJ, 145, 101
Kruijssen J. M. D., 2015, MNRAS, 454, 1658
Lisker T., Grebel E. K., Binggeli B., Glatt K., 2007, ApJ, 660, 1186
Lisker T., Grebel E. K., Binggeli B., 2008, AJ, 135, 380
Lisker T. et al., 2009, ApJ, 706, L124
Łokas E. L., Mamon G. A., 2003, MNRAS, 343, 401
McConnachie A. W., 2012, AJ, 144, 4
McLaughlin D. E., 1999, AJ, 117, 2398
Miller B. W., Lotz J. M., Ferguson H. C., Stiavelli M., Whitmore B. C., 1998, ApJ, 508, L133
Mistani P. A. et al., 2016, MNRAS, 455, 2323
Müller O., Rejkuba M., Pawlowski M. S., Ibata R., Lelli F., Hilker M., Jerjen H., 2019, A&A, 629, A18
Muñoz R. P. et al., 2015, ApJ, 813, L15
Neumayer N., Seth A., Böker T., 2020, A&AR, 28, 4
Ordenes-Briceño Y. et al., 2018, ApJ, 859, 52
Peng C. Y., Ho L. C., Impey C. D., Rix H.-W., 2002, AJ, 124, 266
Peng E. W. et al., 2008, ApJ, 681, 197
Pfeffer J., Baumgardt H., 2013, MNRAS, 433, 1997
Pillepich A. et al., 2018, MNRAS, 475, 648
R Development Core Team R., 2019, A Language and Environment for Statistical Computing. R Foundation for Statistical Computing, Vienna, Austria, Available at: http://www.r-project.org
Ryden B. S., Terndrup D. M., 1994, ApJ, 425, 43
Sánchez-Janssen R., Aguerri J. A., 2012, MNRAS, 424, 2614
Sánchez-Janssen R. et al., 2016, ApJ, 820, 69
Sánchez-Janssen R. et al., 2019a, MNRAS, 486, L1
Sánchez-Janssen R. et al., 2019b, ApJ, 878, 18
Schlafly E. F., Finkbeiner D. P., 2011, ApJ, 737, 103
Scott N., Graham A. W., 2013, ApJ, 763, 76
Seth A. C. et al., 2014, Nature, 513, 398
Tamm A., Tempel E., Tenjes P., Tihhonova O., Tuvikene T., 2012, A&A, 546, A4
Taylor C., Boylan-Kolchin M., Torrey P., Vogelsberger M., Hernquist L., 2016, MNRAS, 461, 3483
Tonry J. L., Blakeslee J. P., Ajhar E. A., Dressler A., 1997, ApJ, 475, 399
Tremaine S. D., Ostriker J. P., Spitzer L. J., 1975, ApJ, 196, 407
Turner M. L., Côté P., Ferrarese L., Jordán A., Blakeslee J. P., Mei S., Peng E. W., West M. J., 2012, ApJS, 203, 5
van den Bergh S., 2000, AJ, 119, 609
Walcher C. J. et al., 2005, ApJ, 618, 237
Yagi M., Koda J., Komiyama Y., Yamanoi H., 2016, ApJS, 225, 11

APPENDIX A: REFERENCES FOR THE DATA USED IN THIS WORK NOT FROM THE COMA CLUSTER

In this work, we study the nucleation fraction in the Coma Cluster and in other environments using the literature data. In Table A1, we list the other systems included in the analysis, namely the Virgo and Fornax clusters, as well as local volume groups ($D < 12$ Mpc)

Table A1. Source of the photometry and nucleation classification for the data used in this work. From left to right: first column is the central galaxy for a given group in the local volume or the galaxy cluster. For local volume groups the second column indicates the morphology of the central galaxy (ET for early types and LT for late types). The next column is the number of quiescent satellite galaxies in each system, with the two subsequent columns presenting the sources for the photometry and the nucleation classification, respectively.

			Local volume groups	
ID	Morph.	*N*	Photometry source	Nucleation source
NGC 1023	ET	15	Carlsten et al. (2020b)	Carlsten et al. (2020a)
M104	ET	23	Carlsten et al. (2020b)	Carlsten et al. (2020a)
Cen A	ET	31	Carlsten et al. (2020b), Müller et al. (2019)[a]	Carlsten et al. (2020a), Müller et al. (2019), Fahrion et al. (2020)[b]
NGC 3115	ET	24	Chies-Santos et al. (in preparation)	Chies-Santos et al. (in preparation)
NGC 4631	LT	7	Carlsten et al. (2020b)	Carlsten et al. (2020a)
NGC 4565	LT	16	Carlsten et al. (2020b)	Carlsten et al. (2020a)
NGC 4258	LT	9	Carlsten et al. (2020b)	Carlsten et al. (2020a)
M51	LT	4	Carlsten et al. (2020b)	Carlsten et al. (2020a)
MW	LT	11	Karachentsev, Makarov & Kaisina (2013)	Sánchez-Janssen et al. (2019b)
M81	LT	13	Karachentsev et al. (2013)	Sánchez-Janssen et al. (2019b)
M31	LT	30	Karachentsev et al. (2013)	Sánchez-Janssen et al. (2019b)
			Galaxy clusters	
Coma		255	This work, dB14	This work, dB14
Virgo		382	Sánchez-Janssen et al. (2019b)	Sánchez-Janssen et al. (2019b)
Fornax		263	Muñoz et al. (2015)	Muñoz et al. (2015)

[a] Müller et al. (2019) is the source photometry for the galaxies KK 54 and KK 58, and source nucleation for KK 54.
[b] Fahrion et al. (2020) is the source nucleation for the galaxy KK 58.

with both early-type (ET) and late-type (LT) centrals. In the table we indicate the number of quiescent satellites in each environment, as well as the literature sources for the photometry and the nucleation classification.

Where applicable, we have converted the published magnitudes to the *I* band. We adopt conversions based on the ones presented in Blanton & Roweis (2007):

$$(B - i) \approx 1.10, \quad (A1)$$

$$(i - I) \approx 0.06. \quad (A2)$$

The selection of quiescent satellites in the Local Group and around M81 is detailed in Sánchez-Janssen et al. (2019b). The majority of the low-density systems are drawn from Carlsten et. al. (2020a). We only select galaxies classified as dEs and discard dwarf irregular (dIrr) galaxies and transition dwarfs. Carlsten et. al. (2020b) present surface brightness fluctuation distances for the galaxies in the original sample. We make use of these and consider only galaxies that are flagged as 'possible' or 'confirmed' satellites in their table 4. The nucleation classification and photometry for the final sample of group satellites are then taken from Carlsten et. al. (2020a) and Carlsten et. al. (2020b), respectively.

APPENDIX B: ADDITIONAL DETAILS FROM THE HIERARCHICAL BAYESIAN LOGISTIC ANALYSIS

In this section, we discuss briefly some additional details from the Bayesian analysis described in Section 4.

In Fig. B1, we show the individual posterior distributions from the Bayesian logistic regression alongside binned data points for every environment from the literature considered in Fig. 6, with the same captions as in the bottom panel of Fig. 5. It is clear that the logistic regression follows closely the binned data despite not relying on arbitrary defined bins. We stress the advantages of not relying on a binned fit, especially when dealing with data from different sources and with different sample sizes. Notice that the local environments have noticeable larger confidence intervals than Virgo, Fornax, and Coma (show in Fig. 5). Our method of choice is able to efficiently compare the nucleation fraction in different environments in a homogeneous way while not underestimating the uncertainties arisen from small sample sizes.

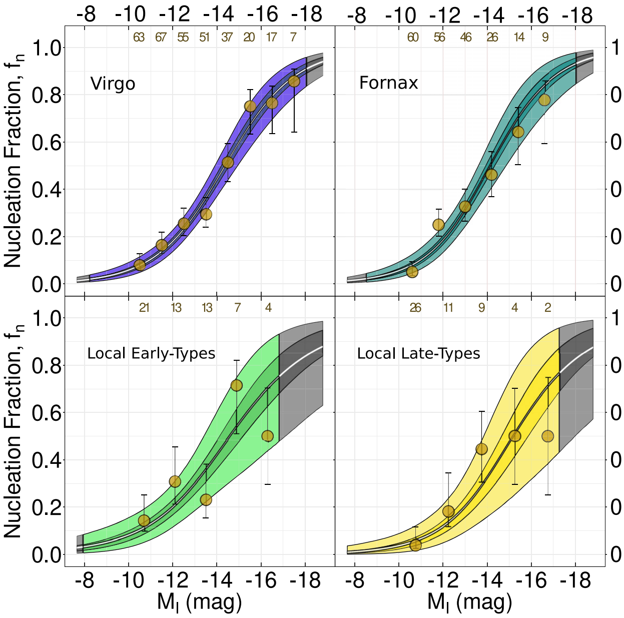

Figure B1. Same as the bottom panel of Fig. 5, but for every other environment considered in this work, gathered from the literature references described in Section 2.1. Notice the excellent agreement between the binned data and the logistic regression.

APPENDIX C: ESTIMATION OF PHOTOMETRIC UNCERTAINTIES

To estimate the uncertainties in the recovered parameters shown in Table 1, we run the photometry procedure presented in Section 3 for mock galaxies randomly placed in the *HST* images used in this work. Mock galaxies are created using GALFIT using a Sérsic+PSF component, with parameters sampled from the values in Table 1. Galaxy magnitudes are chosen randomly from a uniform distribution $U_{m_{\rm gal}}(-14.0, -10.0)$. NSC magnitudes, effective radii, and Sérsic indices show significant correlations with galaxy magnitude, with Pearson correlation coefficients of 0.42, −0.54, and −0.44, respectively. Because of this, we group these quantities in 10 bins of galaxy magnitude and calculate the mean, $\mu_{\rm bin}$, and standard deviation $\sigma_{\rm bin}$. Then, in each bin, we randomly generate new values for such quantities following a normal distribution $N(\mu_{\rm bin}, \sigma_{\rm bin})$. We do not detect a significant correlation between axis ratios and galaxy magnitude (Pearson correlation coefficient of −0.09). For this reason, mock values for the axial ratio are obtained from a uniform distribution $U_q(0.35, 1.0)$. Position angles are set to a fixed value of 75° for every mock galaxy, as this parameter has little impact on the uncertainties we aim to estimate. This sampling technique ensures that we simulated only realistic representations of galaxies as detected in our catalogue. We created a total of 10 000 nucleated galaxies, 5000 for each *HST* field. Mock galaxies are added in random positions in the *HST* images with all galaxies masked. Then we proceed with photometry exactly as done for our real detections and described in Section 3, except for the step of visual classification.

The results of these simulations are presented in Fig. C1. The median uncertainty in galaxy magnitude is ∼0.2 mag. The 95 per cent and 68 per cent confidence intervals show that GALFIT estimates magnitudes brighter than the true values for galaxies fainter than $M_I \sim 11$ mag. This behaviour was also observed in the simulations of Ferrarese et al. (2020) for the NGVS. Therefore, we do not consider this to be evidence for any systematic bias from our method or observations. Regarding NSC magnitudes the uncertainties are considerably lower, never surpassing 0.1 mag even considering the 95 per cent confidence intervals. Finally, results for effective radii and Sérsic index show a median uncertainty of ∼20 per cent.

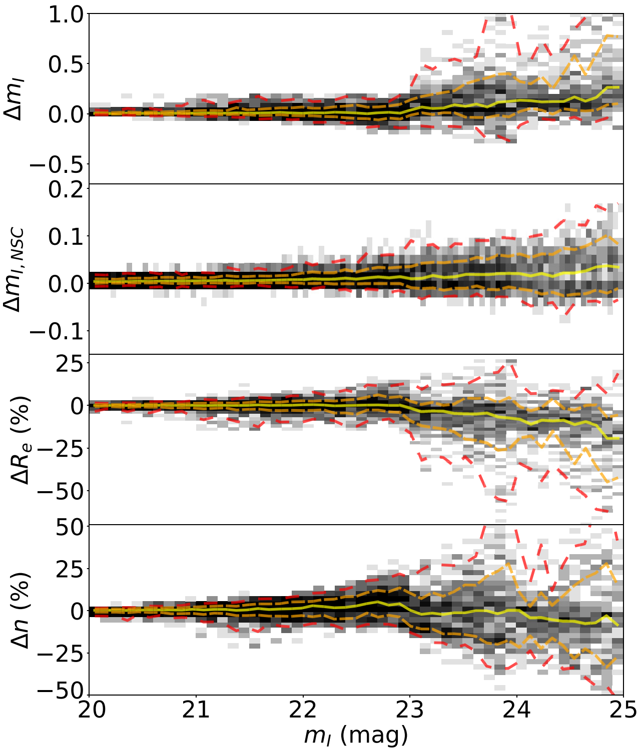

Figure C1. Results of our photometry procedure applied to 10 000 mock galaxies randomly positioned in both *HST*/ACS fields studied in this work; 5000 in the NGC 4874 field and 5000 in the NGC 4889 field. We show the difference between the 'true' and 'fitted' quantities in the form ΔX, where X can be galaxy magnitudes ($m_{I,\rm gal}$), NSC magnitudes ($m_{I,\rm NSC}$), effective radii ($R_{\rm e}$), and Sérsic index (n). For $R_{\rm e}$ and n we show this difference in percentages. In the x-axis, we show 'true' values of $m_{I,\rm gal}$. The grey scale shows the density of galaxies in bins of galaxy magnitude. Solid yellow lines show the median distribution of points, while orange and red dashed lines show the 95 per cent and 68 per cent confidence intervals, respectively.

This paper has been typeset from a TEX/LATEX file prepared by the author.

Appendix B

Press-Release

Aglomerados estelares extragaláticos em ambientes de alta densidade:
Nos ajudando a entender outras galáxias

Emílio Zanatta
Sob Orientação de Ana Chies Santos e Rúben Sánchez-Janssen

Nas nuvens de gás primordiais, todas as estrelas se formam em grupos. *Com o tempo, elas podem se afastar -- como aconteceu com o nosso Sol, que hoje é uma estrela sozinha, sem companheiras que a orbitam. Mas também podem ter nascido em um ambiente tão propício que centenas de milhares de estrelas se formaram quase ao mesmo tempo e permaneceram ligadas pela gravidade, formando o que chamamos de* **aglomerados estelares.**

Aglomerados estelares são conjuntos de estrelas - milhares delas - localizadas muito próximas umas as outras. Eles podem ser de vários tipos -- abertos, globulares, nucleares, inter-galáticos, e afins. **Todas as galáxias que conhecemos possuem os seus.** *Na astronomia, acreditamos que grande parte dos aglomerados de estrelas se formaram a muito tempo, provavelmente junto com as galáxias as quais fazem parte hoje. Este fato faz com que alguns tipos de aglomerados de estrelas, como os globulares, sejam em geral bem velhos e reais* **testemunhas oculares da evolução das galáxias onde habitam**. *Juntando a isto o fato que estes objetos são muito brilhantes, por serem grupos de milhares de estrelas, eles se tornam excelentes ferramentas para estudarmos galáxias distantes, onde não conseguimos mais observar estrelas individuais, que são muito fracas. Porém, ainda temos muitas questões em aberto de como é a natureza desses objetos. Neste trabalho, estudamos duas questões importantes em aberto sobre aglomerados estelares em outras galáxias, em especial dois tipos deles:* **os aglomerados nucleares e os globulares.**

Usando dados do telescópio espacial Hubble, **contamos o número de galáxias no aglomerado de galáxias de Coma que possuem aglomerados estelares nucleares.** *Como esta na figura no canto inferior direito.* **Nós encontramos que em Coma as galáxias tem mais aglomerados nucleares do que em qualquer outro ambiente que temos dados parecidos, como os aglomerados de Virgem e Fornax.** *Nós não sabemos ainda se o ambiente tem um impacto na formação dos aglomerados nucleares, mas este trabalho indica que sim!*

Também estudamos os aglomerados globulares que orbitam as galáxias elítipicas centrais dos aglomerados de Virgem e Hydra. *Esta parte do trabalho teve como motivação testar modelos que o astronomos usam para determinar coisas como as idades e composição química das estrelas. Estes modelos são construídos usando dados de estrelas próximas a nós, dentro da nossa galáxia, a Via Láctea.* **Mas as estrelas em outras galáxias, em especial nos aglomerados globulares, podem não ser sempre parecidas com as estrelas da nossa vizinhança.** *Por isso, neste trabalho, testamos modelos com variações importantes nas abundâncias químicas, especialmente no que chamamos de* **elementos alfa**. *Acredita-se que variações químicas como esta possam ser a chave no que existe de diferente entre as estrelas da nossa galáxia e nos aglomerados dos ambientes mais extremos do Universo, como no centro de* **galáxias gigantes**. *No final, descobrimos que embora um acréscimo na variação de elementos alfa nos aproxime um pouco mais de entender como são as estrelas que compõem os aglomerados globulares em outras galáxias,* **ainda temos muito a aprender.** *Nossos resultados mostram que ainda há inconsistências importantes nos modelos de populações estelares, mas esperamos ter contribuído para apontar a direção onde os esforços para melhora-los devem caminhar.*

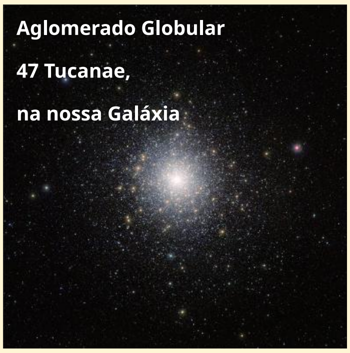

Créditos: ESO/M.-R. Cioni/VISTA

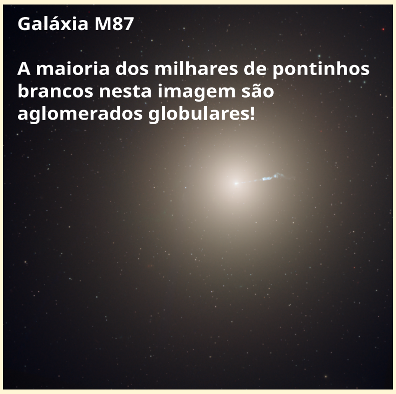

Credits: NASA

Contato: emiliojbzanatta@gmail.com

Bibliography

(2015). *Galactocentric variation of the abundance structure in the Milky Way stellar disk - results from the Gaia-ESO survey.*

Abadi, M. G., Navarro, J. F., Steinmetz, M., and Eke, V. R. (2003). Simulations of Galaxy Formation in a Λ Cold Dark Matter Universe. I. Dynamical and Photometric Properties of a Simulated Disk Galaxy. *Astrophysical Journal*, 591(2):499–514.

Adami, C., Picat, J. P., Savine, C., Mazure, A., West, M. J., Cuillandre, J. C., Pelló, R., Biviano, A., Conselice, C. J., Durret, F., Gallagher, J. S., Gregg, M., Moreau, C., and Ulmer, M. (2006a). Deep and wide field imaging of the Coma cluster: The data. *Astronomy and Astrophysics*, 451(3):1159–1170.

Adami, C., Scheidegger, R., Ulmer, M., Durret, F., Mazure, A., West, M. J., Conselice, C. J., Gregg, M., Kasun, S., Pelló, R., and Picat, J. P. (2006b). A deep wide survey of faint low surface brightness galaxies in the direction of the Coma cluster of galaxies. *Astronomy and Astrophysics*, 459(3):679–692.

Alabi, A. B., Forbes, D. A., Romanowsky, A. J., Brodie, J. P., Strader, J., Janz, J., Usher, C., Spitler, L. R., Bellstedt, S., and Ferré-Mateu, A. (2017). The SLUGGS survey: dark matter fractions at large radii and assembly epochs of early-type galaxies from globular cluster kinematics. *Monthly Notices of the Royal Astronomical Society*, 468(4):3949–3964. arXiv: 1701.05904 tex.adsnote: Provided by the SAO/NASA Astrophysics Data System tex.adsurl: http://adsabs.harvard.edu/abs/2017MNRAS.468.3949A.

Alves-Brito, A., Hau, G. K. T., Forbes, D. A., Spitler, L. R., Strader, J., Brodie, J. P., and

Rhode, K. L. (2011). Spectra of globular clusters in the Sombrero galaxy: evidence for spectroscopic metallicity bimodality. *Monthy Notices of the Royal Astronomical Society*, 417(3):1823–1838.

Alves-Brito, A., Meléndez, J., Asplund, M., Ramírez, I., and Yong, D. (2010). Chemical similarities between Galactic bulge and local thick disk red giants: O, Na, Mg, Al, Si, Ca, and Ti. *Astronomy & Astrophysics*, 513:A35.

Amorisco, N. C. and Loeb, A. (2016). Ultradiffuse galaxies: the high-spin tail of the abundant dwarf galaxy population. *Monthy Notices of the Royal Astronomical Society*, 459(1):L51–L55.

Anderson, J. and Bedin, L. R. (2010). An Empirical Pixel-Based Correction for Imperfect CTE. I. HST 's Advanced Camera for Surveys1 . *Publications of the Astronomical Society of the Pacific*, 122(895):1035–1064.

Antonini, F. (2013). Origin and growth of nuclear star clusters around massive black holes. *The Astrophysical Journal*, 763(1):62. arXiv: 1207.6589 [astro-ph.GA] tex.adsnote: Provided by the SAO/NASA Astrophysics Data System tex.adsurl: https://ui.adsabs.harvard.edu/abs/2013ApJ...763...62A tex.eid: 62.

Antonini, F., Barausse, E., and Silk, J. (2015). The coevolution of nuclear star clusters, massive black holes, and their host galaxies. *The Astrophysical Journal*, 812(1):72. arXiv: 1506.02050 [astro-ph.GA] tex.adsnote: Provided by the SAO/NASA Astrophysics Data System tex.adsurl: https://ui.adsabs.harvard.edu/abs/2015ApJ...812...72A tex.eid: 72.

Arca-Sedda, M. and Capuzzo-Dolcetta, R. (2014). The globular cluster migratory origin of nuclear star clusters. *Monthly Notices of the Royal Astronomical Society*, 444(4):3738–3755. arXiv: 1405.7593 [astro-ph.GA] tex.adsnote: Provided by the SAO/NASA Astrophysics Data System tex.adsurl: https://ui.adsabs.harvard.edu/abs/2014MNRAS.444.3738A.

Arnaboldi, M., Ventimiglia, G., Iodice, E., Gerhard, O., and Coccato, L. (2012). A tale of two tails and an off-centered envelope: diffuse light around the cD galaxy NGC 3311 in the Hydra I cluster. *Astronomy & Astrophysics*, 545:A37.

Ashman, K. M. and Zepf, S. E. (2001). Some constraints on the formation of globular clusters. *The Astronomical Journal*, 122(4):1888–1895. arXiv: astro-ph/0107146 [astro-ph] tex.adsnote: Provided by the SAO/NASA Astrophysics Data System tex.adsurl: https://ui.adsabs.harvard.edu/abs/2001AJ....122.1888A.

Baldassare, V. F., Gallo, E., Miller, B. P., Plotkin, R. M., Treu, T., Valluri, M., and Woo, J. H. (2014). Amuse-field. II. Nucleation of early-type galaxies in the field versus cluster environment. *The Astrophysical Journal*, 791(2):133.

Baldwin, C., McDermid, R. M., Kuntschner, H., Maraston, C., and Conroy, C. (2018). Comparison of stellar population model predictions using optical and infrared spectroscopy. *Monthy Notices of the Royal Astronomical Society*, 473(4):4698–4721.

Barbuy, B., Cantelli, E., Muniz, L., Souza, S. O., Chiappini, C., Hirschi, R., Cescutti, G., Pignatari, M., Ortolani, S., Kerber, L., Maia, F. F. S., Bica, E., and Depagne, E. (2021). UVES analysis of red giants in the bulge globular cluster NGC 6522. *Astronomy & Astrophysics*, 654:A29.

Barmby, P. and Huchra, J. P. (2001). M31 Globular Clusters in the Hubble Space Telescope Archive. I. Cluster Detection and Completeness. *Astronomical Journal*, 122(5):2458–2468.

Bastian, N. and Lardo, C. (2018). Multiple Stellar Populations in Globular Clusters. *Annual Review of Astronomy and Astrophysics*, 56:83–136.

Beasley, M. A., Baugh, C. M., Forbes, D. A., Sharples, R. M., and Frenk, C. S. (2002). On the formation of globular cluster systems in a hierarchical Universe. *\mnras*, 333(2):383–399.

Beasley, M. A., Bridges, T., Peng, E., Harris, W. E., Harris, G. L. H., Forbes, D. A., and Mackie, G. (2008). A 2dF spectroscopic study of globular clusters in NGC 5128: probing the formation history of the nearest giant elliptical. *\mnras*, 386:1443–1463.

Beasley, M. A., Brodie, J. P., Strader, J., Forbes, D. A., Proctor, R. N., Barmby, P., and Huchra, J. P. (2005). The Chemical Properties of Milky Way and M31 Globular Clusters. II. Stellar Population Model Predictions. *Astronomical Journal*, 129(3):1412–1427.

Beasley, M. A., Leaman, R., Gallart, C., Larsen, S., Battaglia, G., Monelli, M., and Pedreros, M. H. (2019). An old, metal-poor globular cluster in Sextans A and the metallicity floor of globular cluster systems. *Mon. Not. R. Astron. Soc.*, 487(2):1986–1993.

Beasley, M. A., Trujillo, I., Leaman, R., and Montes, M. (2018). A single population of red globular clusters around the massive compact galaxy NGC 1277. Nature, 555(7697):483–486.

Beckman, J., Carretero, C., and Vazdekis, A. (2008). The Role of Mergers in Galaxy Evolution. *Chinese Journal of Astronomy and Astrophysics Supplement*, 8(SUPPL.):77–83.

Behroozi, P. S., Wechsler, R. H., Lu, Y., Hahn, O., Busha, M. T., Klypin, A., and Primack, J. R. (2014). Mergers and mass accretion for infalling halos both end well outside cluster virial radii. *The Astrophysical Journal*, 787(2):156. arXiv: 1310.2239 [astro-ph.CO] tex.adsnote: Provided by the SAO/NASA Astrophysics Data System tex.adsurl: https://ui.adsabs.harvard.edu/abs/2014ApJ...787..156B tex.eid: 156.

Bekki, K. (2019). Formation of globular clusters with multiple stellar populations from massive gas clumps in high-z gas-rich dwarf galaxies. *Astronomy & Astrophysics*, 622:A53.

Bekki, K., Beasley, M. A., Brodie, J. P., and Forbes, D. A. (2005). Kinematics of globular cluster systems and the formation of early-type galaxies. *Monthly Notices of the Royal Astronomical Society*, 363(4):1211–1222. tex.adsnote: Provided by the SAO/NASA Astrophysics Data System tex.adsurl: http://adsabs.harvard.edu/abs/2005MNRAS.363.1211B tex.eprint: astro-ph/0509077.

Bekki, K. and Chiba, M. (2004). Formation of giant globular cluster G1 and the origin of the M 31 stellar halo. *Astronomy and Astrophysics*, 417(2):437–442. arXiv: astro-ph/0401229 [astro-ph] tex.adsnote: Provided by the SAO/NASA Astrophysics Data System tex.adsurl: https://ui.adsabs.harvard.edu/abs/2004A&A...417..437B.

Bekki, K., Couch, W. J., and Shioya, Y. (2002). Passive spiral formation from halo gas starvation: Gradual transformation into s0s. *The Astrophysical Journal*, 577(2):651–657. tex.adsnote: Provided by the SAO/NASA Astrophysics Data System tex.adsurl: http://adsabs.harvard.edu/abs/2002ApJ...577..651B tex.eprint: astro-ph/0206207.

Bekki, K., Couch, W. J., and Shioya, Y. (2006). Dissipative transformation of nonnucleated dwarf galaxies into nucleated systems. *The Astrophysical Journal*, 642(2):L133–l136. arXiv: astro-ph/0604340 [astro-ph] tex.adsnote: Provided by the SAO/NASA Astrophysics Data System tex.adsurl: https://ui.adsabs.harvard.edu/abs/2006ApJ...642L.133B.

Bekki, K., Forbes, D. A., Beasley, M. A., and Couch, W. J. (2003). Dynamical evolution of globular cluster systems in clusters of galaxies - I. The case of NGC 1404 in the Fornax cluster. *Monthly Notices of the Royal Astronomical Society*, 344(4):1334–1344. arXiv: astro-ph/0308202 [astro-ph] tex.adsnote: Provided by the SAO/NASA Astrophysics Data System tex.adsurl: https://ui.adsabs.harvard.edu/abs/2003MNRAS.344.1334B.

Bellini, A., Vesperini, E., Piotto, G., Milone, A. P., Hong, J., Anderson, J., van der Marel, R. P., Bedin, L. R., Cassisi, S., D'Antona, F., Marino, A. F., and Renzini, A. (2015). The Hubble Space Telescope UV Legacy Survey of galactic globular clusters. VI. The internal kinematics of the multiple stellar populations in NGC 2808. *ApJ*, 810(1):L13.

Bensby, T., Alves-Brito, A., Oey, M. S., Yong, D., and Meléndez, J. (2010). The first chemical abundance analysis of K giants in the inner Galactic disc. *Astronomy & Astrophysics*, 516:L13.

Bensby, T., Alves-Brito, A., Oey, M. S., Yong, D., and Meléndez, J. (2011). A First Constraint on the Thick Disk Scale Length: Differential Radial Abundances in K Giants at Galactocentric Radii 4, 8, and 12 kpc. *Astrophysical Journal*, 735(2):L46.

Bensby, T., Feltzing, S., and Lundström, I. (2003). Elemental abundance trends in the Galactic thin and thick disks as traced by nearby F and G dwarf stars. *Astronomy & Astrophysics*, 410:527–551.

Bertin, E. (2011). Automated Morphometry with SExtractor and PSFEx. In Evans, I. N., Accomazzi, A., Mink, D. J., and Rots, A. H., editors, *Astronomical Data Analysis Software and Systems XX*, volume 442 of *Astronomical Society of the Pacific Conference Series*, page 435.

Bertin, E. and Arnouts, S. (1996). SExtractor: Software for source extraction. *Astronomy and Astrophysics Supplement Series*, 117(2):393–404. tex.adsnote: Provided by the SAO/NASA Astrophysics Data System tex.adsurl: https://ui.adsabs.harvard.edu/abs/1996A&AS..117..393B.

Bertin, E., Mellier, Y., Radovich, M., Missonnier, G., Didelon, P., and Morin, B. (2002). *The TERAPIX Pipeline*, volume 281 of *Astronomical Society of the Pacific Conference Series*, page 228.

Bertola, F. (2002). Putting galaxies on the scale. *Science*, 295(5553):283–284.

Bessell, M. and Murphy, S. (2012). Spectrophotometric libraries, revised photonic passbands, and zero points for *ubvri* , *hipparcos* , and tycho photometry. *Publications of the Astronomical Society of the Pacific*, 124(912):140–157.

Binggeli, B. and Cameron, L. M. (1991). Dwarf galaxies in the Virgo cluster. I. The systematic photometric properties of early-type dwarfs. *Astronomy and astrophysics (Berlin. Print)*, 252(1):27. tex.adsnote: Provided by the SAO/NASA Astrophysics Data System tex.adsurl: https://ui.adsabs.harvard.edu/abs/1991A&A...252...27B.

Binggeli, B., Tammann, G. A., and Sandage, A. (1987). Studies of the virgo cluster. VI. Morphological and kinematical structure of the virgo cluster. *The Astronomical Journal*, 94:251. tex.adsnote: Provided by the SAO/NASA Astrophysics Data System tex.adsurl: https://ui.adsabs.harvard.edu/abs/1987AJ.....94..251B.

Blakeslee, J. P. (1997). Globular clusters in brightest cluster galaxies. In *American astronomical society meeting abstracts #190*, volume 29 of *Bulletin of the american astronomical society*, page 848. tex.adsnote: Provided by the SAO/NASA Astrophysics Data System tex.adsurl: http://adsabs.harvard.edu/abs/1997AAS...190.5205B tex.eid: 52.05.

Blakeslee, J. P., Anderson, K. R., Meurer, G. R., Benítez, N., and Magee, D. (2003). An Automatic Image Reduction Pipeline for the Advanced Camera for Surveys. In Payne, H., Jedrzejewski, R., and Hook, R., editors, *Astronomical Data Analysis Software and Systems*

XII ASP Conference Series, volume 295 of *Astronomical Society of the Pacific Conference Series*, page 257.

Blakeslee, J. P., Cantiello, M., and Peng, E. W. (2010). The mass-metallicity relation of globular clusters in the context of nonlinear color-metallicty relations. *The Astrophysical Journal*, 710(1):51–63. arXiv: 1001.0979 [astro-ph.CO] tex.adsnote: Provided by the SAO/NASA Astrophysics Data System tex.adsurl: http://adsabs.harvard.edu/abs/2010ApJ...710...51B.

Blakeslee, J. P., Cho, H., Peng, E. W., Ferrarese, L., Jordán, A., and Martel, A. R. (2012). Optical and Infrared Photometry of Globular Clusters in NGC 1399: Evidence for Color-Metallicity Nonlinearity. *\apj*, 746(1):88.

Blanton, M. R. and Roweis, S. (2007). K-Corrections and Filter Transformations in the Ultraviolet, Optical, and Near-Infrared. *Astronomical Journal*, 133(2):734–754.

Bonatto, C., Chies-Santos, A. L., Coelho, P. R. T., Varela, J., Larsen, S. S., Javier Cenarro, A., San Roman, I., Marín-Franch, A., Mendes de Oliveira, C., Molino, A., Ederoclite, A., Cortesi, A., López-Sanjuan, C., Cristóbal-Hornillos, D., Vázquez Ramió, H., Sodré, L., Sampedro, L., Costa-Duarte, M. V., Novais, P. M., Dupke, R., Overzier, R. A., Ribeiro, T., Santos, W. A., and Schoennell, W. (2019). J-PLUS: A wide-field multi-band study of the M 15 globular cluster. Evidence of multiple stellar populations in the RGB. *Astronomy & Astrophysics*, 622:A179.

Borlaff, A., Eliche-Moral, M. C., Rodríguez-Pérez, C., Querejeta, M., Tapia, T., Pérez-González, P. G., Zamorano, J., Gallego, J., and Beckman, J. (2014). Formation of S0 galaxies through mergers. Antitruncated stellar discs resulting from major mergers. *Astronomy and Astrophysics*, 570:A103. arXiv: 1407.5097 tex.adsnote: Provided by the SAO/NASA Astrophysics Data System tex.adsurl: http://adsabs.harvard.edu/abs/2014A%26A...570A.103B tex.eid: A103.

Borne, K. D. and Richstone, D. O. (1991). A Merger Scenario for NGC 7252: A Tale of Two Tails. *Astrophysical Journal*, 369:111.

Boselli, A. (2000). *The History of Star Formation in Normal Late-Type Galaxies*, volume 215 of *Astronomical Society of the Pacific Conference Series*, page 166.

Boselli, A. and Gavazzi, G. (2006). Environmental effects on late-type galaxies in nearby clusters. *Publications of the Astronomical Society of the Pacific*, 118(842):517–559. tex.adsnote: Provided by the SAO/NASA Astrophysics Data System tex.adsurl: http://adsabs.harvard.edu/abs/2006PASP..118..517B tex.eprint: astro-ph/0601108.

Boselli, A., Voyer, E., Boissier, S., Cucciati, O., Consolandi, G., Cortese, L., Fumagalli, M., Gavazzi, G., Heinis, S., Roehlly, Y., and Toloba, E. (2014). The GALEX Ultraviolet Virgo Cluster Survey (GUViCS). IV. The role of the cluster environment on galaxy evolution. *Astronomy & Astrophysics*, 570:A69.

Bothun, G., Impey, C., and McGaugh, S. (1997). Low-Surface-Brightness Galaxies: Hidden Galaxies Revealed. *Publications of the Astronomical Society of the Pacific*, 109:745–758.

Brodie, J. P. and Larsen, S. S. (2002). New members of the cluster family in nearby lenticular galaxies. *The Astronomical Journal*, 124(3):1410–1417. tex.adsnote: Provided by the SAO/NASA Astrophysics Data System tex.adsurl: http://adsabs.harvard.edu/abs/2002AJ....124.1410B tex.eprint: astro-ph/0203454.

Brodie, J. P., Larsen, S. S., and Kissler-Patig, M. (2000a). A New Look at Globular Cluster Colors in NGC 3311 and the Case for Exclusively Metal-rich Globular Cluster Systems. *The Astrophysical Journal*, 543(1):L19–L22.

Brodie, J. P., Larsen, S. S., and Kissler-Patig, M. (2000b). A New Look at Globular Cluster Colors in NGC 3311 and the Case for Exclusively Metal-rich Globular Cluster Systems. *Astrophys. J.*, 543(1):L19–l22.

Brodie, J. P., Romanowsky, A. J., Strader, J., Forbes, D. A., Foster, C., Jennings, Z. G., Pastorello, N., Pota, V., Usher, C., Blom, C., Kader, J., Roediger, J. C., Spitler, L. R., Villaume, A., Arnold, J. A., Kartha, S. S., and Woodley, K. A. (2014). The SAGES legacy unifying globulars and GalaxieS survey (SLUGGS): Sample definition, methods, and initial results. *The Astrophysical Journal*, 796(1):52. arXiv: 1405.2079 tex.adsnote: Provided by the SAO/NASA

Astrophysics Data System tex.adsurl: http://adsabs.harvard.edu/abs/2014ApJ...796...52B tex.eid: 52.

Brodie, J. P. and Strader, J. (2006). Extragalactic Globular Clusters and Galaxy Formation. *\araa*, 44:193–267.

Bruzual, G. and Charlot, S. (2003). Stellar population synthesis at the resolution of 2003. *Monthly Notices of the Royal Astronomical Society*, 344(4):1000–1028. arXiv: astro-ph/0309134 [astro-ph] tex.adsnote: Provided by the SAO/NASA Astrophysics Data System tex.adsurl: https://ui.adsabs.harvard.edu/abs/2003MNRAS.344.1000B.

Böker, T., Laine, S., van der Marel, R. P., Sarzi, M., Rix, H.-W., Ho, L. C., and Shields, J. C. (2002). A hubble space telescope census of nuclear star clusters in late-type spiral galaxies. I. Observations and image analysis. 123(3):1389–1410. arXiv: astro-ph/0112086 [astro-ph] tex.adsnote: Provided by the SAO/NASA Astrophysics Data System tex.adsurl: https://ui.adsabs.harvard.edu/abs/2002AJ....123.1389B.

Caldwell, N., Schiavon, R., Morrison, H., Rose, J. A., and Harding, P. (2011). Star Clusters in M31. II. Old Cluster Metallicities and Ages from Hectospec Data. *Astronomical Journal*, 141(2):61.

Cantiello, M. and Blakeslee, J. P. (2007). On the Metallicity-Color Relations and Bimodal Color Distributions in Extragalactic Globular Cluster Systems. *\apj*, 669(2):982–989.

Cantiello, M., Blakeslee, J. P., Raimondo, G., Chies-Santos, A. L., Jennings, Z. G., Norris, M. A., and Kuntschner, H. (2014). Globular clusters of NGC 3115 in the near-infrared. Demonstrating the correctness of two opposing scenarios. *\aap*, 564:L3.

Cantiello, M., Grado, A., Rejkuba, M., Arnaboldi, M., Capaccioli, M., Greggio, L., Iodice, E., and Limatola, L. (2018). A vst and vista study of globular clusters in ngc 253. *A&a*, 611:A21.

Carlsten, S. G., Greco, J. P., Beaton, R. L., and Greene, J. E. (2020a). Wide-field Survey of Dwarf Satellite Systems around 10 Hosts in the Local Volume. *The Astrophysical Journal*, 891(2):144.

Carlsten, S. G., Greene, J. E., Beaton, R. L., and Greco, J. P. (2021). ELVES II: GCs and Nuclear Star Clusters of Dwarf Galaxies; The Importance of Environment. *arXiv e-prints*, page arXiv:2105.03440.

Carlsten, S. G., Greene, J. E., Peter, A. H. G., Greco, J. P., and Beaton, R. L. (2020b). Radial Distributions of Dwarf Satellite Systems in the Local Volume. *The Astrophysical Journal*, 902(2):124.

Carollo, C. M., Stiavelli, M., and Mack, J. (1998). Spiral galaxies with WFPC2. II. The nuclear properties of 40 objects. *The Astronomical Journal*, 116(1):68–84. arXiv: astro-ph/9804007 [astro-ph] tex.adsnote: Provided by the SAO/NASA Astrophysics Data System tex.adsurl: https://ui.adsabs.harvard.edu/abs/1998AJ....116...68C.

Carter, D., Goudfrooij, P., Mobasher, B., Ferguson, H. C., Puzia, T. H., Aguerri, A. L., Balcells, M., Batcheldor, D., Bridges, T. J., Davies, J. I., Erwin, P., Graham, A. W., Guzmán, R., Hammer, D., Hornschemeier, A., Hoyos, C., Hudson, M. J., Huxor, A., Jogee, S., Komiyama, Y., Lotz, J., Lucey, J. R., Marzke, R. O., Merritt, D., Miller, B. W., Miller, N. A., Mouhcine, M., Okamura, S., Peletier, R. F., Phillipps, S., Poggianti, B. M., Sharples, R. M., Smith, R. J., Trentham, N., Tully, R. B., Valentijn, E., and Verdoes Kleijn, G. (2008). The hubble space telescope advanced camera for surveys coma cluster survey. I. Survey objectives and design. *The Astrophysical Journal Supplement Series*, 176(2):424–437. arXiv: 0801.3745 [astro-ph] tex.adsnote: Provided by the SAO/NASA Astrophysics Data System tex.adsurl: https://ui.adsabs.harvard.edu/abs/2008ApJS..176..424C.

Casali, M., Pirard, J.-F., Kissler-Patig, M., Moorwood, A., Bedin, L., Biereichel, P., Delabre, B., Dorn, R., Finger, G., Gojak, D., Huster, G., Jung, Y., Koch, F., Lizon, J.-L., Mehrgan, L., Pozna, E., Silber, A., Sokar, B., and Stegmeier, J. (2006). HAWK-I: the new wide-field IR imager for the VLT. In *Ground-based and Airborne Instrumentation for Astronomy*, volume 6269, page 62690w.

Cenarro, A. J., Cardiel, N., Gorgas, J., Peletier, R. F., Vazdekis, A., and Prada, F. (2001). Empirical calibration of the near-infrared Ca ii triplet - I. The stellar library and index definition. *Monthy Notices of the Royal Astronomical Society*, 326(3):959–980.

Ceverino, D., Dekel, A., Tweed, D., and Primack, J. (2015). Early formation of massive, compact, spheroidal galaxies with classical profiles by violent disc instability or mergers. *Monthly Notices of the Royal Astronomical Society*, 447(4):3291–3310. arXiv: 1409.2622 tex.adsnote: Provided by the SAO/NASA Astrophysics Data System tex.adsurl: http://adsabs.harvard.edu/abs/2015MNRAS.447.3291C.

Chiboucas, K., Jacobs, B. A., Tully, R. B., and Karachentsev, I. D. (2013). Confirmation of faint dwarf galaxies in the M81 group. *Astronomical Journal*, 146(5):126. arXiv: 1309.4130 [astro-ph.CO] tex.adsnote: Provided by the SAO/NASA Astrophysics Data System tex.adsurl: https://ui.adsabs.harvard.edu/abs/2013AJ....146..126C tex.eid: 126.

Chies-Santos, A. L., Cortesi, A., Fantin, D. S. M., Merrifield, M. R., Bamford, S., and Serra, P. (2013). The nature of faint fuzzies from the kinematics of NGC 1023. *Astronomy and Astrophysics Review*, 559:A67. arXiv: 1310.4508 tex.adsnote: Provided by the SAO/NASA Astrophysics Data System tex.adsurl: http://adsabs.harvard.edu/abs/2013A%26A...559A..67C tex.eid: A67.

Chies-Santos, A. L., Larsen, S. S., Cantiello, M., Strader, J., Kuntschner, H., Wehner, E. M., and Brodie, J. P. (2012). An optical/NIR survey of globular clusters in early-type galaxies. III. On the colour bimodality of globular cluster systems. *Astronomy & Astrophysics*, 539:A54.

Chies-Santos, A. L., Larsen, S. S., Cantiello, M., Strader, J., Kuntschner, H., Wehner, E. M., and Brodie, J. P. (2012a). An optical/NIR survey of globular clusters in early-type galaxies: III. on the colour bimodality of globular cluster systems. *Astronomy and Astrophysics*, 539:A54.

Chies-Santos, A. L., Larsen, S. S., Cantiello, M., Strader, J., Kuntschner, H., Wehner, E. M., and Brodie, J. P. (2012b). An optical/NIR survey of globular clusters in early-type galaxies. III. On the colour bimodality of globular cluster systems. *\aap*, 539:A54.

Chies-Santos, A. L., Larsen, S. S., Kuntschner, H., Anders, P., Wehner, E. M., Strader, J., Brodie, J. P., and Santos, J. F. C. (2011a). An optical/NIR survey of globular clusters in early-type galaxies. II. Ages of globular cluster systems and the relation to galaxy morphology. \ *aap*, 525:A20.

Chies-Santos, A. L., Larsen, S. S., Wehner, E. M., Kuntschner, H., Strader, J., and Brodie, J. P. (2011b). An optical/NIR survey of globular clusters in early-type galaxies. I. Introduction and data reduction procedures. \ *aap*, 525:A19.

Chies-Santos, A. L., Larsen, S. S., Wehner, E. M., Kuntschner, H., Strader, J., and Brodie, J. P. (2011c). An optical/NIR survey of globular clusters in early-type galaxies. I. Introduction and data reduction procedures. *Astronomy and Astrophysics*, 525(1):A19. arXiv: 1010.0687 tex.adsnote: Provided by the SAO/NASA Astrophysics Data System tex.adsurl: http://adsabs.harvard.edu/abs/2011A%26A...525A..19C tex.eid: A19.

Chies-Santos, A. L., Santiago, B. X., and Pastoriza, M. G. (2007). High resolution imaging of the early-type galaxy NGC 1380: an insight into the nature of extended extragalactic star clusters. *Astronomy & Astrophysics*, 467(3):1003–1009.

Chiosi, C. and Carraro, G. (2002). Formation and evolution of elliptical galaxies. *Monthy Notices of the Royal Astronomical Society*, 335(2):335–357.

Cho, H., Blakeslee, J. P., Chies-Santos, A. L., Jee, M. J., Jensen, J. B., Peng, E. W., and Lee, Y.-W. (2016). The Globular Cluster System of the Coma cD Galaxy NGC 4874 from Hubble Space Telescope ACS and WFC3/IR Imaging. \ *apj*, 822(2):95.

Choi, J., Conroy, C., and Johnson, B. D. (2019). The imprint of element abundance patterns on quiescent galaxy spectral energy distributions. *The Astrophysical Journal*, 872(2):136. arXiv: 1901.06391 [astro-ph.GA] tex.adsnote: Provided by the SAO/NASA Astrophysics Data System tex.adsurl: https://ui.adsabs.harvard.edu/abs/2019ApJ...872..136C tex.eid: 136.

Choi, J., Dotter, A., Conroy, C., Cantiello, M., Paxton, B., and Johnson, B. D. (2016). Mesa Isochrones and Stellar Tracks (MIST). I. Solar-scaled Models. *Astrophysical Journal*, 823(2):102.

Cleveland, W. S., Grosse, E., and Shyu, W. M. (1992). Wadsworth & Brooks/Cole.

Coccato, L., Gerhard, O., Arnaboldi, M., and Ventimiglia, G. (2011). Stellar population and the origin of intra-cluster stars around brightest cluster galaxies: the case of NGC 3311. *ArXiv11083834 Astro-Ph*, 533.

Coccato, L., Jaffé, Y. L., Cortesi, A., Merrifield, M., Johnston, E., Rodríguez del Pino, B., Haeussler, B., Chies-Santos, A. L., Mendes de Oliveira, C. L., Sheen, Y.-K., and Menéndez-Delmestre, K. (2020). Formation of S0s in extreme environments I: clues from kinematics and stellar populations. *Monthy Notices of the Royal Astronomical Society*, 492(2):2955–2972.

Coelho, P., Barbuy, B., Meléndez, J., Schiavon, R. P., and Castilho, B. V. (2005). A library of high resolution synthetic stellar spectra from 300 nm to 1.8 μm with solar and α-enhanced composition. *Astronomy & Astrophysics*, 443(2):735–746.

Coelho, P., Bruzual, G., Charlot, S., Weiss, A., Barbuy, B., and Ferguson, J. W. (2007). Spectral models for solar-scaled and α-enhanced stellar populations. *Monthy Notices of the Royal Astronomical Society*, 382(2):498–514.

Coelho, P. R. T. (2014). A new library of theoretical stellar spectra with scaled-solar and α-enhanced mixtures. *Monthy Notices of the Royal Astronomical Society*, 440(2):1027–1043.

Cohen, J. G. (1988). The Globular Cluster Systems of Three Virgo Ellipticals. *Astronomical Journal*, 95:682.

Cohen, J. G., Blakeslee, J. P., and Côté, P. (2003). The Ages and Abundances of a Sample of Globular Clusters in M49 (NGC 4472). *\apj*, 592(2):866–883.

Cohen, J. G., Blakeslee, J. P., and Ryzhov, A. (1998). The Ages and Abundances of a Large Sample of M87 Globular Clusters. *\apj*, 496(2):808–826.

Conroy, C., Graves, G. J., and van Dokkum, P. G. (2014). Early-type Galaxy Archeology: Ages, Abundance Ratios, and Effective Temperatures from Full-spectrum Fitting. *Astrophysical Journal*, 780(1):33.

Conroy, C. and Gunn, J. E. (2010). The Propagation Of Uncertainties In Stellar Population

Synthesis Modeling. Iii. Model Calibration, Comparison, And Evaluation. *Astrophys. J.*, 712(2):833–857.

Conroy, C., Gunn, J. E., and White, M. (2009). The propagation of uncertainties in stellar population synthesis modeling. I. The relevance of uncertain aspects of stellar evolution and the initial mass function to the derived physical properties of galaxies. *The Astrophysical Journal*, 699(1):486–506. arXiv: 0809.4261 [astro-ph] tex.adsnote: Provided by the SAO/NASA Astrophysics Data System tex.adsurl: https://ui.adsabs.harvard.edu/abs/2009ApJ...699..486C.

Conroy, C. and van Dokkum, P. G. (2012). The Stellar Initial Mass Function in Early-type Galaxies From Absorption Line Spectroscopy. II. Results. *Astrophysical Journal*, 760(1):71.

Conroy, C., Villaume, A., van Dokkum, P. G., and Lind, K. (2018). Metal-rich, Metal-poor: Updated Stellar Population Models for Old Stellar Systems. *Astrophysical Journal*, 854(2):139.

Cordoni, G., Milone, A. P., Mastrobuono-Battisti, A., Marino, A. F., Lagioia, E. P., and Tailo, M. (2019). Kinematics of Multiple Stellar Populations in Globular Clusters with Gaia. *arXiv e-prints*, page arXiv:1908.11692.

Cortesi, A., Chies-Santos, A. L., Pota, V., Foster, C., Coccato, L., Mendes de Oliveira, C., Forbes, D. A., Merrifield, M. M., Bamford, S. P., Romanowsky, A. J., Brodie, J. P., Kartha, S. S., Alabi, A. B., Proctor, R. N., and Almeida, A. (2016). The SLUGGS survey: chromodynamical modelling of the lenticular galaxy NGC 1023. *\mnras*, 456(3):2611–2621.

Cortesi, A., Merrifield, M. R., Coccato, L., Arnaboldi, M., Gerhard, O., Bamford, S., Napolitano, N. R., Romanowsky, A. J., Douglas, N. G., Kuijken, K., Capaccioli, M., Freeman, K. C., Saha, K., and Chies-Santos, A. L. (2013). Planetary Nebula Spectrograph survey of S0 galaxy kinematics - II. Clues to the origins of S0 galaxies. *Monthy Notices of the Royal Astronomical Society*, 432(2):1010–1020.

Côté, P., Marzke, R. O., and West, M. J. (1998). The Formation of Giant Elliptical Galaxies and Their Globular Cluster Systems. *Astrophysical Journal*, 501(2):554–570.

Cushing, M. C., Rayner, J. T., and Vacca, W. D. (2005). An Infrared Spectroscopic Sequence of M, L, and T Dwarfs. *Astrophysical Journal*, 623(2):1115–1140.

Côté, P., McLaughlin, D. E., Cohen, J. G., and Blakeslee, J. P. (2003). Dynamics of the globular cluster system associated with M49 (NGC 4472): Cluster orbital properties and the distribution of dark matter. *The Astrophysical Journal*, 591(2):850–877. tex.adsnote: Provided by the SAO/NASA Astrophysics Data System tex.adsurl: http://adsabs.harvard.edu/abs/2003ApJ...591..850C tex.eprint: astro-ph/0303229.

Côté, P., Piatek, S., Ferrarese, L., Jordán, A., Merritt, D., Peng, E. W., Hasegan, M., Blakeslee, J. P., Mei, S., West, M. J., Milosavljević, M., and Tonry, J. L. (2006). The ACS virgo cluster survey. VIII. The nuclei of early-type galaxies. *The Astrophysical Journal Supplement Series*, 165(1):57–94. arXiv: astro-ph/0603252 [astro-ph] tex.adsnote: Provided by the SAO/NASA Astrophysics Data System tex.adsurl: https://ui.adsabs.harvard.edu/abs/2006ApJS..165...57C.

Dalal, N., White, M., Bond, J. R., and Shirokov, A. (2008). Halo assembly bias in hierarchical structure formation. *The Astrophysical Journal*, 687(1):12–21. arXiv: 0803.3453 [astro-ph] tex.adsnote: Provided by the SAO/NASA Astrophysics Data System tex.adsurl: https://ui.adsabs.harvard.edu/abs/2008ApJ...687...12D.

Dalcanton, J. J., Spergel, D. N., Gunn, J. E., Schmidt, M., and Schneider, D. P. (1997). The Number Density of Low-Surface Brightness Galaxies with 23 < mu_0 < 25 V Mag/arcsec$\hat{2}$. *Astronomical Journal*, 114:635–654.

Dantas, M. L., Coelho, P. R., de Souza, R. S., and Gonçalves, T. S. (2020). UV bright red-sequence galaxies: How do UV upturn systems evolve in redshift and stellar mass? *Monthly Notices of the Royal Astronomical Society*, 492(2):2996–3011.

Davis, M., Efstathiou, G., Frenk, C. S., and White, S. D. M. (1985). The evolution of large-scale structure in a universe dominated by cold dark matter. *The Astrophysical Journal*, 292:371–394. tex.adsnote: Provided by the SAO/NASA Astrophysics Data System tex.adsurl: https://ui.adsabs.harvard.edu/abs/1985ApJ...292..371D.

de Souza, R. S., Cameron, E., Killedar, M., Hilbe, J., Vilalta, R., Maio, U., Biffi, V., Ciardi, B., and Riggs, J. D. (2015). The overlooked potential of Generalized Linear Models in astronomy, I: Binomial regression. *Astronomy and Computing*, 12(0):21–32.

de Souza, R. S., Dantas, M. L., Krone-Martins, A., Cameron, E., Coelho, P., Hattab, M. W., de Val-Borro, M., Hilbe, J. M., Elliott, J., and Hagen, A. (2016). Is the cluster environment quenching the Seyfert activity in elliptical and spiral galaxies? *Monthly Notices of the Royal Astronomical Society*, 461(2):2115–2125.

de Vaucouleurs, G., de Vaucouleurs, A., Corwin, Herold G., J., Buta, R. J., Paturel, G., and Fouque, P. (1991). *Third Reference Catalogue of Bright Galaxies.*

den Brok, M., Peletier, R. F., Seth, A., Balcells, M., Dominguez, L., Graham, A. W., Carter, D., Erwin, P., Ferguson, H. C., Goudfrooij, P., Guzmán, R., Hoyos, C., Jogee, S., Lucey, J., Phillipps, S., Puzia, T., Valentijn, E., Verdoes Kleijn, G., and Weinzirl, T. (2014). The HST/ACS Coma Cluster Survey - X. Nuclear star clusters in low-mass early-type galaxies: scaling relations. *Monthly Notices of the Royal Astronomical Society*, 445(3):2385–2403. arXiv: 1409.4766 [astro-ph.GA] tex.adsnote: Provided by the SAO/NASA Astrophysics Data System tex.adsurl: https://ui.adsabs.harvard.edu/abs/2014MNRAS.445.2385D.

Di Matteo, P. (2016). The Disc Origin of the Milky Way Bulge. *Publications of the Astron. Soc. of Australia*, 33:e027.

Dotter, A. (2016). MESA Isochrones and Stellar Tracks (MIST) 0: Methods for the Construction of Stellar Isochrones. *Astrophysical Journal, Supplement*, 222(1):8.

Dotter, A., Conroy, C., Cargile, P., and Asplund, M. (2017). The Influence of Atomic Diffusion on Stellar Ages and Chemical Tagging. *Astrophysical Journal*, 840(2):99.

Dressler, A. (1980). Galaxy morphology in rich clusters - Implications for the formation and evolution of galaxies. *The Astrophysical Journal*, 236:351–365. tex.adsnote: Provided by the SAO/NASA Astrophysics Data System tex.adsurl: http://adsabs.harvard.edu/abs/1980ApJ...236..351D.

Dressler, A., Oemler, Jr., A., Couch, W. J., Smail, I., Ellis, R. S., Barger, A., Butcher, H., Poggianti, B. M., and Sharples, R. M. (1997). Evolution since z = 0.5 of the morphology-density relation for clusters of galaxies. *The Astrophysical Journal*, 490(2):577–591. tex.adsnote: Provided by the SAO/NASA Astrophysics Data System tex.adsurl: http://adsabs.harvard.edu/abs/1997ApJ...490..577D tex.eprint: astro-ph/9707232.

Drinkwater, M. J., Gregg, M. D., and Colless, M. (2001). Substructure and Dynamics of the Fornax Cluster. *The Astrophysical Journal*, 548(2):L139–L142.

Drinkwater, M. J., Gregg, M. D., Hilker, M., Bekki, K., Couch, W. J., Ferguson, H. C., Jones, J. B., and Phillipps, S. (2003). A class of compact dwarf galaxies from disruptive processes in galaxy clusters. 423(6939):519–521. arXiv: astro-ph/0306026 [astro-ph] tex.adsnote: Provided by the SAO/NASA Astrophysics Data System tex.adsurl: https://ui.adsabs.harvard.edu/abs/2003Natur.423..519D.

Drinkwater, M. J., Jones, J. B., Gregg, M. D., and Phillipps, S. (2000). Compact stellar systems in the fornax cluster: Super-massive star clusters or extremely compact dwarf galaxies? 17(3):227–233. arXiv: astro-ph/0002003 [astro-ph] tex.adsnote: Provided by the SAO/NASA Astrophysics Data System tex.adsurl: https://ui.adsabs.harvard.edu/abs/2000PASA...17..227D.

Durrell, P. R., Côté, P., Peng, E. W., Blakeslee, J. P., Ferrarese, L., Mihos, J. C., Puzia, T. H., Lançon, A., Liu, C., Zhang, H., Cuillandre, J.-C., McConnachie, A., Jordan, A., Accetta, K., Boissier, S., Boselli, A., Courteau, S., Duc, P.-A., Emsellem, E., Gwyn, S., Mei, S., and Taylor, J. E. (2014). The Next Generation Virgo Cluster Survey. VIII. The Spatial Distribution of Globular Clusters in the Virgo Cluster. *ApJ*, 794(2):103.

Ebeling, H. and Kalita, B. S. (2019). Jellyfish: Ram Pressure Stripping As a Diagnostic Tool in Studies of Cluster Collisions. *ApJ*, 882(2):127.

Eigenthaler, P., Puzia, T. H., Taylor, M. A., Ordenes-Briceño, Y., Muñoz, R. P., Ribbeck, K. X., Alamo-Martínez, K. A., Zhang, H., Ángel, S., Capaccioli, M., Côté, P., Ferrarese, L., Galaz, G., Grebel, E. K., Hempel, M., Hilker, M., Lançon, A., Mieske, S., Miller, B., Paolillo, M., Powalka, M., Richtler, T., Roediger, J., Rong, Y., Sánchez-Janssen, R., and

Spengler, C. (2018). The Next Generation Fornax Survey (NGFS). II. The Central Dwarf Galaxy Population. *The Astrophysical Journal*, 855(2):142.

Elmegreen, B. G. and Efremov, Y. N. (1997). A universal formation mechanism for open and globular clusters in turbulent gas. 480(1):235–245. tex.adsnote: Provided by the SAO/NASA Astrophysics Data System tex.adsurl: https://ui.adsabs.harvard.edu/abs/1997ApJ...480..235E.

Eso (2012). GASGANO: Data File Organizer.

ESO CPL Development Team (2015). EsoRex: ESO Recipe Execution Tool.

Fahrion, K., Lyubenova, M., van de Ven, G., Leaman, R., Hilker, M., Martín-Navarro, I., Zhu, L., Alfaro-Cuello, M., Coccato, L., Corsini, E. M., Falcón-Barroso, J., Iodice, E., McDermid, R. M., Sarzi, M., and de Zeeuw, T. (2019). Constraining nuclear star cluster formation using MUSE-AO observations of the early-type galaxy FCC 47. *Astronomy and Astrophysics*, 628:A92. arXiv: 1907.01007 [astro-ph.GA] tex.adsnote: Provided by the SAO/NASA Astrophysics Data System tex.adsurl: https://ui.adsabs.harvard.edu/abs/2019A&A...628A..92F tex.eid: A92.

Fahrion, K., Müller, O., Rejkuba, M., Hilker, M., Lyubenova, M., Van De Ven, G., Georgiev, I. Y., Lelli, F., Pawlowski, M. S., and Jerjen, H. (2020). Metal-poor nuclear star clusters in two dwarf galaxies near Centaurus A suggesting formation from the in-spiraling of globular clusters. *Astronomy and Astrophysics*, 634:A53.

Faifer, F. R., Forte, J. C., Norris, M. A., Bridges, T., Forbes, D. A., Zepf, S. E., Beasley, M., Gebhardt, K., Hanes, D. A., and Sharples, R. M. (2011). Gemini/GMOS imaging of globular cluster systems in five early-type galaxies. *\mnras*, 416(1):155–177.

Falcón-Barroso, J., Sánchez-Blázquez, P., Vazdekis, A., Ricciardelli, E., Cardiel, N., Cenarro, A. J., Gorgas, J., and Peletier, R. F. (2011). An updated MILES stellar library and stellar population models. *Astronomy & Astrophysics*, 532:A95.

Feltzing, S. and Gilmore, G. (2000). Age and metallicity gradients in the Galactic Bulge. A differential study using HST/WFPC2. *Astronomy & Astrophysics*, 355(1-4):949–965.

Ferguson, H. C. and Sandage, A. (1989). The spatial distributions and intrinsic shapes of dwarf elliptical galaxies in the Virgo and Fornax Clusters. *The Astrophysical Journal*, 346:L53.

Ferrarese, L., Côté, P., MacArthur, L. A., Durrell, P. R., Gwyn, S. D. J., Duc, P.-A., Sánchez-Janssen, R., Santos, M., Blakeslee, J. P., Boselli, A., Boyer, F., Cantiello, M., Courteau, S., Cuillandre, J.-C., Emsellem, E., Erben, T., Gavazzi, G., Guhathakurta, P., Huertas-Company, M., Jordán, A., Lançon, A., Liu, C., Mei, S., Mihos, J. C., Peng, E. W., Puzia, T. H., Roediger, J., Schade, D., Taylor, J. E., Toloba, E., and Zhang, H. (2020). The Next Generation Virgo Cluster Survey (NGVS). XIV. The Discovery of Low-mass Galaxies and a New Galaxy Catalog in the Core of the Virgo Cluster. *The Astrophysical Journal*, 890(2):128.

Ferrarese, L., Côté, P., Cuilland re, J.-C., Gwyn, S. D. J., Peng, E. W., MacArthur, L. A., Duc, P.-A., Boselli, A., Mei, S., Erben, T., McConnachie, A. W., Durrell, P. R., Mihos, J. C., Jordán, A., Lançon, A., Puzia, T. H., Emsellem, E., Balogh, M. L., Blakeslee, J. P., van Waerbeke, L., Gavazzi, R., Vollmer, B., Kavelaars, J. J., Woods, D., Ball, N. M., Boissier, S., Courteau, S., Ferriere, E., Gavazzi, G., Hildebrandt, H., Hudelot, P., Huertas-Company, M., Liu, C., McLaughlin, D., Mellier, Y., Milkeraitis, M., Schade, D., Balkowski, C., Bournaud, F., Carlberg, R. G., Chapman, S. C., Hoekstra, H., Peng, C., Sawicki, M., Simard, L., Taylor, J. E., Tully, R. B., van Driel, W., Wilson, C. D., Burdullis, T., Mahoney, B., and Manset, N. (2012). The next generation virgo cluster survey (NGVS). I. Introduction to the survey. *Astrophysical Journal, Supplement Series*, 200(1):4. tex.adsnote: Provided by the SAO/NASA Astrophysics Data System tex.adsurl: https://ui.adsabs.harvard.edu/abs/2012ApJS..200....4F tex.eid: 4.

Ferrarese, L., Côté, P., Sánchez-Janssen, R., Roediger, J., McConnachie, A. W., Durrell, P. R., MacArthur, L. A., Blakeslee, J. P., Duc, P.-A., Boissier, S., Boselli, A., Courteau, S., Cuillandre, J.-C., Emsellem, E., Gwyn, S. D. J., Guhathakurta, P., Jordán, A., Lançon, A., Liu, C., Mei, S., Mihos, J. C., Navarro, J. F., Peng, E. W., Puzia, T. H., Taylor, J. E., Toloba, E., and Zhang, H. (2016). The next generation virgo cluster survey (NGVS). XIII. The luminosity and mass function of galaxies in the core of the virgo cluster and the contribution from disrupted satellites. *The Astrophysical Journal*, 824(1):10. arXiv: 1604.06462 [astro-ph.GA] tex.adsnote: Provided by the SAO/NASA Astrophysics Data System tex.adsurl: https://ui.adsabs.harvard.edu/abs/2016ApJ...824...10F tex.eid: 10.

Fisher, D. B., Glazebrook, K., Abraham, R. G., Damjanov, I., White, H. A., Obreschkow, D., Basset, R., Bekiaris, G., Wisnioski, E., Green, A., and Bolatto, A. D. (2017). Connecting clump sizes in turbulent disk galaxies to instability theory. *arXiv*, 839:L5. arXiv: 1703.00458 tex.adsnote: Provided by the SAO/NASA Astrophysics Data System tex.adsurl: http://adsabs.harvard.edu/abs/2017ApJ...839L...5F tex.eid: L5.

Fitzpatrick, P. J. and Graves, G. J. (2015). Early-type galaxy star formation histories in different environments. *Monthy Notices of the Royal Astronomical Society*, 447(2):1383–1397.

Forbes, D. A., Almeida, A., Spitler, L. R., and Pota, V. (2014). Extended star clusters in NGC 1023 from HST/ACS mosaic imaging. *Monthly Notices of the Royal Astronomical Society*, 442(2):1049–1053. arXiv: 1405.2578 tex.adsnote: Provided by the SAO/NASA Astrophysics Data System tex.adsurl: http://adsabs.harvard.edu/abs/2014MNRAS.442.1049F.

Forbes, D. A., Brodie, J. P., and Grillmair, C. J. (1997). On the origin of globular clusters in elliptical and cD galaxies. *The Astronomical Journal*, 113:1652. tex.adsnote: Provided by the SAO/NASA Astrophysics Data System tex.adsurl: http://adsabs.harvard.edu/abs/1997AJ....113.1652F tex.eprint: astro-ph/9702146.

Forbes, D. A., Brodie, J. P., and Larsen, S. S. (2001). Bulge globular clusters in spiral galaxies. *The Astrophysical Journal*, 556(2):L83–l86. tex.adsnote: Provided by the SAO/NASA Astrophysics Data System tex.adsurl: http://adsabs.harvard.edu/abs/2001ApJ...556L..83F tex.eprint: astro-ph/0106459.

Forte, J. C., Geisler, D., Ostrov, P. G., Piatti, A. E., and Gieren, W. (2001). The globular cluster system of the low-luminosity elliptical galaxy NGC 1427. *The Astronomical Journal*, 121(4):1992–2002. tex.adsnote: Provided by the SAO/NASA Astrophysics Data System tex.adsurl: http://adsabs.harvard.edu/abs/2001AJ....121.1992F.

Foster, C., Spitler, L. R., Romanowsky, A. J., Forbes, D. A., Pota, V., Bekki, K., Strader, J., Proctor, R. N., Arnold, J. A., and Brodie, J. P. (2011). Global properties of 'ordinary' early-type galaxies: photometry and spectroscopy of stars and globular clusters in NGC 4494. *Monthly Notices of the Royal Astronomical Society*, 415(4):3393–3416. arXiv: 1104.5503 tex.adsnote: Provided by the SAO/NASA Astrophysics Data System tex.adsurl: http://adsabs.harvard.edu/abs/2011MNRAS.415.3393F.

Fujii, M. S., Saitoh, T. R., and Portegies Zwart, S. F. (2012). The Formation of Young Dense Star Clusters through Mergers. *Astrophysical Journal*, 753(1):85.

Gajda, G., Gerhard, O., Blaña, M., Zhu, L., Shen, J., Saglia, R. P., and Bender, R. (2021). Unravelling stellar populations in the Andromeda Galaxy. *Astronomy & Astrophysics*, 647:A131.

Gao, L. and White, S. D. M. (2007). Assembly bias in the clustering of dark matter haloes. *Monthy Notices of the Royal Astronomical Society*, 377(1):L5–L9.

Garland, C. A., Pisano, D. J., Mac Low, M.-M., Kreckel, K., Rabidoux, K., and Guzmán, R. (2015). Nearby clumpy, gas rich, star-forming galaxies: Local analogs of high-redshift clumpy galaxies. *The Astrophysical Journal*, 807(2):134. arXiv: 1506.04649 tex.adsnote: Provided by the SAO/NASA Astrophysics Data System tex.adsurl: http://adsabs.harvard.edu/abs/2015ApJ...807..134G tex.eid: 134.

Gavazzi, G., Boselli, A., Donati, A., Franzetti, P., and Scodeggio, M. (2003). Introducing GOLDMine: A new galaxy database on the WEB. *Astronomy & Astrophysics*, 400(2):451–455.

Gavazzi, G., Donati, A., Cucciati, O., Sabatini, S., Boselli, A., Davies, J., and Zibetti, S. (2005). The structure of elliptical galaxies in the Virgo cluster. Results from the INT Wide Field Survey. *Astronomy & Astrophysics*, 430:411–419.

Gelman, A. and Rubin, D. B. (1992). Inference from iterative simulation using multiple sequences. *Statistical Science*, 7(4):457–472.

Genzel, R., Newman, S., Jones, T., Förster Schreiber, N. M., Shapiro, K., Genel, S., Lilly,

S. J., Renzini, A., Tacconi, L. J., Bouché, N., Burkert, A., Cresci, G., Buschkamp, P., Carollo, C. M., Ceverino, D., Davies, R., Dekel, A., Eisenhauer, F., Hicks, E., Kurk, J., Lutz, D., Mancini, C., Naab, T., Peng, Y., Sternberg, A., Vergani, D., and Zamorani, G. (2011). The sins survey of z 2 galaxy kinematics: Properties of the giant star-forming clumps. *The Astrophysical Journal*, 733(2):101. arXiv: 1011.5360 tex.adsnote: Provided by the SAO/NASA Astrophysics Data System tex.adsurl: http://adsabs.harvard.edu/abs/2011ApJ...733..101G tex.eid: 101.

Georgiev, I. Y. and Böker, T. (2014). Nuclear star clusters in 228 spiral galaxies in the HST/WFPC2 archive: catalogue and comparison to other stellar systems. *Monthly Notices of the Royal Astronomical Society*, 441(4):3570–3590. arXiv: 1404.5956 [astro-ph.GA] tex.adsnote: Provided by the SAO/NASA Astrophysics Data System tex.adsurl: https://ui.adsabs.harvard.edu/abs/2014MNRAS.441.3570G.

Georgiev, I. Y., Böker, T., Leigh, N., Lützgendorf, N., and Neumayer, N. (2016). Masses and scaling relations for nuclear star clusters, and their co-existence with central black holes. *Monthly Notices of the Royal Astronomical Society*, 457(2):2122–2138. arXiv: 1601.02613 [astro-ph.GA] tex.adsnote: Provided by the SAO/NASA Astrophysics Data System tex.adsurl: https://ui.adsabs.harvard.edu/abs/2016MNRAS.457.2122G.

Georgiev, I. Y., Goudfrooij, P., and Puzia, T. H. (2012). New insights into the star formation histories of candidate intermediate-age early-type galaxies from K'-band imaging of globular clusters. *Monthy Notices of the Royal Astronomical Society*, 420(2):1317–1332.

Georgiev, I. Y., Hilker, M., Puzia, T. H., Goudfrooij, P., and Baumgardt, H. (2009). Globular cluster systems in nearby dwarf galaxies - II. Nuclear star clusters and their relation to massive Galactic globular clusters. *Monthly Notices of the Royal Astronomical Society*, 396(2):1075–1085. arXiv: 0903.2857 [astro-ph.GA] tex.adsnote: Provided by the SAO/NASA Astrophysics Data System tex.adsurl: https://ui.adsabs.harvard.edu/abs/2009MNRAS.396.1075G.

Georgiev, I. Y., Puzia, T. H., Goudfrooij, P., and Hilker, M. (2010). Globular cluster systems in nearby dwarf galaxies - III. Formation efficiencies of old globular clusters. *Monthly*

Notices of the Royal Astronomical Society, 406(3):1967–1984. arXiv: 1004.2039 [astro-ph.CO] tex.adsnote: Provided by the SAO/NASA Astrophysics Data System tex.adsurl: https://ui.adsabs.harvard.edu/abs/2010MNRAS.406.1967G.

Georgy, C., Ekström, S., Eggenberger, P., Meynet, G., Haemmerlé, L., Maeder, A., Granada, A., Groh, J. H., Hirschi, R., Mowlavi, N., Yusof, N., Charbonnel, C., Decressin, T., and Barblan, F. (2013). Grids of stellar models with rotation. III. Models from 0.8 to 120 $M_\odot$ at a metallicity Z = 0.002. *Astronomy & Astrophysics*, 558:A103.

Girardi, L., Bressan, A., Bertelli, G., and Chiosi, C. (2000). Evolutionary tracks and isochrones for low- and intermediate-mass stars: From 0.15 to 7 M_{sun}, and from Z=0.0004 to 0.03. *Astronomy and Astrophysics, Supplement*, 141(3):371–383.

Gnedin, O. Y., Ostriker, J. P., and Tremaine, S. (2014). Co-evolution of galactic nuclei and globular cluster systems. *The Astrophysical Journal*, 785(1):71. arXiv: 1308.0021 [astro-ph.CO] tex.adsnote: Provided by the SAO/NASA Astrophysics Data System tex.adsurl: https://ui.adsabs.harvard.edu/abs/2014ApJ...785...71G tex.eid: 71.

Godwin, J. G., Metcalfe, N., and Peach, J. V. (1983). The Coma Cluster – I. A catalogue of magnitudes, colours, ellipticities and position angles for 6724 galaxies in the field of the Coma cluster. *Monthly Notices of the Royal Astronomical Society*, 202(1):113–124.

Gonçalves, G., Coelho, P., Schiavon, R., and Usher, C. (2020). How well can we determine ages and chemical abundances from spectral fitting of integrated light spectra? *Monthy Notices of the Royal Astronomical Society*, 499(2):2327–2339.

Gonzalez, O. A., Rejkuba, M., Zoccali, M., Hill, V., Battaglia, G., Babusiaux, C., Minniti, D., Barbuy, B., Alves-Brito, A., Renzini, A., Gomez, A., and Ortolani, S. (2011). Alpha element abundances and gradients in the Milky Way bulge from FLAMES-GIRAFFE spectra of 650 K giants. *Astronomy & Astrophysics*, 530:A54.

González-Lópezlira, R. A., Mayya, Y. D., Loinard, L., Álamo-Martínez, K., Heald, G., Georgiev, I. Y., Órdenes-Briceño, Y., Lançon, A., Lara-López, M. A., Lomelí-Núñez, L., Bruzual, G., and Puzia, T. H. (2019). Spectroscopy of NGC 4258 Globular Cluster Candidates: Membership Confirmation and Kinematics. *Astrophysical Journal*, 876(1):39.

Göttgens, F., Husser, T.-O., Kamann, S., Dreizler, S., Giesers, B., Kollatschny, W., Weilbacher, P. M., Roth, M. M., and Wendt, M. (2019). A stellar census in globular clusters with MUSE: A spectral catalogue of emission-line sources. *Astronomy & Astrophysics*, 631:A118.

Greene, J. E., Strader, J., and Ho, L. C. (2020). Intermediate-Mass Black Holes. *Annual Review of Astronomy and Astrophysics*, 58:257–312.

Gregg, M. D., Silva, D., Rayner, J., Worthey, G., Valdes, F., Pickles, A., Rose, J., Carney, B., and Vacca, W. (2006). The HST/STIS Next Generation Spectral Library. In Koekemoer, A. M., Goudfrooij, P., and Dressel, L. L., editors, *The 2005 HST Calibration Workshop: Hubble After the Transition to Two-Gyro Mode*, page 209.

Grevesse, N. and Sauval, A. J. (1998). Standard Solar Composition. Space Sci. Rev., 85:161–174.

Grillmair, C., Pritchet, C., and van den Bergh, S. (1986). The distribution of globular clusters associated with M 87 = NGC 4486. *Astronomical Journal*, 91:1328–1335.

Gunn, J. E. and Gott, III, J. R. (1972). On the infall of matter into clusters of galaxies and some effects on their evolution. *The Astrophysical Journal*, 176:1. tex.adsnote: Provided by the SAO/NASA Astrophysics Data System tex.adsurl: http://adsabs.harvard.edu/abs/1972ApJ...176....1G.

Harris, W. E., Smith, M. G., and Myra, E. S. (1983). Globular cluster systems in the Hydra I elliptical galaxies. II. *Astrophysical Journal*, 272:456–472.

Hasegan, M., Jordán, A., Côté, P., Djorgovski, S. G., McLaughlin, D. E., Blakeslee, J. P., Mei, S., West, M. J., Peng, E. W., Ferrarese, L., Milosavljević, M., Tonry, J. L., and Merritt, D. (2005). The ACS virgo cluster survey. VII. Resolving the connection between globular clusters and ultracompact dwarf galaxies. *The Astrophysical Journal*, 627(1):203–223. arXiv: astro-ph/0503566 [astro-ph] tex.adsnote: Provided by the SAO/NASA Astrophysics Data System tex.adsurl: https://ui.adsabs.harvard.edu/abs/2005ApJ...627..203H.

Hattab, M. W., De Souza, R. S., Ciardi, B., Paardekooper, J. P., Khochfar, S., and Vecchia, C. D. (2019). A case study of hurdle and generalized additive models in astronomy: The escape of ionizing radiation. *Monthly Notices of the Royal Astronomical Society*, 483(3):3307–3321.

Hayakawa, A., Hoshino, A., Ishida, M., Furusho, T., Yamasaki, N. Y., and Ohashi, T. (2006). Detailed XMM-Newton Observation of the Cluster of Galaxies Abell 1060. *Publications of the Astronomical Society of Japan*, 58:695–702.

Hempel, M., Geisler, D., Hoard, D. W., and Harris, W. E. (2005). Extragalactic globular clusters in the near-infrared. V. IC 4051 and NGC 3311. *Astronomy & Astrophysics*, 439(1):59–73.

Hilbe, J. M., de Souza, R. S., and Ishida, E. E. O. (2017). *Bayesian Models for Astrophysical Data*. Cambridge University Press.

Hilker, M., Infante, L., Vieira, G., Kissler-Patig, M., and Richtler, T. (1999). The central region of the Fornax cluster. II. Spectroscopy and radial velocities of member and background galaxies. *Astronomy and Astrophysics Supplement Series*, 134(1):75–86. arXiv: astro-ph/9807144 [astro-ph] tex.adsnote: Provided by the SAO/NASA Astrophysics Data System tex.adsurl: https://ui.adsabs.harvard.edu/abs/1999A&AS..134...75H.

Hilker, M. and Richtler, T. (2016). Globular clusters as tracers of the halo assembly of nearby central cluster galaxies. In Bragaglia, A., Arnaboldi, M., Rejkuba, M., and Romano, D., editors, *The General Assembly of Galaxy Halos: Structure, Origin and Evolution*, volume 317, pages 128–133.

Hilker, M., Richtler, T., Barbosa, C. E., Arnaboldi, M., Coccato, L., and de Oliveira, C. M. (2018). The Hydra I cluster core - II. Kinematic complexity in a rising velocity dispersion profile around the cD galaxy NGC 3311. *A&a*, 619:A70.

Howes, L. M., Asplund, M., Keller, S. C., Casey, A. R., Yong, D., Lind, K., Frebel, A., Hays, A., Alves-Brito, A., Bessell, M. S., Casagrande, L., Marino, A. F., Nataf, D. M., Owen, C. I., Da Costa, G. S., Schmidt, B. P., and Tisserand, P. (2016). The EMBLA survey -

metal-poor stars in the Galactic bulge. *Monthy Notices of the Royal Astronomical Society*, 460(1):884–901.

Hoyos, C., Den Brok, M., Kleijn, G. V., Carter, D., Balcells, M., Guzmán, R., Peletier, R., Ferguson, H. C., Goudfrooij, P., Graham, A. W., Hammer, D., Karick, A. M., Lucey, J. R., Matković, A., Merritt, D., Mouhcine, M., and Valentijn, E. (2011). The HST/ACS Coma Cluster Survey - III. Structural parameters of galaxies using single Sérsic fits. *Monthly Notices of the Royal Astronomical Society*, 411(4):2439–2460.

Huang, S., Ho, L. C., Peng, C. Y., Li, Z.-Y., and Barth, A. J. (2016). The Carnegie-Irvine Galaxy Survey. IV. A Method to Determine the Average Mass Ratio of Mergers That Built Massive Elliptical Galaxies. *Astrophysical Journal*, 821(2):114.

Iglesias-Páramo, J., Boselli, A., Gavazzi, G., Cortese, L., and Vílchez, J. M. (2003). The r-band luminosity function of Abell 1367: A comparison with Coma. *Astronomy and Astrophysics*, 397(2):421–430.

Inagaki, T., Lin, Y.-T., Huang, H.-J., Hsieh, B.-C., and Sugiyama, N. (2015). Stellar mass assembly of brightest cluster galaxies at late times. *Monthy Notices of the Royal Astronomical Society*, 446(1):1107–1114.

Iodice, E., Sarzi, M., Bittner, A., Coccato, L., Costantin, L., Corsini, E. M., van de Ven, G., de Zeeuw, P. T., Falcòn-Barroso, J., Gadotti, D. A., Lyubenova, M., Martìn-Navarro, I., McDermid, R. M., Nedelchev, B., Pinna, F., Pizzella, A., Spavone, M., and Viaene, S. (2019). The Fornax3D project: Tracing the assembly history of the cluster from the kinematic and line-strength maps. *ArXiv190608187 Astro-Ph*.

Jackson, R. A., Martin, G., Kaviraj, S., Ramsøy, M., Devriendt, J. E. G., Sedgwick, T., Laigle, C., Choi, H., Beckmann, R. S., Volonteri, M., Dubois, Y., Pichon, C., Yi, S. K., Slyz, A., Kraljic, K., Kimm, T., Peirani, S., and Baldry, I. (2021). The origin of low-surface-brightness galaxies in the dwarf regime. *Monthy Notices of the Royal Astronomical Society*, 502(3):4262–4276.

Jacoby, W. G. (2000). Loess:: a nonparametric, graphical tool for depicting relationships between variables. *Electoral Studies*, 19(4):577–613.

James, P. A. and Prescott, M. (2008). *The Star Formation History of Late-type Galaxies*, volume 390 of *Astronomical Society of the Pacific Conference Series*, page 242.

Jedrzejewski, R. I. (1987). CCD surface photometry of elliptical galaxies - I. Observations, reduction and results. *Monthy Notices of the Royal Astronomical Society*, 226(4):747–768.

Jennings, Z. G., Strader, J., Romanowsky, A. J., Brodie, J. P., Arnold, J. A., Lin, D., Irwin, J. A., Sivakoff, G. R., and Wong, K.-W. (2014). The SLUGGS survey: HST/ACS mosaic imaging of the NGC 3115 globular cluster system. *Astronomical Journal*, 148(2):32. arXiv: 1405.0008 tex.adsnote: Provided by the SAO/NASA Astrophysics Data System tex.adsurl: http://adsabs.harvard.edu/abs/2014AJ....148...32J tex.eid: 32.

Jester, S., Schneider, D. P., Richards, G. T., Green, R. F., Schmidt, M., Hall, P. B., Strauss, M. A., Vanden Berk, D. E., Stoughton, C., Gunn, J. E., Brinkmann, J., Kent, S. M., Smith, J. A., Tucker, D. L., and Yanny, B. (2005). The Sloan Digital Sky Survey View of the Palomar-Green Bright Quasar Survey. *The Astronomical Journal*, 130(3):873–895.

Johnston, E. J., Merrifield, M., and Aragón-Salamanca, A. (2018). Spectroscopic decomposition of the galaxy and halo of the cD galaxyNGC 3311. *Mon. Not. R. Astron. Soc.*, 478(3):4255–4267.

Johnston, E. J., Puzia, T. H., D'Ago, G., Eigenthaler, P., Galaz, G., Häußler, B., Mora, M. D., Ordenes-Briceño, Y., Rong, Y., Spengler, C., Vogt, F., Côté, P., Grebel, E. K., Hilker, M., Mieske, S., Miller, B., Sánchez-Janssen, R., Taylor, M. A., and Zhang, H. X. (2020). The next generation fornax survey (NGFS): VII. A MUSE view of the nuclear star clusters in Fornax dwarf galaxies. *Monthly Notices of the Royal Astronomical Society*, 495(2):2247–2264.

Jordan, A., Blakeslee, J. P., Peng, E. W., Mei, S., Cote, P., Ferrarese, L., Tonry, J. L., Merritt, D., Milosavljević, M., and West, M. J. (2004). The ACS Virgo Cluster Survey. II. Data Reduction Procedures. *The Astrophysical Journal Supplement Series*, 154(2):509–517.

Jordán, A., Peng, E. W., Blakeslee, J. P., Côté, P., Eyheramendy, S., and Ferrarese, L. (2015). The ACS Fornax Cluster Survey. XI. Catalog of Globular Cluster Candidates. *Astrophysical Journal, Supplement*, 221(1):13.

Kacharov, N., Neumayer, N., Seth, A. C., Cappellari, M., McDermid, R., Walcher, C. J., and Böker, T. (2018). Stellar populations and star formation histories of the nuclear star clusters in six nearby galaxies. *Monthy Notices of the Royal Astronomical Society*, 480(2):1973–1998.

Karachentsev, I. D., Dolphin, A. E., Geisler, D., Grebel, E. K., Guhathakurta, P., Hodge, P. W., Karachentseva, V. E., Sarajedini, A., Seitzer, P., and Sharina, M. E. (2002). The M 81 group of galaxies: New distances, kinematics and structure. *Astronomy and Astrophysics*, 383(1):125–136.

Karachentsev, I. D., Makarov, D. I., and Kaisina, E. I. (2013). Updated nearby galaxy catalog. *Astronomical Journal*, 145(4):101. arXiv: 1303.5328 [astro-ph.CO] tex.adsnote: Provided by the SAO/NASA Astrophysics Data System tex.adsurl: https://ui.adsabs.harvard.edu/abs/2013AJ....145..101K tex.eid: 101.

Kaviraj, S., Sohn, S. T., O'Connell, R. W., Lee, Y.-W., Yoon, S.-J., and Yi, S. K. (2007). UV Bright Globular Clusters in M87: More Evidence for Super-helium-rich Stellar Populations? *Mon. Not. R. Astron. Soc.*, 377(3):987–996.

Khochfar, S. and Silk, J. (2009). Dry mergers: a crucial test for galaxy formation. *Monthy Notices of the Royal Astronomical Society*, 397(1):506–510.

Kirby, E. N., Guhathakurta, P., Bolte, M., Sneden, C., and Geha, M. C. (2009). Multi-element Abundance Measurements from Medium-resolution Spectra. I. The Sculptor Dwarf Spheroidal Galaxy. *Astrophysical Journal*, 705(1):328–346.

Knowles, A. T., Sansom, A. E., Allende Prieto, C., and Vazdekis, A. (2021). sMILES: a library of semi-empirical MILES stellar spectra with variable [α/Fe] abundances. *Monthy Notices of the Royal Astronomical Society*, 504(2):2286–2311.

Ko, Y., Hwang, H. S., Lee, M. G., Park, H. S., Lim, S., Sohn, J., Jang, I. S., Hwang, N., and

Park, B.-G. (2017). To the Edge of M87 and Beyond: Spectroscopy of Intracluster Globular Clusters and Ultracompact Dwarfs in the Virgo Cluster. *Astrophysical Journal*, 835(2):212.

Koleva, M. and Vazdekis, A. (2012). Stellar population models in the UV. I. Characterisation of the New Generation Stellar Library. *Astronomy & Astrophysics*, 538:A143.

Kormendy, J., Fisher, D. B., Cornell, M. E., and Bender, R. (2009). Structure and Formation of Elliptical and Spheroidal Galaxies. *Astrophysical Journal, Supplement*, 182(1):216–309.

Korn, A. J., Maraston, C., and Thomas, D. (2005). The sensitivity of Lick indices to abundance variations. *Astronomy & Astrophysics*, 438(2):685–704.

Kruijssen, J. M. D. (2015). Globular clusters as the relics of regular star formation in ‘normal’ high-redshift galaxies. *Monthly Notices of the Royal Astronomical Society*, 454(2):1658–1686. arXiv: 1509.02163 [astro-ph.GA] tex.adsnote: Provided by the SAO/NASA Astrophysics Data System tex.adsurl: https://ui.adsabs.harvard.edu/abs/2015MNRAS.454.1658K.

Kruijssen, J. M. D., Pfeffer, J. L., Crain, R. A., and Bastian, N. (2019). The E-MOSAICS project: tracing galaxy formation and assembly with the age-metallicity distribution of globular clusters. *Monthy Notices of the Royal Astronomical Society*, 486(3):3134–3179.

Kuijken, K. and Rich, R. M. (2002). Hubble Space Telescope WFPC2 Proper Motions in Two Bulge Fields: Kinematics and Stellar Population of the Galactic Bulge. *Astronomical Journal*, 124(4):2054–2066.

Kuntschner, H., Smith, R. J., Colless, M., Davies, R. L., Kaldare, R., and Vazdekis, A. (2002). Early-type galaxies in low-density environments. *Monthy Notices of the Royal Astronomical Society*, 337(1):172–198.

La Barbera, F., Pasquali, A., Ferreras, I., Gallazzi, A., de Carvalho, R. R., and de la Rosa, I. G. (2014). SPIDER - X. Environmental effects in central and satellite early-type galaxies through the stellar fossil record. *Monthy Notices of the Royal Astronomical Society*, 445(2):1977–1996.

Lacerna, I., Ibarra-Medel, H., Avila-Reese, V., Hernández-Toledo, H. M., Vázquez-Mata, J. A., and Sánchez, S. F. (2020). SDSS-IV MaNGA: global and local stellar population properties of elliptical galaxies and their assembly histories. *arXiv e-prints*, 644:arXiv:2001.05506.

Larsen, S. S. and Brodie, J. P. (2000). Hubble space telescope observations of star clusters in NGC 1023: Evidence for three cluster populations? *The Astronomical Journal*, 120(6):2938–2949. tex.adsnote: Provided by the SAO/NASA Astrophysics Data System tex.adsurl: http://adsabs.harvard.edu/abs/2000AJ....120.2938L tex.eprint: astro-ph/0008435.

Larsen, S. S., Brodie, J. P., Wasserman, A., and Strader, J. (2018). Detailed abundance analysis of globular clusters in the Local Group: NGC 147, NGC 6822, and Messier 33. *A&a*, 613:A56.

Lee, H.-c., Worthey, G., Dotter, A., Chaboyer, B., Jevremović, D., Baron, E., Briley, M. M., Ferguson, J. W., Coelho, P., and Trager, S. C. (2009). Stellar Population Models and Individual Element Abundances. II. Stellar Spectra and Integrated Light Models. *Astrophysical Journal*, 694(2):902–923.

Lee, S.-Y., Chung, C., and Yoon, S.-J. (2018). Nonlinear Color-Metallicity Relations of Globular Clusters. VIII. Reproducing Color Distributions of Individual Globular Cluster Systems in the Virgo and Fornax Galaxy Clusters. *ApJS*, 240(1):2.

Lee, S.-Y., Chung, C., and Yoon, S.-J. (2019). Nonlinear Color-Metallicity Relations of Globular Clusters. VIII. Reproducing Color Distributions of Individual Globular Cluster Systems in the Virgo and Fornax Galaxy Clusters. *Astrophysical Journal, Supplement*, 240(1):2.

Liao, S., Gao, L., Frenk, C. S., Grand, R. J. J., Guo, Q., Gómez, F. A., Marinacci, F., Pakmor, R., Shao, S., and Springel, V. (2019). Ultra-diffuse galaxies in the Auriga simulations. *Monthy Notices of the Royal Astronomical Society*, 490(4):5182–5195.

Lidman, C., Iacobuta, G., Bauer, A. E., Barrientos, L. F., Cerulo, P., Couch, W. J., Delaye, L., Demarco, R., Ellingson, E., Faloon, A. J., Gilbank, D., Huertas-Company, M., Mei, S., Meyers, J., Muzzin, A., Noble, A., Nantais, J., Rettura, A., Rosati, P., Sánchez-Janssen, R., Strazzullo, V., Webb, T. M. A., Wilson, G., Yan, R., and Yee, H. K. C. (2013). The importance of major mergers in the build up of stellar mass in brightest cluster galaxies at z = 1. *Monthy Notices of the Royal Astronomical Society*, 433(1):825–837.

Lim, J., Wong, E., Ohyama, Y., Broadhurst, T., and Medezinski, E. (2020). Sustained formation of progenitor globular clusters in a giant elliptical galaxy. *Nature Astronomy*, 4(2):153–158.

Lim, S., Peng, E. W., Cote, P., Sales, L. V., Brok, M. d., Blakeslee, J. P., and Guhathakurta, P. (2018). The Globular Cluster Systems of Ultra-Diffuse Galaxies in the Coma Cluster. *ArXiv180605425 Astro-Ph*, 862(1):82.

Lisker, T., Grebel, E. K., and Binggeli, B. (2008). Virgo Cluster Early-Type Dwarf Galaxies with the Sloan Digital Sky Survey. Iv. The Color-Magnitude Relation. *Astronomical Journal*, 135(1):380–399.

Lisker, T., Grebel, E. K., Binggeli, B., and Glatt, K. (2007). Virgo cluster early-type dwarf galaxies with the sloan digital sky survey. III. Subpopulations: Distributions, shapes, origins. *The Astrophysical Journal*, 660(2):1186–1197. arXiv: astro-ph/0701429 [astro-ph] tex.adsnote: Provided by the SAO/NASA Astrophysics Data System tex.adsurl: https://ui.adsabs.harvard.edu/abs/2007ApJ...660.1186L.

Lisker, T., Janz, J., Hensler, G., Kim, S., Rey, S.-C., Weinmann, S., Mastropietro, C., Hielscher, O., Paudel, S., and Kotulla, R. (2009). The first generation of virgo cluster dwarf elliptical galaxies? *The Astrophysical Journal*, 706(1):L124–l128. arXiv: 0910.3209 [astro-ph.CO] tex.adsnote: Provided by the SAO/NASA Astrophysics Data System tex.adsurl: https://ui.adsabs.harvard.edu/abs/2009ApJ...706L.124L.

Łokas, E. L. and Mamon, G. A. (2003). Dark matter distribution in the Coma cluster from galaxy kinematics: Breaking the mass-anisotropy degeneracy. *Monthly Notices of the Royal Astronomical Society*, 343(2):401–412.

Lotz, J. M., Telford, R., Ferguson, H. C., Miller, B. W., Stiavelli, M., and Mack, J. (2001). Dynamical friction in DE globular cluster systems. *The Astrophysical Journal*, 552(2):572–581. arXiv: astro-ph/0102079 [astro-ph] tex.adsnote: Provided by the SAO/NASA Astrophysics Data System tex.adsurl: https://ui.adsabs.harvard.edu/abs/2001ApJ...552..572L.

Maraston, C. and Strömbäck, G. (2011). Stellar population models at high spectral resolution. *Monthy Notices of the Royal Astronomical Society*, 418(4):2785–2811.

Maraston, C., Strömbäck, G., Thomas, D., Wake, D. A., and Nichol, R. C. (2009). Modelling the colour evolution of luminous red galaxies - improvements with empirical stellar spectra. *Monthy Notices of the Royal Astronomical Society*, 394(1):L107–L111.

Marigo, P., Girardi, L., Bressan, A., Groenewegen, M. A. T., Silva, L., and Granato, G. L. (2008). Evolution of asymptotic giant branch stars. II. Optical to far-infrared isochrones with improved TP-AGB models. *Astronomy & Astrophysics*, 482(3):883–905.

Martin, N. F., McConnachie, A. W., Irwin, M., Widrow, L. M., Ferguson, A. M. N., Ibata, R. A., Dubinski, J., Babul, A., Chapman, S., Fardal, M., Lewis, G. F., Navarro, J., and Rich, R. M. (2009). PAndAS' CUBS: Discovery of Two New Dwarf Galaxies in the Surroundings of the Andromeda and Triangulum Galaxies. *Astrophysical Journal*, 705(1):758–765.

Martín-Navarro, I., Vazdekis, A., Falcón-Barroso, J., La Barbera, F., Yıldırım, A., and van de Ven, G. (2018). Timing the formation and assembly of early-type galaxies via spatially resolved stellar populations analysis. *Monthy Notices of the Royal Astronomical Society*, 475(3):3700–3729.

Martínez-Delgado, D., Läsker, R., Sharina, M., Toloba, E., Fliri, J., Beaton, R., Valls-Gabaud, D., Karachentsev, I. D., Chonis, T. S., Grebel, E. K., Forbes, D. A., Romanowsky, A. J., Gallego-Laborda, J., Teuwen, K., Gómez-Flechoso, M. A., Wang, J., Guhathakurta, P., Kaisin, S., and Ho, N. (2016). Discovery of an Ultra-diffuse Galaxy in the Pisces–Perseus Supercluster. *Astronomical Journal*, 151(4):96.

Massari, D., Koppelman, H. H., and Helmi, A. (2019). Origin of the system of globular clusters in the Milky Way. *Astronomy & Astrophysics*, 630:L4.

McConnachie, A. W. (2012). The Observed Properties of Dwarf Galaxies in and around the Local Group. *Astronomical Journal*, 144(1):4.

McGaugh, S. S., Schombert, J. M., and Bothun, G. D. (1995). The Morphology of Low Surface Brightness Disk Galaxies. *Astronomical Journal*, 109:2019.

McLaughlin, D. E. (1995). Was the Compact Nucleus in M87 Formed by Destroyed Globular Clusters? *Astronomical Journal*, 109:2034.

McLaughlin, D. E. (1999). The efficiency of globular cluster formation. *The Astronomical Journal*, 117(5):2398–2427. arXiv: astro-ph/9901283 [astro-ph] tex.adsnote: Provided by the SAO/NASA Astrophysics Data System tex.adsurl: https://ui.adsabs.harvard.edu/abs/1999AJ....117.2398M.

Mei, S., Blakeslee, J. P., Côté, P., Tonry, J. L., West, M. J., Ferrarese, L., Jordán, A., Peng, E. W., Anthony, A., and Merritt, D. (2007). The ACS virgo cluster survey. XIII. SBF distance catalog and the three-dimensional structure of the virgo cluster. *Astrophysical Journal*, 655(1):144–162. arXiv: astro-ph/0702510 [astro-ph] tex.adsnote: Provided by the SAO/NASA Astrophysics Data System tex.adsurl: https://ui.adsabs.harvard.edu/abs/2007ApJ...655..144M.

Merritt, A., van Dokkum, P., Abraham, R., and Zhang, J. (2016). The Dragonfly nearby Galaxies Survey. I. Substantial Variation in the Diffuse Stellar Halos around Spiral Galaxies. *Astrophysical Journal*, 830(2):62.

Mieske, S., Hilker, M., and Infante, L. (2005). The distance to Hydra and Centaurus from surface brightness fluctuations: Consequences for the Great Attractor model. *Astronomy & Astrophysics*, 438(1):103–119.

Mieske, S., Jordán, A., Côté, P., Kissler-Patig, M., Peng, E. W., Ferrarese, L., Blakeslee, J. P., Mei, S., Merritt, D., Tonry, J. L., and West, M. J. (2006). The ACS virgo cluster survey. XIV. Analysis of color-magnitude relations in globular cluster systems. *The Astrophysical Journal*, 653(1):193–206. arXiv: astro-ph/0609079 [astro-ph] tex.adsnote: Provided by the SAO/NASA Astrophysics Data System tex.adsurl: https://ui.adsabs.harvard.edu/abs/2006ApJ...653..193M.

Miller, B. W., Lotz, J. M., Ferguson, H. C., Stiavelli, M., and Whitmore, B. C. (1998). The specific globular cluster frequencies of dwarf elliptical galaxiesfrom the hubble space telescope. *The Astrophysical Journal*, 508(2):L133–l137. arXiv: astro-ph/9809400 [astro-ph] tex.adsnote: Provided by the SAO/NASA Astrophysics Data System tex.adsurl: https://ui.adsabs.harvard.edu/abs/1998ApJ...508L.133M.

Miller, T. B., Bosch, F. C. v. d., Green, S. B., and Ogiya, G. (2020). Dynamical self-friction: how mass loss slows you down. *ArXiv200106489 Astro-Ph*.

Milone, A. D. C., Sansom, A. E., and Sánchez-Blázquez, P. (2011). Element abundances in the stars of the MILES spectral library: the Mg/Fe ratio. *Monthy Notices of the Royal Astronomical Society*, 414(2):1227–1252.

Milosavljević, M. (2004). On the origin of nuclear star clusters in late-type spiral galaxies. *The Astrophysical Journal*, 605(1):L13–l16. arXiv: astro-ph/0310574 [astro-ph] tex.adsnote: Provided by the SAO/NASA Astrophysics Data System tex.adsurl: https://ui.adsabs.harvard.edu/abs/2004ApJ...605L..13M.

Misgeld, I., Mieske, S., Hilker, M., Richtler, T., Georgiev, I. Y., and Schuberth, Y. (2011). A large population of ultra-compact dwarf galaxies in the Hydra I cluster. *A&a*, 531:A4.

Mistani, P. A., Sales, L. V., Pillepich, A., Sanchez-Janssen, R., Vogelsberger, M., Nelson, D., Rodriguez-Gomez, V., Torrey, P., and Hernquist, L. (2016). On the assembly of dwarf galaxies in clusters and their efficient formation of globular clusters. *Monthly Notices of the Royal Astronomical Society*, 455(3):2323–2336. arXiv: 1509.00030 [astro-ph.GA] tex.adsnote: Provided by the SAO/NASA Astrophysics Data System tex.adsurl: https://ui.adsabs.harvard.edu/abs/2016MNRAS.455.2323M.

Montes, M., Acosta-Pulido, J. A., Prieto, M. A., and Fernández-Ontiveros, J. A. (2014). The innermost globular clusters of M87. *Mon. Not. R. Astron. Soc.*, 442(2):1350–1362.

Morelli, L., Corsini, E. M., Pizzella, A., Dalla Bontà, E. M., Coccato, L., Méndez-Abreu, J., and Cesetti, M. (2013). A spectroscopic view of stellar populations in bulges of low surface brightness galaxies . *Memorie della Societa Astronomica Italiana Supplementi*, 25:29.

Morelli, L., Pompei, E., Pizzella, A., Méndez-Abreu, J., Corsini, E. M., Coccato, L., Saglia, R. P., Sarzi, M., and Bertola, F. (2008). Stellar populations of bulges in 14 cluster disc galaxies. *Monthly Notices of the Royal Astronomical Society*, 389(1):341–363.

Mould, J. R., Oke, J. B., and Nemec, J. M. (1987). Spectroscopy of the Globular Clusters in M87. *Astronomical Journal*, 93:53.

Müller, O., Rejkuba, M., Pawlowski, M. S., Ibata, R., Lelli, F., Hilker, M., and Jerjen, H. (2019). The dwarf galaxy satellite system of Centaurus A. *Astronomy and Astrophysics*, 629:A18.

Muratov, A. L. and Gnedin, O. Y. (2010). Modeling the metallicity distribution of globular clusters. *The Astrophysical Journal*, 718(2):1266–1288. arXiv: 1002.1325 tex.adsnote: Provided by the SAO/NASA Astrophysics Data System tex.adsurl: http://adsabs.harvard.edu/abs/2010ApJ...718.1266M.

Muñoz, R. P., Eigenthaler, P., Puzia, T. H., Taylor, M. A., Ordenes-Briceño, Y., Alamo-Martínez, K., Ribbeck, K. X., Ángel, S., Capaccioli, M., Côté, P., Ferrarese, L., Galaz, G., Hempel, M., Hilker, M., Jordán, A., Lançon, A., Mieske, S., Paolillo, M., Richtler, T., Sánchez-Janssen, R., and Zhang, H. (2015). Unveiling a rich system of faint dwarf galaxies in the next generation fornax survey. *Astrophysical Journal Letters*, 813(1):L15. arXiv: 1510.02475 [astro-ph.GA] tex.adsnote: Provided by the SAO/NASA Astrophysics Data System tex.adsurl: https://ui.adsabs.harvard.edu/abs/2015ApJ...813L..15M tex.eid: L15.

Muñoz, R. P., Puzia, T. H., Lançon, A., Peng, E. W., Côté, P., Ferrarese, L., Blakeslee, J. P., Mei, S., Cuillandre, J.-C., Hudelot, P., Courteau, S., Duc, P.-A., Balogh, M. L., Boselli, A., Bournaud, F., Carlberg, R. G., Chapman, S. C., Durrell, P., Eigenthaler, P., Emsellem, E., Gavazzi, G., Gwyn, S., Huertas-Company, M., Ilbert, O., Jordán, A., Läsker, R., Licitra, R., Liu, C., MacArthur, L., McConnachie, A., McCracken, H. J., Mellier, Y., Peng, C. Y., Raichoor, A., Taylor, M. A., Tonry, J. L., Tully, R. B., and Zhang, H. (2013). The Next Generation Virgo Cluster Survey-infrared (Ngvs-ir). I. A New Near-ultraviolet, Optical, And Near-infrared Globular Cluster Selection Tool. *Astrophys. J. Suppl. Ser.*, 210(1):4.

Neumayer, N., Seth, A., and Böker, T. (2020). Nuclear star clusters. *Astronomy and Astrophysics Review*, 28(1):4.

Nissen, P. E. and Schuster, W. J. (2010). Two distinct halo populations in the solar neighborhood. Evidence from stellar abundance ratios and kinematics. *Astronomy & Astrophysics*, 511:L10.

Nomoto, K., Tominaga, N., Umeda, H., Kobayashi, C., and Maeda, K. (2006). Nucleosynthesis yields of core-collapse supernovae and hypernovae, and galactic chemical evolution. Nucl. Phys. A, 777:424–458.

Oldham, L. J. and Auger, M. W. (2016a). Galaxy structure from multiple tracers - I. A census of M87's globular cluster populations. *Monthly Notices of the Royal Astronomical Society*, 455(1):820–830. arXiv: 1511.07046 tex.adsnote: Provided by the SAO/NASA Astrophysics Data System tex.adsurl: http://adsabs.harvard.edu/abs/2016MNRAS.455..820O.

Oldham, L. J. and Auger, M. W. (2016b). Galaxy structure from multiple tracers – I. A census of M87's globular cluster populations. *Mon. Not. R. Astron. Soc.*, 455(1):820–830.

Oliva-Altamirano, P., Brough, S., Jimmy, Tran, K.-V., Couch, W. J., McDermid, R. M., Lidman, C., von der Linden, A., and Sharp, R. (2015). The accretion histories of brightest cluster galaxies from their stellar population gradients. *Monthy Notices of the Royal Astronomical Society*, 449(4):3347–3359.

Oliva-Altamirano, P., Brough, S., Lidman, C., Couch, W. J., Hopkins, A. M., Colless, M., Taylor, E., Robotham, A. S. G., Gunawardhana, M. L. P., Ponman, T., Baldry, I., Bauer, A. E., Bland-Hawthorn, J., Cluver, M., Cameron, E., Conselice, C. J., Driver, S., Edge, A. C., Graham, A. W., van Kampen, E., Lara-López, M. A., Liske, J., López-Sánchez, A. R., Loveday, J., Mahajan, S., Peacock, J., Phillipps, S., Pimbblet, K. A., and Sharp, R. G. (2014). Galaxy And Mass Assembly (GAMA): testing galaxy formation models through the most massive galaxies in the Universe. *Monthy Notices of the Royal Astronomical Society*, 440(1):762–775.

Ordenes-Briceño, Y., Eigenthaler, P., Taylor, M. A., Puzia, T. H., Alamo-Martínez, K., Ribbeck, K. X., Muñoz, R. P., Zhang, H., Grebel, E. K., Ángel, S., Côté, P., Ferrarese, L., Hilker, M., Lançon, A., Mieske, S., Miller, B. W., Rong, Y., and Sánchez-Janssen, R. (2018). The next generation fornax survey (NGFS): III. Revealing the spatial substructure of the dwarf galaxy population inside half of fornax's virial radius. *arXiv*, 859(1):52.

Oser, L., Ostriker, J. P., Naab, T., Johansson, P. H., and Burkert, A. (2010). The two phases of galaxy formation. *The Astrophysical Journal*, 725(2):2312–2323. arXiv: 1010.1381 tex.adsnote: Provided by the SAO/NASA Astrophysics Data System tex.adsurl: http://adsabs.harvard.edu/abs/2010ApJ...725.2312O.

Östlin, G., Cumming, R. J., Amram, P., Bergvall, N., Kunth, D., Márquez, I., Masegosa, J., and Zackrisson, E. (2004). Stellar dynamics of blue compact galaxies. I. Decoupled star-gas kinematics in ESO 400-G43. *Astronomy & Astrophysics*, 419:L43–l47.

Pastorello, N., Forbes, D. A., Usher, C., Brodie, J. P., Romanowsky, A. J., Strader, J., Spitler, L. R., Alabi, A. B., Foster, C., Jennings, Z. G., Kartha, S. S., and Pota, V. (2015). The SLUGGS survey: combining stellar and globular cluster metallicities in the outer regions of early-type galaxies. *Monthy Notices of the Royal Astronomical Society*, 451(3):2625–2639.

Peng, C. Y., Ho, L. C., Impey, C. D., and Rix, H.-W. (2002). Detailed structural decomposition of galaxy images. *The Astronomical Journal*, 124(1):266–293. tex.adsnote: Provided by the SAO/NASA Astrophysics Data System tex.adsurl: http://adsabs.harvard.edu/abs/2002AJ....124..266P tex.eprint: astro-ph/0204182.

Peng, E., Takamiya, M., Cote, P., West, M. J., Blakeslee, J. P., Ferrarese, L., Jordan, A., and Mei, S. (2006a). The spatial distributions of globular cluster systems. In *American astronomical society meeting abstracts*, volume 38 of *Bulletin of the american astronomical society*, page 1062. tex.adsnote: Provided by the SAO/NASA Astrophysics Data System tex.adsurl: http://adsabs.harvard.edu/abs/2006AAS...20911205P tex.eid: 112.05.

Peng, E. W., Jordan, A., Cote, P., Blakeslee, J. P., Ferrarese, L., Mei, S., West, M. J., Merritt, D., Milosavljevic, M., and Tonry, J. L. (2006b). The ACS Virgo Cluster Survey IX: The Color Distributions of Globular Cluster Systems in Early-Type Galaxies. *ApJ*, 639(1):95–119.

Peng, E. W., Jordán, A., Côté, P., Blakeslee, J. P., Ferrarese, L., Mei, S., West, M. J., Merritt, D., Milosavljević, M., and Tonry, J. L. (2006c). The ACS Virgo Cluster Survey. IX. The Color Distributions of Globular Cluster Systems in Early-Type Galaxies. *\apj*, 639(1):95–119.

Peng, E. W., Jordán, A., Côté, P., Takamiya, M., West, M. J., Blakeslee, J. P., Chen, C.-W., Ferrarese, L., Mei, S., Tonry, J. L., and West, A. A. (2008). The ACS virgo cluster survey. XV. The formation efficiencies of globular clusters in early-type galaxies: The effects of mass and environment. *The Astrophysical Journal*, 681(1):197–224. arXiv: 0803.0330 [astro-ph] tex.adsnote: Provided by the SAO/NASA Astrophysics Data System tex.adsurl: https://ui.adsabs.harvard.edu/abs/2008ApJ...681..197P.

Pessev, P. M., Goudfrooij, P., Puzia, T. H., and Chand ar, R. (2008). A comparison of optical and near-infrared colours of Magellanic Cloud star clusters with predictions of simple stellar population models. *Monthy Notices of the Royal Astronomical Society*, 385(3):1535–1560.

Pfeffer, J. and Baumgardt, H. (2013). Ultra-compact dwarf galaxy formation by tidal stripping of nucleated dwarf galaxies. *Monthly Notices of the Royal Astronomical Society*, 433(3):1997–2005. arXiv: 1305.3656 [astro-ph.GA] tex.adsnote: Provided by the SAO/NASA Astrophysics Data System tex.adsurl: https://ui.adsabs.harvard.edu/abs/2013MNRAS.433.1997P.

Pietrinferni, A., Cassisi, S., Salaris, M., and Castelli, F. (2004). A Large Stellar Evolution Database for Population Synthesis Studies. I. Scaled Solar Models and Isochrones. *Astrophysical Journal*, 612(1):168–190.

Pildis, R. A., Schombert, J. M., and Eder, A. (1997). Gas-rich Dwarf Galaxies from the Second Palomar Sky Survey. II. Optical Properties. *Astrophysical Journal*, 481(1):157–168.

Pillepich, A., Nelson, D., Hernquist, L., Springe, V., Rüdiger Pakmor, Torrey, P., Weinberger, R., Gene, S., Naiman, J. P., Marinacci, F., and Vogelsberger, M. (2018). First results from the illustristng simulations: The stellar mass content of groups and clusters of galaxies. *Monthly Notices of the Royal Astronomical Society*, 475(1):648–675.

Piotto, G., Milone, A. P., Bedin, L. R., Anderson, J., King, I. R., Marino, A. F., Nardiello, D., Aparicio, A., Barbuy, B., Bellini, A., Brown, T. M., Cassisi, S., Cool, A. M., Cunial, A., Dalessandro, E., D'Antona, F., Ferraro, F. R., Hidalgo, S., Lanzoni, B., Monelli, M., Ortolani, S., Renzini, A., Salaris, M., Sarajedini, A., van der Marel, R. P., Vesperini, E., and Zoccali, M. (2015). The Hubble Space Telescope UV Legacy Survey of Galactic Globular Clusters. I. Overview of the Project and Detection of Multiple Stellar Populations. *Astronomical Journal*, 149(3):91.

Postman, M., Franx, M., Cross, N. J. G., Holden, B., Ford, H. C., Illingworth, G. D., Goto, T., Demarco, R., Rosati, P., Blakeslee, J. P., Tran, K.-V., Benítez, N., Clampin, M., Hartig, G. F., Homeier, N., Ardila, D. R., Bartko, F., Bouwens, R. J., Bradley, L. D., Broadhurst, T. J., Brown, R. A., Burrows, C. J., Cheng, E. S., Feldman, P. D., Golimowski, D. A., Gronwall, C., Infante, L., Kimble, R. A., Krist, J. E., Lesser, M. P., Martel, A. R., Mei, S., Menanteau, F., Meurer, G. R., Miley, G. K., Motta, V., Sirianni, M., Sparks, W. B., Tran, H. D., Tsvetanov, Z. I., White, R. L., and Zheng, W. (2005). The morphology-density relation in z 1 clusters. *The Astrophysical Journal*, 623(2):721–741. tex.adsnote: Provided by the SAO/NASA Astrophysics Data System tex.adsurl: http://adsabs.harvard.edu/abs/2005ApJ...623..721P tex.eprint: astro-ph/0501224.

Pota, V., Forbes, D. A., Romanowsky, A. J., Brodie, J. P., Spitler, L. R., Strader, J., Foster, C., Arnold, J. A., Benson, A., Blom, C., Hargis, J. R., Rhode, K. L., and Usher, C. (2013). The SLUGGS Survey: kinematics for over 2500 globular clusters in 12 early-type galaxies. *Monthly Notices of the Royal Astronomical Society*, 428(1):389–420. arXiv: 1209.4351 tex.adsnote: Provided by the SAO/NASA Astrophysics Data System tex.adsurl: http://adsabs.harvard.edu/abs/2013MNRAS.428..389P.

Powalka, M., Lançon, A., Puzia, T. H., Peng, E. W., Liu, C., Muñoz, R. P., Blakeslee, J. P., Côté, P., Ferrarese, L., Roediger, J., Sánchez-Janssen, R., Zhang, H., Durrell, P. R., Cuillandre, J.-C., Duc, P.-A., Guhathakurta, P., Gwyn, S. D. J., Hudelot, P., Mei, S., and Toloba, E. (2016a). The Next Generation Virgo Cluster Survey (Ngvs). Xxv. Fiducial Panchromatic Colors Of Virgo Core Globular Clusters And Their Comparison To Model Predictions. *ApJS*, 227(1):12.

Powalka, M., Lançon, A., Puzia, T. H., Peng, E. W., Liu, C., Muñoz, R. P., Blakeslee, J. P., Côté, P., Ferrarese, L., Roediger, J., Sánchez-Janssen, R., Zhang, H., Durrell, P. R., Cuillandre, J.-C., Duc, P.-A., Guhathakurta, P., Gwyn, S. D. J., Hudelot, P., Mei, S., and Toloba, E. (2017). The Next Generation Virgo Cluster Survey (NGVS). XXVI. The Issues of Photometric Age and Metallicity Estimates for Globular Clusters. *Astrophys. J.*, 844(2):104.

Powalka, M., Puzia, T. H., Lançon, A., Peng, E. W., Schönebeck, F., Alamo-Martínez, K., Ángel, S., Blakeslee, J. P., Côté, P., Cuillandre, J.-C., Duc, P.-A., Durrell, P., Ferrarese, L., Grebel, E. K., Guhathakurta, P., Gwyn, S. D. J., Kuntschner, H., Lim, S., Liu, C., Lyubenova, M., Mihos, J. C., Muñoz, R. P., Ordenes-Briceño, Y., Roediger, J., Sánchez-Janssen, R., Spengler, C., Toloba, E., and Zhang, H. (2016b). New Constraints on a complex relation between globular cluster colors and environment. *Astrophys. J.*, 829(1):L5.

Press, W. H. and Schechter, P. (1974). Formation of galaxies and clusters of galaxies by self-similar gravitational condensation. *The Astrophysical Journal*, 187:425–438. tex.adsnote: Provided by the SAO/NASA Astrophysics Data System tex.adsurl: https://ui.adsabs.harvard.edu/abs/1974ApJ...187..425P.

Pritzl, B. J., Venn, K. A., and Irwin, M. (2005). A Comparison of Elemental Abundance Ratios in Globular Clusters, Field Stars, and Dwarf Spheroidal Galaxies. *Astronomical Journal*, 130(5):2140–2165.

Puzia, T. (2005). Intermediate-Age Globular Clusters in M31. HST Proposal.

Puzia, T. H., Zepf, S. E., Kissler-Patig, M., Hilker, M., Minniti, D., and Goudfrooij, P. (2002). Extragalactic globular clusters in the near-infrared. II. The globular clusters systems of NGC 3115 and NGC 4365. *Astronomy & Astrophysics*, 391(2):453–470.

R Development Core Team, R. (2019). *A Language and Environment for Statistical Computing*. R Foundation for Statistical Computing, Vienna, Austria.

Rayner, J. T., Cushing, M. C., and Vacca, W. D. (2009). The Infrared Telescope Facility (IRTF) Spectral Library: Cool Stars. *Astrophysical Journal, Supplement*, 185(2):289–432.

Reddy, B. E., Tomkin, J., Lambert, D. L., and Allende Prieto, C. (2003). The chemical compositions of Galactic disc F and G dwarfs. *Monthy Notices of the Royal Astronomical Society*, 340(1):304–340.

Reina-Campos, M., Kruijssen, J. M. D., Pfeffer, J. L., Bastian, N., and Crain, R. A. (2019). Formation histories of stars, clusters, and globular clusters in the E-MOSAICS simulations. *Monthy Notices of the Royal Astronomical Society*, 486(4):5838–5852.

Renaud, F. and Gieles, M. (2015). The effect of secular galactic growth on the evolution of star clusters. *Monthy Notices of the Royal Astronomical Society*, 449(3):2734–2740.

Renzini, A., D'Antona, F., Cassisi, S., King, I. R., Milone, A. P., Ventura, P., Anderson, J., Bedin, L. R., Bellini, A., Brown, T. M., Piotto, G., van der Marel, R. P., Barbuy, B., Dalessandro, E., Hidalgo, S., Marino, A. F., Ortolani, S., Salaris, M., and Sarajedini, A. (2015). The Hubble Space Telescope UV Legacy Survey of Galactic Globular Clusters - V. Constraints on formation scenarios. *Monthy Notices of the Royal Astronomical Society*, 454(4):4197–4207.

Ricciardelli, E., Vazdekis, A., Cenarro, A. J., and Falcón-Barroso, J. (2012). MIUSCAT: extended MILES spectral coverage - II. Constraints from optical photometry. *Monthy Notices of the Royal Astronomical Society*, 424(1):172–189.

Richtler, T., Hilker, M., Arnaboldi, M., and Barbosa, C. E. (2020). Dust and star formation in the centre of NGC 3311. *Astronomy & Astrophysics*, 643:A119.

Richtler, T., Salinas, R., Misgeld, I., Hilker, M., Hau, G. K. T., Romanowsky, A. J., Schuberth, Y., and Spolaor, M. (2011). The dark halo of the Hydra I galaxy cluster: core, cusp, cosmological? Dynamics of NGC 3311 and its globular cluster system. *Astronomy & Astrophysics*, 531:A119.

Riffel, R., Rodríguez-Ardila, A., Brotherton, M. S., Peletier, R., Vazdekis, A., Riffel, R. A., Martins, L. P., Bonatto, C., Zanon Dametto, N., Dahmer-Hahn, L. G., Runnoe, J., Pastoriza, M. G., Chies-Santos, A. L., and Trevisan, M. (2019). Optical/NIR stellar absorption and emission-line indices from luminous infrared galaxies. *Mon. Not. R. Astron. Soc.*, 486(3):3228–3247.

Röck, B., Vazdekis, A., Peletier, R. F., Knapen, J. H., and Falcón-Barroso, J. (2015). Stellar population synthesis models between 2.5 and 5 μm based on the empirical IRTF stellar library. *Monthy Notices of the Royal Astronomical Society*, 449(3):2853–2874.

Röck, B., Vazdekis, A., Ricciardelli, E., Peletier, R. F., Knapen, J. H., and Falcón-Barroso,

J. (2016). MILES extended: Stellar population synthesis models from the optical to the infrared. *Astronomy & Astrophysics*, 589:A73.

Romanowsky, A. J., Strader, J., Brodie, J. P., Mihos, J. C., Spitler, L. R., Forbes, D. A., Foster, C., and Arnold, J. A. (2012). The ongoing assembly of a central cluster galaxy: Phase-space substructures in the halo of M87. *Astrophys. J.*, 748(1):29.

Ryden, B. S. and Terndrup, D. M. (1994). The Flattening Distribution of Dwarf Elliptical Galaxies in the Virgo Cluster. *Astrophysical Journal*, 425:43.

Salinas, R., Alabi, A., Richtler, T., and Lane, R. R. (2015). Isolated ellipticals and their globular cluster systems: III. NGC 2271, NGC 2865, NGC 3962, NGC 4240, and IC 4889 . *A&a*, 577:A59.

Salpeter, E. E. (1955). The Luminosity Function and Stellar Evolution. *Astrophysical Journal*, 121:161.

Sánchez-Blázquez, P., Gorgas, J., Cardiel, N., and González, J. J. (2006). Stellar populations of early-type galaxies in different environments. II. Ages and metallicities. *Astronomy & Astrophysics*, 457(3):809–821.

Sánchez-Janssen, R., Puzia, T. H., Ferrarese, L., Côté, P., Eigenthaler, P., Miller, B., Ordenes-Briceño, Y., Peng, E. W., Ribbeck, K. X., Roediger, J., Spengler, C., and Taylor, M. A. (2019). How nucleation and luminosity shape faint dwarf galaxies. *Monthy Notices of the Royal Astronomical Society*, 486(1):L1–L5.

Sansom, A. E., Milone, A. d. C., Vazdekis, A., and Sánchez-Blázquez, P. (2013). Tests of model predictions for the responses of stellar spectra and absorption-line indices to element abundance variations. *Monthy Notices of the Royal Astronomical Society*, 435(2):952–974.

Sbordone, L., Bonifacio, P., Buonanno, R., Marconi, G., Monaco, L., and Zaggia, S. (2007). The exotic chemical composition of the Sagittarius dwarf spheroidal galaxy. *Astronomy & Astrophysics*, 465(3):815–824.

Schiavon, R. P. (2007). Population Synthesis in the Blue. IV. Accurate Model Predictions for Lick Indices and UBV Colors in Single Stellar Populations. *Astrophysical Journal, Supplement*, 171(1):146–205.

Schlafly, E. F. and Finkbeiner, D. P. (2011). Measuring Reddening with Sloan Digital Sky Survey Stellar Spectra and Recalibrating SFD. *Astrophysical Journal*, 737(2):103.

Schuberth, Y., Richtler, T., Dirsch, B., Hilker, M., and Larsen, S. (2005). The outer cluster system of NGC 1399: Preliminary results. *ArXiv Astrophys. E-Prints*, 2004-October. tex.adsnote: Provided by the SAO/NASA Astrophysics Data System tex.adsurl: http://adsabs.harvard.edu/abs/2005astro.ph..1166S tex.eprint: astro-ph/0501166.

Schweizer, F. (2001). Galaxy interactions: Overview. In *American astronomical society meeting abstracts #198*, volume 33 of *Bulletin of the american astronomical society*, page 830. tex.adsnote: Provided by the SAO/NASA Astrophysics Data System tex.adsurl: http://adsabs.harvard.edu/abs/2001AAS...198.3402S tex.eid: 34.02.

Scott, N. and Graham, A. W. (2013). Updated mass scaling relations for nuclear star clusters and a comparison to supermassive black holes. *The Astrophysical Journal*, 763(2):76. arXiv: 1205.5338 [astro-ph.CO] tex.adsnote: Provided by the SAO/NASA Astrophysics Data System tex.adsurl: https://ui.adsabs.harvard.edu/abs/2013ApJ...763...76S tex.eid: 76.

Secker, J., Geisler, D., McLaughlin, D. E., and Harris, W. E. (1995). Washington photometry of the globular cluster system around NGC 3311. I. Analysis of the metallicities. *Astronomical Journal*, 109:1019–1032.

Seth, A. C., Dalcanton, J. J., Hodge, P. W., and Debattista, V. P. (2006). Clues to nuclear star cluster formation from edge-on spirals. *The Astronomical Journal*, 132(6):2539–2555. arXiv: astro-ph/0609302 [astro-ph] tex.adsnote: Provided by the SAO/NASA Astrophysics Data System tex.adsurl: https://ui.adsabs.harvard.edu/abs/2006AJ....132.2539S.

Shapiro, K. L., Genzel, R., and Förster Schreiber, N. M. (2010). Star-forming galaxies at z 2 and the formation of the metal-rich globular cluster population. *Monthly Notices of the Royal Astronomical Society: Letters*, 403(1):L36–l40. arXiv:

1001.1740 tex.adsnote: Provided by the SAO/NASA Astrophysics Data System tex.adsurl: http://adsabs.harvard.edu/abs/2010MNRAS.403L..36S.

Skrutskie, M. F., Cutri, R. M., Stiening, R., Weinberg, M. D., Schneider, S., Carpenter, J. M., Beichman, C., Capps, R., Chester, T., Elias, J., Huchra, J., Liebert, J., Lonsdale, C., Monet, D. G., Price, S., Seitzer, P., Jarrett, T., Kirkpatrick, J. D., Gizis, J. E., Howard, E., Evans, T., Fowler, J., Fullmer, L., Hurt, R., Light, R., Kopan, E. L., Marsh, K. A., McCallon, H. L., Tam, R., Van Dyk, S., and Wheelock, S. (2006). The two micron all sky survey (2MASS). *The Astronomical Journal*, 131(2):1163–1183. tex.adsnote: Provided by the SAO/NASA Astrophysics Data System tex.adsurl: http://adsabs.harvard.edu/abs/2006AJ....131.1163S.

Steinmetz, M. and Navarro, J. F. (2002). The hierarchical origin of galaxy morphologies. New A, 7(4):155–160.

Strader, J., Romanowsky, A. J., Brodie, J. P., Spitler, L. R., Beasley, M. A., Arnold, J. A., Tamura, N., Sharples, R. M., and Arimoto, N. (2011). Wide-field precision kinematics of the M87 globular cluster system. *Astrophysical Journal, Supplement Series*, 197(2):33. arXiv: 1110.2778 tex.adsnote: Provided by the SAO/NASA Astrophysics Data System tex.adsurl: http://adsabs.harvard.edu/abs/2011ApJS..197...33S tex.eid: 33.

Sánchez-Janssen, R. and Aguerri, J. A. L. (2012). Globular cluster systems as tracers of environmental effects on Virgo early-type dwarfs. *Monthly Notices of the Royal Astronomical Society*, 424(4):2614–2624. arXiv: 1205.3176 [astro-ph.CO] tex.adsnote: Provided by the SAO/NASA Astrophysics Data System tex.adsurl: https://ui.adsabs.harvard.edu/abs/2012MNRAS.424.2614S.

Sánchez-Janssen, R., Côté, P., Ferrarese, L., Peng, E. W., Roediger, J., Blakeslee, J. P., Emsellem, E., Puzia, T. H., Spengler, C., Taylor, J., Álamo Martínez, K. A., Boselli, A., Cantiello, M., Cuillandre, J.-C., Duc, P.-A., Durrell, P., Gwyn, S., MacArthur, L. A., Lançon, A., Lim, S., Liu, C., Mei, S., Miller, B., Muñoz, R., Mihos, J. C., Paudel, S., Powalka, M., and Toloba, E. (2019). The next generation virgo cluster survey. XXIII. Fundamentals of nuclear star clusters over seven decades in galaxy mass. *The Astrophysical Journal*, 878(1):18.

arXiv: 1812.01019 [astro-ph.GA] tex.adsnote: Provided by the SAO/NASA Astrophysics Data System tex.adsurl: https://ui.adsabs.harvard.edu/abs/2019ApJ...878...18S tex.eid: 18.

Sánchez-Janssen, R., Ferrarese, L., MacArthur, L. A., Côté, P., Blakeslee, J. P., Cuillandre, J.-C., Duc, P.-A., Durrell, P., Gwyn, S., McConnacchie, A. W., Boselli, A., Courteau, S., Emsellem, E., Mei, S., Peng, E., Puzia, T. H., Roediger, J., Simard, L., Boyer, F., and Santos, M. (2016). The next generation virgo cluster survey. VII. The intrinsic shapes of low-luminosity galaxies in the core of the virgo cluster, and a comparison with the local group. *The Astrophysical Journal*, 820(1):69. arXiv: 1602.00012 [astro-ph.GA] tex.adsnote: Provided by the SAO/NASA Astrophysics Data System tex.adsurl: https://ui.adsabs.harvard.edu/abs/2016ApJ...820...69S tex.eid: 69.

Tamm, A., Tempel, E., Tenjes, P., Tihhonova, O., and Tuvikene, T. (2012). Stellar mass map and dark matter distribution in M 31. *Astronomy and Astrophysics*, 546:A4.

Tamura, N., Sharples, R. M., Arimoto, N., Onodera, M., Ohta, K., and Yamada, Y. (2006). A Subaru/Suprime-Cam wide-field survey of globular cluster populations around M87 - II: Colour and spatial distribution. *Mon. Not. R. Astron. Soc.*, 373(2):601–612.

Taylor, C., Boylan-Kolchin, M., Torrey, P., Vogelsberger, M., and Hernquist, L. (2016). The mass profile of the Milky Way to the virial radius from the Illustris simulation. *Monthly Notices of the Royal Astronomical Society*, 461(4):3483–3493.

Taylor, J. E., Shin, J., Ouellette, N. N.-Q., and Courteau, S. (2019). The Assembly of the Virgo Cluster, Traced by its Galaxy Halos. *ArXiv190607724 Astro-Ph.*

Tegmark, M., Silk, J., Rees, M. J., Blanchard, A., Abel, T., and Palla, F. (1997). How Small Were the First Cosmological Objects? *Astrophysical Journal*, 474:1.

Thomas, D., Greggio, L., and Bender, R. (1999). Stellar yields and chemical evolution - The solar neighborhood as a calibrator. *arXiv e-prints*, pages astro–ph/9912416.

Thronson, Harley A., J. and Telesco, C. M. (1986). Star formation in active dwarf galaxies. *Astrophysical Journal*, 311:98–112.

Tinsley, B. M. (1979). Stellar lifetimes and abundance ratios in chemical evolution. *Astrophysical Journal*, 229:1046–1056.

Tody, D. (1986). *The IRAF Data Reduction and Analysis System*, volume 627 of *Society of Photo-Optical Instrumentation Engineers (SPIE) Conference Series*, page 733.

Tonry, J. L., Blakeslee, J. P., Ajhar, E. A., and Dressler, A. (1997). The SBF Survey of Galaxy Distances. I. Sample Selection, Photometric Calibration, and the Hubble Constant. *The Astrophysical Journal*, 475(2):399–413.

Tremaine, S. D., Ostriker, J. P., and Spitzer, L., J. (1975). The formation of the nuclei of galaxies. I. M31. *The Astrophysical Journal*, 196:407–411. tex.adsnote: Provided by the SAO/NASA Astrophysics Data System tex.adsurl: https://ui.adsabs.harvard.edu/abs/1975ApJ...196..407T.

Tripicco, M. J. and Bell, R. A. (1995). Modeling the LICK/IDS Spectral Feature Indices Using Synthetic Spectra. *Astronomical Journal*, 110:3035.

Turner, M. L., Côté, P., Ferrarese, L., Jordán, A., Blakeslee, J. P., Mei, S., Peng, E. W., and West, M. J. (2012). The ACS fornax cluster survey. VI. The nuclei of early-type galaxies in the fornax cluster. *Astrophysical Journal, Supplement Series*, 203(1):5. arXiv: 1208.0338 [astro-ph.CO] tex.adsnote: Provided by the SAO/NASA Astrophysics Data System tex.adsurl: https://ui.adsabs.harvard.edu/abs/2012ApJS..203....5T tex.eid: 5.

Usher, C., Brodie, J. P., Forbes, D. A., Romanowsky, A. J., Strader, J., Pfeffer, J., and Bastian, N. (2019). The SLUGGS Survey: Measuring globular cluster ages using both photometry and spectroscopy. *ArXiv190905753 Astro-Ph.*

Valdes, F., Gupta, R., Rose, J. A., Singh, H. P., and Bell, D. J. (2004). The Indo-US Library of Coudé Feed Stellar Spectra. *Astrophysical Journal, Supplement*, 152(2):251–259.

Valenti, E., Zoccali, M., Renzini, A., Brown, T. M., Gonzalez, O. A., Minniti, D., Debattista, V. P., and Mayer, L. (2013). Stellar ages through the corners of the boxy bulge. *Astronomy & Astrophysics*, 559:A98.

van den Bergh, S. (2000). The Mass of the Centaurus A Group of Galaxies. *The Astronomical Journal*, 119(2):609–611.

Van Dokkum, P., Abraham, R., Romanowsky, A. J., Brodie, J., Conroy, C., Danieli, S., Lokhorst, D., Merritt, A., Mowla, L., and Zhang, J. (2017). Extensive globular cluster systems associated with ultra diffuse galaxies in the coma cluster. *arXiv*, 844(1):L11.

van Dokkum, P. G. and Conroy, C. (2012). The Stellar Initial Mass Function in Early-type Galaxies from Absorption Line Spectroscopy. I. Data and Empirical Trends. *Astrophysical Journal*, 760(1):70.

Vargas, L. C., Geha, M., Kirby, E. N., and Simon, J. D. (2013). The Distribution of Alpha Elements in Ultra-faint Dwarf Galaxies. *Astrophysical Journal*, 767(2):134.

Vazdekis, A., Casuso, E., Peletier, R. F., and Beckman, J. E. (1996). A New Chemo-evolutionary Population Synthesis Model for Early-Type Galaxies. I. Theoretical Basis. *Astrophysical Journal, Supplement*, 106:307.

Vazdekis, A., Coelho, P., Cassisi, S., Ricciardelli, E., Falcón-Barroso, J., Sánchez-Blázquez, P., La Barbera, F., Beasley, M. A., and Pietrinferni, A. (2015). Evolutionary stellar population synthesis with MILES - II. Scaled-solar and α-enhanced models. *Monthy Notices of the Royal Astronomical Society*, 449(2):1177–1214.

Vazdekis, A., Koleva, M., Ricciardelli, E., Röck, B., and Falcón-Barroso, J. (2016). UV-extended E-MILES stellar population models: young components in massive early-type galaxies. *Monthy Notices of the Royal Astronomical Society*, 463(4):3409–3436.

Vazdekis, A., Ricciardelli, E., Cenarro, A. J., Rivero-González, J. G., Díaz-García, L. A., and Falcón-Barroso, J. (2012). MIUSCAT: extended MILES spectral coverage - I. Stellar population synthesis models. *Monthy Notices of the Royal Astronomical Society*, 424(1):157–171.

Vazdekis, A., Sánchez-Blázquez, P., Falcón-Barroso, J., Cenarro, A. J., Beasley, M. A., Cardiel, N., Gorgas, J., and Peletier, R. F. (2010). Evolutionary stellar population synthesis with

MILES - I. The base models and a new line index system. *Monthy Notices of the Royal Astronomical Society*, 404(4):1639–1671.

Venables, B. and Ripley, B. (2002). *Modern Applied Statistics With S.*

Venn, K. A., Tolstoy, E., Kaufer, A., and Kudritzki, R. P. (2004). Stellar Abundances in Dwarf Irregular Galaxies. In McWilliam, A. and Rauch, M., editors, *Origin and Evolution of the Elements*, page 58.

Villaume, A., Conroy, C., Johnson, B., Rayner, J., Mann, A. W., and van Dokkum, P. (2017). The Extended IRTF Spectral Library: Expanded Coverage in Metallicity, Temperature, and Surface Gravity. *Astrophysical Journal, Supplement*, 230(2):23.

Villaume, A., Romanowsky, A. J., Brodie, J., and Strader, J. (2019). New Constraints on Early-type Galaxy Assembly from Spectroscopic Metallicities of Globular Clusters in M87. *ApJ*, 879(1):45.

Vulcani, B., Poggianti, B. M., Gullieuszik, M., Moretti, A., Tonnesen, S., Jaffé, Y. L., Fritz, J., Fasano, G., and Bettoni, D. (2018). Enhanced Star Formation in Both Disks and Ram-pressure-stripped Tails of GASP Jellyfish Galaxies. *Astrophysical Journal*, 866(2):L25.

Walcher, C. J., van der Marel, R. P., McLaughlin, D., Rix, H. W., Böker, T., Häring, N., Ho, L. C., Sarzi, M., and Shields, J. C. (2005). Masses of star clusters in the nuclei of bulge-less spiral galaxies. *The Astrophysical Journal*, 618(1):237–246. arXiv: astro-ph/0409216 [astro-ph] tex.adsnote: Provided by the SAO/NASA Astrophysics Data System tex.adsurl: https://ui.adsabs.harvard.edu/abs/2005ApJ...618..237W.

Wehner, E., Harris, B., Whitmore, B., Rothberg, B., and Woodley, K. (2008a). The Globular Cluster Systems around NGC 3311 and NGC 3309. *ApJ*, 681(2):1233–1247.

Wehner, E., Harris, B., Whitmore, B., Rothberg, B., and Woodley, K. (2008b). The Globular Cluster Systems around NGC 3311 and NGC 3309. *ApJ*, 681(2):1233–1247.

Wehner, E., Harris, B., Whitmore, B., Rothberg, B., and Woodley, K. (2008c). The Globular Cluster Systems around NGC 3311 and NGC 3309. *ApJ*, 681(2):1233–1247.

Wenger, M., Ochsenbein, F., Egret, D., Dubois, P., Bonnarel, F., Borde, S., Genova, F., Jasniewicz, G., Laloë, S., Lesteven, S., and Monier, R. (2000). The SIMBAD astronomical database. The CDS reference database for astronomical objects. *Astronomy and Astrophysics, Supplement*, 143:9–22.

White, S. D. M. and Rees, M. J. (1978). Core condensation in heavy halos: a two-stage theory for galaxy formation and clustering. *Monthly Notices of the Royal Astronomical Society*, 183(3):341–358. tex.adsnote: Provided by the SAO/NASA Astrophysics Data System tex.adsurl: https://ui.adsabs.harvard.edu/abs/1978MNRAS.183..341W.

White, S. D. M. and Rees, M. J. (1978). Core condensation in heavy halos: a two-stage theory for galaxy formation and clustering. *Monthy Notices of the Royal Astronomical Society*, 183:341–358.

Whitmore, B. C., Gilmore, D. M., and Jones, C. (1993). What determines the morphological fractions in clusters of galaxies? *The Astrophysical Journal*, 407:489–509. tex.adsnote: Provided by the SAO/NASA Astrophysics Data System tex.adsurl: http://adsabs.harvard.edu/abs/1993ApJ...407..489W.

Woo, J., Courteau, S., and Dekel, A. (2008). Scaling relations and the fundamental line of the local group dwarf galaxies. *Monthly Notices of the Royal Astronomical Society*, 390(4):1453–1469. arXiv: 0807.1331 [astro-ph] tex.adsnote: Provided by the SAO/NASA Astrophysics Data System tex.adsurl: https://ui.adsabs.harvard.edu/abs/2008MNRAS.390.1453W.

Woodley, K. A., Harris, W. E., Puzia, T. H., Gomez, M., Harris, G. L. H., and Geisler, D. (2010). The Ages, Metallicities and Alpha Element Enhancements of Globular Clusters in the Elliptical NGC 5128: A Homogeneous Spectroscopic Study with Gemini/GMOS. *ApJ*, 708(2):1335–1356.

Woosley, S. E. and Weaver, T. A. (1995). The Evolution and Explosion of Massive Stars. II. Explosive Hydrodynamics and Nucleosynthesis. *Astrophysical Journal, Supplement*, 101:181.

Wright, A. C., Tremmel, M., Brooks, A. M., Munshi, F., Nagai, D., Sharma, R. S., and Quinn,

T. R. (2021). The formation of isolated ultradiffuse galaxies in ROMULUS25. *Monthy Notices of the Royal Astronomical Society*, 502(4):5370–5389.

Wu, X. and Tremaine, S. (2006). Deriving the Mass Distribution of M87 from Globular Clusters. *Astrophysical Journal*, 643(1):210–221.

Yagi, M., Koda, J., Komiyama, Y., and Yamanoi, H. (2016). Catalog of Ultra-Diffuse Galaxies in the Coma Clusters From Subaru Imaging Data. *The Astrophysical Journal Supplement Series*, 225(1):11.

Yamasaki, N. Y., Ohashi, T., and Furusho, T. (2002). Chandra Observation of the Central Galaxies in the A1060 Cluster of Galaxies. *Astrophysical Journal*, 578(2):833–841.

Yoon, S.-J., Lee, S.-Y., Blakeslee, J. P., Peng, E. W., Sohn, S. T., Cho, J., Kim, H.-S., Chung, C., Kim, S., and Lee, Y.-W. (2011a). Nonlinear Color-Metallicity Relations of Globular Clusters. III. On the Discrepancy in Metallicity between Globular Cluster Systems and Their Parent Elliptical Galaxies. *\apj*, 743(2):150.

Yoon, S.-J., Sohn, S. T., Lee, S.-Y., Kim, H.-S., Cho, J., Chung, C., and Blakeslee, J. P. (2011b). Nonlinear Color-Metallicity Relations of Globular Clusters. II. A Test on the Nonlinearity Scenario for Color Bimodality Using the u-band Colors: The Case of M87 (NGC 4486). *\apj*, 743(2):149.

Yoon, S.-J., Yi, S. K., and Lee, Y.-W. (2006). Explaining the color distributions of globular cluster systems in elliptical galaxies. *Science*, 311(5764):1129–1132. tex.adsnote: Provided by the SAO/NASA Astrophysics Data System tex.adsurl: http://adsabs.harvard.edu/abs/2006Sci...311.1129Y tex.eprint: astro-ph/0601526.

Yoon, Y., Im, M., and Kim, J.-W. (2017). Massive Galaxies Are Larger in Dense Environments: Environmental Dependence of Mass-Size Relation of Early-type Galaxies. *Astrophysical Journal*, 834(1):73.

Zanatta, E., Sánchez-Janssen, R., Chies-Santos, A. L., de Souza, R. S., and Blakeslee, J. P. (2021). A high occurrence of nuclear star clusters in faint Coma galaxies, and the roles of mass and environment. *Monthy Notices of the Royal Astronomical Society*.

Zanatta, E. J. B., Cortesi, A., Chies-Santos, A. L., Forbes, D. A., Romanowsky, A. J., Alabi, A. B., Coccato, L., Mendes de Oliveira, C., Brodie, J. P., and Merrifield, M. (2018). Chromodynamical analysis of lenticular galaxies using globular clusters and planetary nebulae. *Monthy Notices of the Royal Astronomical Society*, 479(4):5124–5135.